University of Crete
Department of Physics

Spatial and temporal variability in the atmosphere and surface of Titan's atmosphere: Simulation and interpretation through space and ground-based observations

by

Panayotis Lavvas

Thesis

submitted for the Degree of Doctor of Philosophy in Physics

PhD Thesis

Spatial and temporal variability in the atmosphere and surface of Titan's atmosphere: Simulation and interpretation through space and ground-based observations

Thesis Author : P. Lavvas

Thesis Supervisor : I.M. Vardavas

Thesis Committee :

S. Anastasiadis
Member

A. Coustenis
External supervisor

D. Hatzidimitriou
Member

P. Kelires
Member

N. Mihalopoulos
Member

I. Papadakis
Member

I. Papamastorakis
Member

I.M. Vardavas
Thesis supervisor

Vast the seas of knowledge,
Vastest the thirst of man.

Acknowledgements

I would like to thank my supervisor, Prof. Ilias M. Vardavas for his guidance and encouragement. We had great discussions and he has provided fruitful suggestions for my study. But most of all I would like to thank him for his confidence in me and his warm support all this time.

The accomplishment of this research would not be possible without the help and support by Dr HDR. Athena Coustenis of the Paris Observatory. Dr. Coustenis has provided far more than simple suggestions and scientific information. Her advice, support and encouragement has helped me immensely during my research. Furthermore, she has provided me with the opportunity to visit the observatory many times where I had valuable discussions with other scientists in the field and was informed about the progress of the Cassini/Huygens mission.

I would also like to thank Profs. I. Papamastorakis and D. Hatzidimitriou for their support in the progress of my work.

Furthermore, I would like to thank the Department of Physics of the University of Crete and the Foundation for Research and Technology - Hellas (FORTH) for supporting my research.

Last but not least, I would like to thank my friends and family for their love and support. But mostly I would like to thank my parents for their confidence in my pursuits and for teaching me, through their way of living, how to address life with patience and persistence. These assets were the most valuable during the years of my study.

This research was co-funded by the European Social Fund & National Resources - EPEAEK II - HERAKLEITOS (contract: 1857) and by the General Secretary for Research and Technology within the framework of the Greek-French collaboration program Platon (contract: 2143).

Περίληψη

Ένα νέο μονοδιάστατο υπολογιστικό μοντέλο το οποίο συνδέει τη διάδοση της ακτινοβολίας, τη φωτοχημεία και τη μικροφυσική σε μια πλανητική ατμόσφαιρα, κατασκευάστηκε και εφαρμόστηκε για τη μελέτη των χωρικών και χρονικών μεταβολών της ατμόσφαιρας του Τιτάνα, και ειδικότερα τη φωτοχημική παραγωγή των αερολυμάτων της ατμόσφαιράς του. Οι χωρικές μεταβολές αφορούν την καθ΄ ύψος δομή της ατμόσφαιρας όπως αυτή καθορίζεται από τις διαφορετικές φυσικές και χημικές διεργασίες καθώς και τη διάδοση της ακτινοβολίας που λαμβάνουν χώρα. Οι χρονικές μεταβολές αφορούν την επίδραση του 11-ετούς ηλιακού κύκλου στην καθ΄ ύψος δομή της ατμόσφαιρας.

Το μοντέλο περιλαμβάνει λεπτομερείς υπολογισμούς για τον υπολογισμό της ροής της ακτινοβολίας για τα μικρά (υπεριώδες, ορατό και κοντινό υπέρυθρο) και μεγάλα (υπέρυθρο) μήκη κύματος, που παρέχουν την καθ΄ ύψος δομή του πεδίου της ακτινοβολίας και καθορίζουν τη δομή της θερμοκρασίας. Αυτές χρησιμοποιούνται για τη περιγραφή της δημιουργίας της φωτοχημικής σύστασης και της δομής των αερολυμάτων οι οποίες ξεκινούν με τη φωτόλυση των κύριων συστατικών της ατμόσφαιρας του Τιτάνα, του αζώτου και του μεθανίου. Τα χημικά στοιχεία που δημιουργούνται χρησιμοποιούνται για την παραγωγή των δομικών δομών των αερολυμάτων, η εξέλιξη των οποίων περιγράφεται από το μικροφυσικό τμήμα του μοντέλου. Οι υπολογισμένες δομές της χημικής σύστασης και αυτή των αερολυμάτων στη συνέχεια, εισέρχονται στους υπολογισμούς της διάδοσης της ακτινοβολίας έτσι ώστε να ελεγχθεί η επίδρασή τους στη δομή της ακτινοβολίας και στη γεωμετρική ανάκλαση της ατμόσφαιρας. Ο βασικός στόχος αυτού του υπολογιστικού μοντέλου είναι η κατανόηση του άγνωστου μέχρι στιγμής κρίκου μεταξύ της παραγωγής των αέριων στοιχείων στην ατμόσφαιρα του Τιτάνα και της μετατροπής τους στα παρατηρούμενα αερολύματα.

Το μοντέλο δημιουργεί τη δομή των αερολυμάτων από την αέρια φωτοχημεία. Τα αποτελέσματα του μοντέλου για την καθ΄ ύψος συγκέντρωση του κάθε στοιχείου, τη δημιουργία των αερολυμάτων και τις οπτικές τους ιδιότητες, την καθ΄ ύψος δομή της θερμοκρασίας και της ατμοσφαιρικής πυκνότητας και τη γεωμετρική ανάκλαση παρουσιάζονται και συγκρίνονται με τα τελευταία αποτελέσματα από τη διαστημική αποστολή Cassini/Huygens καθώς και με προηγούμενες επίγειες και διαστημικές παρατηρήσεις. Το μοντέλο καταφέρνει να αναπαράγει σωστά τις περισσότερες από τις τελευταίες μετρήσεις για τη συγκέντρωση και καθ΄ ύψος δομή των χημικών στοιχείων της ατμόσφαιρας του Τιτάνα. Για την παραγωγή των

αερολυμάτων χρησιμοποιήθηκαν διαδικασίες οι οποίες περιλαμβάνουν καθαρούς υδρογονάνθρακες (μόνο άνθρακας και υδρογόνο), αζωτούχους υδρογονάνθρακες (περιλαμβάνουν και N) καθώς και συνδυασμούς των δύο (συν-πολυμερή). Από αυτούς, οι αζωτούχοι υδρογονάνθρακες και τα συν-πολυμερή, βρέθηκε να έχουν τη σημαντικότερη συνεισφορά στη παραγωγή των αερολυμάτων. Αυτό το αποτέλεσμα είναι σε συμφωνία και με τις μετρήσεις από το όργανο ACP της ακάτου Huygens, το οποίο έδωσε ενδείξεις για την ύπαρξη αζώτου στη δομή των αερολυμάτων. Το μοντέλο αποκαλύπτει την ύπαρξη μια νέας σημαντικής ζώνης παραγωγής αερολυμάτων μεταξύ 500 και 900 χλμ. η οποία προέρχεται από τα συν-πολυμερή και η οποία έχει σημαντικές επιδράσεις για τη δομή της θερμοκρασίας και τη γεωμετρική ανάκλαση. Πιο συγκεκριμένα, η ύπαρξη αυτής της δεύτερης κορυφής καθορίζει την καθ' ύψος παραγωγή των αερολυμάτων. Ο 11-ετής ηλιακός κύκλος επηρεάζει τη δομή των χημικών στοιχείων και τελικά έχει ως αποτέλεσμα την αύξηση της παραγωγής αερολυμάτων κατά 60% μεταξύ ηλιακού ελαχίστου και μεγίστου. Αυτό έχει περαιτέρω επιδράσεις στη δομή της θερμοκρασίας και στη γεωμετρική ανάκλαση.

Τα αποτελέσματα του μοντέλου συγκρίθηκαν και με την καθ' ύψος δομή των οπτικών ιδιοτήτων των αερολυμάτων, όπως αυτή μετρήθηκε από το όργανο DISR, με την οποία βρέθηκε να είναι σε καλή συμφωνία. Επίσης, ετερογενείς χημικές διαδικασίες στην επιφάνεια των αερολυμάτων, οι οποίες μετατρέπουν ατομικό υδρογόνο σε μοριακό, συμπεριλήφθηκαν στο μοντέλο. Αυτές είχαν σαν αποτέλεσμα τη βελτίωση των αποτελεσμάτων για το μοριακό υδρογόνο σε σχέση με τις μετρήσεις από το όργανο INMS και για τη δι-ασετιλίνη με βάση τις μετρήσεις από το όργανο CIRS.

Abstract

A new 1D coupled Radiative / Convective - Photochemical - Microphysical model for a planetary atmosphere was developed and applied to the investigation of the spatial and temporal variability of Titan's atmosphere, and in particular to photochemical haze production. The spatial variability corresponds to the vertical structure of the atmosphere and the way this is determined by the different physical, chemical and radiative processes that take place. The temporal variability, addresses the impact of the 11-year solar cycle on the vertical structure of the atmosphere.

The model incorporates detailed radiation transfer calculations for the description of the shortwave and longwave fluxes which provide the vertical structure of the radiation field and determine the temperature profile. These are used for the generation of the photochemical and haze structure in the atmosphere, initiated by the photolysis of Titan's main constituents, nitrogen (N_2) and methane (CH_4). The resulting hydrocarbons and nitriles are used for the production of the haze precursors, whose evolution is described by the microphysical part of the model. The calculated aerosol and gas opacities are iteratively included in the radiation transfer calculations in order to investigate their effect on the resulting temperature profile and geometric albedo. The main purpose of this model is to help in the understanding of the missing link between the production of gaseous species and their transformation to haze particles in Titan's atmosphere.

The model generates the haze structure from the gaseous species photochemistry. Model results are presented for the species vertical concentration profiles, haze formation and its radiative properties, vertical temperature/density profiles and geometric albedo. These are validated against the very recent Cassini/Huygens observations and also against other ground-based and spaceborne measurements. The model reproduces well most of the latest measurements from the Cassini/Huygens instruments for the chemical composition of Titan's atmosphere and the vertical profiles of the observed species. For the haze production, we have included pathways that are based on pure hydrocarbons, pure nitriles and hydrocarbon/nitrile copolymers. From these, the nitrile and copolymer pathways provide the stronger contribution, in agreement with the results from the ACP instrument, which support the incorporation of nitrogen in the pyrolised haze structures. The haze model reveals a new second major peak in the vertical profile of haze production rate between 500 and 900 km.

This peak is produced by the copolymer family used and has important ramifications for the vertical atmospheric temperature profile and geometric albedo. In particular, the existence of this second peak determines the vertical profile of haze extinction. The solar cycle variability affects the species vertical profiles and eventually results in increase in the haze production of about 60% from solar minimum to solar maximum. This has further effects on the geometric albedo and the vertical temperature structure.

The model results have been compared with the DISR retrieved haze extinction profiles and are found to be in very good agreement. Furthermore, heterogeneous chemistry on the haze particles that converts atomic hydrogen to molecular hydrogen has been incorporated in the model. The resultant H_2 profile is closer to the INMS measurements, while the vertical profile of the diacetylene formed is found to be closer to that of the CIRS profile when this heterogeneous chemistry is included.

Contents

Introduction **1**

1 Titan's Properties **7**
1.1 From mythology to discovery 7
1.2 Physical properties 10
1.2.1 Atmospheric structure 10
1.2.2 Geometric albedo 15
1.2.3 Observed gas species 17
1.2.4 Aerosols 19
1.2.5 Spatial & temporal variability 21
1.2.6 Condensates & clouds 23
1.2.7 Surface properties 24
1.2.8 Open questions 26

2 Simulation of Atmospheric Processes **31**
2.1 Energy sources 32
2.1.1 Solar photons 32
2.1.2 Electron flux 35
2.1.3 Galactic cosmic rays 35
2.2 Radiation transfer 37
2.2.1 Spectral division & opacity sources 37
2.2.2 Shortwave radiation transfer 39
2.2.3 Longwave radiation transfer 40
2.2.4 Temperature calculation 41
2.3 Photochemistry 43
2.3.1 Photolysis 43
2.3.2 Chemical schemes 49
2.3.3 Vertical transport 66
2.3.4 Condensation 67
2.3.5 Simulation method 68
2.4 Microphysics 75
2.4.1 Radial grid 76
2.4.2 Physical parameters 77
2.4.3 Coagulation kernels 81

2.4.4 Method of solution 85

3 Pathways of Haze Formation 105
3.1 Laboratory measurements 105
3.2 Huygens in situ measurements 109
3.3 Suggested pathways 109
3.3.1 Monomer size 114
3.3.2 Chemical loss to haze 115

4 Chemical Composition 121
4.1 Eddy mixing profile 121
4.2 Validation with Cassini/Huygens 126
4.2.1 Hydrocarbons 127
4.2.2 Nitriles 143
4.3 Solar cycle effects 154

5 Haze Production 165
5.1 Haze pathways 165
5.1.1 Aromatics 165
5.1.2 Polyynes 166
5.1.3 Aliphatic copolymers 167
5.1.4 Pure nitriles 168
5.1.5 Haze production profile and the role of GCR 169
5.2 Chemical loss to haze 174
5.3 Solar cycle effects 178

6 Haze Opacity & Atmospheric Structure 181
6.1 Haze radiative properties 181
6.1.1 Size distribution 181
6.1.2 Opacity and structure 184
6.1.3 Geometric & surface albedo 189
6.2 Atmospheric structure 193
6.3 Solar cycle effects 197

7 Discussion & Conclusions 203
7.1 Discussion 203
7.1.1 Haze pathways and chemical loss 203
7.1.2 N_2 dissociative photoionization and nitriles 204
7.1.3 Heterogeneous chemistry 204
7.1.4 The role of methyl radicals 205
7.1.5 Solar cycle effects 205
7.2 Conclusions 206

Epilogue 209

A Light Interaction with Matter **211**
A.1 Absorption 212
A.1.1 Spectroscopic data 214
A.1.2 Spectral line profiles 216
A.1.3 Methane coefficients 219
A.1.4 Correlated k-distribution coefficients 221
A.1.5 Collision induced absorption (CIA) 224
A.2 Scattering 225
A.2.1 Rayleigh scattering 228
A.2.2 Mie scattering 230

B Multiple Scattering **239**
B.1 Isotropic scattering solution 239
B.2 Anisotropic scattering solution 241
B.2.1 Enhancement factor for photolysis 244
B.2.2 Delta-Eddington approximation 245
B.2.3 Inhomogeneous layers 245

Acronyms **249**

List of Figures **251**

List of Tables **255**

Index **257**

Introduction

From the initial observation by Huygens (1655) and the methane detection by Kuiper (1944) to the recent Cassini/Huygens space mission, Titan has been the subject of many studies that have aimed towards understanding its climate and the important role of the haze that is formed in its atmosphere and obscures its surface from direct observations in the visible. The processes that control haze formation and its radiative properties have been the least understood to date. The recent success of the Cassini/Huygens mission has provided valuable validation data that supplement the earlier Voyager mission data and many years of ground-based observations.

The most prominent characteristic of Titan's atmosphere is the well defined haze structure, observed since the Voyager era (Rages & Pollack, 1980). The haze is directly observed since it provides the orange color of Titan's atmosphere in the visible images and its origin is linked to the photochemistry taking place in its atmosphere. Nitrogen and methane, the most abundant constituents in Titan's atmosphere, are photodissociated by solar ultraviolet radiation, energetic particles from Saturn's magnetosphere and galactic cosmic rays (GCR), leading to the initiation of a complex organic photochemistry, which finally produces the haze. This coupling between the photochemistry and haze formation is the subject of the present thesis.

The neutral photochemistry in Titan's atmosphere was investigated even before the Voyager era (Strobel, 1974; Allen et al., 1980). The Voyager mission provided data that led to the first detailed photochemical model developed by Yung et al. (1984) which described the basic photochemical schemes that control the abundance of the observed hydrocarbons and nitriles in Titan's atmosphere. Based on this early work, further analysis of Voyager data and ground-based observations, more advanced photochemical models were developed. Toublanc et al. (1995) used an elaborate Monte Carlo description for solar radiation transfer within the atmosphere to investigate the possible production of oxygen-containing species arising from an influx of water vapor at the top of the atmosphere. Lara *et al.* (1996) used an ablation profile for the water vapor influx, included the effects of GCR and presented a physical description of the condensation processes taking place in Titan's lower stratosphere. Lebonnois et al. (2001) investigated the seasonal variation of the composition in Titan's stratosphere using a 2-D (latitude-altitude) model. Beyond neutral species chemistry, models have included ionospheric chemistry, as in the recent

work of Wilson & Atreya (2004) where the contributions of energetic electrons and photoelectrons were included.

A common approach to modelling the photochemistry has been to generate the vertical temperature distribution, from the surface to the thermosphere, using temperature vertical profiles that were synthesized by combining measurements from Voyager I (Lindal et al., 1983) and model results for the temperature structure at different altitudes (Lellouch et al., 1989; Yelle, 1991; Yelle et al., 1997). Further, in order to include the effects of the aerosols in the radiation transfer calculations, vertical profiles of haze opacity were either specified by a simple exponential decrease with altitude or in more recent work generated by microphysical models using a specified vertical haze production rate (Yung et al., 1984; Lebonnois et al., 2001; Wilson & Atreya, 2004). Using this approach, photochemical models have managed to fit most of the atmospheric species concentrations available from observations before the Cassini/Huygens mission (Coustenis & Bézard, 1995). Here, a modelling approach that generates the thermal structure, the atmospheric composition and the haze structure, in a self-consistent manner is developed. The haze is produced from polymer production governed by the photochemistry, which is determined by and determines both the radiation field and atmospheric temperature structure.

The microphysical models used to derive the haze vertical structure and its optical properties are usually validated against Titan's spectral geometric albedo from the ultraviolet to the near-infrared based on ground-based and space observations. As was first shown by McKay et al. (1989), the fit to the spectral geometric albedo depends mainly on three parameters; the haze particles' optical properties (refractive index, size, shape and amount), the methane profile and Titan's surface reflectivity; using different spectral domains of the above region, constraints can be set on the values of parameters controlling the haze structure.

The haze particles' refractive index is based on laboratory measurements, while the size and amount is generated by the microphysical models, assuming their shape. The shape of the haze particles in Titan's atmosphere has been the subject of debate for a long time due to different size estimates derived by different observations. In order to overcome this problem, two possible solutions were suggested; one of a bimodal distribution (Courtin et al., 1991; Toon et al., 1992) and the other of fractal aggregates constructed from spherical units (West & Smith, 1991; Rannou et al., 1995, 1997). Since then many microphysical models using the fractal aggregates have been published (Rannou et al. 2003 and references therein) although they still have some drawbacks which are discussed in more detail in Chapter 2. The most important is the requirement for a haze clearing at low altitudes, below 100 km. Yet, the recent results from the DISR instrument on board the Huygens probe (Tomasko et al., 2005) show that the haze opacity extends down to the surface. In this work the particles are assumed to attain a spherical shape, starting from the monomer's size which corresponds to the smallest aerosol particle generated by the photochemical description. No fractal structures are considered.

In addition to the shape/size, the haze particles' refractive index is an important parameter in the model calculations. Until recently, most models used

the first laboratory measurements for the refractive index of Titan haze-type analogs (tholins) made by Khare et al. (1984a); scaled by a factor which depends on the wavelength and the type of particles used; for spherical particles 4/3 in the shortwave region of the geometric albedo (McKay et al., 1989), while for fractal particles 3 in the UV and 1.5 in the visible (Rannou et al., 1995). More recent measurements have shown that the optical properties of the laboratory haze analogs depend significantly on the experimental conditions (McKay et al., 2001). Recently, Imanaka et al. (2004) have shown that the pressure under which the analogs are made defines their chemical structure and hence their radiative properties. Hence, photochemically produced particles at different altitudes in Titan's atmosphere could exhibit different optical properties.

An important simplification made in current haze microphysical models has been the adopted haze particle production rate. In most cases this is done by a symmetrical distribution (usually Gaussian) centered at some chosen altitude, usually between 350 and 600 km depending on the model, and the total column production rate varied to fit the geometric albedo. In addition, some models, calculate the radiation field but do not calculate the temperature profile that results from the model haze structure, but use synthetic temperature profiles. Recent photochemical calculations have demonstrated that vertical haze production profiles generated from the photochemistry (Lebonnois et al., 2002; Wilson & Atreya, 2003) are significantly different from the simple profiles adopted in current haze microphysical models.

In the present work, the haze production profile is generated from the photochemistry and then is used to produce the haze vertical structure and its radiative properties. The model temperature structure then depends on the vertical haze profile. The model temperature structure, the spectral geometric albedo and the vertical distributions of the concentrations of the chemical species are validated against measurements. In particular, the model results are validated against the so far available Cassini/Huygens data. With this process, insight to the atmospheric processes and answers to many issues can be given. These include:

1. How does photochemistry leads to the haze formation? Which are the main species involved and the important pathways that lead to the gas-particle transformation?

2. What is the impact of haze formation on the observed chemical composition?

3. What is the vertical structure of haze and its optical properties based on the photochemical origin?

4. How does the photochemically produced haze structure correlate with the observed temperature structure and geometric albedo?

5. What is the impact of different laboratory refractive indexes for the haze particles on the temperature structure and radiation field?

In the chapters which follow, first a quick but detailed description of Titan's observed properties is provided based on the latest measurements from Cassini/Huygens mission and previous ground-based and space-born observations (Chapter 1). Following, the description of the developed model an the physical processes included is given (Chapter 2). Chapter 3 provides a discussion about what is currently understood for the properties of the haze particles based on the simulation of their production in laboratory experiments and from the in situ measurements performed from the Huygens probe. Further, the haze pathways which are used for the description of the gas to particle transformation are presented. Chapter 4 presents the results of the model simulation regarding the species vertical profiles which are validated against the observed abundances from Cassini/Huygens while in Chapter 5 the haze production generated from the used pathways is discussed. The vertical structure and optical properties of the evolved haze particles based on the photochemical description are described in Chapter 6 followed by the model simulated geometric albedo and vertical temperature structure which are validates against observations (Chapter 7). Finally, discussion of the model results and final conclusions are given in Chapter 8.

Bibliography

Allen, M., Pinto, J.P., Yung, Y.L., 1980. Titan: aerosol photochemistry and variations related to the sunspot cycle. Astrophys. J. 242, L125-L128.

Courtin, R., Wagener, R., McKay, C.P., Caldwell, J., Fricke, K.-H., Raulin, F., Bruston, P., 1991. UV spectroscopy of Titan's atmosphere, planetary organic chemistry and prebiological synthesis II. Interpretation of new IUE observations in the 220•335 nm range. Icarus 90, 43-•56.

Coustenis, A., Lellouch, E., Maillard, J.P., McKay, C.P., 1995. Titan's surface: Composition and variability from the near-infrared albedo. Icarus 118, 87-104.

Imanaka, H., Khare, B.N., Elsila, J.E., Bakes, E.L.O., McKay, C.P., Cruikshank, D.P., Sugita, S., Matsui, T., Zare, R.N., 2004. Laboratory experiments of Titan tholin formed in cold plasma at various pressures: implications for nitrogen-containing polycyclic aromatic compounds in Titan haze. Icarus 168, 344-366.

Khare, B.N., Sagan, C., Arakawa, E.T., Suits, F., Calcott, T.A., Williams, M.W., 1984a. Optical constants of organic tholins produced in a simulated Titanian atmosphere: from soft X-ray to microwave frequencies. Icarus 60, 127-137.

Kuiper, G.P. (1944). Titan: A satellite with an atmosphere. Astrophys. J. 100, 378-383

Lara, L.M., Lellouch, E., Lopez-Moreno, J., Rodrigo, R., 1996. Vertical distribution of Titan's atmospheric neutral constituents. J. Geophys. Res. 101, 23261•23283.

Lebonnois, S., Toublanc, D., Hourdin, F., Rannou, P., 2001. Seasonal variations of Titan's atmospheric composition. Icarus 152, 384-406.

Lebonnois, S., Bakes, E.L.O., McKay, C.P., 2002. Transition from gaseous compounds to aerosols in Titan's atmosphere. Icarus 159, 505-517.

Lellouch, E., Coustenis, A., Gautier, D., Raulin, F., Dubouloz, N., Frere, C., 1989. Titan's atmosphere and hypothesized ocean•A reanalysis of the Voyager 1 radio-occultation and IRIS 7.7 μm data. Icarus 79, 328•349.

Lindal, G.F., Wood, G.E., Hotz, H.B., Sweetnam, D.N., Eshleman, V.R., Tyler, G.L., 1983. The atmosphere of Titan: An analysis of the Voyager 1 radio occultation measurements. Icarus 53, 348-363.

McKay, C.P., Pollack, J.B., Courtin, R., 1989. The thermal structure of Titan's atmosphere. Icarus 80, 23-53.

McKay, C.P., Coustenis, A., Samuelson, R.E., Lemmon, M.T., Lorenz, R.D., Cabane, M., Rannou, P., Drossart, P., 2001. Physical properties of the organic aerosols and clouds on Titan. Planet. Space Sci. 49, 79•99.

Rages, K., Pollack, J.B., 1980. Titan aerosols: Optical properties and vertical distribution. Icarus 41, 119-130.

Rages, K., Pollack, J.B., Smith, P.H., 1983. Size estimate of Titan's aerosols based on Voyager high-phase-angle images. J. Geophys. Res. 88, 8721-8728.

Rannou, P., Cabane, M., Chassefiere, E., Botet, R., McKay, C.P., Courtin, R., 1995. Titan's geometric albedo: Role of the fractal structure of the aerosols. Icarus 118, 355-372.

Rannou, P., Cabane, M., Botet, R., Chassefiere, E., 1997. A new interpretation of scattered light measurements at Titan's limb. J. Geophys. Res. 102, 10997-11014.

Rannou, P., McKay, C.P., Lorenz, R.D., 2003. A model of Titan's haze of fractal aerosols constrained by multiple observations. Planet. Space Sci. 51, 963-976.

Strobel, D.F., 1974. The photochemistry of hydrocarbons in the atmosphere of Titan. Icarus 21, 466-470.

Tomasko, M.G., Smith, P.H., 1982. Photometry and polarimetry of Titan: Pioneer 11 observations and their implications for aerosols properties. Icarus 51, 65-95.

Tomasko, M.G., Lemmon, M., Roose, L.R., Smith, P.H., Eibl, A., West, R.A., 1997. Models of the penetration of sunlight into the atmosphere of Titan. ESASP-1177, 345-358.

Tomasko, M.G., and 39 co-authors, 2005. Rain, winds, and haze during the Huygens probe's descent to Titan's surface. Nature, doi:10.1038/nature04126.

Toon, O.B., McKay, C.P., Griffith, C.A., Turco, R.P., 1992. A physical model of Titan's aerosols. Icarus 95, 24-53.

Toublanc, D., Parisot, J.P., Brillet, J., Gautier, D., Raulin, F., McKay, C.P., 1995. Photochemical modeling of Titan's atmosphere. Icarus 113, 2•26.

West, R.A., Lane, A.L., Hart, H., Simmons, K.E., Hord, C.W., Coffeen, D.L., Esposito, L.W., Sato, M., Pomphrey, R.B., 1983. Voyager 2 photopolarimeter observations of Titan. J. Geophys. Res. 88, 8699•8708.

West, R.A., Smith, P.H., 1991. Evidence for aggregate particles in the atmospheres of Titan and Jupiter. Icarus 90, 330•333.

Wilson, E.H., Atreya S.K., 2003. Chemical sources of haze formation in Titan's atmosphere. Planet. Space Sci. 51, 1017-1033.

Wilson, E.H., Atreya, S.K., 2004. Current state of modeling the photochemistry of Titan's mutually dependent atmosphere and ionosphere. J. Geophys. Res. 109, doi:10.1029/2003JE002181.

Yelle, R.V., 1991. Non-LTE models of Titan's upper atmosphere. Astrophys. J. 383, 380-400.

Yelle R.V., Strobel, D.F., Lellouch, E., Gautier, D., 1997. Engineering models for Titan's atmosphere, ESA SP-1177, 243-256, European Space Agency, Noordwijk

Young, E.F., Rannou, P., McKay, C.P., Griffith, C.A., Noll, K., 2002. A three dimensional map of Titan's tropospheric haze distribution based on HST imaging. Astron. J. 123, 3473•3486.

Yung, Y. L., Allen, M., Pinto J.P., 1984. Photochemistry of the atmosphere of Titan: Comparison between model and observations. Astrophys. J. Supp. 55, 465-506.

Chapter 1

Titan's status from Cassini/Huygens mission & previous observations

Titan's intriguing atmosphere has been the focus of the scientific community for a long time. From ground-based to space-borne observatories and dedicated space missions, Titan is becoming day by day a more familiar environment. Questions about the processes that define its properties are answered but at the same time new aspects of its complex atmosphere arise that require better understanding. With the unprecedented success of the Cassini/Huygens mission it became clear that Titan resembles our home planet like no other object in our Solar System, hence it is well worth our interest and dedication. In this chapter a description of observed properties of Titan's atmosphere and surface are given along with the main unanswered questions that arise from these observations.

1.1 From mythology to discovery

According to Greek mythology, as this is described in Hesiode's Theogony, Titans where the 12 children of Ouranos and Gea, 6 male and 6 female. The youngest of them was Kronos (known as Saturn in Latin) who led the rest to overthrow their father. The Titans were on their turn overthrown in the Titanomachy against the Olympian gods that were led by Krono's son, Zeus (Jupiter in Latin).

Titan the satellite, was for the first time considered as a natural satellite by the famous Dutch mathematician, physicist and astronomer Christian Huygens in 1655. (Huygens was the first to use the term 'moon' for natural satellites calling Titan, *Luna Saturnia*-Saturn's moon. The term was replaced by *satellites* by Giovanni Domenico Cassini with the detection of Saturn's other natural satellites. See *wikipedia* : *natural satellites*.) Titan acquired its current name after

Figure 1.1: Christian Huygens

the suggestion of John Herschel, son of William Herschel, discoverer of Mimas and Enceladus, that the names of Kronos's brothers and sisters should be used for Saturn's satellites (Lassell, 1847). The first observations at that time did not have the ability to discriminate the presence of the thick atmosphere on Titan. The latter is significantly extended above the solid surface of the satellite and gives to its apparent size a magnitude that is significantly larger than that of the other satellites. This justified the adaptation of 'Titan' as the name of the biggest of the Saturnian satellites at that time. Nevertheless, although now we know that Titan is not the biggest among the satellites of our Solar System, it is the presence of its atmosphere and the processes that take place inside it, which justify its name.

Titan is the only satellite that has a dense atmosphere. The first clear verification of a gaseous species in Titan's atmosphere, took place right after the Second World War with the detection of methane absorption lines in Titan's spectrum (Kuiper, 1944). Such absorption lines were not detected on other satellites and led to the conclusion that Titan was unique regarding the presence of a methane atmosphere, which was considered responsible for the orange color

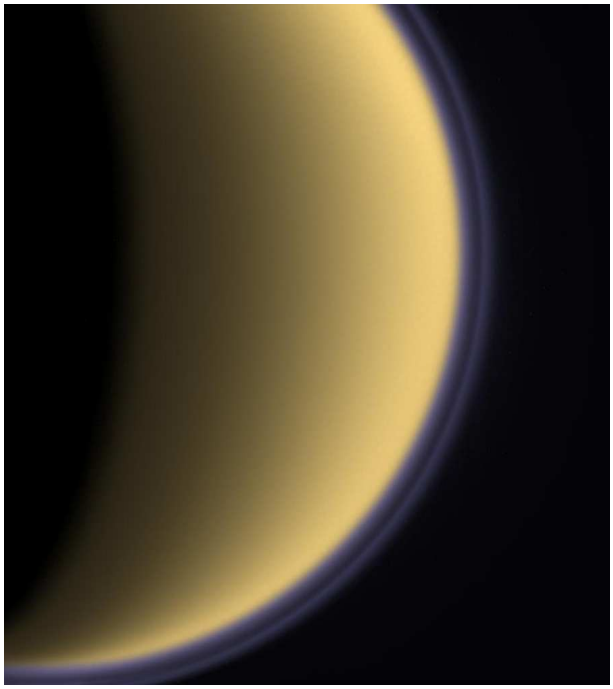

Figure 1.2: Titan as observed by the Cassini spacecraft. The main haze layer provides the orange color of the satellite and obscures any surface features, while the detached haze layer (in purple) is observable only at the limb of the atmosphere. Credit: NASA/JPL/Space Science Institute.

of the satellite in the visible images. It was not before the Voyager space missions that it became clear that molecular nitrogen is the dominant species in Titan's atmosphere (Broadfoot et al., 1991).

After the methane detection, Titan's atmosphere has been under continuous observation through ground-based and space-borne instruments. Today, we know that Titan's atmosphere is characterized by a highly complex organic chemistry that leads to the formation of hydrocarbon and nitrile species not found anywhere else in our Solar System, which eventually produce the observed haze structure. These have a strong interaction with the radiation field and affect the observed atmospheric conditions (temperature structure, composition, scattered radiation by the atmosphere, etc). Further, these conditions present now on Titan, bear significant resemblance to those that are believed to have been present on Earth before the evolution of life. These characteristics demonstrate the importance of Titan in our understanding of atmospheric processes and how these processes define the evolution of planetary atmospheres and the emergence of conditions that favor the evolution of life.

1.2 Physical properties

Titan is the largest moon of the Saturnian system with a radius of R_T=2575 km. This makes Titan the second largest satellite in the Solar System after Jupiter's Ganymede and even bigger than planet Mercury. It is at an average distance of 20 Saturnine radii, phase locked to Saturn and has an orbital period of ∼16 days (Table 1.1). Titan is 2.5 times smaller than Earth but has a surface pressure that is 50% larger.

After the detection of methane in Titan's atmosphere, the presence of complex organic chemistry based on the products of methane's photolysis was suggested to take place inside its atmosphere. Even before the Voyager missions, ground-based observations of Titan's thermal emission spectrum suggested the presence of ethane (C_2H_6), ethylene (C_2H_4) and acetylene (C_2H_6). The Voyager missions epoch has brought a 'promethean' enlightening in our understanding of Titan's properties. Although the encounter was only of a few hours, a large amount of data was collected that allowed scientist to retrieve for the first time a picture of the complexity found in Titan's atmosphere. Some of these data are still being analyzed. This improved picture, aroused the scientific interest for this satellite for answers to new questions. This eventually led to the more complicated, ambitious and eventually unprecedentedly successful Cassini/Huygens space mission.

The latest results from Cassini/Huygens have provided better constraints on the abundance of the dominant species. Methane's stratospheric mixing ratio was measured at 1.41 ± 0.05 % from GCMS (Niemann et al., 2005) and 1.6 ± 0.5 % from CIRS (Flasar et al., 2005). The two results are compatible within error bars. Below 32 km GCMS has measured an increase in the mixing ratio down to about 8 km, below which altitude the mixing ratio was constant at 4.9 % until the surface. The DISR measurements on board the Huygens probe, have given a similar value of 5 ± 1 % for the methane mixing ratio close to the surface (Tomasko et al., 2005). The analysis of the INMS measurements (Waite et al., 2005; Yelle et al., 2006), showed that methane's mole fraction is 2.71 ± 0.1 % at 1174 km, putting an end to the controversy originating from the initially retrieved value by the Voyager UVS observations (Smith et al., 1982) and their later re-analysis by Vervack et al. (2004). The only noble gas species detected is Argon with a mole fraction of $4.32 \pm 0.1 \times 10^{-5}$ close to the surface (Niemann et al., 2005).

1.2.1 Atmospheric structure

Due to the large distance of Saturn from the Sun (∼10 a.u.), the solar luminosity that reaches Titan is on average about the 1/100th of what reaches the Earth's outer atmosphere. This means that the temperatures found in Titan's atmosphere will be significantly smaller that the ones observed on Earth. The straight-forward estimation of the effective temperature in Titan's atmosphere, using the spectrally averaged atmospheric albedo α and the average solar constant S_T, at Titan's distance (see Table 1.1), gives:

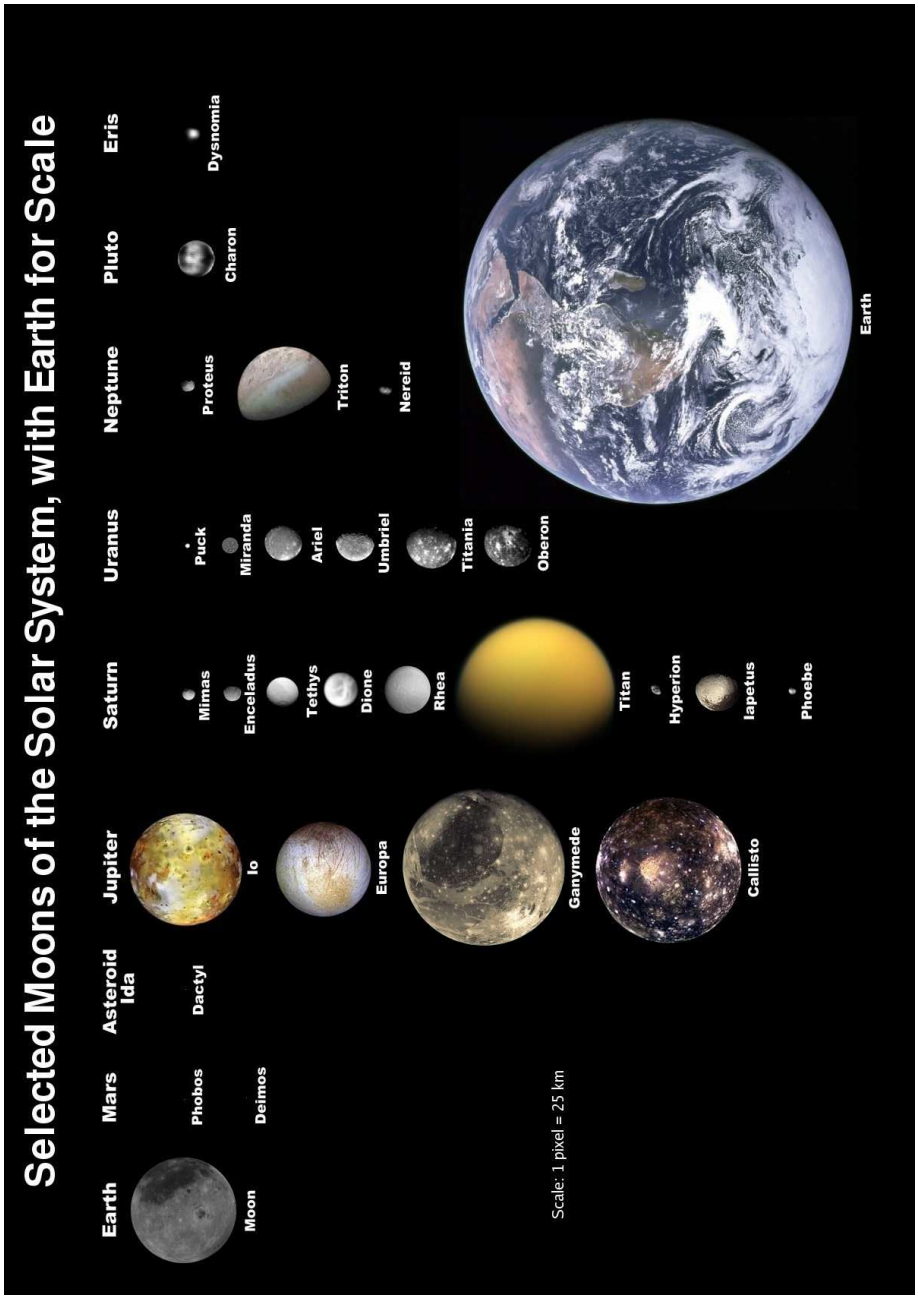

Figure 1.3: Natural Satellites of our Solar System

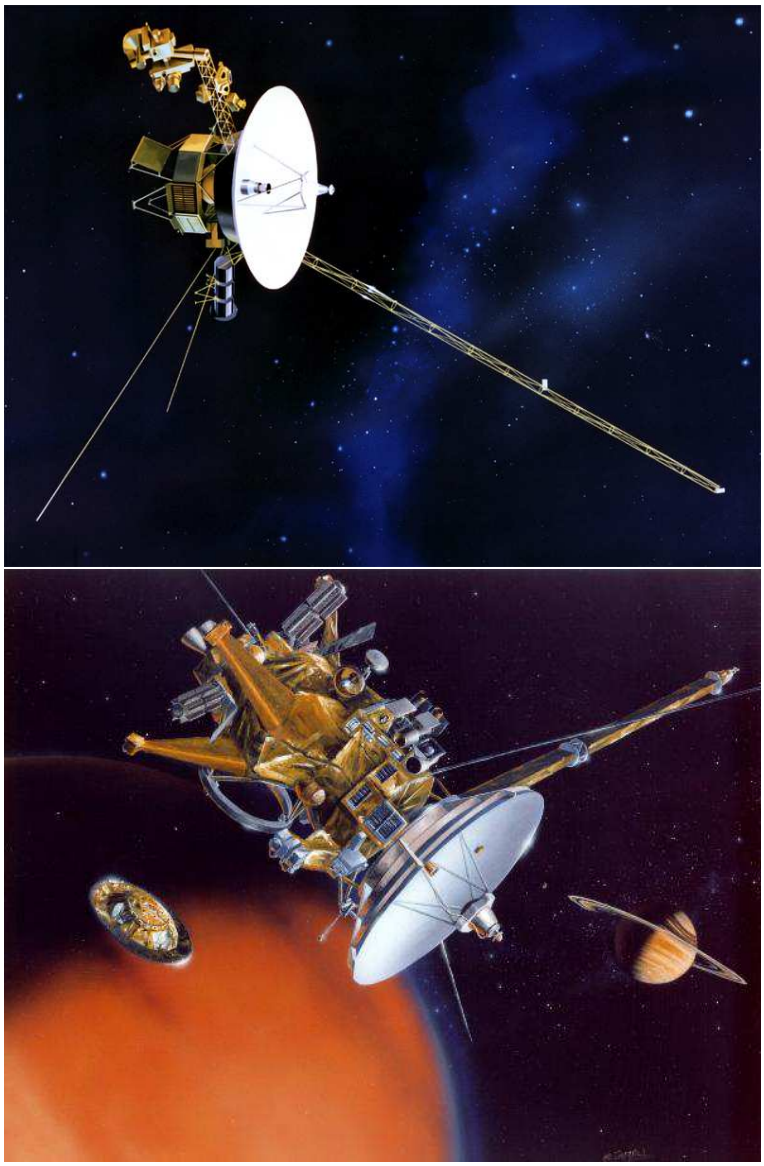

Figure 1.4: The Voyager 1 and Cassini/Huygens spacecrafts

$$4\pi R^2 \sigma T_{eff}^4 = (1-\alpha)\pi R^2 S_T$$
$$T_{eff} \sim 84 \text{ K}.$$

The first vertical profile of Titan's temperature structure was obtained by the Voyager Radio Occultation experiment between the surface and 200 km. Although, the retrieved vertical profile was based on the assumption of a pure molecular nitrogen atmosphere, it has been verified from the profiles retrieved by the instruments on board the Cassini/Huygens mission (see Fig. 1.5). From these, the surface temperature was measured at 93.65 K by the HASI instrument on board the Huygens probe and the surface pressure at 1.467 bar. This temperature is higher than the one suggested by the above T_{eff} and the reason for this is the methane induce greenhouse effect and the contribution of pressure induced absorption between the main three species, molecular nitrogen (N_2), methane (CH_4) and molecular hydrogen (H_2) that produces a greenhouse effect that raises the temperature in the troposphere. The tropopause is located at about 40 km and at higher altitudes the absorption of solar radiation by haze particles and methane produces a sharp increase in the temperature.

The retrieval of the vertical temperature profile was also aided by the analysis of methane's emission line in its ν_4 band in the thermal IR. This was based on the spectra retrieved from Voyager's IRIS instrument (Lellouch et al., 1989; Coustenis et al., 1989) and from ISO (Coustenis et al., 2003), and is sensitive to the stratospheric temperature structure.

From ground-based observations, the retrieval of a disk-average vertical temperature profile has become possible through millimeter observations by the IRAM telescope. High resolution spectra of rotational lines of specific species present in Titan's atmosphere probe different altitude regions and are sensitive to the temperature profile. By fitting the observed spectra with computer generated spectra it became possible to retrieve a vertical temperature profile. This profile (A. Marten private communication) is in close agreement in the lower

Table 1.1: Physical Properties of Titan's & Earth's atmospheres

Physical Parameter	Titan	Earth
Mass	1.346×10^{23}kg	5.98×10^{24}kg
Equatorial Radius	2575 km	6371 km
Rotational Period	15.945 days	1 day
Period around Sun	29.46 years	1 year
Mean Distance from Sun	9.546 a.u.	1 a.u.
Orbital eccentricity	0.0292	0.017
Obliquity	27°	23.5°
Average Albedo	30 %	30 %
Solar 'Constant'	15 W/m^2	1366 W/m^2
Surface Pressure	1.496 atm	1 atm
Surface Temperature	94K	288K
Escape Velocity	2.65 km/s	11.2 km/s

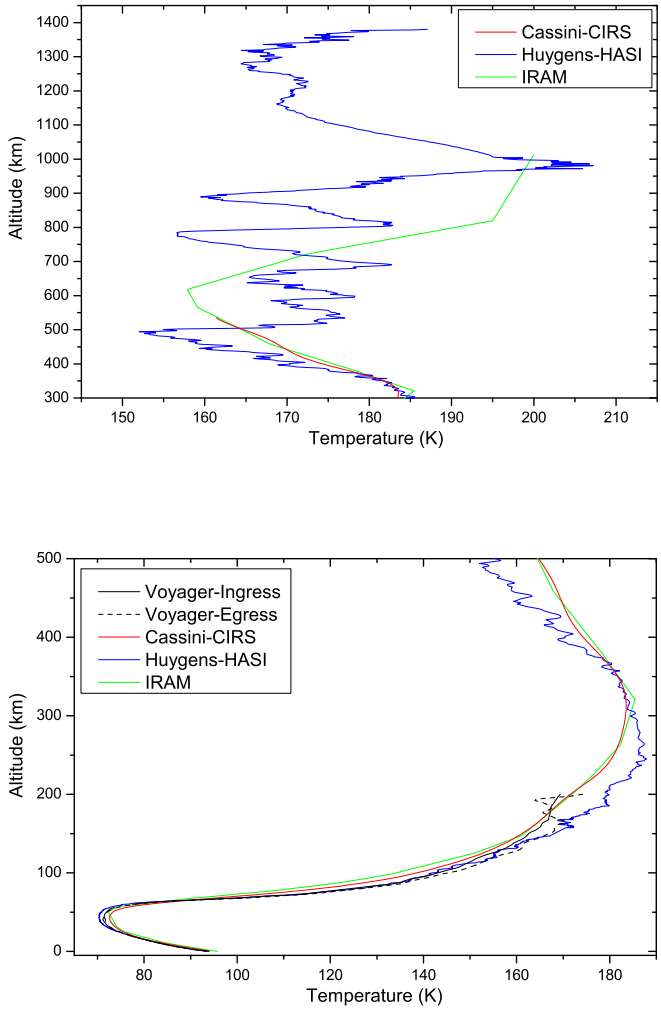

Figure 1.5: Vertical temperature profiles retrieved by different instruments for the upper and lower atmosphere. The black solid and dashed lines correspond to the Voyager retrieved profiles during ingress and egress, respectively (Lindal et al., 1983). The red line presents the Cassini-CIRS retrieved profile at the equator (with a 1.6% methane mole fraction, R. Achterberg and B. Conrath, personal communication), the blue line is the Huygens-HASI is situ measurements (F.Ferri, personal communication) and the green line is the ground-based retrieved profile from millimeter measurements from the IRAM telescope that corresponds to disk-average conditions.

atmosphere, below the stratopause, with the above discussed profiles from Voyager.

Recently, ground-based thermal infrared observations with NASA's ITF-TEXES have managed to retrieve information from the mesospheric thermal structure of Titan's atmosphere (Griffith et al., 2005a). The high resolution spectra obtained, allowed for the retrieval of the temperature structure between 100 and 600 km providing for the first time clear evidence of the presence of a mesopause, which was predicted by theoretical models (Yelle, 1991).

Although rare, occultation events of Titan's disk by transient stars have also aided in the investigation of its upper atmosphere. During these phenomena, the light from the occulting star is diminished as Titan passes in front of it. From the measurement of the light reduction and the geometry of the observations, information for the temperature structure and density profile in the region between 250 and 550 km was retrieved and further inferred the presence of temperature oscillations with altitude and of a sharp inversion layer (Hubbard et al., 1993; Sicardy et al., 1999, 2006).

The CIRS and HASI instruments have both retrieved vertical temperature profiles. The HASI profile corresponds to the Huygens's vertical path through the atmosphere while the CIRS profiles are retrieved for different latitudes along Titan's disk. The profile shown in Fig. 1.5 corresponds to the equatorial region. Nevertheless, the two profiles are not in complete agreement. HASI suggests a hotter stratosphere compared to CIRS with the stratopause located at about 250 km and temperature slightly above 185 K. CIRS on the other hand suggests a stratopause at a higher altitude located close to 320 km and with a few degrees colder temperature. This discrepancy between the two profile remains so far unsolved.

At higher altitudes HASI has detected the presence of significant inversion layers and wave effects. These were also observed by ISS and INMS instruments on board Cassini and are located at similar altitudes with those inferred from the occultation observations. The reasons for the production of these effects are still under investigation and the most probable explanation for the moment is the presence of gravity waves.

1.2.2 Geometric albedo

The geometric albedo is the disk averaged ratio of the outgoing to incoming radiation from an atmosphere, in the direction of an external observer. The spectrally resolved geometric albedo is one of the most important measurements of an atmosphere. This is because the reflected spectrum contains cumulative information from all the processes that take place inside the atmosphere and the surface. Different energy photons reach different altitudes of the atmosphere, hence the spectrally resolved geometric albedo depends on the haze structure, the chemical composition and the surface albedo. In this way, its correct reproduction by a model, is a strong indication of a correct representation of the simulated atmospheric processes. The observed geometric albedo of Titan's disk is presented in Fig. 6.7 at different wavelength regions for the leading and the

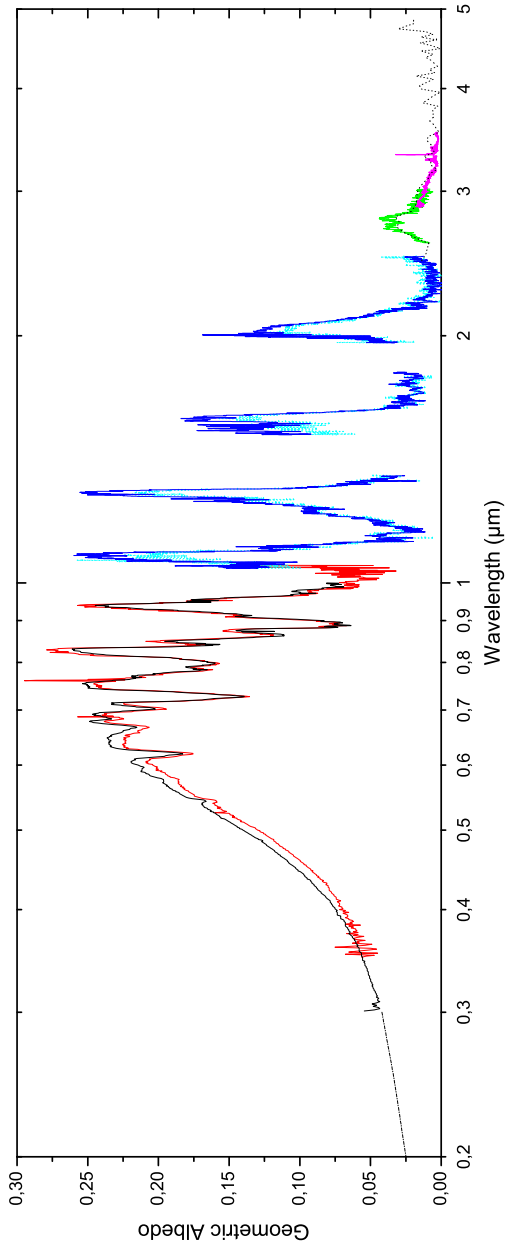

Figure 1.6: Observed spectrally resolved geometric albedo from Titan's atmosphere. For instruments and references see Table 1.2.

Table 1.2: Geometric albedo observations

Instrument	Region (μm)	Year	Hemisphere	Reference
HST	0.2-0.3	1991-92		McGrath et al. (1998)
	0.35-1.05	1981		Neff et al. (1984)
ESO	0.3-1.0	1993		Karkoscka (1994)
CFHT	0.8-2.5	1993	Leading	Negrão et al. (2006)
	〃	1995	Trailing	〃
Keck II	2.9-3.5	2001		Geballe et al. (2003)
ISO-PHT	2.6-3.0	1997	Leading	Coustenis et al. (2003)
ISO-SWS	2.5-4.8	〃	Leading	Coustenis et al. (2003)

trailing sides of Titan. The references and instruments for these measurements are given in Table 1.2.

1.2.3 Observed gas species

A detailed detection of Titan's chemical composition was for the first time possible through the thermal emission spectra obtained by the Voyager-IRIS instrument. These have shown the presence of significant number of hydrocarbon and nitrile gas species but also of carbon dioxide (CO_2) (Coustenis & Bézard, 1995). During observations from a spacecraft there are two possible ways for viewing an atmosphere. These are the nadir and limb observations. In the first, the spacecraft's instruments observe vertically through the atmosphere in a line of site that intersects the surface. This allows for a stronger signal that translates to higher signal to noise ratios and hence better accuracy in the observations. On the other hand, although the emission futures observed can originate from different regions of the atmosphere, during nadir viewing geometry this information is lost since the observed features are dominated by the atmospheric regions where the emission is stronger (where the contribution function peaks). This is where the limb-viewing geometry has an advantage. With limb observations the instruments point away from the surface, in a line of site the does not intersect the surface. In this way the retrieved spectra, pass through a significantly large part of the atmosphere that corresponds to different altitude regions. Hence by comparing different limb spectra, information on the vertical distribution of species can be retrieved. The difficulty with limb-viewing is that when viewing high altitudes, the density is smaller compared to lower ones, hence the emission features are weaker. This requires longer observation times in order to have good signal-to-noise ratios.

During the Voyager mission, a sequence of observations focused on the North polar region where 30 spectra were obtained from which 9 were in limb-viewing mode. From this it was possible to retrieve for the first time information about the vertical structure for some of the observed species (Coustenis et al., 1991). These had as a general trend an increase mole fraction towards higher altitudes. This verified the predictions of photochemical models that suggested a similar

altitude variability due to the production of the observed species at high altitudes, their transportation towards the lower atmosphere by diffusion and their loss to the surface due to condensation.

With the ISO observations better constraints, although disk-averaged, on the abundances of these species along with the detection for the first time of benzene (C_6H_6) (Coustenis et al., 2003) and water vapor (H_2O) (Coustenis et al., 1998) were possible due to the much higher resolution of the obtained spectra relative to those from the Voyager mission. In addition, it was possible to retrieve from the data information about the vertical profile of acetylene. This happened because the wings of the acetylene emission futures are sensitive (probe) different altitude regions compared to that probed by the center of the band. Using a constant mixing profile, in order to fit both the core and wings of the acetylene band did not provide a result as good as that with a varying mole fraction, which was also suggested by the photochemical models at that time (Lara *et al.*, 1996). In this way, the disk-averaged vertical structure of acetylene was inferred.

Ground-based millimeter and sub-millimeter observations have also aided in the detection of species based on their rotational transition features and further in the retrieval of their vertical profiles for some cases. Millimeter observations were the first to detect acrylonitriles (CH_3CN) (Bézard et al., 1993) and further set constraints on its vertical profile along with the profiles of hydrogen cyanide (HCN) and cyanoacetylene (HC_3N) (Hidayat et al., 1997; Marten *et al.*, 2002; Gurwell, 2004). In addition upper limits for the stratospheric abundances of acrylonitrile (C_2H_3CN) and propionitrile (C_2H_5CN) were set and estimates for the $^{15}N/^{14}N$ and $^{12}C/^{13}C$ isotopic ratios were retrieved. The latter along with other isotopic ratios, are important for the validation of scenarios regarding the formation and time evolution of Titan's atmosphere.

Carbon monoxide (CO) was expected to exist in Titan's atmosphere since it is a direct product of CO_2 photolysis with the latter detected in Voyager's spectra. Further, its vertical profile is expected to be constant since CO has a very large photochemical life time and hence its profile would be defined by mixing. The production of CO and CO_2 is believed to be maintained by the influx of water vapor at the top of the atmosphere (Samuelson et al., 1983a). The first detection of CO came from ground-based near-infrared spectra (Lutz et al., 1983), while millimeter observations have also derived estimates for its abundance in the stratosphere and troposphere. Yet, these suggested abundances are not in agreement. The abundances derived for the stratosphere are $\sim$50 ppm although there have been observations that suggested as low mole fractions as 2 ppm. On the other hand, the tropospheric abundances derived, ranged between values consistent with the average stratospheric one and values of lower abundance that questioned the expected, well mixed profile. The latest results from Cassini/CIRS suggest an abundance of 47 ± 8 ppm for CO with a constant profile, although a slightly varying (increasing) with altitude profile is within the error bars of the measurements (de Kok, 2007).

Although the Cassini/Huygens mission is still in operation, the first results are indicative of what will follow. The CIRS retrieved spectra both in nadir and

limb observation geometry have so far provided information for the stratospheric abundance and vertical profiles of the observed species, respectively (Coustenis et al., 2007; Vinatier et al., 2007; de Kok, 2007; Teanby et al., 2006, 2007). So far there has not been a detection of new species relative to what was known to exist in Titan's stratosphere before the Casssini/Huygens mission. Yet, the new data are far more accurate and provide higher resolution information on the latitudinal variation of the composition and the vertical profiles of each species, which has not been seen before. These are vital for the validation of photochemical and dynamical models and will help us to better understand the radiative, chemical and dynamical processes in Titan's atmosphere.

Yet, the situation becomes much more exciting in the upper atmosphere. The thermospheric composition retrieved by the neutral and ion spectra of INMS (Waite et al., 2005; Vuitton et al., 2006a,b) suggests the presence of a large number of new nitrile species, which are not present in the lower atmosphere. The production and evolution of these is now being considered for the first time and possibly is related to the ion-neutral chemistry that takes place at those altitudes. Although most of these species are present in small amounts their contribution to the formation of the haze structures observed in the lower atmosphere is also investigated. The up-to-date observations for the gas composition in Titan's atmosphere are presented in Table 1.3.

1.2.4 Aerosols

The most obvious characteristic of Titan's atmosphere is its well defined haze layer that interacts strongly with the solar radiation, providing the orange color of the satellite in the visible images, and obscures any surface futures. The origin of the haze particles is believed to lie in the photochemical processes of the atmosphere.

Before the Voyager missions, the presence of an aerosol layer was suggested from ground-based observations: the sharp drop of the observed geometric albedo towards short wavelengths indicated the presence of absorbing, at short wavelengths, matter located at high altitudes, where most of the high energy photons are either absorbed or scattered back to space. The IR spectra suggested the presence of an inversion layer in Titan's temperature profile that also favored the presence of an absorbing layer, while the morphology of methane's absorption bands could not be reproduced by a simple reflecting layer model for the surface, but required the presence of significant scattering inside the atmosphere. Finally, polarization measurements have shown that Titan was optically thick at visible wavelengths with the opacity originating from a non-molecular component (see Rages & Pollack (1980) and references therein). From these observations it became obvious that an aerosol layer was present in Titan's atmosphere and an estimate for the size of the particles ($0.2\mu\text{m}<\bar{r}\leq 0.35\mu\text{m}$) and their real refractive index ($1.5\leq n_r<2.0$)was retrieved.

The measurements during the Voyager mission have provided a more complex picture of Titan's aerosols and raised new issues. The extinction profiles retrieved by the high phase angle images have clearly demonstrated the presence

Table 1.3: Titan's Chemical Gas Composition

Species	Ground-Based[a]	Stratosphere Voyager IRIS[b] (equator)	Stratosphere ISO[c]	Thermosphere Cassini CIRS[d]	Thermosphere Cassini INMS[e] (equator)
		Hydrocarbons			
Hydrogen, H_2		$0.002\pm0.001^{(f)}$			$4\pm1\times10^{-3(g)}$
Acetylene, C_2H_2		$2.85^{+1}_{-1.2}\times10^{-6}$	$5.5\pm0.5\times10^{-6}$	$3.7\pm0.8\times10^{-6}$	3×10^{-4}
Ethylene, C_2H_4		$1.5^{+0.5}_{-0.8}\times10^{-7}$	$1.2\pm0.3\times10^{-7}$	$1.6\pm0.6\times10^{-7}$	1×10^{-3}
Ethane, C_2H_6		$1.5^{+0.6}_{-0.8}\times10^{-5}$	$2.0\pm0.8\times10^{-5}$	$9.3\pm3.0\times10^{-6}$	1×10^{-4}
Methylacetylene, CH_3C_2H		$6.5^{+2.0}_{-2.5}\times10^{-9}$	$1.2\pm0.4\times10^{-8}$	$6.5\pm1.6\times10^{-9}$	$3.86\pm0.22\times10^{-6(h)}$
Allene, CH_2CCH_2			$<2.0\times10^{-9}$		
Propane, C_3H_8	$6.2\pm1.2\times10^{-7(i)}$	$7.0\pm0.4\times10^{-7}$	$2.0\pm1.0\times10^{-7}$	$8.2\pm1.8\times10^{-7}$	$2.3\times10^{-6(h)}$
Diacetylene, C_4H_2		$1.5\pm0.7\times10^{-9}$	$2.0\pm0.5\times10^{-9}$	$1.4\pm0.3\times10^{-9}$	1×10^{-5}
Benzene, C_6H_6			$4.0\pm3.0\times10^{-10}$	$3.5^{+1.5}_{-2.0}\times10^{-10}$	$\sim5.0\times10^{6(h)}$
		Nitriles			
Ammonia, NH_3					4×10^{-6}
Hydrogen Cyanide, HCN	$(5\rightarrow8)\times10^{-7}$	$1.95^{+0.5}_{-0.9}\times10^{-7}$	$3.0\pm0.5\times10^{-7}$	$1.5^{+4.0}_{-3.5}\times10^{-7}$	2×10^{-4}
Methyleneimine, CH_2NH					3×10^{-6}
Acetonitrile, CH_3CN	$(0.8\rightarrow4)\times10^{-8}$				3×10^{-6}
Cyanoacetylene, HC_3N	$(0.003\rightarrow4)\times10^{-8}$	$<1.0\times10^{-9}$	$5.0\pm3.5\times10^{-10}$	$4.5\pm1.0\times10^{-10}$	4×10^{-5}
Acrylonitrile, C_2H_3CN	$<2\times10^{-9}$				1×10^{-5}
Propionitrile, C_2H_5CN	$<2\times10^{-9}$				5×10^{-7}
Cyanogen, C_2N_2		$<2\text{x}10^{-9}$		$<5\times10^{-10(j)}$	
		Oxygen Species			
Water Vapor, H_2O			8×10^{-9} (400 km)$^{(k)}$	$<9\times10^{-10(l)}$	
Carbon Monoxide, CO	see text			$4.7\pm0.8\times10^{-5(l)}$	
Carbon Dioxide, CO_2		$1.45^{+0.35}_{-0.55}\times10^{-8}$	$2.0\pm0.2\times10^{-8}$	$1.4\pm0.4\times10^{-8(l)}$	

[a] Marten *et al.* (2002), [b] Coustenis & Bézard (1995) as given in [c] Coustenis et al. (2003), [d] Coustenis et al. (2007), [e] Vuitton et al. (2006a,b), [f] Samuelson et al. (1983b), [g] Yelle et al. (2006), [h] Waite et al. (2005), [i] Roe et al. (2003), [j] Teanby et al. (2006), [k] Coustenis et al. (1998), [l] de Kok (2007)
For measurements without superscript the reference is the one in the title bar.
For the Marten *et al.* (2002) results the arrow indicates the mole fraction variation between 200 and 450 km.

of a detached haze layer above the main haze deck, between 300 and 350 km which merged with the main haze layer above 60^oN (Rages & Pollack, 1983) where the presence of a polar hood was observed. For these, a dynamical explanation has been suggested which is discussed in the following section.

The shape and size of the haze particles in Titan's atmosphere has been the subject of debate for a long time. Photopolarimetry measurements of scattered light from the Pioneer 11 (Tomasko & Smith, 1982) and Voyager (West et al., 1983) space missions have given high polarization at $\sim 90^\circ$ phase angle, which if the particles are spherical, constrains their size to 0.1 μm. On the other hand, high phase angle brightness measurements from Voyager (Rages et al., 1983), required particles between 0.2 and 0.5 μm with the upper limit more plausible. In order to overcome this problem, two possible solutions were suggested; one of a bimodal distribution (Courtin et al., 1991; Toon et al., 1992) and the other of fractal aggregates constructed from spherical units (West & Smith, 1991; Rannou et al., 1995, 1997).

Since then many microphysical models using the fractal aggregates have been published (Rannou et al. (2003) and references therein). The advantage of the fractal approach is that it provides, in general, a good fit to the geometric albedo both in the UV, visible and near-IR regions while at the same time matches the polarization data. However, fractal models have been unable to provide a good fit to the methane absorption feature at 0.62 μm in comparison with the success of the spherical particle models. The fit to the data was improved by applying a haze cut-off below 100 km, (Tomasko et al., 1997; Rannou et al., 2003) as suggested by HST measurements at that time (Young et al., 2002). A haze clearing was also included in the spherical particle models but at lower altitudes (below 30 km in McKay et al. 1989). The recent results from the DISR instrument on board the Huygens probe (Tomasko et al., 2005) show that the haze opacity extends down to the surface.

In addition, images from Cassini/ISS have shown that the location of the detached haze layer has moved to higher altitudes, while new detached layers are present, probably produced by the wave effects observed also in the temperature structure (Porco et al., 2005).

1.2.5 Spatial & temporal variability

The disk-resolved observations by Voyager have shown that for some species there was a significant latitudinal variation in their observed stratospheric abundance. The retrieved mole fractions for most of them, showed a rather small variation from south pole to equator followed by a strong increase towards the north pole (Coustenis & Bézard, 1995). Similar variability was also observed in the Cassini/CIRS retrieved abundances, although of different magnitude (Coustenis et al., 2007; Vinatier et al., 2007). Further, the brightness of Titan's disk at the Voyager epoch exhibited a pronounced asymmetry with the north hemisphere being darker than the south one, while at the north pole a dark hood was present. This was attributed to a latitudinal variability of the haze opacity that was verified by the measured extinction profiles at different latitudes

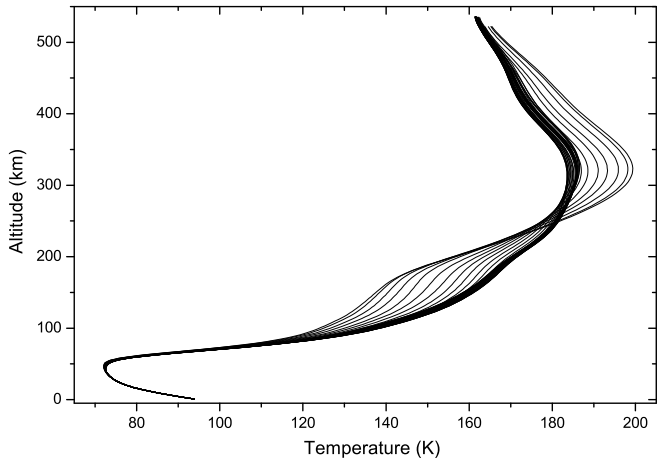

Figure 1.7: Vertical temperature profiles by CIRS, retrieved at different locations of Titan's disk (R. Achterberg and B. Conrath, personal communication). For the retrieval a 1.6% methane mole fraction was used. The thick line formed by the convergence of many mid-latitude and equatorial profiles defines the disk average temperature profile, while as we move towards the winter pole the local enhancement of aerosol particles increase the absorption of solar radiation in the stratosphere which is then heated, while the atmosphere above, is cooled since less photons arrive there.

(Rages & Pollack, 1983). The latter showed an increase in the opacity of the aerosol layer towards the north pole where the detached haze converged with the main haze layer at the region of the polar hood. In addition, to the chemical composition and haze opacity, the vertical temperature profiles retrieved at different latitudes also exhibited a variability that was mostly prominent at the region of the stratopause, where the absorption by the haze particles presents its maximum. The high latitudinal resolution vertical profiles retrieved by CIRS (Fig. 1.7) provide a clear manifestation of this effect once again.

Later observations by HST in 1990 have shown the this North-South asymmetry (NSA) has reversed (Caldwell et al., 1992) with the south hemisphere being darker than the north one, while more recent observations from 1997 and on, again by HST have reported a new reversal in the asymmetry (see Lorenz et al. (2004) and references therein). This variability suggested that there is a strong seasonal oscillation in Titan's atmospheric structure. The large obliquity of Titan's rotational axis, allows the manifestation of seasonal effects like those on Earth. Each Titan year lasts about 30 Earth years, while the period between equinox and solstice is about 7 years.

At the time of the Voyager observations, Titan had just passed the spring equinox, while later on in 1992 it was in North summer. During seasonal changes the Hadley cell circulation pattern varies both in direction and also structure, and this leads to variabilities in the haze abundance at each hemisphere due to circulation effects. Further, at the winter hemisphere, the solar illumination is reduced and towards the winter pole the photolysis rates are expected to be significantly reduced. This could explain the observed enhancement of the minor species observed at the winter hemisphere.

Rannou et al. (2002) has tested the possible impact of dynamical effects in the haze structure and opacity through a General Circulation Model (GCM). In their work they have managed to reproduce the general characteristics of the dynamical haze structure (NSA, detached haze and polar hood) giving credit to the role of seasonal effects in Titan's atmosphere. This oscillation explains why the Cassini/CIRS results of the stratospheric abundances present the same latitudinal variability with those retrieved by Voyager IRIS about 25 years ago.

It is important to note that the NSA also exhibits a strong wavelength dependence. The asymmetry is stronger at blue wavelengths and at 889 nm (but reversed) and weaker at UV, while it reverses at red and longer wavelengths above 700nm. Different energy photons scattered out of the atmosphere, originate from different altitude regions, which in turn have a different response time in the variability of the atmosphere due to seasonal effects. Furthermore, the scattering properties of the haze particles are strongly wavelength dependent. This suggests a more complex picture for the NSA variability that couples dynamics, microphysics and photochemistry.

1.2.6 Condensates & clouds

In the lower atmosphere below the stratopause, hydrocarbons (with the exception of ethylene) and nitriles condense and are removed from the atmosphere. The condensed gases are expected to precipitate to the surface and some verification for the presence of condensates has been retrieved by the Voyager-IRIS north pole spectra. The latter clearly showed the presence of dicyanogen (C_4N_2) which was not detected in the gas phase (Samuelson et al., 1997), while other candidates have been suggested by Coustenis et al. (1999).

Since the temperature and pressure conditions favor the condensation of ethane and methane, above and below the tropopause, respectively, the possibility of cloud formation based on these two species that are present in high amounts, was suggested. Theoretical work from radiation transfer models (McKay et al., 1989) have shown that the impact of clouds, if present, should be small on a global scale. This suggested that, if present, clouds should be thin and/or patchy.

The first indication of cloud formation in Titan's atmosphere, came from ground-based observations which showed a scintillation of the methane spectrum (Griffith *et al.*, 1998) while more recently, direct observation of cloud features became possible through ground-based imaging Brown et al. (2002); Gendron et al. (2004). Most of the clouds were observed at and close to the south pole,

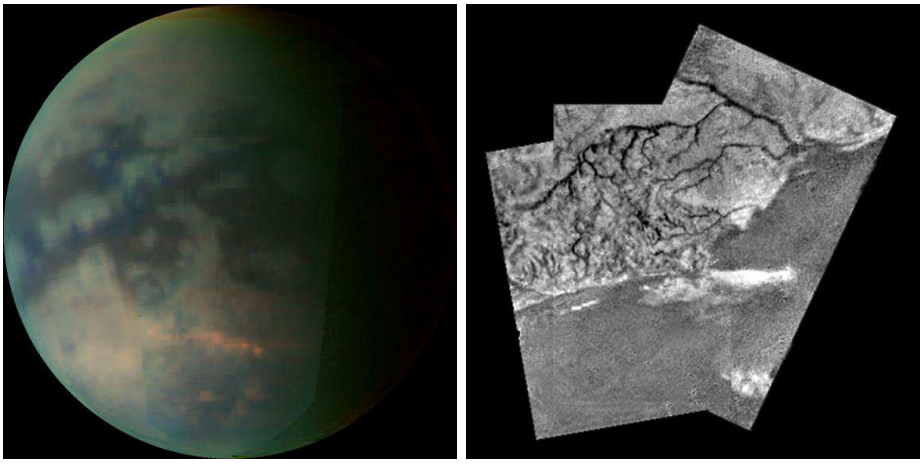

Figure 1.8: Cloud futures (bright patches) observed in Titan's south hemisphere (credit: NASA/JPL/University of Arizona) and river futures observed by Huygens/DISR (Tomasko et al., 2005).

which is expected because at the time of these observations, Titan was in the southern summer season and the large solar heating in this region induces strong convective fluxes due the up-welling air motion. Nonetheless, observations by Roe et al. (2005) have reported cloud features constrained at $\sim 40^o$S, and which were attributed to circulation effects or surface topographic features.

The imaging from Cassini instruments has verified the above ground-based observations. Cloud formation has been observed in specific locations on Titan's disk. The south pole cloud system observed from the Earth (Hirtzig et al., 2006) which was still visible in the first Titan flybys, had later disappeared marking the seasonal change in Titan atmosphere (Porco et al., 2005). The structure and temporal evolution of the observed cloud features verified their dependence on the circulation patterns (Griffith *et al.*, 2005b), while GCM modelling has shown that the production of clouds using the haze particles as nucleation sites, is possible in certain latitudinal regions, similar to the ones where clouds are observed (Rannou et al., 2006). Lately, and while new observations are taking place, Griffith *et al.* (2006) have reported the detection of a large tropospheric cloud in Titan's north pole. This is made of ethane, which is believed to condense much faster there, due to the low temperatures present in the winter conditions.

1.2.7 Surface properties

The large amounts of methane in the atmosphere along with the high absorbing and scattering properties of the haze layers, did not allow for the observation of the surface almost in all the spectrum from UV to IR by the instruments

on board the Voyager spacecrafts. Only in specific and narrow regions of the spectrum were the methane absorption decreases by orders of magnitude (the methane windows) photons reach Titan's surface and return back to the observer. This 'denial' of Titan to reveal its surface had increased the interest in its mystifying dense atmosphere and provided the basis for the generation of scenarios on the possible presence of seas or lakes of methane and other hydrocarbons along with other surface processes such as cryovolcanism.

With the evolution of observation technics and the discovery of the adaptive optics technology that allowed for the observation from the surface of the Earth, the first maps of Titan's surface were produced in wavelengths corresponding to the methane windows. Even though the resolution of the maps was constrained by the large distance of Titan from the Earth, they clearly showed that the satellite's surface wasn't homogeneous but had distinct regions of high and low reflectivity.

The dedicated analysis of high resolution spectra of Titan's geometric albedo inside the methane windows with ground-based observations from adaptive optics and images from HST, has revealed the highly variable spectroscopic character of the surface reflectivity (Griffith *et al.*, 2003; Lellouch *et al.*, 2004; Negrão et al., 2006; Coustenis *et al.*, 2006). This is suggestive of a non-homogeneous composition for the material covering the surface of the satellite.

With the images taken by the Cassini/Huygens mission, a whole new amazing world has been discovered on Titan's surface. The most impressive characteristic observed from the first pictures obtained by the Huygens probe were the forms of river structures, mountain hills and shores which suggested a world similar to the one we are used to here in Earth. Methane, is believed to be the flowing liquid which has formed these features although so far, no large-scale bodies of liquids have been observed and possible lakes of liquids have been detected only close to the North polar region from Cassini/RADAR (Stofan et al., 2007).

In addition, desert like regions covered with dunes have been observed close to the equator (Lorenz et al., 2006). These are aligned in a west-east direction covering hundreds of kilometers and rise up to 100 m. They are believed to be caused by Saturn's tidal forces and the sand composing them is expected to be fine grains of ice of organic material.

Further, indications for the detection of a cryovolcano have been reported from Cassini/VIMS images along with the presence of topographical variability (Sotin et al., 2005). The presence of cryovolcanic processes on the surface of Titan is becoming more and more important because it could explain the so far absence of a methane reservoir. Since, no seas or large lakes of methane have been observed so far, the question of the source, sustaining the methane in the atmosphere is raised. With out such a reservoir, methane would be photochemically depleted from the atmosphere within a few tenths of millions of years. So if we assume that the methane we observe now on Titan is in a steady state and not a transient phenomenon, locating this reservoir is vital. Cryovolcanos could provide a solution to this problem with the release of volatiles and mainly methane from an underground reservoir.

The young character of Titan's surface and/or its highly erosion and modification by geological/fluvial and aeolian processes is further suggested by the lack of significant cratering.

1.2.8 Open questions

Our knowledge of Titan's properties is becoming deeper everyday. The Cassini / Huygens mission has given insight into certain issues that were raised by previous observations and is still providing new data which will help us understand better the processes that define its atmospheric structure. Yet, new questions are opened and some of the older ones still remain:

- How Titan came to have a dense atmosphere while all other satellites in the Solar System do not?
- Is there a methane reservoir and where is it located?
- What is the origin of the observed haze structure and how is it modified by dynamical/seasonal effects?
- What is the degree of complexity of the organic chemistry found in Titan's upper and lower atmosphere?
- Which are the spectral properties and the composition of the different brightness surface features observed.
- What is the extent at which geological, fluvial and aeolian processes define the observed surface diversity.

The work described in this thesis, addresses only a small, but very important part of our questions about Titan's atmosphere.

Bibliography

Bézard, B., Marten, A., Paubert, G., 1993. Detection of acetonitrile on Titan. Bull. Am. Astr. Soc. 25, 1100.

Broadfoot, A.L., and 16 co-authors, 1981. Extreme ultraviolet observations from Voyager 1 encounter with Saturn, Science 212, 206-211.

Brown, M.E., Bouchez, A.H., Griffith, C.A., 2002. Direct detection of variable tropospheric clouds near Titan's south pole. Nature 420, 795-797.

Caldwell, J.D., Smith, P.H., Tomasko, M.G., Weaver, H., 1992. Titan: Evidence of seasonal changes-A comparison of Voyager and Hubble Space Telescope images, Icarus 103, 1-9.

Courtin, R., Wagener, R., McKay, C.P., Caldwell, J., Fricke, K.-H., Raulin, F., Bruston, P., 1991. UV spectroscopy of Titan's atmosphere, planetary organic chemistry and prebiological synthesis II. Interpretation of new IUE observations in the 220•335 nm range. Icarus 90, 43-•56.

Coustenis, A., Bézard, B., Gautier, D., 1989. The gas composition of Titan's equatorial region. Icarus 80, 54-76.

Coustenis, A., Bézard, B., Gautier, D., Marten, A., Samuelson, R.E., 1991. Titan's atmosphere from Voyager infrared observations,III: Vertical distributions of hydrocarbons and nitriles near Titan's north pole. Icarus 89, 152-167.

Coustenis, A. and B. Bézard (1995). Titan's atmosphere from Voyager infrared observations. IV. Latitudinal variations of temperature and composition, Icarus 115, 126-140.

Coustenis, A., and 8 co-authors, 1998. Evidence for water vapor in Titan's atmosphere from ISO/SWS data. Astronomy and Astrophysics 336, L85-L89.

Coustenis, A., Schmitt, B., Khanna, R.K., Trotta, F., 1999. Plausible condensates in Titan's stratosphere from Voyager infrared spectra. Planetary and Space Science 47, 1305-1329.

Coustenis, A., Salama, A., Schulz, B., Ott, S., Lellouch, E., Encrenaz, Th., Gautier, D., Feuchtgruber, H., 2003. Titan's atmosphere from ISO mid-infrared spectroscopy. Icarus 161, 383-403.

Coustenis, A., Negrão, A., Salama, A., Schulz, B., Lellouch, E., Rannou, P., Drossart, P., Encrenaz, T., Schmitt, B., Boudon, V., Nikitin, A., 2006. Titan's 3-micron spectral region from ISO high-resolution spectroscopy, Icarus 180, 176-185.

Coustenis, A., and 24 co-authors, 2007. The composition of Titan's stratosphere from Cassini/CIRS mid-infrared spectra. Icarus, *in press*.

Flasar, F.M., and 44 co-authors, 2005. Titan's atmospheric temperatures, winds, and composition. Science 308, 975•978.

Fulcignoni, M. and 42 coworkers (2005). In situ measurements of the physical characteristics of Titan's enviroment. Nature,doi:10.1038/nature04314.

Geballe, T.R., Kim, S.J., Noll, K.S., Griffith, C.A., 2003 High-Resolution 3 Micron Spectroscopy of Molecules in the Mesosphere and Troposphere of Titan. Astrophys. J. 583, L39-L42

Gendron, E. et al., 2004. VLT/NACO adaprtive optics imaging of Titan. Astronomy and Astrophysics 417, L21-L24.

Griffith, C.A.,Owen, T., Miller, G.A., Geballe, T., 1998. TRansient clouds in Titan's lower atmosphere. Nature 395, 575-578.

Griffith, C.A., Owen, T., Geballe, T.R., Rayner, J., Rannou, P., 2003. Evidence for the exposure of water ice on Titan's surface, Science 300, 628-630.

Griffith, C.A., Penteado, P., Greathouse, T.K., Roe, H.G., Yelle, R.V., 2005. Observations of Titan's mesosphere. Astr. J. 629, L57-L60.

Griffith, C.A. and 26 co-workers, 2005. The evolution of Titan's mid-latitude clouds. Science 310, 474-477.

Griffith, C.A. and 13 co-workers, 2006. Evidence for a polar ethane cloud on Titan. Science 313, 1620-1622.

Gurwell, M., 2004. Submillimeter observations of Titan: Global measures of stratospheric temperature CO, HCN HC_3N and the isotopic ratios $^{12}C/^{13}C$ and $^{14}N/^{15}N$. Ap. J. 616, L7-L10.

Hidayat, T., Marten, A., Bézard, B., Gautier, D., Owen, T., Matthews, H.E., Paubert, G., 1997. Millimeter and submillimeter heterodyne observations of Titan: Retrieval of the vertical profile of HCN and the $^{12}C/^{13}C$ ratio, Icarus 126, 170•182.

Hirtzig, M., Coustenis, A., Gendron, E., Drossart, P., Negrao, A., Combes, M., Lai, O., Rannou, P., Lebonnois, S., Luz, D., 2006. Monitoring atmospheric phenomena on Titan. Astron. Astrophys. 456, 761-774.

Hubbard, W.B., and 45 co-authors, 1993. The occultation of 28 Sgr by Titan. Astronomy and Astrophysics 269, 541-563.

Karkoschka, E., 1994. Spectrophotometry of the jovian planets and Titan at 300 to 1000 nm wavelength: The methane spectrum. Icarus 111, 174•192.

de Kok, R. and 12 co-authors, 2007. Oxygen compounds in Titan's stratosphere as observed by Cassini/CIRS data. Icarus 186, 354-363.

Kuiper, G.P., 1944. Titan: A satellite with an atmosphere. Astrophys. J. 100, 378-383.

Lara, L. M., E. Lellouch, J. Lopez-Moreno, and R. Rodrigo (1996), Vertical distribution of Titan"s atmospheric neutral constituents, *J. Geophys. Res.*, **101**, 23,261•-23,283.

Lassell, Mr., 1847.Satellites of Saturn. Observations of Mimas, the closest and most interior satellite of Saturn. Monthly Notices of the Royal Astronomical Society, volume 8, p.42.

Lellouch, E., Schmitt, B., Coustenis, A., Cuby, J.-G., 2004. Titan's 5-micron lightcurve, Icarus 168, 209-214.

Lorenz, R.D., Smith, P.H., Lemmon, M.T., 2004. Seasonal change in Titan's haze 1992-2002 from Hubble Space Telescope observations. Geophys. Res. Lett. 31, L10702, doi:10.1029/2004GL019864.

Lorenz, R.D., et al., 2006. The sand seas of Titan: Cassini RADAR observations of longtitudinal dunes. Science 312, 724-727.

Lutz, B.L., de Berge, C., Owen, T., 1983. Titan: Discovery of carbon monoxide in its atmosphere. Science 220, 1374-1375.

Marten, A., Hidayat, T., Biraud, Y., Moreno, R., 2002. New millimeter heterodyne observations of Titan: Vertical distributions of HCN HC_3N, CH_3CN, and the isotopic ratio $^{15}N/^{14}N$ in its atmosphere. Icarus 158, 532•544.

McGrath, M.A., Courtin, R., Smith, T., Feldman, P.D., Strobell, D.F., 1998. The ultravionet albedo of Titan. Icarus 131, 382-392.

McKay, C.P., Pollack, J.B., Courtin, R., 1989. The thermal structure of Titan's atmosphere. Icarus 80, 23-53.

Neff, J.S., Humm, D., Bergstralh, J.T., Cochran, A.L., Cochran, W.D., Barker, E.S., Tull, R.G.. Absolute spectrophotometry of Titan, Uranus, and Neptune 3500-10,500 Å. Icarus 60, 221-235.

Negrão, A., Coustenis, A., Lellouch, E., Maillard, J.-P., Rannou, P., Schmitt, B., McKay, C.P., Boudon, V., 2006. Titan's surface albedo variations over a Titan season from near-infrared CFHT/FTS spectra, Planet. Space Sci. 54, 1225-1246.

Niemann, H.B., and 17 co-authors, 2005. The abundance of constituents of Titan's atmosphere from the GCMS instrument on the Huygens probe. Nature doi:10.1038/nature04122.

Porco, C.C., and 35 co-authors, 2005. Imaging of Titan from Cassini spacecraft. Science 434, 159-168.

Rages, K., Pollack, J.B., 1980. Titan aerosols: Optical properties and vertical distribution. Icarus 41, 119-130.

Rages, K., Pollack, J.B., 1983. Vertical distribution of scattering hazes in Titan's upper atmosphere. Icarus 55, 50-62.

Rages, K., Pollack, J.B., Smith, P.H., 1983. Size estimate of Titan's aerosols based on Voyager high-phase-angle images. J. Geophys. Res. 88, 8721-8728.

Rannou, P., Cabane, M., Chassefiere, E., Botet, R., McKay, C.P., Courtin, R., 1995. Titan's geometric albedo: Role of the fractal structure of the aerosols. Icarus 118, 355-372.

Rannou, P., Cabane, M., Botet, R., Chassefiere, E., 1997. A new interpretation of scattered light measurements at Titan's limb. J. Geophys. Res. 102, 10997-11014.

Rannou, P., Hourdin, F., McKay, C.P., 2002. A wind origin for Titan's haze structure. Nature 418, 853-856.

Rannou, P., McKay, C.P., Lorenz, R.D., 2003. A model of Titan's haze of fractal aerosols constrained by multiple observations. Planet. Space Sci. 51, 963-976.

Rannou, P., Montmessin, F., Hourdin, F., Lebonnois, S., 2006. The latitudinal distribution of clouds on Titan. Science 311, 201-204.

Roe, H.G., Greathouse, T.K., Richter, M.J., Lacy, J.H., 2003. Propane on Titan. Astrophys. J. 597,L65-L68.

Roe, H.G., Bouchez, A.H., Trujillo, C.A., Schaller, E.L., Brown, M.E., 2005. Discovery of temperate latitude clouds on Titan. Ap. J. 618, L49-L52.

Samuelson, R.E., Maguire, W.C., Hanel, R.A., Kunde, V.G., Jennings, D.E., Yung, Y.L., Aikin, A.C., 1983. CO_2 on Titan. J. Geophys. Res. 88, 8709-8715.

Samuelson, R.E., Hanel, R.A., Kunde, V.G., Maguire, W.C., 1983. Mean molecular weight and hydrogen abundance of Titan's atmosphere. Nature 292, 688-693.

Samueslon, R.E., Mayo, L.A., Knuckles, M.A., Khanna, R.K., 1997. C_4N_2 ice in Titan's north polar stratosphere. Planet. Space Sci. 45, 941-948.

Sicardy, B., and 23 co-authors, 1999. The structure of Titan's stratosphere from the 28 Sgr occulation. Icarus 142, 357-390.

Sicardy, B., and 51 co-authors, 2006. The two Titan stellar occulations of 14 November 2003. JGR 111, E11S91 doi:10.1029/2005JE002624.

Smith, G.R., Strobel, D.F., Broadfoot, A.L., Sandel, B.R., Shemansky, D.E., Holdberg, J.B., 1982. Titan's upper atmosphere: Composition and temperature from the EUV solar occultation results. J. Geophys. Res. 87, 1351-1359.

Sotin, C. et al., 2005. Release of volatiles from a possible cryovolcano from near-infrared imaging of Titan. NAture 435, 786-789.

Stofan, E.R. et al., 2007. The lakes of Titan. Nature 445, doi:10.1038/nature05438.

Teanby, N.A., and 11 co-authors, 2006. Latitudinal variations of HCN, HC_3N, and C_2N_2 in Titan's stratosphere derived from Cassini CIRS data. Icarus 181, 243-255.

Teanby, N.A., and 11 co-authors, 2007. Vertical profiles of HCN, HC_3N and C_2H_2 in Titan's atmosphere derived from Cassini/CIRS data. Icarus 186, 364-384.

Tomasko, M.G., Smith, P.H., 1982. Photometry and polarimetry of Titan: Pioneer 11 observations and their implications for aerosols properties. Icarus 51, 65-95.

Tomasko, M.G., Lemmon, M., Roose, L.R., Smith, P.H., Eibl, A., West, R.A., 1997. Models of the penetration of sunlight into the atmosphere of Titan. ESASP-1177, 345-358.

Tomasko, M.G., and 39 co-authors, 2005. Rain, winds, and haze during the Huygens probe's descent to Titan's surface. Nature, doi:10.1038/nature04126.

Toon, O.B., McKay, C.P., Griffith, C.A., Turco, R.P., 1992. A physical model of Titan's aerosols. Icarus 95, 24-53.

Vervack, R.J., Sandel, B.R., Strobel,D.F., 2004. New perspectives on Titan's upper atmosphere from a reanalysis of the Voyager 1 UVS solar occultations. Icarus 170, 91-112.

Vinatier, S., et al., 2006. Vertical abundance profiles of hydrocarbons in Titan's atmosphere at 15°S and 80 °N retrieved from Cassini/CIRS spectra, *in press*.

Vuitton V., Yelle, R.V., Anicich, V.G., 2006a. The nitrogen chemistry of Titan's upper atmosphere revealed. Ap. J. 647, L175-L178.

Vuitton V., Yelle, R.V., Anicich, V.G., 2006b. Detection of complex molecules in Titan's upper atmosphere. DPS meeting, #38, #36.03.

Waite J.H. Jr. and 21 coauthors, 2005. Ion neutral mass spectrometry results from the first flyby of Titan. Science 308, 982-986.

West, R.A., Lane, A.L., Hart, H., Simmons, K.E., Hord, C.W., Coffeen, D.L., Esposito, L.W., Sato, M., Pomphrey, R.B., 1983. Voyager 2 photopolarimeter observations of Titan. J. Geophys. Res. 88, 8699•8708.

West, R.A., Smith, P.H., 1991. Evidence for aggregate particles in the atmospheres of Titan and Jupiter. Icarus 90, 330•333.

Yelle, R.V., 1991. Non-LTE models of Titan's upper atmosphere. Astrophys. J. 383, 380-400.

Yelle, R.V., Borggren, N., de la Haye, V., Kasprzal, W.T., Niemann, H.B., Müller-Wodarg, I., Waite, J.H., 2006. The vertical structure of Titan's upper atmosphere from the Cassini ion neutral mass spectrometer measurements. Icarus 182, 567-576.

Young, E.F., Rannou, P., McKay, C.P., Griffith, C.A., Noll, K., 2002. A three dimensional map of Titan's tropospheric haze distribution based on HST imaging. Astron. J. 123, 3473•3486.

Chapter 2

Simulation of Atmospheric Processes

Titan's atmospheric structure is the result of different processes that act simultaneously and have an impact on each other. These are radiation transfer, photochemistry and microphysics. In order to describe the coupling between photochemistry and haze formation in one dimension, it is necessary to have a model, which can simulate these three main processes. The flow chart in Fig. 2.1 provides a simplified view of the way this is accomplished. The Radiation sub-models perform the radiation transfer and calculate the thermal balance of the atmosphere. Hence, they provide the radiation flux at each altitude of the atmosphere that controls the chemical species photodissociation rates and the temperature vertical profile. These are coupled to the chemistry sub-model that solves the time-dependent continuity equation for the vertical distribution of species mole fractions. In this sub-model, the haze pathways considered lead to the haze monomer production at each altitude. This is then used as input in the third sub-model, which describes the microphysical growth of the haze monomers. Finally, the vertical distribution of chemical species concentrations and haze particle radiative properties are transferred back to the radiation sub-models. The above solution proceeds in time until equilibrium is reached.

The temporal evolution of Titan's atmosphere and haze can also be examined using different scenarios regarding Titan's past and future. In the present computations, we consider the solar flux reaching Titan to be today's. Since each process has a different characteristic time to reach equilibrium, a time integration process with varying step must be used and a fairly long total time of integration must be considered in order to take into account all the different physico-chemical processes (condensation, coagulation, photolysis, chemistry, mixing and diffusion), starting from an initial atmospheric structure. In the current chapter, a description for each of the simulated atmospheric processes is provided along with a discussion of the energy sources that set the atmospheric engine in action.

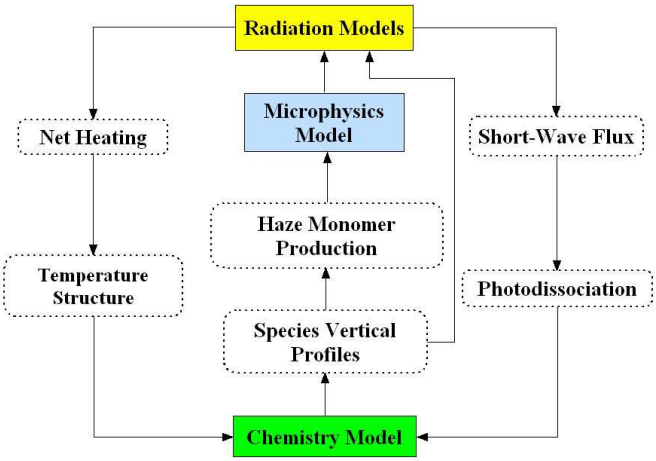

Figure 2.1: Model Flow Chart

2.1 Energy sources

Titan's position in the solar system allows for many types of energy sources to penetrate its atmosphere and influence the structure and composition inside it. A thorough discussion of the energy sources in Titan's atmosphere can be found in Sagan & Thompson (1984), who used measurements from the Voyager I & II missions along with results from the Pioneer 11 mission, which were available at that time, to identify the main contributions. The three most important types of energy influx are: solar photons, high energy particles from Saturn's magnetosphere and galactic cosmic ray (GCR) particles.

2.1.1 Solar photons

From the above energy sources, the dominant one is the solar radiation. Considering Saturn's location as the average distance of Titan from the Sun, ($\sim$ 9.55 a.u., see Table 1.1), the solar radiation reaching the upper region of Titan's atmosphere is about 1/100th of that reaching Earth's outer atmosphere. With the value of the solar constant being 1366.1 W/m^2 (Gueymard, 2004; Fröhlich, 2006), the corresponding value for Titan is about 15 W/m^2.

Due to the 11-year solar cycle (SC), which is related to the oscillation of the Sun's magnetic field, the total solar irradiance is not constant. Furthermore, the 27-day period of solar rotation, enhances the variation of its energy output. This variability has a strong spectral dependence that is related to the fact that different energy photons originate from different regions of the solar atmosphere. For wavelengths longer than 260 nm, which originate from the photosphere, the variability is very small, less than 0.1% during the solar cycle (Woods &

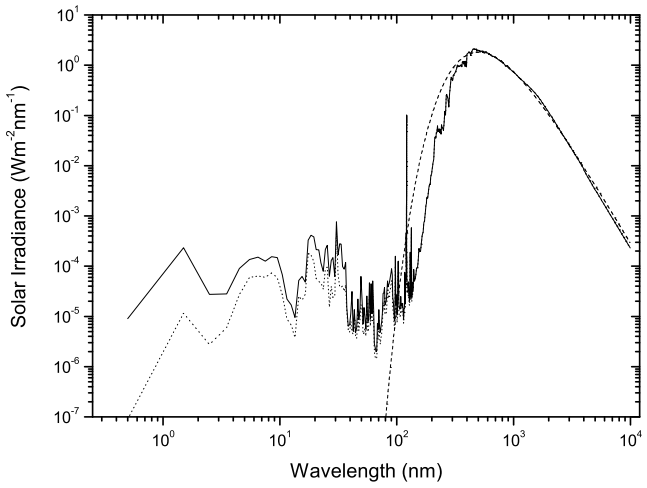

Figure 2.2: Solar flux at the Earth's orbit. Photon's in the UV region (λ <0.4μm) are involved in the photochemistry of the atmosphere. The pronounced peak at 121 nm corresponds to the Lyman-α emission line. The two profiles correspond to solar cycle minimum (dotted-line) and maximum (solid-line) observed emissions. The spectra are a synthesis from the data of Woods & Rottman (2002) between 0.5 - Ly-α and Ly-α - 200 nm, Lemaire et al. (2005) for the Ly-α spectrally resolved profile and Gueymard (2004) for the 200 nm - 10 μm region. The dashed line represents the blackbody emission for a temperature of 5,800 K.

Rottman, 2002). This is the spectral region of the solar irradiance that can be approximated by a blackbody emission (although, between 400 and 200 nm, strong absorption lines and absorption-edge effects lead to a deviation from a blackbody curve). Higher energy (shorter wavelength) photons originate from regions extending above the photosphere (chromosphere, transition region and corona) which are in non-LTE conditions. At these wavelengths, the observed solar irradiance is dominated by the presence of strong emission lines, which are sensitive to the solar magnetic activity. Here the solar cycle variability exhibits an increasing magnitude towards smaller wavelengths. At 200 nm the variation between the minimum and maximum observed irradiance is about 10%, while at Lyman-α (121.6 nm) the largest observed increase is a factor of about. For higher energies the variability is even larger (Woods & Rottman, 2002).

Solar photon's in the UV part of the spectrum are able to ionize and dissociate methane and nitrogen in Titan's atmosphere and in this way initiate the photochemistry that finally leads to the formation of the complex hydrocarbons

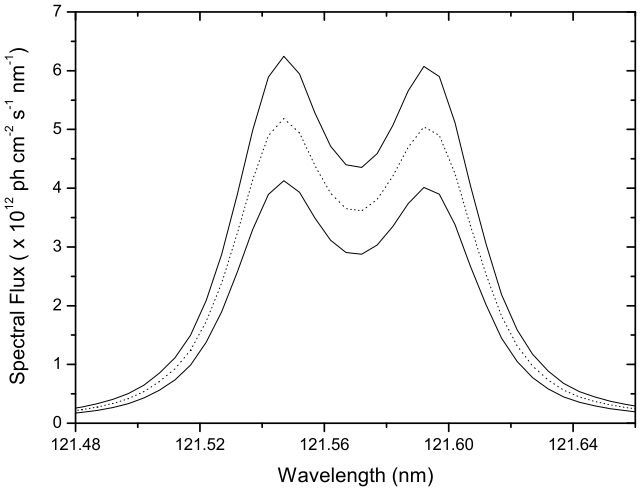

Figure 2.3: Lyman-α profiles for solar minimum, average and maximum emission conditions. The spectral variation is based on the observed profiles from Lemaire et al. (2005) for SC 23, while the integrated flux for maximum and minimum conditions corresponds to observations from 1947 to 1999 reported by Woods et al. (2000) with values of 3.5 and 5.6 $\times 10^{11}$ ph $s^{-1}cm^{-2}$ for average minimum to average maximum emission, respectively.

and the observed haze structure. Hence, the observed SC variability will have an impact on the derived chemical composition, inducing temporal variations. Fig. 2.2 presents the spectral variation of the incoming solar flux at the Earth's orbit for solar maximum and minimum conditions. The profiles are a composition of different measurements. Above 200 nm the suggested spectrum by Gueymard (2004) was used. The last is an average spectrum over SC, derived from measurements from 1978. For smaller wavelengths the presented profiles are based on the measurements of Woods & Rottman (2002) that cover the range down to 0.5 nm and are an average over SC22 (1986 - 1996). Further, in the solar Lyman-α region, the Lemaire et al. (2005) high resolution measurements are used that correspond to measurements during SC23. The observed profiles during different steps of the cycle show that the spectral shape of the profile doesn't change significantly but only shifts to higher or lower values. Based on this fact, the profiles used in the calculations are scaled to the total flux at this region reported by Woods et al. (2000) for average solar minimum and maximum conditions. These authors reported that over the period between 1946 and 1997 the average solar Lyman-α emission smoothed over 2 year bins, varied from 3.5×10^{11} ph/cm^2/s to 5.7×10^{11} ph/cm^2/s. This high resolution

representation of the solar Lyman-α along with its SC variability are presented in Fig. 2.3. In the calculations, the logarithmic mean between the profiles has been used, for the investigation of the average conditions in Titan's atmosphere, while the individual profiles were used, for the evaluation of chemical composition variations over the solar cycle.

2.1.2 Electron flux

The ionization initiated by the UV solar photons, leads to the production of photoelectrons which also interact with the atmospheric species, leading finally to the formation of the ionosphere. In addition to the photoelectrons, energetic particles from Saturn's magnetosphere also contribute to the total energetic particles influx in Titan's atmosphere, with the major contribution coming from the high-energy electrons. Until now, no internal magnetic field has been detected on Titan. This means that even if such a field exists, it so weak that it can't shield the atmosphere from the impact of any charged particles. The contribution of the last, depends on Titan's position relative to Saturn and the activity of the Sun. Titan is orbiting Saturn at an average distance of about 20 Saturn radii, which corresponds to the boundary region between Saturn's magnetosphere and the Solar wind. Hence, at times of low solar activity Titan is within Saturn's magnetosphere, while at times of enhanced solar activity the upper region of its atmosphere is influenced by the solar wind. Since the energy input due to energetic particles in Titan's atmosphere is smaller than that of solar photons they have not been included in the current calculations.

2.1.3 Galactic cosmic rays

Particles in galactic cosmic rays (GCR), due to their high energies penetrate to the very deep layers of the atmosphere, reaching down to the stratosphere before they encounter densities large enough to attenuate them. These rays are mainly composed of protons and alpha particles with kinetic energies in excess of 1 GeV (Capone et al., 1983). The interaction of these particles with Titan's neutral atmosphere leads to the ionization of the main species and also, depending on their initial energy, to the production of secondary energetic particles (neutrons, pions, etc.) which also contribute to the ionization (particle cascade). Since N_2 is the main component of the atmosphere, GCR act as a source of atomic N in the lower atmosphere where solar UV photons can not reach and hence contribute to the production of nitrile species in this region. Analytical models for the description of the GCR penetration into Titan's atmosphere (Capone et al., 1983; Lellouch et al., 1994; Wilson & Atreya, 2004), have shown that the maximum deposition of the cosmic rays is situated around 100 km and that the magnitude of the N_2 destruction peaks between 10 and 20 $cm^{-3}s^{-1}$. In order to include the contribution of GCR in the model calculations we have considered a loss rate for N_2 due to this process. The shape of the loss rate was based on the work of the above authors and is presented in Fig. 2.4. The contribution

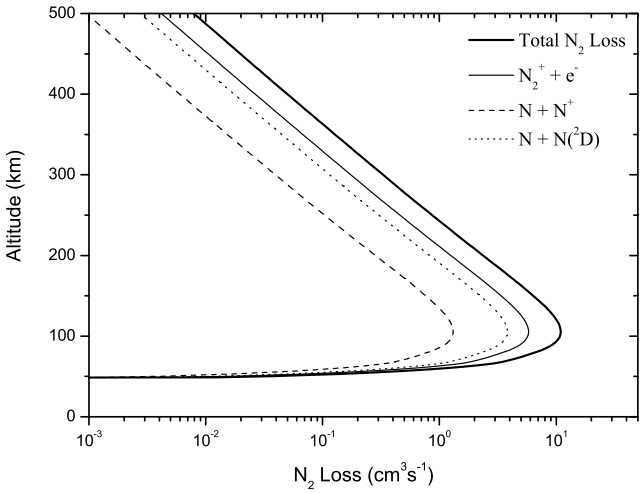

Figure 2.4: The loss rate of N_2 due to interaction with GCR. The contributions for each product pathway are also shown. Production due to the cascade particles below the peak at $\sim$ 100 km is not included in the calculations.

from the cascade particles is not included. The products from the interaction of GCR with N_2 and their yields are taken from Lellouch et al. (1994):

$$\begin{array}{lll} N_2 + GCR & \rightarrow N(^4S) + N^+ + e^- & 12\ \% \\ & \rightarrow N_2^+ + e^- & 53\ \% \\ & \rightarrow N(^4S) + N(^2D) & 35\ \% \end{array}$$

The impact of GCR on methane, the second most abundant species was also included, but the impact was found to be negligible. The interaction of GCR with methane was assumed to lead to:

$$\begin{array}{lll} CH_4 + GCR & \rightarrow CH_3 + H & 45\ \% \\ & \rightarrow {}^3CH_2 + 2\ H & 45\ \% \\ & \rightarrow CH + H_2 + H & 10\ \% \end{array}$$

The rate of the reaction was estimated based on the reported rate for the N_2 interaction and the cross sections of electron impact absorption of N_2 and CH_4 (Wilson & Atreya, 2004):

$$L_{GCR}(CH_4) = \frac{\sigma_{CH_4}}{\sigma_{N_2}} L_{GCR}(N_2) \tag{2.1}$$

where the cross sections correspond to the peak values over the energy range of electron impact.

2.2 Radiation transfer

In order to generate the photolysis rates and the vertical temperature structure used in the photochemical description of the atmosphere, the solar and thermal radiation transfer through the atmosphere must be performed. This is done with the use of a radiative/convective model that is based on the work of Vardavas & Carver (1984b).

The simulated atmosphere corresponds to the altitude region defined from the surface (∼1.5 bar) up to a pressure altitude of 10^{-9} mbar (∼ 1400 km). This is divided in to an expanding width pressure grid of 300 levels. The pressure grid is preferred from an altitude grid because in this way we can avoid pressure-dependent changes in the atmospheric temperature and composition (e.g. the methane absorption coefficients in the near-IR region have a strong pressure dependence which in the case of an altitude grid would have to be calculated every time the temperature structure changes). The altitude scale of the model is derived from the pressure grid and the calculated vertical temperature profile using the hydrostatic equilibrium equation:

$$\frac{\partial p}{\partial r} = -\varrho g(r) \tag{2.2}$$

where p, is the pressure, $r = R_T + z$ with z the altitude, ϱ the atmospheric mass density and $g(r)$ the gravity acceleration, while the atmospheric number density is calculated from the ideal-gas law taking into consideration the non-ideal correction factor (f) in the lower atmosphere suggested by Yelle et al. (1997):

$$p(f + 1) = nk_BT \tag{2.3}$$

with n the atmospheric number density, k_B the Boltzmann constant and T the temperature.

The radiation transfer is accomplished with the use of two separate high resolution radiation transfer models for the shortwave and longwave parts of the spectrum. These calculate the fluxes within every atmospheric layer, which are then used for the derivation of the vertical temperature structure. A short description of the process is following.

2.2.1 Spectral division & opacity sources

In order to perform the radiation transfer for each spectral domain (shortwave & longwave radiation) the spectrum has to be divided into fine intervals within which the monochromatic radiation transfer equation can be solved. For the shortwave radiation transfer the division must be of a high resolution because the source function can vary significantly over small wavelength regions, while for the longwave radiation the broad character of the Plank function allows for a coarser division. This considerations are with respect to the application in mind. Although such a division is appropriate for temperature calculations, for spectroscopic investigations, high resolution is necessary for the longwave radiation also.

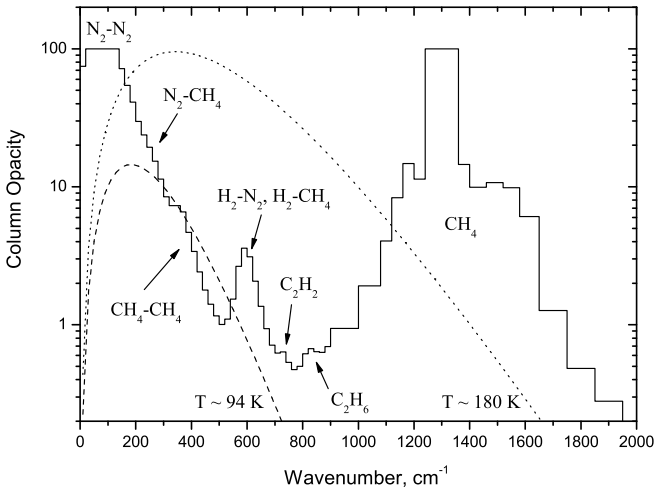

Figure 2.5: Model column opacities in the thermal infrared. Up to $\sim$ 700 cm^{-1} the main contribution comes from the collision induced absorption between the $N_2/CH_4/H_2$ pairs with the spectral dominance of each pair shown. At higher wavenumbers the opacity is controlled by methane, acetylene and ethane. The abundances for the absorbing species were calculated in the photochemical part of the model. The dashed and dotted lines are Planck functions (in arbitrary units) for about 94 and 180 K, respectively, representing the spectral coverage of Titan's thermal radiation.

In the model, the shortwave radiation corresponds to the wavelength region between 0.5 nm and 10 μm and is dominated by the solar flux. This spectrum is divided into 660 wavelengths with increasing intervals towards the near-IR region. In the UV region, gas opacity is provided by the major species included in the photochemical model (see Table 2.2 in next section, where references for their cross sections and branching ratios can be found), while from the visible to the near-IR, methane is the dominant gas absorber. Haze particles have an important scattering/absorbing contribution in the whole part of the spectrum, while the most important Rayleigh scatterer is N_2.

The longwave radiation that is the thermal radiation from Titan's surface and the atmosphere, corresponds to wave numbers between 0 and 8200 cm^{-1} and is divided in 71 domains. From 0 to 900 cm^{-1}, where the major part of Titan's surface thermal radiation is emitted, there are 45 regions of 20 cm^{-1} width, while the spectrum interval increases for higher wave numbers. Up to $\sim$ 700 cm^{-1} the opacity is mainly controlled by collision-induced absorption (CIA) between nitrogen, methane and hydrogen molecules. Above 700 cm^{-1} the thermal opacity is controlled by methane, ethane and acetylene absorption.

The major contribution comes from the ν_4 band of CH_4 which is centered at 1300 cm^{-1}. Opacities due to C_2H_6 and C_2H_2 contribute mainly in the region between 600 and 900 cm^{-1} and were calculated from the HITRAN database spectroscopic values. In addition to the above, opacity from the rotational lines of HCN has been included based again on the spectroscopic values given in the HITRAN database. Haze opacity in the IR was calculated in the same way as for the solar region.

In Fig. 2.5 the model column opacity in the region 0 - 2000 cm^{-1} is shown along with the calculated thermal emission for temperatures of 93.7 K (characteristic of Titan's surface, Fulchignoni et al. 2005) and 180 K (characteristic of the stratopause temperature, Flasar et al. 2005). The abundances for the absorbing molecules where provided from their vertical profiles, calculated in the photochemical part of the model. The effect of the so-called Titan's thermal window (Samuelson et al., 1983; McKay et al., 1991) is obvious in the 400-600 cm^{-1} region where the decrease in opacity allows thermal radiation from the surface to escape to space.

A detailed description of the calculation of the absorption coefficients of methane and other hydrocarbons based on band model formulation and line by line spectroscopic data is given in the appendix, along with the Rayleigh/Mei scattering properties for the molecules and haze particles.

2.2.2 Shortwave radiation transfer

From the above description of the opacity sources it becomes evident that Titan's atmosphere is inhomogeneous and multiple scattering will play an important role in the radiation transfer. A solution for the transfer equation, for such an absorbing-scattering atmosphere can be calculated based on the Eddington method (Shettle & Weinman, 1970), which was later updated to the well known Delta-Eddington method (Joseph et al., 1976). The later method takes in to consideration anisotropic scattering with the inclusion of a truncated phase function, and provides an analytical solution for a two-boundary valued problem given the extinction opacity, τ, the single scattering albedo, ω, and the asymmetry factor, g of each layer (homogeneous layers).

In the later method, for an atmosphere of N layers the computational time for the calculation of the radiation field at a single wavelength would require $(2N)^3$ steps. For the 300 layers included in the model and the 660 monochromatic domains considered, that would require an enormous computational time for the calculation of the shortwave radiation transfer. A common approach for solving this problem is the summation of the atmospheric structure in a more coarse grid in order to reduce the number of homogeneous atmospheric layers. Yet, this summation simplifies the structure of the atmosphere and can produce artificial features in the cooling/heating rates. For the case of Titan's atmosphere, where the haze contribution has a variable vertical structure and extends over a large range of altitudes, this simplification could have an impact on the calculated temperature structure and in the photolysis rates used for the generation of the photochemistry.

In order to solve this problem an approach to the Delta-Eddington solution was developed and used in the model calculations. In the new description, the radiation transfer equation is differentiated into a three term finite-difference matrix which can be rapidly solve using the Thomas algorithm. With this method the number of step required varies linearly with the number of atmospheric layers, which reduces significantly the computational time for each wavelength. A description of the new method is provided in the appendix.

2.2.3 Longwave radiation transfer

The longwave radiation transfer, depends on and further defines the temperature structure through the black-body emission described by the Planck function. Thermal emission by methane and other hydrocarbon and nitrile species, balances the heating induced by the absorption of solar radiation from molecules (mainly methane) and haze particles and controls the surface temperature and the vertical temperature profile.

The thermal flux into each layer k can be written as the sum over each spectral domain i:

$$F_k = \sum_i F_{i,k} \tag{2.4}$$

with the contribution of each domain being:

$$F_{i,k} = B_i(T_g)t(z_k, 0) + \int \varepsilon(z')B(T_{z'})\frac{dt(z_k, z_i)}{dz}dz' \tag{2.5}$$

where T_g is the surface temperature, B_i corresponds to the average value of the Planck function, over the spectral domain i multiplied by the width of the domain, $t(z_k,\ z_i)$ is the atmospheric transmission between layers i and k and $\varepsilon(\mathrm{z}_i)$ is the emissivity of the layer i which is given by:

$$\varepsilon = 1 - e^{-\tau} \tag{2.6}$$

with τ the optical depth of the layer. The latter provides a description for the divergence of each atmospheric layer from a black-body emitter. The first term in eq. 2.5 corresponds to the contribution of the surface emitted thermal radiation into layer k, while the integral describes the emitted thermal radiation from all other layers into layer k.

In the calculation of transmittances between different layers, the atmospheric paths can be highly inhomogeneous (different temperature and pressures). The molecular absorption coefficients have a strong dependence on pressure and temperature which means that the curves of growth over spectral lines will have a significantly different structure between inhomogeneous layers. Under the broad-band model structure used, the transmissions between different layers can not be estimated with the product of the individual transmissions because the lines inside each spectral bin can have a significantly different variation with the conditions of each atmospheric layer.

An approach to solve this problem is the Curtis-Godson (C-S) approximation. In this, an average pressure and temperature for the atmospheric path is calculated and used for the estimation of the opacities. The averaging is weighted by the abundance of the absorbing species:

$$\begin{aligned} \bar{p} &= \frac{1}{w} \int\limits_{path} p dw \\ \bar{T} &= \frac{1}{w} \int\limits_{path} T dw \end{aligned} \tag{2.7}$$

where w is the total amount of the absorber in the path under investigation. The C-G approximation provides the pressure and temperature for a homogeneous path of the same total amount, which would give a transmission as close as possible with that of the inhomogeneous path. Note that all absorber amounts in the thermal transfer calculations have been multiplied with the diffusivity factor (1.66) in order to take into account the non-vertical radiation transfer (e.g. Vardavas & Taylor (2007)).

2.2.4 Temperature calculation

The modelled atmosphere is separated in two regions. One close to the surface which is in convective equilibrium (CE) and a second one above, which is in radiative equilibrium (RE). In the first region (CE), the temperature structure is controlled by the atmospheric lapse rate, Γ. For the Earth's atmosphere the convective region of the atmosphere corresponds to the troposphere. Yet for Titan, although we use the observed temperature minimum at ~ 40 km to define the position of the tropopause, the troposphere -defined as the region of convective equilibrium- corresponds to a small layer with width of only a few km above the surface. This was derived initially from the Voyager observed vertical temperature profile (Lindal et al., 1983; Eshleman et al., 1983) and also by model results (McKay et al., 1989).

The slopes of the temperature profiles from the observed temperature structures derived by HASI and CIRS in the lower atmosphere (Fig. 2.6) are similar and very close to the expected dry adiabatic lapse rate:

$$\Gamma_d = \frac{g(r)}{c_P} \tag{2.8}$$

with *g(r)* the gravity acceleration at radial distance r and c_P the atmospheric specific heat capacity. Hence, in the model calculations we have adopted the dry adiabatic lapse rate as given by this expression for the calculation of the temperature structure inside the convective region. Keep in mind that the lapse rate is not constant but has a small variability due to the temperature and altitude dependence of the heat capacity and gravity acceleration, respectively.

In the rest of the atmosphere along with the value at the surface, the temperature is controlled by the balance between the absorption of solar and the emission of thermal radiation. In addition to the above, the conduction between

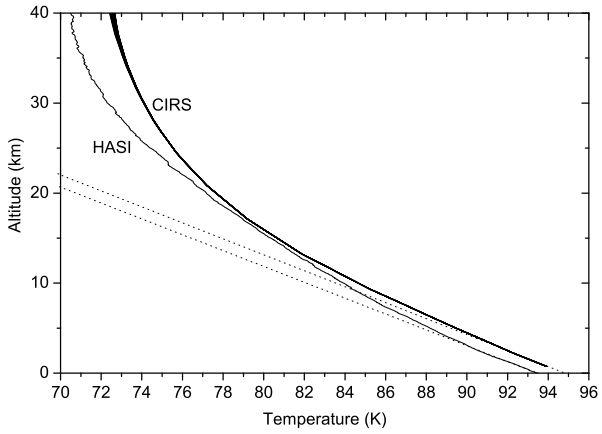

Figure 2.6: Tropospheric temperature profiles, in situ measured by HASI (F. Ferri, personal communication) and derived by CIRS (R. Achterberg and B. Conrath, personal communication). The dotted lines have similar slopes of ∼1.1. The altitude range above which the observed temperature profiles diverge from the constant slope marks the transition region between convective and radiative equilibrium.

adjacent layers has been included in the energy balance. For each atmospheric layer in the RE region, the balance is described by:

$$\Delta F_{IR} = \Delta F_{\odot} + \Delta F_C \tag{2.9}$$

where for each process, $\Delta F_{\odot}$ corresponds to F_{i+1}-F_i with F_i the net outgoing solar flux of each layer i. The conductive flux is given by the expression:

$$F_C = -K\frac{dT}{dz} = \frac{g(r)Mp}{R}\frac{K}{T}\frac{dT}{dp} \tag{2.10}$$

where K is the atmospheric conduction coefficient, M the atmospheric mean molecular weight, p the pressure and T the temperature. In the second part, the altitude dependance was transformed to pressure dependence based on the hydrostatic equilibrium condition. The conduction coefficient can be written in the form K=αT$^{\beta}$ with α=56 and β=0.69 for N_2 (Banks & Kockarts, 1973).

The position of the transition region between convective and radiative equilibrium is determined for the lowest altitude where the condition (Vardavas & Carver, 1984a; Ramanathan & Coakley, 1978; Manabe & Wetherland, 1967):

$$\left(\frac{dT}{dz}\right)_{boundary} \geq -\Gamma_d \tag{2.11}$$

is valid. The convective boundary derived with the above criterion corresponds to the lower level of the layer at which the temperature gradient defined by RE is larger than the one from the convective profile. Once the atmospheric lapse rate (-dT/dz) is less than the dry adiabatic lapse rate the atmosphere is stable against convection and the temperature is defined by radiative equilibrium. Due to the iterative character of the model, the altitude of the convective region is allowed to adjust during the simulation.

The calculation of the vertical temperature structure can be easily performed with the Newton-Raphson method as described in Vardavas & Carver (1984a). In short, the method solves for the average temperature within each atmospheric layer (and not that of each level which leads into instability and oscillations along the vertical structure) and that of the surface, which are necessary for satisfying equation 2.9. The vertical temperature structure of the modelled atmosphere, is calculated for each time step of photochemical and microphysical evolution, in order to include feedbacks from chemical composition and haze opacity changes on the temperature structure and the radiation field, and vice versa.

2.3 Photochemistry

The photochemical part of the model uses the grid of the Radiative/Convective sub-model in order to solve the time-dependent continuity equation in 1D for the species considered. Its description is based on the Vardavas (1984) model for reactive gas flows within shock tunnels. There are 68 chemical species included in the simulation of Titan's photochemistry, the evolution of which is controlled by 538 reactions. A thorough search has been performed for the use of the latest parameters (photolysis cross sections, branching ratios and chemical reaction rates) which correspond, as closely as possible, to the low temperature conditions found in Titan's atmosphere (Tables 2.2 & 2.3). The main processes defining the vertical profile of each species in the model are: photodissociation, chemical production and loss, vertical transport, loss due to condensation, surface deposition and escape to space. A description of each process follows along with the simulation method for the species mole fractions.

2.3.1 Photolysis

The complex organic photochemistry in Titan's atmosphere is initiated with the photodissociation / photo-ionization of methane and molecular nitrogen, which are the most abundant species. N_2 is dissociated and ionized by vacuum UV (VUV) photons with $\lambda < 1000$ Å, electrons and GCR particles with the first having the most important contribution due to their higher influx in comparison with the other energy sources. Depending on the energy of the incident photon or energetic particle, N_2 can be dissociated or ionized into:

- different energy states of atomic nitrogen ($N(^4S)$, $N(^2D)$, $N(^2P)$, etc.)
- become ionized (N_2^+)

- get dissociativelly ionized giving a neutral ($N(^4S)$ or $N(^2D)$) and an ionized nitrogen atom (N^+).

In the dissociation region, since the higher energy states of atomic nitrogen have a small life time and de-excite fast to the first excited energy state $N(^2D)$ (Zipf et al., 1980), photochemical models include only the last product species along with the ground state one $N(^4S)$ in their calculations. N_2 has its first ionization limit at 795.8 Å that means that below this limit the N_2^+ production starts to dominate. At 510.5 Å the first dissociative ionization limit is found. The products at these energies have been studied by Nicolas et al. (2003) who found that for wavelengths smaller than 464.8 Å the major production of the neutral nitrogen atom is in its excited $N(^2D)$ state. Based on these results the scheme used in the model is:

$$\begin{array}{lll} N_2 + h\nu & \rightarrow N(^4S) + N^+ + e^- & \lambda < 510 \text{ nm} \quad 10\% \\ & \rightarrow N(^2D) + N^+ + e^- & \lambda < 510 \text{ nm} \quad 90\% \\ & \rightarrow N_2^+ + e^- & 510 \text{ nm} < \lambda < 796 \text{ nm} \\ & \rightarrow N(^2D) + N & 796 \text{ nm} < \lambda < 1000 \text{ nm}. \end{array}$$

The current photolysis scheme of N_2 is significantly different from that used in previous photochemical models of Titan's atmosphere. The Yung et al. (1984) model considered N_2 destruction by energetic electrons and galactic cosmic rays but not by high energy photons. Toublanc et al. (1995) considered only neutral dissociation production assuming excited nitrogen atoms as single products and included also an influx of $N(^2D)$ and $N(^4S)$ atoms for the production of atomic nitrogen by magnetospheric electrons from Saturn. Lara *et al.* (1996) also considered only the neutral dissociation of N_2 in the range 80 - 800 Å and assumed that excited atoms are the sole product, an approach which was adopted also by Lebonnois et al. (2001). In the latest published photochemical model, Wilson & Atreya (2004) provided a more detailed and realistic description of the N_2 photolysis by including the ionization, dissociative ionization and neutral dissociation pathways, in a way similar to the above. The current scheme diverges from theirs only in one point. Based on the latest measurements of Nicolas et al. (2003), the neutral nitrogen atoms released in the dissociative ionization are mainly in their excited state in contrast to the previous suggestions which favored the $N(^4S)$ production. This difference has an impact on the upper atmosphere profiles for some of the nitrile but also hydrocarbon species and is discussed in the next chapter.

The structure of N_2 absorption spectrum below 1000 Å presents significant variability due to presence of a number of rotational absorption bands which are super-imposed on the ionization continuum (see Fig. 2.7). For the calculations the measurements of Chan et al. (1993) have been used. The produced nitrogen atoms react readily with the hydrocarbons in the atmosphere and lead to the formation of the nitrile species described in the following sections.

Methane's photo-absorption spectrum starts at ∼150 nm. Below this wavelength, the cross section takes high values (see Fig. 2.8) and solar photons of these energies are able to dissociating methane. The major contribution in the

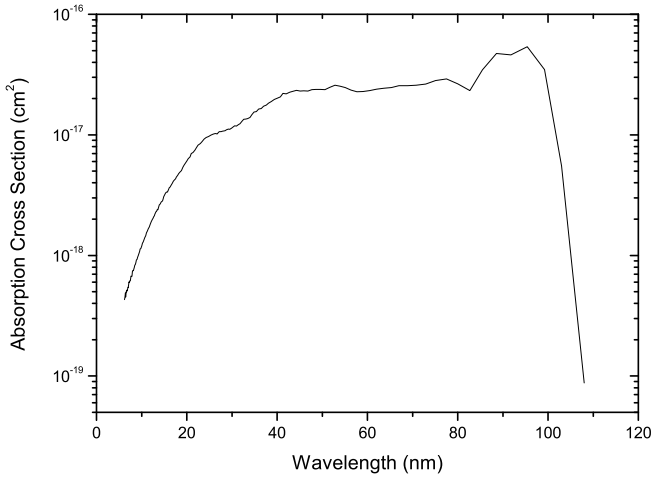

Figure 2.7: N_2 absorption cross section from the measurements of Chan et al. (1993).

photolysis comes from the Lyman-α region of the solar spectrum due to the large photon flux in this and the high values of the absorption cross section there. Hence, knowledge of the dissociation products in this region is very important and has been investigated by many authors. The energetically possible and spin conserving channels through which methane photolysis can proceed at Ly-α, are :

$$\begin{array}{lll} CH_4 + h\nu \rightarrow & CH_3 + H & I \\ & {}^1CH_2 + 2\ H & II \\ & {}^3CH_2 + 2\ H & III \\ & CH + H_2 + H & IV \\ & {}^1CH_2 + H_2 & V. \end{array}$$

The significance of each of the above channels has been under considerable debate over time. A review of the up-to-date measurements for methane's photodissociation products and suggested photochemical schemes can be found in Romanzin (2005). Due to the high reactivity of the methane photolysis products, reliable experiments for the initial dissociation products have to be performed in collision free conditions. Slanger & Black (1982) performed resonance fluorescence measurements for the estimation of the H atom yield at Ly-α and based on estimations regarding yields for H_2 (ϕ_{H_2}=0.59, Laufer & McNesby (1968)) and CH (ϕ_{CH}=0.08, Rebbert & Ausloos (1973)), concluded that the main photodissociation channels of methane were II, III and V with channels I and IV having at most a minor contribution. These assumptions were used in

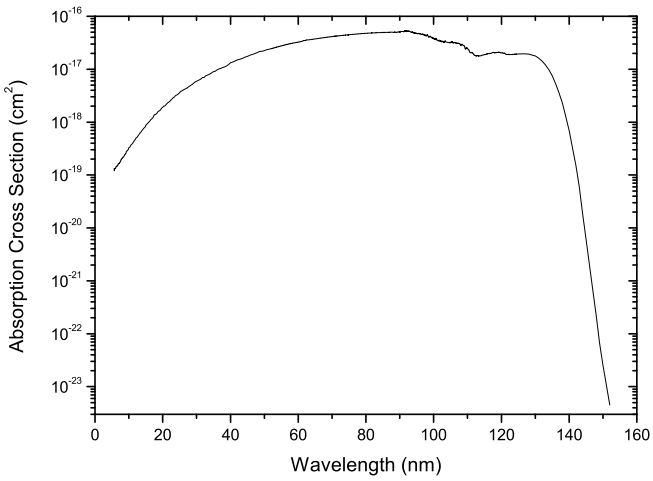

Figure 2.8: Methane cross section in the UV region. The presented spectrum is a composite based on the measurement of Au et al. (1993) (5.64 - 51.7 nm), Kameta et al. (2002) (52.05 - 123.63 nm) and Lee et al. (2001) above.

the Yung et al. (1984) photochemical model of Titan's atmosphere.

Later, Mordaunt et al. (1993) using H atom photofragment translational spectroscopy, again at Ly-α, found the C-H bond fission to be the dominant channel (I) at this wavelength, in contrast to previous results. A considerable part of the methyl radicals formed (25%) were found to have significant internal energy, enough to undergo further unimolecular decay. Depending on the possible results of this decay (channels II, III and IV) and assuming a total hydrogen atom yield of unity, they suggested two possible photolysis schemes for the two limiting cases (Table 2.1) pointing out though that the real methane photolysis scheme must be somewhere in between these two cases. These results were used in the Lebonnois et al. (2001) photochemical model of Titan's atmosphere.

Romani (1996) in an attempt to match all previous yield measurements for the possible products CH, H, H_2 and CH_3 performed a list-squares optimization with the assumption that channel II has zero yield. The derived photochemical scheme has been used in many models of the Jovian planets. Heck *et al.* (1996) using photofragment imaging techniques concluded that the methyl radical channel is six times more important than all the other H atom exit channels together and that channel V is approximately a factor 2 more important than channel IV. Brownsword et al. (1997b), using laser induced fluorescence, measured the hydrogen atom yield at Ly-α and found it ϕ_H=0.47$\pm$0.11 in marked contrast to the previous measurements (ϕ_H=1.16 from Slanger & Black (1982), ϕ_H=1.0$\pm$0.5 from Mordaunt et al. (1993)). Based on the last two results, Smith

Table 2.1: Suggested methane photochemical schemes at Ly-α

	Yung	Mordaunt (1993)		Romani	Smith & Raulin	Wang
	(1984)	Scheme 1	Scheme 2	(1996)	(1999)	(2000)
CH_3 + H	-	0.51	0.49	0.41	0.41	0.291
$^1CH_2$ + 2 H	-	-	-	-	-	0.055
$^3CH_2$ + 2 H	0.51	0.25	-	0.21	-	-
CH + H_2 + H	0.08	-	0.51	0.10	0.06	0.070
$^1CH_2$ + H_2	0.41	0.24	-	0.28	0.53	0.584

& Raulin (1999) suggested a new scheme in which the total H atom formation is reduced compared to the previous suggestions and with the ground state methylene radical channel absent.

Wilson & Atreya (2000) investigated the impact of the different suggested pathways on the produced hydrocarbons and concluded that the choice of a quantum yield scheme affects mostly the C_3 species production in the Lyman-α region (where the major destruction of CH_4 molecules takes place) leaving the simpler C_2 species unaffected and that the Romani (1996) scheme provided an intermediate result between the other schemes. Lebonnois et al. (2001) have found similar results for the photochemical schemes of Mordaunt et al. (1993) and Smith & Raulin (1999).

Finally, Wang & Liu (1998) and Wang et al. (2000) have performed the most complete up to date measurements for the methane photolysis yields at Ly-α. By measuring the relative velocities of the atomic H produced and the relative abundances of the methyl (CH_3) and methylene ($^{1,3}CH_2$) fragments, they concluded that the major product is methylene which is released in its excited state ($^1CH_2$). We adopted these latest results for the methane photolysis in this spectral region.

For other wavelengths the energetically possible pathways are only channels I and V. There has not been any recent published investigation of the branching ratios for this region. Older measurements at 1236 Å (Mahan & Mandal, 1962; Ausloos et al., 1964) and 1048-1067 Å (Magee, 1963) that suggested the methylene radical as the main product, were performed under collision conditions and hence they can not be considered reliable since the measured end products could be the result of secondary reactions. Most photochemical models consider photons of non-Lyman wavelengths to dissociate methane following the first channel (CH_3 production). Wilson & Atreya (2000), investigated the two limiting cases (CH_2 or CH_3) for the non-Lyman methane photodissociation and concluded that the impact of the channel used was minor compared to the one at Ly-α, and that the only species showing variation was ethane (C_2H_6) due to its production dependance on the CH_3 radical. In the current calculations, only the production of methyl radicals was considered at these wavelengths.

For the other species included in the model, the references for the cross sections used and the considered pathways of photodissociation with their yields are presented in Table 2.2. Plots of the absorption cross sections of these species are presented in the appendix.

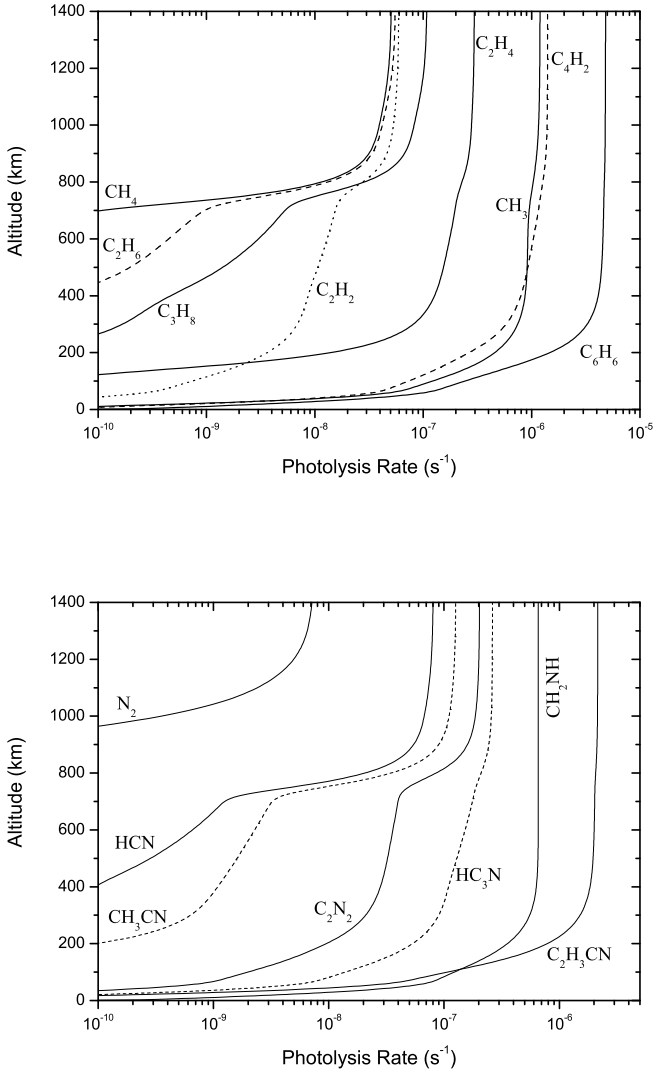

Figure 2.9: Model calculated photolysis rates for the most important hydrocarbons (top panel) and nitriles (bottom panel) in Titan's atmosphere. The solar zenith angle is set to 60°. Secondary photolysis regions for some of the hydrocarbons (e.g. C_2H_2) are due to their extended absorption cross section profiles above the methane dissociation limit at 145 nm and their presence in significant amounts.

The photolysis rate, $J(\mathrm{s}^{-1})$, for each species at altitude z is calculated by the usual formula:

$$J(z) = \int \chi_\lambda(z)\Phi_\lambda q_\lambda(z)\sigma_\lambda d\lambda \tag{2.12}$$

where Φ_λ is the incoming solar spectral flux, χ(z) is the enhancement factor, q_λ is the quantum yield for photodissociation and σ_λ the wavelength-dependent absorption cross section. The radiation field along with the enhancement factor at each altitude are calculated in the RC sub-model. Some vertical profiles of the photolysis rates of the most important hydrocarbons and nitriles in Titan's atmosphere are shown in Fig. 2.9 for a solar zenith angle of 60°.

2.3.2 Chemical schemes

The derived photodissociation products react together to give all the observed species considered in the model following the chemical reactions presented in Table 2.3. Although many photochemical models have been developed in the past for the simulation of Titan's neutral atmospheric composition, (Yung et al., 1984; Toublanc et al., 1995; Lara *et al.*, 1996; Lebonnois et al., 2001; Wilson & Atreya, 2004) significant differences can be found among them regarding the rates used for some of the reactions. In the current simulations the previously, well established, reaction schemes for the production of most of the observed species in Titan's atmosphere have been used and also new species have been included.

The absence of measurements for the reaction rates in the temperature range 100 - 200 K, which is characteristic of Titan's atmosphere, has always been a problem in the photochemical models. This is more clearly shown in the last column of Table 2.3, where the temperature range of the measurements for each reaction used is given. Although a significant number of new measurements have been performed at low temperatures since the early photochemical models, the majority of the reaction rates used, are measured at T$\geq$200 K and extrapolation to Titan's atmospheric temperatures is applied, a common approach between all photochemical models. The good agreement between the measurements and the simulated profiles presented in the next chapter, for most of the species, suggests that the extrapolation procedure applied is adequate. Nevertheless, the high accuracy measurements provided by the Cassini/Huygens mission require the use of accurate and realistic laboratory measurements which will constrain better the photochemistry and allow a safer interpretation of the haze production processes. A short description of the main pathways thta lead to the formation of the most important hydrocarbons and nitriles in Titan's atmosphere follows.

Hydrocarbons

The most abundant hydrocarbon found in Titan's atmosphere after methane, is ethane (C_2H_6) which is mainly produced in the collisional addition of two methyl radicals:

Table 2.2: Photolysis Reactions

	Reaction			Branching Ratio	Reference	
					Cross Sections	Yields
	HydroCarbons					
R1	$H_2 + h\nu$	→	2 H	1	Backx et al. (1976)	Est.
R2	$CH_3 + h\nu$	→	$^1CH_2$ + H	$\lambda \leq$ 165nm: 0; other: 1	Adachi et al. (1980)	Wilson et al. (1994)
R3		→	CH + H_2	$\lambda \leq$ 165nm: 1; other: 0	Pilling et al. (1971)	Kassner &Stuhl (1994)
R4	$CH_4 + h\nu$	→	$^1CH_2$ + H_2	$\lambda \leq$Ly-α: 0.584; other: 0	Samson et al. (1989)	
R5		→	$^1CH_2$ + 2 H	$\lambda \leq$Ly-α: 0.055; other: 0	Lee et al. (2001)	Wang & Liu (1998)
R6		→	CH + H + H_2	$\lambda \leq$Ly-α: 0.070; other: 0	Hudson (1971)	Wang et al. (2000)
R7		→	CH_3 + H	$\lambda \leq$Ly-α: 0.291; other: 1	Chen & Wu (2004)	
R8	$C_2H + h\nu$	→	C_2 + H	1	Fahr (2003)	Mebel et al. (2001)
R9	$C_2H_2 + h\nu$	→	C_2 + H_2	0.1	Cooper et al. (1995a)	Okabe (1981)
R10		→	C_2H + H	$\lambda <$ 124nm: 0.1;$\lambda <$ 150nm: 0.3; $\lambda <$ 190nm: 0.06;$\lambda <$ 225nm: 0.3	Smith et al. (1991) Bénilan et al. (2000)@173K	Okabe (1983) Seki & Okabe (1993)
R11	$C_2H_3 + h\nu$	→	C_2H_2 + H	1	Fahr et al. (1998)	Ahmed et al. (1999)
R12	$C_2H_4 + h\nu$	→	C_2H_2 + H_2	$\lambda <$ 175nm: 0.460; other: 0.73	Cooper et al. (1995b)	Chang et al. (1998)
R13		→	C_2H_2 + 2 H	$\lambda <$ 175nm: 0.519; other: 0.27	Holland et al. (1997)	Lee et al. (2004)
R14		→	C_2H_3 + H	$\lambda <$ 175nm: 0.021; other: 0.0	Zelikoff et al. (1953)	
R15	$C_2H_5 + h\nu$	→	$^1CH_2$ + CH_3	1	Munk et al. (1986a)	Gladstone et al. (1996)
R16	$C_2H_6 + h\nu$	→	2 CH_3	$\lambda <$ Ly-α: 0.17; Ly-α: 0.03; other: 0.0		
R17		→	CH_4 + $^1CH_2$	$\lambda <$ Ly-α: 0.16; Ly-α: 0.26; other: 0.02	Kameta et al. (1996)	Hampson &
R18		→	C_2H_4 + 2 H	$\lambda <$ Ly-α: 0.41; Ly-α: 0.31; other: 0.13	Lee et al. (2001)	McNesby (1965)
R19		→	C_2H_4 + H_2	$\lambda <$ Ly-α: 0.0 ; Ly-α: 0.15; other: 0.48	Chen & Wu (2004)	Lias et al. (1970)
R20		→	C_2H_2 + 2 H_2	$\lambda <$ Ly-α: 0.26; Ly-α: 0.25; other: 0.37		
R21	$C_3H_3 + h\nu$	→	C_3H_2+ H	1	Fahr et al. (1997)	Jackson et al. (1991)
R22	$CH_3C_2H + h\nu$	→	C_3H_3 + H	$\lambda \leq$Ly-α: 0.0; other: 0.50	Nakayama & Watanabe (1964)	Seki & Okabe (1992)
R23		→	C_3H_2 + H_2	$\lambda \leq$Ly-α: 1.0; other: 0.39	Ho et al. (1998)	Sun et al. (1999)
R24		→	C_2H_2 + $^1CH_2$	$\lambda \leq$Ly-α: 0.0; other: 0.11	LISA* @ 183K	
R25	$CH_2CCH_2 + h\nu$	→	C_3H_3 + H	0.64	Chen et al. (2000)	Sun et al. (1999)
R26		→	C_3H_2 + H_2	0.36	LISA* @ 183K	
R27	$C_3H_6 + h\nu$	→	CH_2CCH_2 + H_2	$\lambda <$ 135 nm: 0.43; $\lambda <$ 155 nm: 0.40; $\lambda <$ 175 nm: 0.015; $\lambda <$ 195 nm: 0.01		
R28		→	CH_3C_2H + H_2	$\lambda <$ 135 nm: 0.25; $\lambda <$ 155 nm: 0.24; $\lambda <$ 175 nm: 0.015; $\lambda <$ 195 nm: 0.01		
R29		→	C_2H_4+$^1CH_2$	$\lambda <$ 135 nm: 0.06; $\lambda <$ 155 nm: 0.04; $\lambda <$ 175 nm: 0.02; $\lambda <$ 195 nm: 0.0	Koizumi et al. (1985)	
R30		→	C_2H_3 + CH_3	$\lambda <$ 135 nm: 0.21; $\lambda <$ 155 nm: 0.27; $\lambda <$ 175 nm: 0.335; $\lambda <$ 195 nm: 0.34	Fahr & Nayak (1996) Samson et al. (1962)	Collin (1988)†
R31		→	C_2H_2 + CH_4	$\lambda <$ 135 nm: 0.05; $\lambda <$ 155 nm: 0.05; $\lambda <$ 175 nm: 0.05; $\lambda <$ 195 nm: 0.04		
R32		→	C_3H_5 + H	$\lambda <$ 135 nm: 0.0; $\lambda <$ 155 nm: 0.0; $\lambda <$ 175 nm: 0.565; $\lambda <$ 195 nm: 0.60		
R33	$C_3H_8 + h\nu$	→	C_3H_6+ H_2	$\lambda \leq$Ly-α: 0.32; other: 0.67		
R34		→	C_2H_6+$^1CH_2$	$\lambda \leq$Ly-α: 0.10; other: 0.05	Kameta et al. (2002)	Obi et al. (1971)
R35		→	C_2H_4 + CH_3 + H	$\lambda \leq$Ly-α: 0.43; other: 0.17	Okabe & Becker (1963)	
R36		→	C_2H_4 + CH_4	$\lambda \leq$Ly-α: 0.15; other: 0.11		
R37	$C_4H_2 + h\nu$	→	C_4H + H	$\lambda <$ 165nm:0.2; else:0	Okabe (1981)	
R38		→	2 C_2H	$\lambda <$ 165nm:0.03; $\lambda <$ 205nm:0.01; else:0	Fahr & Nayak (1994)	Glicker & Okabe (1987)
R39		→	C_2H_2 + C_2	$\lambda <$ 165nm:0.1; $\lambda <$ 205nm:0.06; else:0	Smith et al. (1998) @ 193K	
R40		→	C_4H_2*	$\lambda <$ 165nm:0.67; $\lambda <$ 205nm:0.93; else:1		
R41	$C_4H_4 + h\nu$	→	C_4H_2+ H_2	0.8	Fahr & Nayak (1996)	Gladstone et al. (1996)
R42		→	2 C_2H_2	0.2		
R43	$C_4H_6 + h\nu$	→	C_4H_4 + H_2	0.05		
R44		→	C_2H_4 + C_2H_2	0.17		Bergmann &
R45		→	CH_3 + C_3H_3	0.40	Fahr & Nayak (1994)	Demtroder (1968)
R46		→	C_4H_5 + H	0.28		
R47		→	2 C_2H_3	0.10		
R48	$C_4H_8 + h\nu$	→	C_4H_6 + 2 H	$\lambda <$ 135nm: 0.23; $\lambda <$ 160nm: 0.14; else: 0.06		
R49		→	C_3H_8 + CH_3	$\lambda <$ 135nm: 0.12; $\lambda <$ 160nm: 0.39; else: 0.66		
R50		→	CH_3C_2H + CH_4	$\lambda <$ 135nm: 0.03; $\lambda <$ 160nm: 0.02; else: 0.0		
R51		→	CH_2CCH_2 + CH_4	$\lambda <$ 135nm: 0.14; $\lambda <$ 160nm: 0.10; else: 0.0	Samson et al. (1962)	Wilson & Atreya (2004)
R52		→	C_2H_5 + C_2H_3	$\lambda <$ 135nm: 0.25; $\lambda <$ 160nm: 0.14; else: 0.04	Koizumi et al. (1985)	
R53		→	2 C_2H_4	$\lambda <$ 135nm: 0.02; $\lambda <$ 160nm: 0.04; else: 0.05		
R54		→	C_2H_2 + 2 CH_3	$\lambda <$ 135nm: 0.02; $\lambda <$ 160nm: 0.0; else: 0.04		
R55		→	C_3H_6 + $^1CH_2$	$\lambda <$ 135nm: 0.02; $\lambda <$ 160nm: 0.02; else: 0.0		
R56	$C_4H_{10} + h\nu$	→	C_4H_8 + H_2	$\lambda <$ 135nm: 0.48; other: 0.31		
R57		→	C_2H_6 + C_2H_4	$\lambda <$ 135nm: 0.15; other: 0.17	Okabe & Becker (1963)	Obi et al. (1971)
R58		→	C_3H_6 + CH_3 + H	$\lambda <$ 135nm: 0.28; other: 0.41	Kameta et al. (2002)	
R59		→	C_2H_5 + C_2H_4 + H	$\lambda <$ 135nm: 0.09; other: 0.11		

Table 2.2 continues

	Reaction			Branching Ratio	Reference	
					Cross Sections	Yields
R60	$C_6H_2 + h\nu$	→	$C_2H + C_4H$	$\lambda < 165$nm: 0.03; other: 0.01	Kloster-Jensen et al. (1974)	$\sim C_4H_2 + h\nu \rightarrow 2\ C_2H$
R61		→	$C_6H + H$	$\lambda < 165$nm: 0.20; other: 0.00	Shindo et al. (2003)	$\sim \rightarrow C_4H + H$
R62	$C_6H_4 + h\nu$	→	$C_6H_3 + H$	$\lambda < 220$nm: 1.0; other: 0.0		
R63		→	$C_6H_2 + H_2$	$\lambda < 220$nm: 0.0; other: 0.9	Est. based on C_6H_6, Münzel & Schweig (1988)	
R64		→	$C_4H_2 + C_2H_2$	$\lambda < 220$nm: 0.0; other: 0.1		
R65	$C_6H_6 + h\nu$	→	$C_6H_5 + H$	$\lambda < 220$nm: 0.80; other: 0.00	Suto et al. (1992)	
R66		→	$C_6H_4 + H_2$	$\lambda < 220$nm: 0.16; other: 0.96	Rennie et al. (1998)	Yokoyama et al. (1990)
R67		→	$C_5H_3 + CH_3$	$\lambda < 220$nm: 0.04; other: 0.04		
	Nitriles					
R68	$N + h\nu$	→	$N^+ + e^-$	1	Banks & Kockarts (1973)	
R69	$N_2 + h\nu$	→	$N(^4S) + N^+ + e^-$	$\lambda < 510$ Å: 0.10; other: 0.00		
R70		→	$N(^2D) + N^+ + e^-$	$\lambda < 510$ Å: 0.90; other: 0.00	Chan et al. (1993)	Banks & Kockarts (1973)
R71		→	$N_2^+ + e^-$	510 Å$< \lambda <$ 796 Å: 1.0; other:0.0	Fennelly & Torr (1992)	Nicolas et al. (2003)
R72		→	$N(^2D) + N(^4S)$	796 Å$< \lambda <$ 1000 Å: 1.0; other:0.0		
R73	$NH_3 + h\nu$	→	$NH_2 + H$	1	Burton et al. (1993); Chen et al. (1999)	
R74	$HCN + h\nu$	→	$H + CN$	1	Lee (1980); Nuth & Glicker (1982)	
R75	$CH_2NH + h\nu$	→	$HCN + 2\ H$	1	Teslja et al. (2004)	Nguyen et al. (1996)
R76	$CH_3NH_2 + h\nu$	→	$CH_2NH + 2\ H$	$\lambda < 165$nm: 1.0; other: 0.55		
R77		→	$HCN + H_2 + 2\ H$	$\lambda < 165$nm: 0.0; other: 0.198	Hubin-Franskin et al. (2002)	Gardner & McNesby (1982)
R78		→	$CN + 2\ H_2$	$\lambda < 165$nm: 0.0; other: 0.252		
R79	$C_2H_5N + h\nu$	→	$C_2H_4 + NH$	0.38		
R80		→	$CH_3 + H_2CN$	0.47	Est. as $C_2H_5NH_2$ Hubin-Franskin et al. (2002)	Scala & Solomoon (1976)
R81		→	$C_2H_2 + NH_3$	0.03		
R82	$HC_3N + h\nu$	→	$C_2H + CN$	0.3	Connors et al. (1974)	
R83		→	$C_3N + H$	0.09	Bénilan et al. (1996)	Clarke & Ferris (1995)
R84	$CH_3CN + h\nu$	→	$CH_3 + CN$	1	Nuth & Glicker (1982); Suto et al. (1985)	
R85	$C_2H_3CN + h\nu$	→	$C_2H_2 + HCN$	0.15		
R86		→	$HC_3N + H_2$	0.59	Eden et al. (2003)	Derecski-Kovacs & North (1999)
R87		→	$C_2H_3 + CN$	0.01		
R88		→	$C_2H_2CN + H$	0.25		
R89	$N_2H_4 + h\nu$	→	$N_2H_3 + H$	1	Vaghjiani (1993, 1995)	
R90	$C_2N_2 + h\nu$	→	$2\ CN$	1	Nuth & Glicker (1982); Connors et al. (1974) Bénilan et al. (1996) @ 193K	
R91	$C_4N_2 + h\nu$	→	$C_3N + CN$	1	Connors et al. (1974); Bénilan et al. (1996) @ 233K	

* LISA cross sections are taken from http://www.lisa.univ-paris12.fr/GPCOS/SCOOPweb/SCOOP.html

† Assuming the total quantum yield below 155nm to be one and the ionized products eventually yield $C_3H_4 + H_2$

$$2\ CH_3 + M \rightarrow C_2H_6 + M.$$

The chemical destruction of methane molecules by the methylene radicals enhances the production of methyl radicals and hence the total ethane production:

$$^1CH_2 + CH_4 \rightarrow 2\ CH_3.$$

Because ethane's absorption cross section falls in the same wavelength region as that of methane, its photolysis is constrained by the high amounts of the latter. Hence its destruction is mainly due to chemical reactions with radicals, from which the most important are with excited methylene:

$$^1CH_2 + C_2H_6 \rightarrow CH_3 + C_2H_5$$

and ethynyl (C_2H) that is produced in the photolysis of acetylene (C_2H_2):

$$C_2H_2 + h\nu \rightarrow C_2H + H$$
$$C_2H + C_2H_6 \rightarrow C_2H_2 + C_2H_5.$$

Acetylene and ethylene (C_2H_4) are the next most abundant hydrocarbons after ethane and their formation is initiated in the upper atmosphere directly from the products of methane's photolysis:

$$\begin{gathered} 2\ {}^{1,3}CH_2 \rightarrow C_2H_2 + 2\ H \\ {}^{1,3}CH_2 + CH_3 \rightarrow C_2H_4 + H \\ CH + CH_4 \rightarrow C_2H_4 + H. \end{gathered}$$

Destruction of ethylene through photolysis, acts as the major source of acetylene in the upper atmosphere:

$$C_2H_4 + h\nu \rightarrow C_2H_2 + 2H/H_2$$

while in the lower atmosphere acetylene recycles back to ethylene through the vinyl radical (C_2H_3) according to the following scheme:

$$\begin{gathered} C_2H_2 + H + M \rightarrow C_2H_3 + M \\ \underline{C_2H_3 + H + M \rightarrow C_2H_4 + M} \\ C_2H_2 + 2\ H \rightarrow C_2H_4. \end{gathered}$$

The main loss of acetylene in the upper atmosphere is from reaction with methylene which leads to the formation of propargyl radicals (C_3H_3):

$${}^1CH_2 + C_2H_2 \rightarrow C_3H_3 + H$$

while in the lower atmosphere the main loss is due to photolysis. Acetylene's cross section extends well beyond methane's dissociation limit, up to ∼230 nm and due to its high concentration, it is the main absorber in this part of the spectrum (along with the haze). This means that its photolysis rate retains high values even down to the stratosphere (Figure 2.9). Hence there is a significant production of the radicals formed (C_2 and C_2H) in acetylene's photolysis in this region, which, as in the case of ethane discussed above, lead to the catalytic destruction of saturated hydrocarbons through hydrogen abstraction. The effect of this mechanism has its highest impact on methane due to its high concentration in Titan's atmosphere:

$$\begin{gathered} C_2H_2 + h\nu \rightarrow C_2 + H_2 \\ C_2 + CH_4 \rightarrow C_2H + CH_3 \\ \underline{C_2H + CH_4 \rightarrow C_2H_2 + CH_3} \\ CH_4 \rightarrow CH_3 + H \end{gathered} \quad , \quad \begin{gathered} \\ C_2H_2 + h\nu \rightarrow C_2H + H \\ \underline{C_2H + CH_4 \rightarrow C_2H_2 + CH_3} \\ CH_4 \rightarrow CH_3 + H. \end{gathered}$$

As was shown by previous photochemical models, the overall destruction of methane is dominated by its catalytic destruction by radicals with the above two schemes along with the loss due to excited methylene radicals, having the strongest contribution. The photolysis of methane corresponds only to ∼12% of the total loss, based on our calculations, but is of course the driving force for the initialization of the photochemistry (Fig. 2.10). The three molecules described above (C_2H_6, C_2H_4, C_2H_2) along with molecular hydrogen correspond to the most abundant hydrocarbons observed in Titan's atmosphere since the Voyager

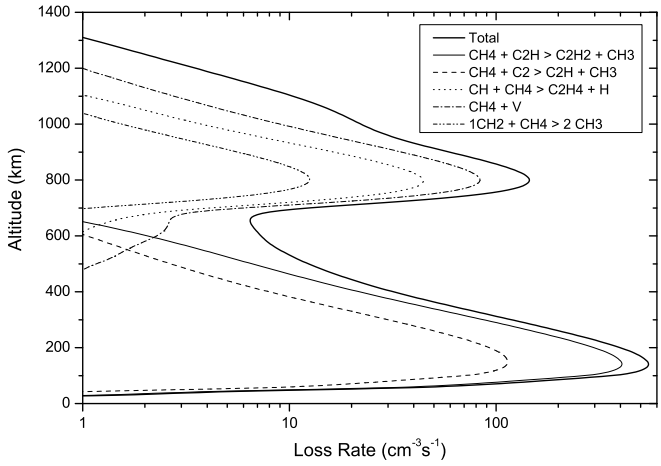

Figure 2.10: Vertical profile of the loss rate for the methane molecules due to different chemical and photolysis processes

missions (see Section 1.2.3). From these, more complex species are produced leading finally to the formation of the haze precursors.

Methylacetylene (CH_3C_2H) and its isomer, allene (CH_2CCH_2), are formed initially in the upper atmosphere through the reaction of CH with ethylene:

$$CH + C_2H_4 \rightarrow (CH_2CCH_2, CH_3C_2H) + H$$

while the isomerization between the two species is balanced through:

$$H + CH_2CCH_2 \rightarrow CH_3C_2H + H.$$

Similarly, propylene (C_3H_6) is produced in the upper atmosphere from ethane with the replacement of H by CH:

$$CH + C_2H_6 \rightarrow C_3H_6 + H$$

while in the lower atmosphere where the C_2H_3 population is significant, there is a secondary production through the collisional addition of CH_3:

$$CH_3 + C_2H_3 + M \rightarrow C_3H_6 + M.$$

In the same way, propane (C_3H_8) is formed in the collisional addition of methyl to ethyl radicals (C_2H_5):

$$CH_3 + C_2H_5 + M \rightarrow C_3H_8 + M.$$

The production of four-C hydrocarbons, starts with the first step of acetylene's polymerization through ethyl radical addition, giving diacetylene (C_4H_2):

$$C_2H + C_2H_2 \rightarrow C_4H_2 + H$$

while the 1,3-butadiene (C_4H_6) is formed by:

$$CH_3 + C_3H_3 \rightarrow C_4H_6 + H$$

1-butene (C_4H_8) is formed in the upper atmosphere through the CH replacement of H in propane:

$$CH + C_3H_8 \rightarrow C_4H_8 + H$$

and in the lower atmosphere through the collisional addition of C_2H_3 with C_2H_5:

$$C_2H_3 + C_2H_5 + M \rightarrow C_4H_8 + M.$$

The different isomers of the last species have not been included in the calculations and we consider that they are finally isomerized to their stable structures considered above. The loss of these species is dominated by their photolysis which recycles them back to their precursors, constraining in this way their net production to small values.

Due to the lack of data regarding the reaction rates and photolysis properties of five-C species, the only one included is C_5H_3, since it is a direct product of benzene (C_6H_6) photolysis. The latter has been included in the photochemical model, based on the work of Wilson et al. (2003) and Lebonnois (2005) which have investigated the possible formation pathways in Titan's atmosphere. No linear isomers of benzene have been included in the calculation since it is considered that they will finally isomerize to their cyclic forms as was suggested by Lebonnois (2005), but also because the reaction rates of benzene formation correspond to high temperatures and the extrapolation of different measurements to Titan's conditions could lead to significantly different profiles. Hence, since the production is not well defined, the inclusion of more complicated schemes would not provide any safer estimation of the final benzene profile. The main production pathway is the addition of two propargyl radicals under high pressure:

$$2\ C_3H_3 + M \rightarrow C_6H_6 + M.$$

A secondary contribution comes from

$$C_2H_2 + C_4H_5 + M \rightarrow C_6H_7 + M \rightarrow C_6H_6 + H$$

where the produced C_6H_7 is considered to provide eventually benzene (Lebonnois, 2005). Finally a small contribution originates from the hydrogen addition on the phenyl radical (C_6H_5):

$$H + C_6H_5 + M \rightarrow C_6H_6 + M$$

with the chemical formation of the last based on diacetylene (there is also a strong production of phenyl from the photolysis of benzene but this does not contribute to the net production):

$$H + C_4H_2 + M \rightarrow C_4H_3 + M$$
$$C_2H_2 + C_4H_3 + M \rightarrow C_6H_5 + M.$$

Nitriles

The basis of the nitrile chemistry is the hydrogen cyanide molecule (HCN) which is formed directly by the reaction of atomic nitrogen with the methyl radical produced in methane photolysis:

$$N + CH_3 \rightarrow HCN + H_2.$$

This pathway is not the dominant one since the H_2CN radical, also produced in the above reaction, reacts readily with atomic hydrogen to give HCN with an overall rate which is bigger that the previous one:

$$\begin{array}{c} N + CH_3 \rightarrow H_2CN + H \\ \underline{H_2CN + H \rightarrow HCN + H_2} \\ N + CH_3 \rightarrow HCN + H_2. \end{array}$$

Since the majority of nitrogen atoms is produced in the upper atmosphere, the production of HCN has a maximum in this region. The photolysis of HCN leads to the production of cyano radicals (CN):

$$HCN + h\nu \rightarrow CN + H$$

which have a double role in atmospheric chemistry. Like C_2H radicals, they enhance the catalytic destruction of molecular hydrogen and saturated hydrocarbons through the hydrogen abstraction mechanism:

$$\begin{array}{c} CN + H_2 \rightarrow HCN + H \\ CN + CH_4 \rightarrow HCN + CH_3 \\ CN + C_2H_6 \rightarrow HCN + C_2H_5 \end{array}$$

leaving a free radical and a HCN molecule, but also lead to the production of other nitrile species in reaction with unsaturated hydrocarbons through the abstraction/addition mechanism. In the last, a hydrogen atom is abstracted from the unsaturated hydrocarbon and the CN radical is added in its place. Typical examples are the formation of cyanoacetylene (HC_3N) and acrylonitrile (C_2H_3CN):

$$\begin{array}{c} CN + C_2H_2 \rightarrow HC_3N + H \\ CN + C_2H_4 \rightarrow C_2H_3CN + H. \end{array}$$

Even though the latest was not observed in Titan's atmosphere before the Cassini/Huygens mission, it was believed to be formed and taken into consideration in all previous photochemical models which included nitrile chemistry in their reactions. Only recently, the analysis of the ionospheric composition by the Ion Neutral Mass Spectrometer (INMS) on the Cassini spacecraft has verified the presence of this species in the upper atmosphere along with other nitrile species (Vuitton et al., 2006a). Another pathway for the production of acrylonitrile, included in previous models, is the one suggested by Monks et al. (1993):

$$HCN + C_2H_3 \rightarrow C_2H_3CN + H$$

who measured the rate for this reaction and found it to be efficient at room temperature. Since C_2H_3 formation has a strong pressure dependance, the contribution of the last reaction on the overall C_2H_3CN production will become significant in the lower atmosphere where the pressure is high. The main loss for acrylonitrile is due to photolysis which is also an important source of cyanoacetylene, since this pathway has a significant branching ratio (59% based on Derecskei-Kovacs & North 1999):

$$C_2H_3CN + h\nu \rightarrow HC_3N + H_2.$$

The production of HC_3N is balanced by its destruction by photolysis but also by its chemical recycling through the cyanovinyl radical (H_2C_3N):

$$\begin{array}{c} HC_3N + H + M \rightarrow H_2C_3N + M \\ H + H_2C_3N \rightarrow C_2H_2 + HCN \\ \hline HC_3N + 2\ H \rightarrow C_2H_2 + HCN. \end{array}$$

Excited nitrogen atoms produced in the upper atmosphere from the photoionization of N_2, lead to the production of other nitriles and amines. Reaction with methane has two possible products, imidogen (NH) and methyleneimine (CH_2NH) (Herron, 1999):

$$\begin{array}{rl} N(^2D) + CH_4 \rightarrow & NH + CH_3\ (20\%) \\ \rightarrow & CH_2NH + H\ (80\%). \end{array}$$

Self reaction of two NH radicals leads to the production of an amino radical (NH_2) which is also formed in the collisional addition of N with H_2:

$$\begin{array}{c} 2\ NH \rightarrow NH_2 + N \\ N + H_2 + M \rightarrow NH_2 + M. \end{array}$$

NH_2 in reaction with H yields ammonia (NH_3) :

$$NH_2 + H + M \rightarrow NH_3 + M.$$

Although the production of ammonia is believed to be related to the ion chemistry (Wilson & Atreya, 2004), recent results (Ge et al., 2006) have shown that in the low temperature conditions found in Titan's atmosphere, this might not be the case. Ammonia has been included in the model, in order to investigate the extent of neutral chemistry contribution in its total production. Another possible pathway for the production of ammonia is from the photolysis of ethyleneimine (C_2H_5N), a possible product of the reaction of $N(^2D)$ with ethane

$$N(^2D) + C_2H_6 \rightarrow C_2H_5N + H.$$

The total rate of this reaction has been measured (Herron, 1999) but the possible products are not well defined. Nevertheless, it has been included in the model in order to investigate the maximum contribution it could have to the final ammonia abundance.

Recently, Redondo et al. (2006) investigated theoretically the possible products of the NH + CH_3 reaction and found that the production of CH_2NH is energetically favored over other products.

$$NH + CH_3 \rightarrow CH_2NH + H.$$

The reaction of methyl radical with the amino radical leads to the formation of methylamine (CH_3NH_2):

$$NH_2 + CH_3 + M \rightarrow CH_3NH_2 + M$$

which when photolyzed, also produces CH_2NH (Gardner & McNesby, 1982):

$$CH_3NH_2 + h\nu \rightarrow CH_2NH + 2\ H.$$

The photolysis of CH_2NH eventually produces HCN, but due to the lack of measurements for its absorption cross section and also the absence of chemical reaction rates, it was not included in photochemical models. Both ammonia and methyleneimine have also been detected by INMS (Vuitton et al., 2006a), hence we have decided to investigate their vertical profiles in Titan's atmosphere based on the available laboratory measurements and theoretical suggestions about their reactivity.

Finally, reaction of excited nitrogen atoms with ethylene and acetylene leads to the production of acetonitrile (CH_3CN) and the CHCN radical, respectively:

$$N(^2D) + C_2H_4 \rightarrow CH_3CN + H$$
$$N(^2D) + C_2H_2 \rightarrow CHCN + H$$

while the production of the latter is dominated in the same region by the CH replacement of H in HCN:

$$CH + HCN \rightarrow CHCN + H.$$

Yung (1987) suggested that the CHCN radical could be the basis for the production of cyanogen (C_2N_2) and dicyanoacetylene (C_4N_2):

$$N + CHCN \rightarrow C_2N_2 + H$$
$$CHCN + CHCN \rightarrow C_4N_2 + H_2$$

which have been detected in the gas and solid phase phase, respectively, on Titan's North pole from the Voyager observations (Coustenis et al., 1991; Samuelson et al., 1997). The latter is included in photochemical models as it is believed to be a possible precursor of haze formation. Finally, another possible path for dicyanoacetylene is the one suggested by Petrie & Osamura (2004) based on quantum chemical calculations:

$$HCN + C_3N \rightarrow C_4N_2 + H$$

while Halpern et al. (1989) measured the rate for reaction:

$$CN + HC_3N \rightarrow \text{products}$$

which is believed to yield C_4N_2 + H. Both these two last process have a minor contribution to the overall dicyanoacetylene production based on our calculations.

Table 2.3: Chemical Reactions

	Reaction			Rate	Reference	T(K)
	Hydrocarbons					
R92	2 H + M	→	H_2 + M	k_0= 1.5 × $10^{-29}T^{-1.3}$	Tsang & Hampson (1986)	77 – 2000
				k_∞= 1.0 × 10^{-11}	Est. from Jacobs et al. (1965)	
R93	H + CH	→	H_2 + C	1.3 × $10^{-10}e^{-80/T}$	Harding et al. (1993)	300 – 2000
R94	H + $^1CH_2$	→	CH + H_2	1.0 × 10^{-10}	Peeters et al. (1994)	290
R95	H + $^1CH_2$	→	$^3CH_2$ + H	2.0 × 10^{-10}	〃	〃
R96	H + $^3CH_2$	→	CH + H_2	3.55 × $10^{-11}T^{0.32}$	Fulle & Hippler (1997)	185 – 800
R97	H + $^3CH_2$ + M	→	CH_3 + M	k_0= 1.7 × $10^{-25}T^{-1.8}$	Est. as 0.1 × k(H + CH_3), Laufer et al. (1983)	
				k_∞= 3.54 × $10^{-10}T^{0.32}$	Fulle & Hippler (1997)	185 – 800
R98	H + CH_3	→	H_2 + $^3CH_2$	1.0 × $10^{-10}e^{-7599/T}$	Baulch et al. (1992)	300 – 2500
R99	H + CH_3 + M	→	CH_4 + M	k_0= 1.7 × $10^{-24}T^{-1.8}$	Baulch et al. (1994)	300 – 1000
				k_∞= 3.5 × 10^{-10}	〃	〃
R100	H + CH_4	→	H_2 + CH_3	2.18 × $10^{-20}T^3e^{-4045/T}$	〃	〃
R101	H + C_2H + M	→	C_2H_2 + M	k_0 = 1.26 × $10^{-18}T^{-3.1}e^{-721/T}$	Tsang & Hampson (1986)	300 – 2500
				k_∞= 3.0 × 10^{-10}	〃	〃
R102	H + C_2H_2 + M	→	C_2H_3 + M	k_0 = 3.3 × $10^{-30}e^{-740/T}$	Baulch et al. (1992)	200 – 400
				k_∞= 1.4 × $10^{-11}e^{-1300/T}$	〃	〃
R103	H + C_2H_3	→	H_2 + C_2H_2	6.86 × $10^{-11}e^{23./T}$	Monks et al. (1995)	213 – 298
R104	H + C_2H_3 + M	→	C_2H_4 + M	k_0 = 5.76 × $10^{-24}T^{-1.3}$	〃	〃
				k_∞= 6.45 × $10^{-11}T^{0.2}$	Harding et al. (2005)	200 – 2000
R105	H + C_2H_4	→	H_2 + C_2H_3	8.42 × $10^{-17}T^{-1.93}e^{-6518/T}$	Knyazev et al. (1996)	200 – 3000
R106	H + C_2H_4 + M	→	C_2H_5 + M	k_0 = 7.7 × $10^{-30}e^{-380/T}$	Baulch et al. (1994)	300 – 800
				k_∞= 6.6 × $10^{-15}T^{1.28}e^{-650/T}$	〃	200 – 1100
R107	H + C_2H_5	→	2 CH_3	1.25 × 10^{-10}	Sillesen et al. (1993)	298
R108	H + C_2H_5	→	H_2 + C_2H_4	3.0 × 10^{-12}	Tsang & Hampson (1986)	300 – 2500
R109	H + C_2H_5+ M	→	C_2H_6 + M	k_0 = 5.5 × $10^{-23}T^{-2}e^{-1040/T}$	Teng & Jones (1972)	
				k_∞= 1.66 × 10^{-10}	Sillesen et al. (1993)	298
R110	H + C_2H_6	→	H_2 + C_2H_5	2.4 × $10^{-15}T^{1.5}e^{-3730/T}$	Baulch et al. (1992)	300 – 2000
R111	H + C_3H_2 + M	→	C_3H_3 + M	k_0 = 1.7 × $10^{-23}T^{-1.8}$	Est. as 10×k_0(H + CH_3),Laufer et al. (1983)	
				k_∞ = 1.0 × 10^{-10}	Peeters et al. (1994)	290
R112	H + C_3H_3 + *M*	→	CH_3C_2H + M	k_0 = 1.7 × $10^{-23}T^{-1.8}$	Est. as 10×k_0(H + CH_3),Laufer et al. (1983)	
				k_∞ = 1.25 × 10^{-10}	Atkinson & Hudgens (1999)	295
R113	H + C_3H_3 + *M*	→	CH_2CCH_2 + M	k_0 = 1.7 × $10^{-23}T^{-1.8}$	Est. as 10×k_0(H + CH_3),Laufer et al. (1983)	
				k_∞ = 1.25 × 10^{-10}	Atkinson & Hudgens (1999)	295
R114	H + CH_2CCH_2	→	CH_3C_2H + H	1.29 × $10^{-11}e^{-1156./T}$	Aleksandrov et al. (1980)	295 – 853
R115	H + CH_2CCH_2	→	H_2 + C_3H_3	4.7 × $10^{-16}T^{1.74}e^{-3873/T}$	Wang et al. (2000)	200 – 500
R116	H + CH_2CCH_2 + M	→	C_3H_5 + M	k_0 = 3.21 × $10^{-20}T^{-2.83}e^{-1985/T}$	Whytock et al. (1976)†	215 – 363
				k_∞= 9.4 × $10^{-11}e^{-1234/T}$	Wang et al. (2000)	200 – 500
R117	H + CH_3C_2H	→	H_2 + C_3H_3	4.7 × $10^{-16}T^{1.74}e^{-3873/T}$	Wang et al. (2000)	200 – 500
R118	H + CH_3C_2H + M	→	C_3H_5 + M	k_0 = 3.21 × $10^{-20}T^{-2.83}e^{-1985/T}$	Whytock et al. (1976)	215 – 363
				k_∞= 9.4 × $10^{-11}e^{-1234/T}$	Wang et al. (2000)	200 – 500
R119	H + C_3H_5	→	CH_2CCH_2 + H_2	1.3 × 10^{-11}	Hanning-Lee & Pilling (1992)	291
R120	H + C_3H_5	→	CH_3C_2H + H_2	1.3 × 10^{-11}	〃	〃
R121	H + C_3H_5+ M	→	C_3H_6 + M	k_0 = 1.0 × 10^{-24}	〃	〃
				k_∞ = 2.54 × 10^{-10}	〃	〃
R122	H + C_3H_6	→	C_3H_5 + H_2	2.87 × $10^{-19}T^{2.5}e^{-1254/T}$	Tsang (1991)	300 – 2500
R123	H + C_3H_6 + M	→	C_3H_7 + M	k_0= 7.7 × $10^{-29}e^{-380/T}$	Est. as 10×k(H + C_2H_4 + M),Laufer et al. (1983)	
				k_∞= 2.2 × $10^{-11}e^{-1640./T}$	Tsang (1991)	300 – 2500
R124	H + C_3H_7	→	C_3H_6 + H_2	3.0 × 10^{-12}	Tsang (1988)	300 – 2500
R125	H + C_3H_7 + M	→	C_3H_8 + M	k_0= 5.5 × $10^{-23}T^{-2}e^{-1040/T}$	Est. as k_0(H + C_2H_5 + M)	
				k_∞= 2.49 × 10^{-10}	Munk et al. (1986b)	298
R126	H + C_3H_8	→	C_3H_7 + H_2	2.2 × $10^{-18}T^{2.54}e^{-3400/T}$	〃	〃
R127	H + C_4H + M	→	C_4H_2 + M	k_0 = 1.26 × $10^{-18}T^{-3.1}e^{-721/T}$	Est. as k_0(H + C_2H + M)	
				k_∞ = 3.0 × 10^{-10}	〃	
R128	H + C_4H_2+ M	→	C_4H_3 + M	k_0 = 1.0 × 10^{-28}	Schwanebeck & Warnatz (1975)	298
				k_∞ = 1.39 × $10^{-10}e^{-1184/T}$	Nava et al. (1986)	210 – 423
R129	H + C_4H_3	→	C_4H_2 +H_2	3.0 × 10^{-11}	Wang & Frenklach (1997)	300 – 2500
R130	H + C_4H_3	→	2 C_2H_2	1.0 × 10^{-11}	〃	〃
R131	H + C_4H_3 + M	→	C_4H_4 + M	k_0 = 5.76 × $10^{-24}T^{-1.3}$	Est. as k_0(H + C_2H_3 + M)	
				k_∞ = 8.55 × $10^{-10}e^{-403/T}$	Duràn et al. (1988)	700 – 1300
R132	H + C_4H_4+ M	→	C_4H_5+ M	k_0 = 1.0 × 10^{-28}	Est. as k_0(H + C_4H_2 + M)	
				k_∞ = 3.3 × 10^{-12}	Schwanebeck & Warnatz (1975)	298
R133	H + C_4H_5	→	C_4H_4 + H_2	6.86 × $10^{-11}e^{23/T}$	Est. as k(H + C_2H_3)	
R134	H + C_4H_5+ M	→	C_4H_6+ M	k_0 = 5.5 × $10^{-23}T^{-2}e^{-1040/T}$	Est. as k_0(H + C_2H_5 + M)	
				k_∞ = 1.0 × 10^{-10}	Gladstone et al. (1996)	Est

† The rate expression was derived by fitting the 5 torr measurements of Whytock et al. (1976)

Table 2.3 continued

	Reaction			Rate	Reference	T(K)
R135	$H + C_4H_6$	→	$C_4H_5 + H_2$	$1.05 \times 10^{-13} T^{0.7} e^{-3019/T}$	Weissman & Benson (1988)	300 – 1500
R136	$H + C_5H_3$	→	$C_2H_2 + C_3H_2$	1.0×10^{-11}	Est. as k(H + C_4H_3)	
R137	$H + C_6H + M$	→	$C_6H_2 + M$	$k_0 = 1.26 \times 10^{-18} T^{-3.1} e^{-721/T}$	Est. as k(H + C_2H +M)	
				$k_\infty = 3.0 \times 10^{-10}$	"	
R138	$H + C_6H_2 + M$	→	$C_6H_3 + M$	$k_0 = 1.0 \times 10^{-28}$	Est. as k(H + C_4H_2 +M)	
				$k_\infty = 1.39 \times 10^{-10} e^{-1184}$	"	
R139	$H + C_6H_3$	→	$C_6H_2 + H_2$	3.0×10^{-11}	Wang & Frenklach (1997)	300 – 2500
R140	$H + C_6H_3$	→	$C_4H_2 + C_2H_2$	1.0×10^{-11}	"	"
R141	$H + C_6H_3 + M$	→	$C_6H_4 + M$	$k_0 = 5.76 \times 10^{-24} T^{-1.3}$	Est. as k_0(H + C_4H_3 + M)	
				$k_\infty = 8.55 \times 10^{-10} e^{-403/T}$	"	
R142	$H + C_6H_4$	→	$C_6H_3 + H_2$	$1.1 \times 10^{-17} T^{2.53} e^{-4648/T}$	Wang & Frenklach (1997)	300 – 2500
R143	$H + C_6H_4 + M$	→	$C_6H_5 + M$	$k_0 = 1.96 \times 10^{33} T^{-18.35} e^{-6694/T}$	Wang & Frenklach (1994)	400 – 2500
				$k_\infty = 1.06 \times 10^{-14} T^{1.11} e^{-705/T}$	"	300 – 2500
R144	$H + C_6H_5$	→	$C_4H_4 + C_2H_2$	$3.16 \times 10^{-5} T^{-1.6} e^{-1117/T}$	Wang & Frenklach (1997)	300 – 2500
R145	$H + C_6H_5 + M$	→	$C_6H_6 + M$	$k_0 = 1.82 \times 10^{28} T^{-16.3} e^{-3521/T}$	"	"
				$k_\infty = 3.65 \times 10^{-10}$	Ackermann et al. (1990)	300
R146	$H + C_6H_6$	→	$C_6H_5 + H_2$	$4.15 \times 10^{-10} e^{-8057/T}$	Wang & Frenklach (1997)	300 – 2500
R147	$H_2 + C + M$	→	$^3CH_2 + M$	$k_0 = 6.89 \times 10^{-32}$	Husain & Young (1975)	300
				$k_\infty = 2.06 \times 10^{-11} e^{-57/T}$	Harding et al. (1993)	300 – 2000
R148	$H_2 + CH + M$	→	$CH_3 + M$	$k_0 = 4.7 \times 10^{-26} T^{-1.6}$	Brownsword et al. (1997a)	53 – 744
				$k_\infty = 2.52 \times 10^{-10} T^{-0.08}$	"	"
R149	$H_2 + CH$	→	$^3CH_2 + H$	$3.10 \times 10^{-10} e^{-1650/T}$	"	"
R150	$H_2 + {}^1CH_2$	→	$^3CH_2 + H_2$	1.26×10^{-11}	Langford et al. (1983)	298
R151	$H_2 + {}^1CH_2$	→	$CH_3 + H$	9.24×10^{-11}	"	"
R152	$H_2 + {}^3CH_2$	→	$CH_3 + H$	5.0×10^{-15}	Tsang & Hampson (1986)	300 – 2500
R153	$H_2 + CH_3$	→	$CH_4 + H$	$1.14 \times 10^{-20} T^{2.74} e^{-4740/T}$	Baulch et al. (1992)	300 – 2500
R154	$H_2 + C_2$	→	$C_2H + H$	$1.77 \times 10^{-10} e^{-1470/T}$	Pitts et al. (1982)	300 – 500
R155	$H_2 + C_2H$	→	$C_2H_2 + H$	$1.20 \times 10^{-11} e^{-998/T}$	Opansky & Leone (1996b)	150 – 359
R156	$H_2 + C_2H_3$	→	$C_2H_4 + H$	$1.57 \times 10^{-20} T^{2.56} e^{-2529/T}$	Knyazev et al. (1996)	200 – 3000
R157	$H_2 + C_2H_5$	→	$C_2H_6 + H$	$5.11 \times 10^{-24} T^{3.6} e^{-4253/T}$	Tsang & Hampson (1986)	300 – 2500
R158	$H_2 + C_3H_5$	→	$C_3H_6 + H$	$1.80 \times 10^{-19} T^{2.38} e^{-9557/T}$	Tsang (1991)	300 – 2500
R159	$H_2 + C_3H_7$	→	$C_3H_8 + H$	$3.0 \times 10^{-21} T^{2.84} e^{-4600/T}$	Tsang (1988)	300 – 2500
R160	$H_2 + C_4H$	→	$C_4H_2 + H$	$1.20 \times 10^{-11} e^{-998/T}$	Est. as k(H_2 + C_2H)	
R161	$H_2 + C_4H_5$	→	$C_4H_6 + H$	$6.61 \times 10^{-15} T^{0.5} e^{-1862/T}$	Weissman & Benson (1988)	300 – 1500
R162	$H_2 + C_6H$	→	$C_6H_2 + H$	$1.20 \times 10^{-11} e^{-998/T}$	Est. as k(H_2 + C_2H)	
R163	$H_2 + C_6H_5$	→	$C_6H_6 + H$	$9.48 \times 10^{-20} T^{2.43} e^{-3159/T}$	Mebel et al. (1997)	300 – 5000
R164	2 C + M	→	$C_2 + M$	$k_0 = 4.97 \times 10^{-27} T^{-1.6}$	Slack (1976)	5000 – 6000
				$k_\infty = 2.16 \times 10^{-11}$	Martinotti et al. (1968)	298
R165	$C + CH_4$	→	C_2H_4	2.0×10^{-15}	Husain & Kirsch (1971)	300
R166	$C + C_2H_2$	→	C_3H_2	$k_0 = 1.0 \times 10^{-30}$	Moses et al. (2005)	Est.
				$k_\infty = 5.75 \times 10^{-10} T^{-0.12}$	Chastaing et al. (2001)	15 – 295
R167	$C + C_2H_4$	→	$C_3H_3 + H$	$5.61 \times 10^{-10} T^{-0.11}$	"	"
R168	$C + CH_3C_2H$	→	$C_4H_3 + H$	$5.05 \times 10^{-10} T^{-0.11}$	"	"
R169	$C + CH_2CCH_2$	→	$C_4H_3 + H$	$3.71 \times 10^{-10} T^{-0.01}$	"	"
R170	$C + C_3H_6$	→	$C_4H_5 + H$	$4.57 \times 10^{-10} T^{-0.08}$	Chastaing et al. (1998)	"
R171	$C + C_4H_6$	→	Products	1.1×10^{-9}	Husain & Ioannou (1997)	300
R172	$C + C_4H_8$	→	Products	4.3×10^{-10}	Haider & Husain (1973)	300
R173	2 CH	→	C_2H_2	1.99×10^{-10}	Braun et al. (1967)	298
R174	$CH + CH_4$	→	$C_2H_4 + H$	$3.96 \times 10^{-8} T^{-1.04} e^{-36.1/T}$	Canosa et al. (1997)	23 – 295
R175	$CH + C_2H_2$	→	$C_3H_2 + H$	$1.59 \times 10^{-9} T^{-0.23} e^{-16/T}$	"	"
R176	$CH + C_2H_4$	→	$CH_3C_2H + H$	$3.87 \times 10^{-9} T^{-0.55} e^{-29.6/T}$	"	"
R177	$CH + C_2H_4$	→	$CH_2CCH_2 + H$	$3.87 \times 10^{-9} T^{-0.55} e^{-29.6/T}$	"	"
R178	$CH + C_2H_6$	→	$C_3H_6 + H$	$1.9 \times 10^{-8} T^{-0.86} e^{-53.2/T}$	"	"
R179	$CH + C_2H_6$	→	$C_2H_4 + CH_3$	$1.9 \times 10^{-8} T^{-0.86} e^{-53.2/T}$	"	"
R180	$CH + CH_3C_2H$	→	$C_4H_4 + H$	4.6×10^{-10}	Butler et al. (1981)	298
R181	$CH + C_3H_6$	→	$C_4H_6 + H$	$5.3 \times 10^{-11} e^{528/T}$	Est. from Zabarnick et al. (1988)	295 – 668
R182	$CH + C_3H_8$	→	$C_3H_6 + CH_3$	$1.9 \times 10^{-10} e^{242/T}$	Baulch et al. (1992)	300 – 700
R183	$CH + C_4H_4$	→	Products + H	$1.59 \times 10^{-9} T^{-0.23} e^{-16/T}$	Est. as k(CH + C_2H_2)	
R184	$CH + C_4H_8$	→	Products	$8.78 \times 10^{-9} T^{-0.53} e^{-33.5/T}$	Canosa et al. (1997)	23 – 295
R185	$CH + C_4H_{10}$	→	$C_4H_8 + CH_3$	$4.4 \times 10^{-10} e^{28/T}$	Baulch et al. (1992)	250 – 700

Table 2.3 continued

	Reaction			Rate	Reference	T(K)
R186	$2\ {}^1CH_2$	→	$C_2H_2 + 2\ H$	5.0×10^{-11}	Tsang & Hampson (1986)	300 – 2500
R187	${}^1CH_2 + {}^3CH_2$	→	$C_2H_2 + 2\ H$	3.0×10^{-11}	〃	〃
R188	${}^1CH_2 + CH_3$	→	$C_2H_4 + H$	3.0×10^{-11}	〃	〃
R189	${}^1CH_2 + CH_4$	→	$2\ CH_3$	5.9×10^{-11}	Böhland et al. (1985a)	
R190	${}^1CH_2 + CH_4$	→	${}^3CH_2 + CH_4$	1.2×10^{-11}	〃	〃
R191	${}^1CH_2 + C_2H$	→	$C_2H_2 + CH$	3.0×10^{-11}	Tsang & Hampson (1986)	300 – 2500
R192	${}^1CH_2 + C_2H_2$	→	${}^3CH_2 + C_2H_2$	9.2×10^{-11}	Blitz et al. (2000)	205
R193	${}^1CH_2 + C_2H_2$	→	$C_3H_3 + H$	3.27×10^{-10}	〃	〃
R194	${}^1CH_2 + C_2H_3$	→	$C_2H_2 + CH_3$	3.0×10^{-11}	Tsang & Hampson (1986)	
R195	${}^1CH_2 + C_2H_4$	→	${}^3CH_2 + C_2H_4$	2.3×10^{-11}	Baulch et al. (1992)	300 – 3000
R196	${}^1CH_2 + C_2H_4 + M$	→	$C_3H_6 + M$	$k_0 = 1.5 \times 10^{-18} T^{-3} e^{-300/T}$	Moses et al. (2005)	Est.
				$k_\infty = 1.5 \times 10^{-10}$	Baulch et al. (1992)	300 – 3000
R197	${}^1CH_2 + C_2H_5$	→	$C_2H_4 + CH_3$	1.5×10^{-11}	Tsang & Hampson (1986)	300 – 2500
R198	${}^1CH_2 + C_2H_5$	→	$C_3H_6 + H$	1.5×10^{-11}	〃	〃
R199	${}^1CH_2 + C_2H_6$	→	${}^3CH_2 + C_2H_6$	3.6×10^{-11}	Baulch et al. (1992)	300 – 3000
R200	${}^1CH_2 + C_2H_6$	→	$C_2H_5 + CH_3$	5.9×10^{-11}	Est. as $k({}^1CH_2 + CH_4)$	
R201	${}^1CH_2 + C_3H_3$	→	$C_4H_4 + H$	3.3×10^{-10}	Est. as $k({}^1CH_2 + C_3H_5)$	
R202	${}^1CH_2 + CH_3C_2H$	→	$C_4H_5 + H$	5.0×10^{-11}	Est. based on other ${}^1CH_2$ reactions	
R203	${}^1CH_2 + CH_2CCH_2$	→	$C_4H_5 + H$	5.0×10^{-11}	〃	
R204	${}^1CH_2 + C_3H_5$	→	$C_4H_6 + H$	3.3×10^{-10}	Tsang (1991)	300 – 2500
R205	${}^1CH_2 + C_3H_5$	→	$C_2H_4 + C_2H_3$	6.67×10^{-11}	〃	〃
R206	${}^1CH_2 + C_3H_6$	→	${}^3CH_2 + C_3H_6$	5.0×10^{-11}	〃	〃
R207	${}^1CH_2 + C_3H_6$	→	$C_3H_5 + CH_3$	8.7×10^{-11}	〃	〃
R208	${}^1CH_2 + C_3H_6 + M$	→	$C_4H_8 + M$	$k_0 = 1.5 \times 10^{-18} T^{-3} e^{-300/T}$	Est. as $k_0({}^1CH_2 + C_2H_4)$	
				$k_\infty = 8.1 \times 10^{-11}$	Tsang (1991)	300 – 2500
R209	${}^1CH_2 + C_3H_7$	→	$C_2H_5 + C_2H_4$	4.29×10^{-11}	Tsang (1988)	300 – 2500
R210	${}^1CH_2 + C_3H_7$	→	$C_3H_6 + CH_3$	1.71×10^{-11}	〃	〃
R211	${}^1CH_2 + C_3H_8$	→	$2\ C_2H_5$	1.6×10^{-10}	〃	〃
R212	${}^1CH_2 + C_4H_4$	→	Product + H	3.27×10^{-10}	Est. as $k({}^1CH_2 + C_2H_2)$	
R213	${}^1CH_2 + C_4H_8 + M$	→	Product + M	$k_0 = 1.5 \times 10^{-18} T^{-3} e^{-300/T}$	Est. as $k_0({}^1CH_2 + C_2H_4)$	
				$k_\infty = 8.1 \times 10^{-11}$	Est. as $k_\infty({}^1CH_2 + C_2H_4)$	
R214	${}^1CH_2 + C_4H_{10}$	→	$C_2H_5 + C_3H_7$	1.6×10^{-10}	Est. as $k({}^1CH_2 + C_3H_8)$	
R215	${}^1CH_2 + N_2$	→	${}^3CH_2 + N_2$	1.0×10^{-11}	Baulch et al. (1992)	300 – 3000
R216	$2\ {}^3CH_2$	→	$C_2H_2 + 2\ H$	$1.8 \times 10^{-10} e^{-400/T}$	〃	〃
R217	$2\ {}^3CH_2$	→	$C_2H_2 + H_2$	$2.0 \times 10^{-11} e^{-400/T}$	〃	〃
R218	${}^3CH_2 + CH_3$	→	$C_2H_4 + H$	7.0×10^{-11}	〃	〃
R219	${}^3CH_2 + CH_4$	→	$2\ CH_3$	$7.13 \times 10^{-12} e^{-5052/T}$	Böhland et al. (1985b)	296 – 707
R220	${}^3CH_2 + C_2H$	→	$C_2H_2 + CH$	3.0×10^{-11}	Tsang & Hampson (1986)	300 – 2500
R221	${}^3CH_2 + C_2H_2$	→	$C_3H_3 + H$	$2.0 \times 10^{-11} e^{-3330/T}$	〃	〃
R222	${}^3CH_2 + C_2H_3$	→	$C_2H_2 + CH_3$	3.0×10^{-11}	Tsang & Hampson (1986)	300 – 2500
R223	${}^3CH_2 + C_2H_4$	→	$C_3H_5 + H$	$5.31 \times 10^{-12} e^{-2658/T}$	Kraus et al. (1993)	296 – 728
R224	${}^3CH_2 + C_2H_5$	→	$C_2H_4 + CH_3$	3.0×10^{-11}	Tsang & Hampson (1986)	300 – 2500
R225	${}^3CH_2 + C_2H_6$	→	$C_2H_5 + CH_3$	$1.07 \times 10^{-11} e^{-3981/T}$	Böhland et al. (1985b)	296 – 707
R226	${}^3CH_2 + C_3H_3$	→	$C_4H_4 + H$	5.0×10^{-11}	Est. as $k({}^3CH_2 + C_3H_5)$	
R227	${}^3CH_2 + CH_3C_2H$	→	$C_4H_5 + H$	5.0×10^{-11}	Est. based on other ${}^3CH_2$ reactions	
R228	${}^3CH_2 + CH_2CCH_2$	→	$C_4H_5 + H$	5.0×10^{-11}	〃	
R229	${}^3CH_2 + C_3H_5$	→	$C_4H_6 + H$	5.0×10^{-11}	Tsang (1991)	300 – 2500
R230	${}^3CH_2 + C_3H_6$	→	$C_3H_5 + CH_3$	$1.2 \times 10^{-12} e^{-3120/T}$	〃	〃
R231	${}^3CH_2 + C_3H_7$	→	$C_3H_6 + CH_3$	3.0×10^{-12}	Tsang (1988)	300 – 2500
R232	${}^3CH_2 + C_3H_7$	→	$C_2H_4 + C_2H_5$	3.0×10^{-11}	〃	〃
R233	${}^3CH_2 + C_3H_8$	→	$C_3H_7 + CH_3$	$1.5 \times 10^{-24} T^{3.65} e^{-3600/T}$	〃	〃
R234	${}^3CH_2 + C_4H_2$	→	$C_4H + CH_3$	$2.16 \times 10^{-11} e^{-2165/T}$	Böhland et al. (1988)	296 – 700
R235	${}^3CH_2 + C_4H_6$	→	$CH_3C_2H + C_2H_4$	$6.14 \times 10^{-12} e^{-1732/T}$	Kraus et al. (1993)	296 – 728
R236	${}^3CH_2 + C_4H_{10}$	→	Products + CH_3	8.1×10^{-12}	Halberstadt & Crump (1973)	304
R237	$2\ CH_3$	→	$C_2H_5 + H$	$8.28 \times 10^{-12} T^{0.1} e^{-5335/T}$	Stewart et al. (1989)	200 – 2500
R238	$2\ CH_3 + M$	→	$C_2H_6 + M$	$k_0 = 2.822 \times 10^{-3} T^{-8.749} e^{-985.4/T}$	See text, Part II	
				$k_\infty = 9.3132 \times 10^{-11} e^{-1.519 \times 10^{-3} \times T}$	Cody et al. (2003)	155 – 906
R239	$CH_3 + C_2H$	→	$C_3H_3 + H$	4.0×10^{-11}	Tsang & Hampson (1986)	300 – 2500
R240	$CH_3 + C_2H_2$	→	$CH_3C_2H + H$	$3.18 \times 10^{-20} T^{2.42} e^{-6488/T}$	Diau & Lin (1994)	300 – 3000
R241	$CH_3 + C_2H_2 + M$	→	$C_3H_5 + M$	$k_0 = 3.3 \times 10^{-30} e^{-740/T}$	Est. as $k_0(H + C_2H_2 + M)$	
				$k_\infty = 1.0 \times 10^{-12} e^{-3880/T}$	Tsang & Hampson (1986)	300 – 2500
R242	$CH_3 + C_2H_3$	→	$C_2H_2 + CH_4$	3.4×10^{-11}	Fahr et al. (1991)	298
R243	$CH_3 + C_2H_3 + M$	→	$C_3H_6 + M$	$k_0 = 1.646 \times 10^{-3} T^{-8.749} e^{-985.4/T}$	Est. as $10 \times k_0(2\ CH_3 + M)$, Laufer et al. (1983)	
				$k_\infty = 1.2 \times 10^{-10}$	Fahr et al. (1991)	298
R244	$CH_3 + C_2H_4$	→	$C_2H_3 + CH_4$	$1.1 \times 10^{-23} T^{3.7} e^{-4780/T}$	Tsang & Hampson (1986)	300 – 2500
R245	$CH_3 + C_2H_4 + M$	→	$C_3H_7 + M$	$k_0 = 7.7 \times 10^{-30} e^{-380/T}$	Est. as $k_0(H + C_2H_4 + M)$	
				$k_\infty = 3.5 \times 10^{-13} e^{-3700/T}$	Baulch et al. (1992)	300 – 600

Table 2.3 continued

	Reaction			Rate	Reference	T(K)
R246	$CH_3 + C_2H_5$	→	$C_2H_4 + CH_4$	$5.04 \times 10^{-14} T^{0.41} e^{429/T}$	Zhu et al. (2004)	200 – 600
R247	$CH_3 + C_2H_5 + M$	→	$C_3H_8 + M$	$k_0 = 1.01 \times 10^{+20} T^{-16.14} e^{-1897/T}$	Laufer et al. (1983)	Est. 100 – 300
				$k_\infty = 2.41 \times 10^{-10} T^{-0.34} e^{259/T}$	Zhu et al. (2004)	200 – 600
R248	$CH_3 + C_2H_6$	→	$C_2H_5 + CH_4$	$2.5 \times 10^{-31} T^{6} e^{-3043/T}$	Baulch et al. (1992)	300 – 1500
R249	$CH_3 + C_3H_3 + M$	→	$C_4H_6 + M$	$k_0 = 2.822 \times 10^{-3} T^{-8.749} e^{-985.4/T}$	Est. as k_0(2 CH_3 + M)	
				$k_\infty = 6.8 \times 10^{-11} e^{131/T}$	Knyazev & Slagle (2001b)	300 – 800
R250	$CH_3 + CH_3C_2H$	→	$C_2H_6 + C_2H$	$8.32 \times 10^{-13} e^{-4428/T}$	Kerr & Parsonage (1972)	379 – 465
R251	$CH_3 + CH_2CCH_2$	→	$C_2H_5 + C_2H_2$	$3.32 \times 10^{-13} e^{-4076/T}$	и	и
R252	$CH_3 + C_3H_5$	→	$CH_2CCH_2 + CH_4$	$5.0 \times 10^{-12} T^{-0.32} e^{66/T}$	Tsang (1991)	300 – 2500
R253	$CH_3 + C_3H_5 + M$	→	$C_4H_8 + M$	$k_0 = 2.822 \times 10^{-3} T^{-8.749} e^{-985.4/T}$	Est. as k_0(2 CH_3 + M)	
				$k_\infty = 1.55 \times 10^{-9} T^{-0.54} e^{117/T}$	Knyazev & Slagle (2001a)	300 – 800
R254	$CH_3 + C_3H_6$	→	$C_3H_5 + CH_4$	$2.66 \times 10^{-13} e^{-4440/T}$	Kinsman & Roscoe (1994)	300 – 580
R255	$CH_3 + C_3H_6$	→	Products	$k_0 = 7.7 \times 10^{-30} e^{-380/T}$	Est. as k_0(H + C_2H_4 + M)	
				$k_\infty = 1.19 \times 10^{-13} e^{-3260/T}$	Kinsman & Roscoe (1994)	300 – 580
R256	$CH_3 + C_3H_7$	→	$C_3H_6 + CH_4$	$1.9 \times 10^{-11} T^{-0.32}$	Tsang (1988)	300 – 2500
R257	$CH_3 + C_3H_7 + M$	→	$C_4H_{10} + M$	$k_0 = 2.822 \times 10^{-3} T^{-8.749} e^{-985.4/T}$	Est. as k_0(2 CH_3 + M)	
				$k_\infty = 3.06 \times 10^{-11} e^{387/T}$	Knyazev & Slagle (2001b)	297 – 600
R258	$CH_3 + C_3H_8$	→	$C_3H_7 + CH_4$	$1.5 \times 10^{-24} T^{3.65} e^{-3600/T}$	Tsang (1988)	300 – 2500
R259	$CH_3 + C_4H_4$	→	$C_4H_3 + CH_4$	$6.61 \times 10^{-13} e^{-2502/T}$	Scherzer et al. (1985)	553 – 593
R260	$CH_3 + C_4H_6$	→	Products	$k_0 = 3.3 \times 10^{-30} e^{-740/T}$	Est. as k_0(H + C_2H_2 + M)	
				$k_\infty = 1.35 \times 10^{-13} e^{-2063/T}$	Kerr & Parsonage (1972)	353 – 453
R261	$CH_3 + C_4H_8$	→	Products	$1.69 \times 10^{-13} e^{-3620/T}$	и	и
R262	$CH_3 + C_4H_{10}$	→	Products + CH_4	$6.64 \times 10^{-13} e^{-4840/T}$	Warnatz (1984)	300 – 1000
R263	$CH_3 + C_5H_3$	→	2 C_3H_3	4.0×10^{-11}	Est. Moses et al. (2005)	
R264	$CH_3 + C_5H_3 + M$	→	$C_6H_6 + M$	$k_0 = 2.822 \times 10^{-3} T^{-8.749} e^{-985.4/T}$	Est. as k_0(2 CH_3 + M)	
				$k_\infty = 3.06 \times 10^{-11} e^{387/T}$	Est. as k_∞(CH_3 + C_3H_7 + M)	
R265	$CH_3 + C_6H_4$	→	$C_6H_3 + CH_4$	$6.61 \times 10^{-13} e^{-2502/T}$	Est. as k(CH_3 + C_4H_4)	
R266	$CH_4 + C_2$	→	$C_2H + CH_3$	$5.05 \times 10^{-11} e^{-297/T}$	Pitts et al. (1982)	300 – 600
R267	$CH_4 + C_2H$	→	$C_2H_2 + CH_3$	$1.2 \times 10^{-11} e^{-491/T}$	Opansky & Leone (1996a)	154 – 359
R268	$CH_4 + C_2H_3$	→	$C_2H_4 + CH_3$	$2.4 \times 10^{-24} T^{4.02} e^{-2754/T}$	Tsang & Hampson (1986)	300 – 2500
R269	$CH_4 + C_2H_5$	→	$C_2H_6 + CH_3$	$1.43 \times 10^{-25} T^{4.14} e^{-6322/T}$	и	и
R270	$CH_4 + C_3H_7$	→	$C_3H_8 + CH_3$	$4.0 \times 10^{-26} T^{4.02} e^{-5473/T}$	Tsang (1988)	300 – 2500
R271	$CH_4 + C_4H$	→	$C_4H_2 + CH_3$	$1.2 \times 10^{-11} e^{-491/T}$	Est. as k(CH_4 + C_2H)	
R272	$CH_4 + C_6H$	→	$C_6H_2 + CH_3$	$1.2 \times 10^{-11} e^{-491/T}$	и	
R273	$CH_4 + C_6H_5$	→	$C_6H_6 + CH_3$	$3.32 \times 10^{-11} e^{-4328/T}$	Heckmann et al. (1996)	560 – 1410
R274	$C_2 + C_2H_2$	→	2 C_2H	4.3×10^{-10}	Reisler et al. (1980)	300
R275	$C_2 + C_2H_4$	→	$C_4H_3 + H$	3.26×10^{-10}	и, Balucani et al. (2001)	и
R276	$C_2 + C_2H_6$	→	$C_2H + C_2H_5$	3.0×10^{-10}	и, Est.	и
R277	$C_2 + CH_3C_2H$	→	$C_2H + C_3H_3$	4.74×10^{-10}	и	и
R278	$C_2 + CH_2CCH_2$	→	$C_2H + C_3H_3$	4.74×10^{-10}	и	и
R279	$C_2 + C_3H_8$	→	$C_2H + C_3H_7$	3.3×10^{-10}	и	и
R280	$C_2 + C_4H_{10}$	→	C_2H + Products	3.19×10^{-10}	Huang et al. (2004)	298
R281	$C_2 + C_6H_6$	→	$C_2H + C_6H_5$	5.2×10^{-10}	Reisler et al. (1980)	300
R282	2 C_2H	→	$C_2H_2 + C_2$	3.0×10^{-12}	Tsang & Hampson (1986)	300 – 2500
R283	$C_2H + C_2H_2$	→	$C_4H_2 + H$	1.3×10^{-10}	Vakhtin et al. (2001a)	103
R284	$C_2H + C_2H_3$	→	2 C_2H_2	1.6×10^{-12}	Tsang & Hampson (1986)	300 – 2500
R285	$C_2H + C_2H_4$	→	$C_4H_4 + H$	1.4×10^{-10}	Vakhtin et al. (2001b)	103
R286	$C_2H + C_2H_5$	→	$C_2H_2 + C_2H_4$	3.0×10^{-12}	Tsang & Hampson (1986)	300 – 2500
R287	$C_2H + C_2H_5$	→	$C_3H_3 + CH_3$	3.0×10^{-11}	и	и
R288	$C_2H + C_2H_6$	→	$C_2H_2 + C_2H_5$	$5.1 \times 10^{-11} e^{-76/T}$	Murphy et al. (2003)	96 – 800
R289	$C_2H + CH_3C_2H$	→	$C_4H_2 + CH_3$	$1.6 \times 10^{-10} e^{71/T}$	Hoobler & Leone (1999)	155 – 298
R290	$C_2H + CH_2CCH_2$	→	$C_2H_2 + C_3H_3$	$1.3 \times 10^{-10} e^{103/T}$	и	и
R291	$C_2H + C_3H_5$	→	$CH_2CCH_2 + C_2H_2$	1.2×10^{-11}	Tsang (1991)	300 – 2500
R292	$C_2H + C_3H_6$	→	Products + H	2.4×10^{-10}	Vakhtin et al. (2001b)	103
R293	$C_2H + C_3H_7$	→	$C_3H_3 + C_2H_5$	2.0×10^{-11}	Tsang (1988)	300 – 2500
R294	$C_2H + C_3H_7$	→	$C_3H_6 + C_2H_2$	1.0×10^{-11}	и	и
R295	$C_2H + C_3H_8$	→	$C_3H_7 + C_2H_2$	$9.8 \times 10^{-11} e^{-71/T}$	Murphy et al. (2003)	96 – 297
R296	$C_2H + C_4H_2$	→	$C_6H_2 + H$	1.3×10^{-10}	Est. as k(C_2H + C_2H_2)	
R297	$C_2H + C_4H_6$	→	$C_6H_6 + H$	3.1×10^{-10}	Nizamov & Leone (2004)	104 – 296
R298	$C_2H + C_4H_8$	→	Products	2.6×10^{-10}	Laufer & Fahr (2004)	296
R299	$C_2H + C_4H_{10}$	→	Products + C_2H_2	$8.3 \times 10^{-11} e^{-112/T}$	Hoobler et al. (1997)	176 – 297
R300	$C_2H_2 + C_2H_3$	→	$C_4H_4 + H$	$3.32 \times 10^{-12} e^{-2516/T}$	Fahr & Stein (1989)	298 – 1330

Table 2.3 continued

	Reaction			Rate	Reference	T(K)
R301	$C_2H_2 + C_2H_3 + M$	→	$C_4H_5 + M$	$k_0 = 1.54 \times 10^{-14} T^{-5.84} e^{-2364/T}$	Wang & Frenklach (1994)	500 – 2500
				$k_\infty = 4.16 \times 10^{-19} T^{1.9} e^{-1058/T}$	Weissman & Benson (1988)	300 – 1500
R302	$C_2H_2 + C_2H_5 + M$	→	Products + M	$k_0 = 3.3 \times 10^{-30} e^{-740/T}$	Est. as $k_0(H + C_2H_2)$	
				$k_\infty = 8.32 \times 10^{-14} e^{-3520/T}$	Kerr & Parsonage (1972)	373 – 473
R303	$C_2H_2 + C_3H_5 + M$	→	Products + M	$k_0 = 3.3 \times 10^{-30} e^{-740/T}$	Est. as $k_0(H + C_2H_2)$	
				$k_\infty = 5.3 \times 10^{-14} e^{-3500/T}$	Tsang (1991)	300 – 2500
R304	$C_2H_2 + C_3H_7$	→	$C_2H_4 + C_3H_5$	$1.2 \times 10^{-12} e^{-4531/T}$	Tsang (1988)	300 – 2500
R305	$C_2H_2 + C_4H$	→	$C_6H_2 + H$	1.3×10^{-10}	Est. as $k(C_2H + C_2H_2)$	
R306	$C_2H_2 + {}^*C_4H_2$	→	$C_6H_2 + 2\,H$	3.5×10^{-13}	Seki et al. (1986) Est. as $k({}^*C_2H_2 + C_2H_2)$	
R307	$C_2H_2 + C_4H_3 + M$	→	$C_6H_5 + M$	$k_0 = 3.3 \times 10^{-30} e^{-740/T}$	Est. as $k_0(H + C_2H_2)$	
				$k_\infty = 5.53\ T^{-3.89} e^{-4635/T}$	Westmoreland et al. (1989)	400 – 1600
R308	$C_2H_2 + C_4H_5$	→	$C_6H_6 + H$	$3.16 \times 10^{-17} T^{1.47} e^{-2471/T}$	〃	〃
R309	$C_2H_2 + C_4H_5 + M$	→	$C_6H_7 + M$	$k_0 = 1.24 \times 10^{-21} T^{-3.28} e^{-5130/T}$	Wang & Frenklach (1994)	600 – 2500
			→ $C_6H_6 + H$	$k_\infty = 4.2 \times 10^{-19} T^{1.8} e^{-602/T}$	Weissman & Benson (1988)	300 – 1500
R310	$2\,C_2H_3$	→	$C_2H_2 + C_2H_4$	3.5×10^{-11}	Laufer & Fahr (2004)	298
R311	$2\,C_2H_3 + M$	→	$C_4H_6 + M$	$k_0 = 2.822 \times 10^{-3} T^{-8.749} e^{-985.4/T}$	Est. as $k_0(2\,CH_3 + M)$	
				$k_\infty = 9.5 \times 10^{-11}$	Laufer & Fahr (2004))	298
R312	$C_2H_3 + C_2H_4$	→	$C_4H_6 + H$	$8.3 \times 10^{-13} e^{-3676/T}$	Tsang & Hampson (1986)	300 – 2500
R313	$C_2H_3 + C_2H_5$	→	$C_2H_2 + C_2H_6$	8.0×10^{-13}	〃	〃
R314	$C_2H_3 + C_2H_5$	→	$2\,C_2H_4$	8.0×10^{-13}	〃	〃
R315	$C_2H_3 + C_2H_5 + M$	→	$C_4H_8 + M$	$k_0 = 2.822 \times 10^{-3} T^{-8.749} e^{-985.4/T}$	Est. as $k_0(2\,CH_3 + M)$	
				$k_\infty = 6.5 \times 10^{-11}$	Laufer & Fahr (2004)	298
R316	$C_2H_3 + C_2H_6$	→	$C_2H_4 + C_2H_5$	$9.98 \times 10^{-22} T^{3.3} e^{-5285/T}$	Tsang & Hampson (1986)	300 – 2500
R317	$C_2H_3 + C_3H_3$	→	$CH_3C_2H + C_2H_2$	8.0×10^{-12}	Est. as $k(C_2H_3 + C_3H_5)$,Vuitton et al. (2006c)	
R318	$C_2H_3 + C_3H_3$	→	Products	$k_0 = 2.822 \times 10^{-3} T^{-8.749} e^{-985.4/T}$	Est. as $k_0(2\,CH_3 + M)$	
				$k_\infty = 8.0 \times 10^{-11}$	Est. as $k(C_2H_3 + C_3H_5)$,Vuitton et al. (2006c)	
R319	$C_2H_3 + C_3H_5$	→	$CH_2CCH_2 + C_2H_4$	4.0×10^{-12}	Tsang (1991)	300 – 2500
R320	$C_2H_3 + C_3H_5$	→	$C_3H_6 + C_2H_2$	8.0×10^{-12}	〃	〃
R321	$C_2H_3 + C_3H_5$	→	Products	$k_0 = 2.822 \times 10^{-3} T^{-8.749} e^{-985.4/T}$	Est. as $k_0(2\,CH_3 + M)$	
				$k_\infty = 8.0 \times 10^{-11}$	Tsang (1991)	300 – 2500
R322	$C_2H_3 + C_3H_6$	→	$C_4H_6 + CH_3$	$1.2 \times 10^{-12} e^{-2520/T}$	〃	〃
R323	$C_2H_3 + C_3H_6$	→	$C_3H_5 + C_2H_4$	$3.68 \times 10^{-24} T^{3.5} e^{-2356/T}$	〃	〃
R324	$C_2H_3 + C_3H_6$	→	Products + H	$1.2 \times 10^{-12} e^{-3240/T}$	〃	〃
R325	$C_2H_3 + C_3H_7$	→	$C_3H_6 + C_2H_4$	2.0×10^{-12}	Tsang (1988)	300 – 2500
R326	$C_2H_3 + C_3H_7$	→	$C_3H_8 + C_2H_2$	2.0×10^{-12}	〃	〃
R327	$C_2H_3 + C_3H_7 + M$	→	Adduct + M	$k_0 = 2.822 \times 10^{-3} T^{-8.749} e^{-985.4/T}$	Est. as $k_0(2\,CH_3 + M)$	
				$k_\infty = 1.6 \times 10^{-11}$	Tsang (1988)	300 – 2500
R328	$C_2H_3 + C_3H_8$	→	$C_3H_7 + C_2H_4$	$1.0 \times 10^{-21} T^{3.3} e^{-5285/T}$	〃	〃
R329	$C_2H_3 + C_4H_3$	→	$C_2H_4 + C_4H_2$	1.75×10^{-12}	Est. as $k(2\,C_2H_3)$	
R330	$C_2H_3 + C_4H_3$	→	$C_2H_2 + C_2H_4$	1.75×10^{-12}	〃	
R331	$C_2H_3 + C_4H_3 + M$	→	$C_6H_6 + M$	$k_0 = 1.646 \times 10^{-3} T^{-8.749} e^{-985.4/T}$	〃	
				$k_\infty = 9.5 \times 10^{-11}$	〃	
R332	$C_2H_3 + C_4H_4$	→	$C_6H_6 + H$	$1.23 \times 10^{-5} T^{-0.66} e^{4235/T}$	Wang & Frenklach (1997)	400 – 1600
R333	$C_2H_3 + C_4H_5$	→	$C_6H_6 + H_2$	$3.05 \times 10^{-37} T^{7.07} e^{1817/T}$	Westmoreland et al. (1989)	400 – 1600
R334	$C_2H_3 + C_4H_6 + M$	→	Adduct + M	$k_0 = 2.822 \times 10^{-3} T^{-8.749} e^{-985.4/T}$	Est. as $k_0(2\,CH_3 + M)$	
				$k_\infty = 2.45 \times 10^{-12} T^{-0.17} e^{-1630/T}$	Westmoreland et al. (1989)	400 – 1600
R335	$C_2H_3 + C_4H_{10}$	→	C_2H_4 + Product	$2.25 \times 10^{-24} T^{3.65} e^{-2600/T}$	Est. from Tsang (1990)	300 – 2500
R336	$C_2H_4 + C_2H_5$	→	$C_2H_6 + C_2H_3$	$1.0 \times 10^{-21} T^{3.13} e^{-9063/T}$	Tsang & Hampson (1986)	300 – 2500
R337	$C_2H_4 + C_2H_5 + M$	→	Product + M	$k_0 = 7.7 \times 10^{-30} e^{-380/T}$	Est. as $k_0(H + C_2H_4 + M)$	
				$k_\infty = 6.6 \times 10^{-21} T^{2.44} e^{-2700/T}$	Knyazev & Slagle (1996)	298 – 1500
R338	$C_2H_4 + C_3H_5$	→	Products + H	$1.0 \times 10^{-14} e^{-5776/T}$	Tsang (1991)	300 – 2500
R339	$C_2H_4 + C_3H_7 + M$	→	Adduct + M	$k_0 = 7.7 \times 10^{-30} e^{-380/T}$	Est. as $k_0(H + C_2H_4 + M)$	
				$k_\infty = 3.24 \times 10^{-14} e^{-3070/T}$	Kerr & Parsonage (1972)	375 – 503
R340	$C_2H_4 + C_4H$	→	$C_4H_2 + C_2H_3$	1.4×10^{-10}	Est. as $k(C_2H + C_2H_4)$	
R341	$C_2H_4 + {}^*C_4H_2$	→	$C_6H_4 + H_2$	3.87×10^{-13}	Zwier & Allen (1996)	Relative to R306
R342	$C_2H_4 + {}^*C_4H_2$	→	$C_6H_5 + H$	1.03×10^{-13}	〃	〃
R343	$C_2H_4 + C_6H$	→	$C_6H_2 + C_2H_3$	1.4×10^{-10}	Est. as $k(C_2H + C_2H_4)$	
R344	$2\,C_2H_5$	→	$C_2H_6 + C_2H_4$	2.4×10^{-12}	Baulch et al. (1992)	300 – 1200
R345	$2\,C_2H_5 + M$	→	$C_4H_{10} + M$	$k_0 = 6.59 \times 10^{-6} T^{-6.39} e^{-301/T}$	Laufer et al. (1983)	100 – 300
				$k_\infty = 1.26 \times 10^{-11} e^{-96/T}$	Teng & Jones (1972)	303 – 603
R346	$C_2H_5 + C_3H_3$	→	$CH_3C_2H + C_2H_4$	$4.3 \times 10^{-12} e^{66/T}$	Est. as $k(C_2H_5 + C_3H_5)$,Vuitton et al. (2006c)	
R347	$C_2H_5 + C_3H_3 + M$	→	Products + M	$k_0 = 2.822 \times 10^{-3} T^{-8.749} e^{-985.4/T}$	Est. as $k(2\,CH_3 + M)$	
				$k_\infty = 9.24 \times 10^{-11}$	Est. as $k(C_2H_5 + C_3H_5)$,Vuitton et al. (2006c)	

Table 2.3 continued

	Reaction			Rate	Reference	T(K)
R348	$C_2H_5 + C_3H_5$	→	$CH_2CCH_2 + C_2H_6$	$1.6 \times 10^{-12} e^{66/T}$	Tsang (1991)	300 – 2500
R349	$C_2H_5 + C_3H_5$	→	$C_3H_6 + C_2H_4$	$4.3 \times 10^{-12} e^{66/T}$	〃	〃
R350	$C_2H_5 + C_3H_5 + M$	→	Products + M	$k_0 = 2.822 \times 10^{-3} T^{-8.749} e^{-985.4/T}$	Est. as k(2 CH_3 + M)	
				$k_\infty = 9.24 \times 10^{-11}$	Garland & Bayers (1990)	300
R351	$C_2H_5 + C_3H_6$	→	$C_2H_6 + C_3H_5$	$3.7 \times 10^{-24} T^{3.50} e^{-3340/T}$	Tsang (1991)	300 – 2500
R352	$C_2H_5 + C_3H_6 + M$	→	Products + M	$k_0 = 7.7 \times 10^{-30} e^{-380/T}$	Est. as k_0(H + C_2H_4 + M)	
				$k_\infty = 1.69 \times 10^{-13} e^{-3620/T}$	Tsang (1991)	300 – 2500
R353	$C_2H_5 + C_3H_7$	→	$C_3H_6 + C_2H_6$	2.4×10^{-12}	Tsang (1988)	300 – 2500
R354	$C_2H_5 + C_3H_7$	→	$C_3H_8 + C_2H_4$	1.9×10^{-12}	〃	〃
R355	$C_2H_5 + C_3H_7$	→	Products	$k_0 = 6.59 \times 10^{-6} T^{-6.39} e^{-301/T}$	Est. as k_0(2 C_2H_5 + M)	
				$k_\infty = 3.3 \times 10^{-11}$	Tsang (1988)	300 – 2500
R356	$C_2H_5 + C_3H_8$	→	$C_2H_6 + C_3H_7$	$1.5 \times 10^{-24} T^{3.65} e^{-4600/T}$	〃	〃
R357	$C_2H_5 + C_4H_3$	→	$C_4H_2 + C_2H_6$	8.0×10^{-13}	Est. as k(C_2H_3 + C_2H_5)	
R358	$C_2H_5 + C_4H_3$	→	$C_4H_4 + C_2H_4$	8.0×10^{-13}	〃	
R359	$C_2H_5 + C_4H_3 + M$	→	C_4H_8 + M	$k_0 = 2.822 \times 10^{-3} T^{-8.749} e^{-985.4/T}$	Est. as k_0(2 CH_3 + M)	
				$k_\infty = 6.5 \times 10^{-11}$	Est. as k_∞(C_2H_3 + C_2H_5 + M)	
R360	$C_2H_5 + C_4H_4 + M$	→	Products + M	$k_0 = 2.822 \times 10^{-3} T^{-8.749} e^{-985.4/T}$	Est. as k_0(2 CH_3 + M)	
				$k_\infty = 6.8 \times 10^{-11} e^{-131/T}$	Est. as k_∞(CH_3 + C_3H_3 + M)	
R361	$C_2H_5 + C_4H_8 + M$	→	Products + M	$k_0 = 7.7 \times 10^{-30} e^{-380/T}$	Est. as k_0(H + C_2H_4 + M)	
				$k_\infty = 1.69 \times 10^{-13} e^{-3620/T}$	Est. as k_∞(C_2H_5 + C_3H_6 + M)	
R362	$C_2H_5 + C_4H_{10}$	→	C_2H_6 + Products	$1.5 \times 10^{-24} T^{3.65} e^{-4600/T}$	Est. as k(C_2H_5 + C_3H_8)	
R363	$C_2H_6 + C_3H_5$	→	$C_3H_6 + C_2H_5$	$3.9 \times 10^{-22} T^{3.30} e^{-9986/T}$	Tsang (1991)	300 – 2500
R364	$C_2H_6 + C_3H_7$	→	$C_3H_8 + C_2H_5$	$4.2 \times 10^{-25} T^{3.82} e^{-4550/T}$	Tsang (1988)	300 – 2500
R365	$C_2H_6 + C_4H$	→	$C_4H_2 + C_2H_5$	$5.1 \times 10^{-11} e^{-76/T}$	Est. as k(C_2H + C_2H_6)	
R366	$C_2H_6 + C_6H$	→	$C_6H_2 + C_2H_5$	$5.1 \times 10^{-11} e^{-76/T}$	Est. as k(C_2H + C_2H_6)	
R367	2 C_3H_3 + M	→	C_6H_6 + M	$k_0 = 6.0 \times 10^{-28} e^{1680/T}$	Moses et al. (2000)	Est.
				$k_\infty = 1.2 \times 10^{-10}$	Morter et al. (1994)	298
R368	$C_3H_3 + C_3H_5$	→	2 CH_2CCH_2	$1.4 \times 10^{-13} e^{132/T}$	Est. as k(2 C_3H_5)	
R369	$C_3H_3 + C_3H_5$ + M	→	Product + M	$k_0 = 1.65 \times 10^{-4} T^{-8.75} e^{-985.4/T}$	〃	
				$k_\infty = 1.7 \times 10^{-11} e^{132/T}$	〃	
R370	$CH_3C_2H + {}^*C_4H_2$	→	$C_6H_2 + CH_3$ + H	2.43×10^{-13}	Zwier & Allen (1996)	Relative to R306
R371	$CH_3C_2H + {}^*C_4H_2$	→	Products + H_2	1.67×10^{-13}	〃	〃
R372	$CH_3C_2H + {}^*C_4H_2$	→	Products + C_2H_2	2.58×10^{-13}	〃	〃
R373	$CH_3C_2H + {}^*C_4H_2$	→	Products + C_2H_3	9.12×10^{-14}	〃	〃
R374	2 C_3H_5	→	$CH_2CCH_2 + C_3H_6$	$1.4 \times 10^{-13} e^{132/T}$	Tsang (1991)	300 – 2500
R375	2 C_3H_5 + M	→	Products + M	$k_0 = 2.822 \times 10^{-3} T^{-8.749} e^{-985.4/T}$	Est.as k_0(2 CH_3 + M)	
				$k_\infty = 1.69 \times 10^{-11} e^{131/T}$	Tsang (1991)	300 – 2500
R376	$C_3H_5 + C_3H_6$	→	Products + H	$1.0 \times 10^{-14} e^{-5776/T}$	〃	〃
R377	$C_3H_5 + C_3H_7$	→	2 C_3H_6	$2.4 \times 10^{-12} e^{66/T}$	〃	〃
R378	$C_3H_5 + C_3H_7$	→	$CH_2CCH_2 + C_3H_8$	$1.2 \times 10^{-12} e^{66/T}$	〃	〃
R379	$C_3H_5 + C_3H_7$ + M	→	Product + M	$k_0 = 2.822 \times 10^{-3} T^{-8.749} e^{-985.4/T}$	Est. as k_0(2 CH_3 + M)	
				$k_\infty = 3.4 \times 10^{-11} e^{66/T}$	Tsang (1991)	300 – 2500
R380	$C_3H_5 + C_3H_8$	→	$C_3H_6 + C_3H_7$	$3.9 \times 10^{-22} T^{3.3} e^{-9986/T}$	〃	〃
R381	$C_3H_6 + C_3H_7$	→	$C_3H_8 + C_3H_5$	$3.7 \times 10^{-24} T^{3.5} e^{-3340/T}$	〃	〃
R382	$C_3H_6 + {}^*C_4H_2$	→	$C_6H_4 + CH_3$ + H	3.94×10^{-13}	Zwier & Allen (1996)	Relative to R306
R383	$C_3H_6 + {}^*C_4H_2$	→	Products + H_2	1.71×10^{-13}	〃	〃
R384	$C_3H_6 + {}^*C_4H_2$	→	Products + C_2H_2	2.4×10^{-13}	〃	〃
R385	$C_3H_6 + {}^*C_4H_2$	→	Products + C_2H_3	5.1×10^{-14}	〃	〃
R386	2 C_3H_7	→	$C_3H_8 + C_3H_6$	2.8×10^{-12}	Tsang (1988)	300 – 2500
R387	2 C_3H_7 + M	→	Product + M	$k_0 = 2.822 \times 10^{-3} T^{-8.749} e^{-985.4/T}$	Est. as k_0(2 CH_3 + M)	
				$k_\infty = 1.7 \times 10^{-11}$	Tsang (1988)	300 – 2500
R388	$^*C_4H_2$	→	C_4H_2	10	Vuitton et al. (2003)	11 – 40
R389	$^*C_4H_2 + N_2$	→	$C_4H_2 + N_2$	1.4×10^{-15}	Zwier & Allen (1996)	Relative to R306
R390	$^*C_4H_2 + C_4H_2$	→	$C_6H_2 + C_2H_2$	8.58×10^{-13}	〃	〃
R391	$^*C_4H_2 + C_4H_2$	→	Products + 2 H	1.59×10^{-12}	〃	〃
R392	$^*C_4H_2 + C_4H_6$	→	$C_6H_6 + C_2H_2$	1.48×10^{-12}	Arrington et al. (1998)	Relative to R306
R393	$^*C_4H_2 + C_4H_6$	→	Products + 2 H	1.48×10^{-12}	〃	〃
R394	2 C_4H_4 + M	→	Product + M	$k_0 = 2.822 \times 10^{-3} T^{-8.749} e^{-985.4/T}$	Est. as k_0(2 CH_3 + M)	
				$k_\infty = 7.25 \times 10^{-14} e^{-9261/T}$	Lungard & Heicklen (1984)	573 – 723

Table 2.3 continued

	Reaction			Rate	Reference	T(K)
	Nitriles					
R395	$N_2^+ + e^-$	→	2 N	$3.5 \times 10^{-7}(300/T_e)^{0.5}$	Keller et al. (1992)	$T_e \sim 1200$ K
R396	$N_2^+ + N$	→	$N^+ + N_2$	1.0×10^{-11}	McEwan & Phillips (1975)	Upper Limit
R397	$N_2^+ + CH_4$	→	$CH_3 + N_2 + H + e^-$	1.0×10^{-9}	Est. based on Keller et al. (1992)	
R398	$N^+ + e^-$	→	N	$3.5 \times 10^{-12}(300/T_e)^{0.7}$	Keller et al. (1992)	$T_e \sim 1200$ K
R399	$N^+ + NH$	→	$N_2^+ + H$	3.7×10^{-10}	〃	〃
R400	$N^+ + CH_4$	→	$CH_3 + NH + e^-$	5.0×10^{-10}	Est. based on Keller et al. (1992)	
R401	$N^+ + CH_4$	→	$H_2CN + H_2 + e^-$	5.0×10^{-10}	〃	
R402	$N(^2D)$	→	N	2.3×10^{-5}	Okabe (1978)	
R403	$N(^2D) + e^-$	→	$N + e^-$	$6.0 \times 10^{-10}(300/T_e)^{-0.5}$	Frederick & Rusch (1977)	$T_e \sim 1200$ K
R404	$N(^2D) + NH_3$	→	$NH + NH_2$	5.0×10^{-11}	Herron (1999)	298
R405	$N(^2D) + N_2$	→	$N + N_2$	1.7×10^{-14}	〃	〃
R406	$N(^2D) + H_2$	→	NH + H	$4.2 \times 10^{-11}e^{-880/T}$	〃	200 – 300
R407	$N(^2D) + CH_4$	→	$NH + CH_3$	$9.6 \times 10^{-12}e^{-750/T}$	〃	232 – 292
R408	$N(^2D) + CH_4$	→	$CH_2NH + H$	$3.84 \times 10^{-11}e^{-750/T}$	〃	232 – 292
R409	$N(^2D) + C_2H_2$	→	CHCN + H	$1.6 \times 10^{-10}e^{-270/T}$	〃	220 – 300
R410	$N(^2D) + C_2H_4$	→	$CH_3CN + H$	$2.3 \times 10^{-10}e^{-503/T}$	Sato et al. (1999)	225 – 292
R411	$N(^2D) + C_2H_6$	→	C_2H_5N	1.9×10^{-11}	Herron (1999)	298
R412	$N(^2D) + CH_3C_2H$	→	$C_2H_3CN + H$	$1.6 \times 10^{-10}e^{-270/T}$	Est. as k($N(^2D) + C_2H_2$)	
R413	$N(^2D) + C_3H_6$	→	Product + H	$2.3 \times 10^{-10}e^{-503/T}$	Est. as k($N(^2D) + C_2H_4$)	
R414	$N(^2D) + C_3H_8$	→	Product + H	2.9×10^{-11}	Herron (1999)	298
R415	$N(^2D) + C_4H_2$	→	Product + H	$1.6 \times 10^{-10}e^{-270/T}$	Est. as k($N(^2D) + C_2H_2$)	
R416	$N(^2D) + C_4H_8$	→	Product + H	$2.3 \times 10^{-10}e^{-503/T}$	Est. as k($N(^2D) + C_2H_4$)	
R417	$N(^2D) + C_4H_{10}$	→	Product + H	3.1×10^{-11}	Herron (1999)	298
R418	$N(^2D) + CH_2NH$	→	Products	$2.3 \times 10^{-10}e^{-503/T}$	Est. as k($N(^2D) + C_2H_4$)	
R419	2 N + M	→	N_2 + M	$k_0 = 1.78 \times 10^{-33}e^{483/T}$	Clyne & Stedman (1967)	90 – 611
				$k_\infty = 5.0 \times 10^{-16}$	Takahashi & Miyazaki (1977)	298
R420	N + H + M	→	NH + M	$k_0 = 5.0 \times 10^{-32}$	Brown (1973)	〃
R421	$N + H_2$ + M	→	NH_2 + M	$k_0 = 1.0 \times 10^{-36}$	Petrishchev et al. (1981)	〃
				$k_\infty = 1.94 \times 10^{-20}$	Aleksandrov *et al.* (1994)	〃
R422	N + C + M	→	CN + M	$k_0 = 9.41 \times 10^{-33}$	Kley et al. (1974)	〃
R423	N + CH	→	CN + H	$2.67 \times 10^{-10}T^{-0.09}$	Brownsword et al. (1996)	216 – 584
R424	$N + CH_3$	→	$H_2CN + H$	5.76×10^{-11}	〃	〃
R425	$N + CH_3$	→	$HCN + H_2$	5.76×10^{-12}	Marston et al. (1989)	200
R426	$N + C_2H_3$	→	CH_3CN	3.1×10^{-12}	Payne et al. (1996)	298
R427	$N + C_2H_3$	→	$C_2H_2 + NH$	1.23×10^{-11}	〃	〃
R428	$N + C_2H_3$	→	Products	6.16×10^{-11}	〃	〃
R429	$N + C_2H_4$	→	$HCN + CH_3$	$3.32 \times 10^{-14}e^{-352/T}$	Kerr & Parsonage (1972)	291 – 600
R430	$N + C_2H_5$	→	$C_2H_4 + NH$	7.1×10^{-11}	Stief et al. (1995)	298
R431	$N + C_2H_5$	→	$H_2CN + CH_3$	3.9×10^{-11}	〃	〃
R432	$N + C_2H_6$	→	$C_2H_5N + H$	4.0×10^{-16}	Aleksandrov et al. (1990)	253
R433	$N + CH_3C_2H$	→	$CHCN + CH_3$	$1.15 \times 10^{-13}e^{-745/T}$	Kerr & Parsonage (1972)	320 – 550
R434	$N + C_3H_6$	→	$C_2H_4 + HCN + H$	$1.94 \times 10^{-13}e^{-654/T}$	〃	338 – 697
R435	$N + C_3H_8$	→	$C_2H_6 + HCN + H$	$3.39 \times 10^{-13}e^{-2561/T}$	Onyszchuk et al. (1953)	336 – 523
R436	$N + C_4H_6$	→	$CH_3C_2H + HCN + H$	$3.09 \times 10^{-13}e^{-926/T}$	Kerr & Parsonage (1972)	320 – 550
R437	$N + C_4H_8$	→	Products	$2.57 \times 10^{-13}e^{-659/T}$	〃	〃
R438	$N + C_4H_{10}$	→	$C_3H_8 + HCN + H$	$2.97 \times 10^{-14}e^{-1812/T}$	Back & Winkler (1954)	348 – 523
R439	N + NH	→	N_2 + H	2.49×10^{-11}	Hack et al. (1994)	298
R440	$N + NH_2$	→	2 NH	1.15×10^{-10}	Dransfeld & Wagner (1987)	〃
R441	N + CN	→	N_2 + C	$3.24 \times 10^{-13}e^{-1771/T}$	Atakan et al. (1992)	298 –534
R442	$N + H_2CN$	→	HCN + NH	$1.0 \times 10^{-10}e^{-200/T}$	Nesbitt et al. (1990)	200 – 363
R443	$N + CH_2NH$	→	$H_2CN + NH$	$3.32 \times 10^{-14}e^{-352/T}$	Est. as k($N + C_2H_4$)	
R444	$N + C_2N$	→	2 CN	1.0×10^{-10}	Whyte & Phillips (1983)	300
R445	N + CHCN	→	C_2N_2 + H	1.0×10^{-12}	Yung (1987)	
R446	NH + H	→	$N + H_2$	$3.12 \times 10^{-12}T^{1.55}e^{-103.2/T}$	Adam et al. (2005)	300 - 2000
R447	2 NH	→	NH_2 + N	$9.9 \times 10^{-22}T^{2.89}e^{1021.5/T}$	Zu et al. (1997)	297
R448	2 NH + M	→	N_2 + 2 H + M	$k_0 = 1.0 \times 10^{-33}$	Yung et al. (1984)	Est.
				$k_\infty = 3.49 \times 10^{-12}$	Nicholas et al. (1986)	298
R449	$NH + CH_3$	→	$CH_2NH + H$	1.0×10^{-11}	Est.	
R450	$NH + CH_4$	→	$NH_2 + CH_3$	2.11×10^{-24}	Xu et al. (1999)	300
R451	$NH + C_2H_2$	→	$CHCN + H_2$	$2.01 \times 10^{-9}T^{-1.07}$	Mullen & Smith (2005)	53–188
R452	$NH + C_2H_4$	→	$CH_3CN + H_2$	$1.15 \times 10^{-9}T^{-1.09}$	〃	〃
R453	$NH + C_2H_6$	→	$NH_2 + C_2H_5$	1.41×10^{-23}	Xu et al. (1999)	300

Table 2.3 continued

	Reaction			Rate	Reference	T(K)
R454	$NH + C_3H_6$	→	Products	$6.24 \times 10^{-9} T^{-1.27}$	Mullen & Smith (2005)	53 – 188
R455	$NH + C_4H_2$	→	Products	$8.24 \times 10^{-9} T^{-1.23}$	〃	〃
R456	$NH + NH_3 + M$	→	$N_2H_4 + M$	$k_0 = 5.02 \times 10^{-35}$	Zetzsch & Stuhl (1981)	298
				$k_\infty = 1.08 \times 10^{-12} e^{820/T}$	Mantei & Bair (1968)	300 – 345
R457	$NH_2 + H + M$	→	$NH_3 + M$	$k_0 = 3.0 \times 10^{-30}$	Schofield (1973)	298
				$k_\infty = 2.66 \times 10^{-11}$	Pagsberg et al. (1979)	348
R458	$NH_2 + H_2$	→	$NH_3 + H$	$4.89 \times 10^{-25} T^{3.89} e^{-1399/T}$	Garrett et al. (1990)	200 – 2400
R459	$NH_2 + CH_4$	→	$NH_3 + CH_3$	$5.11 \times 10^{-23} T^{3.59} e^{-4540/T}$	Mebel & Lin (1999)	300 – 2000
R460	$2\ NH_2$	→	$NH_3 + NH$	$2.26 \times 10^{-21} T^{2.79} e^{-664/T}$	Xu et al. (1998)	300 – 1800
R461	$2\ NH_2 + M$	→	$N_2H_4 + M$	$k_0 = 8.97 \times 10^{-20} T^{-3.9}$	Fagerstrom et al. (1995)	200 – 400
				$k_\infty = 2.5 \times 10^{-11} T^{0.27}$	〃	
R462	$NH_2 + CH_3 + M$	→	$CH_3NH_2 + M$	$k_0 = 6.0 \times 10^{-18} T^{-3.85}$	Jodkowski et al. (1995)	200 – 400
				$k_\infty = 1.2 \times 10^{-11} T^{0.42}$	〃	
R463	$NH_3 + H$	→	$NH_2 + H_2$	$1.14 \times 10^{-23} T^{3.87} e^{-3920/T}$	Garrett et al. (1990)	200 – 2400
R464	$NH_3 + CH$	→	$CH_2NH + H$	$4.11 \times 10^{-9} T^{-0.56} e^{-3/T}$	Bocherel et al. (1996)	23 – 296
R465	$NH_3 + CN$	→	$NH_2 + HCN$	$1.83 \times 10^{-8} T^{-1.14}$	Sims et al. (1994)	25 – 295
R466	$N_2 + CH + M$	→	product + M	$k_0 = 3.86 \times 10^{-25} T^{-2.6}$	Fulle & Hippler (1996)	200 – 715
				$k_\infty = 9.65 \times 10^{-11} T^{-0.15}$	〃	
R467	$N_2H_3 + H$	→	$2\ NH_2$	2.66×10^{-12}	von Gehring et al. (1971)	300
R468	$2\ N_2H_3$	→	$N_2H_4 + N_2 + H_2$	1.84×10^{-11}	Stief (1970)	298
R469	$2\ N_2H_3$	→	$2\ NH_3 + N_2$	4.98×10^{-12}	Schiavello & Volpi (1962)	423
R470	$N_2H_4 + H$	→	$N_2H_3 + H_2$	$1.17 \times 10^{-11} e^{-1260/T}$	Vaghjiani (1995)	222 – 657
R471	$CN + H + M$	→	$HCN + M$	$k_0 = 2.39 \times 10^{-24} T^{-2.2} e^{-569/T}$	Tsang (1992)	500 – 2500
				$k_\infty = 2.99 \times 10^{-9} T^{-0.5}$	〃	〃
R472	$CN + H_2$	→	$HCN + H$	$2.23 \times 10^{-21} T^{3.31} e^{-756/T}$	Sun et al. (1990)	209 – 740
R473	$CN + CH_4$	→	$HCN + CH_3$	$5.73 \times 10^{-12} e^{-674/T}$	Sims et al. (1993)	160 – 298
R474	$CN + C_2H_2$	→	$HC_3N + H$	$5.26 \times 10^{-9} T^{-0.52} e^{-20/T}$	〃, Huang et al. (1999)	25 – 298
R475	$CN + C_2H_4$	→	$C_2H_3CN + H$	$1.36 \times 10^{-8} T^{-0.69} e^{-30/T}$	〃, Balucani et al. (2000)	〃
R476	$CN + C_2H_6$	→	$HCN + C_2H_5$	$5.91 \times 10^{-12} T^{0.22} e^{58/T}$	〃	〃
R477	$CN + CH_3C_2H$	→	Products + H	4.1×10^{-10}	Carty et al. (2001)	15 – 298
R478	$CN + CH_2CCH_2$	→	Products + H	4.1×10^{-10}	〃	〃
R479	$CN + C_3H_6$	→	Products + H	$1.73 \times 10^{-10} e^{101/T}$	Sims et al. (1993)	160 – 298
R480	$CN + C_3H_8$	→	$HCN + C_3H_7$	$3.58 \times 10^{-15} T^{1.14} e^{284/T}$	Hess et al. (1989)	298 – 736
R481	$CN + C_4H_2$	→	Products + H	4.2×10^{-10}	Seki et al. (1996)	298
R482	$CN + C_4H_4$	→	Products + H	$1.07 \times 10^{-7} T^{-0.82} e^{-228/T}$	Yang et al. (1992b)	174 – 740
R483	$CN + C_4H_6$	→	Products + H	$2.57 \times 10^{-10} e^{-171/T}$	Butterfield et al. (1993)	297 – 740
R484	$CN + C_6H_6$	→	Products + H	2.82×10^{-10}	Balucani et al. (1999)	297 – 740
R485	$2\ CN + M$	→	$C_2N_2 + M$	$k_0 = 9.41 \times 10^{-23} T^{-2.61}$	Tsang (1992)	500 – 2500
				$k_\infty = 9.4 \times 10^{-12}$	〃	〃
R486	$CN + HCN$	→	$C_2N_2 + H$	$2.5 \times 10^{-17} T^{1.71} e^{-770/T}$	Yang et al. (1992a)	297 – 740
R487	$CN + CH_2NH$	→	$HCN + H_2CN$	$6.71 \times 10^{-11} e^{-412/T}$	Est. as k(CN + CH_2O),Chang & Wang (1994)	
R488	$CN + CH_3CN$	→	$C_2N_2 + CH_3$	$6.46 \times 10^{-11} e^{-1190/T}$	Zabarnick & Lin (1989)	296 – 578
R489	$CN + HC_3N$	→	$C_4N_2 + H$	1.7×10^{-11}	Halpern et al. (1989)	298
R490	$CN + C_4N_2$	→	$C_2N_2 + C_3N$	$k_0 = 9.41 \times 10^{-23} T^{-2.61}$	Est. as k_0(2 CN + M)	
				$k_\infty = 5.4 \times 10^{-13}$	Seki et al. (1996)	298
				$k = k_\infty - k(p)$		
R491	$HCN + H + M$	→	$H_2CN + M$	$k_0 = 4.4 \times 10^{-24} T^{-2.73} e^{-3860/T}$	Tsang & Herron (1991)	300 – 2500
				$k_\infty = 5.5 \times 10^{-11} e^{-2438/T}$	〃	〃
R492	$HCN + CH$	→	$CHCN + H$	$5.0 \times 10^{-11} e^{498/T}$	Zabarnick & Lin (1991)	296 – 674
R493	$HCN + C_2H$	→	$HC_3N + H$	$5.26 \times 10^{-12} e^{-770/T}$	Hoobler & Leone (1997)	297 – 360
R494	$HCN + C_2H_3$	→	$C_2H_3CN + H$	$1.1 \times 10^{-12} e^{-900/T}$	Monks et al. (1993)	298
R495	$HCN + C_3N$	→	$C_4N_2 + H$	3.0×10^{-11}	Petrie & Osamura (2004)	298
R496	$H_2CN + H$	→	$HCN + H_2$	7.0×10^{-11}	Nesbitt et al. (1990)	lower limit, 298
R497	$2\ H_2CN + M$	→	Product + M	$k_0 = 9.41 \times 10^{-23} T^{-2.61}$	Est. as k_0(2 CN + M)	
				$k_\infty = 2.57 \times 10^{-12}$	Nizamov & Dagdigian (2003),	
R498	$2\ H_2CN$	→	$HCN + CH_2NH$	$k_0 = 5.13 \times 10^{-12}$	Horne & Norrish (1970)	
R499	$CH_2NH + H$	→	$H_2 + H_2CN$	$k_0 = 4.0 \times 10^{-14}$	Est. as k(H + CH_2O),Dobe et al. (1994)	
R500	$CH_2NH + C_2H$	→	Products + H	1.4×10^{-10}	Est. as k(C_2H_4 + C_2H)	

Table 2.3 continued

	Reaction			Rate	Reference	T(K)
R501	$C_2N + CH_4$	→	$CHCN + CH_3$	6.0×10^{-14}	Zhu et al. (2003)	298
R502	$C_2N + C_2H_6$	→	$CHCN + C_2H_5$	2.9×10^{-12}	〃	〃
R503	$C_2N + C_3H_8$	→	$CHCN + C_3H_7$	1.9×10^{-11}	〃	〃
R504	$C_2N + C_4H_{10}$	→	CHCN + Products	4.2×10^{-11}	〃	〃
R505	2 CHCN	→	$C_4N_2 + H_2$	5.0×10^{-11}	Yung (1987)	Est.
R506	$CH_3CN + H$	→	$HCN + CH_3$	$3.39 \times 10^{-12} e^{-3950/T}$	Jamieson et al. (1970)	313 – 780
R507	$CH_3CN + H$	→	$CN + CH_4$	$1.66 \times 10^{-13} e^{-1500/T}$	〃	〃
R508	$CH_3CN + C_2H$	→	$HC_3N + CH_3$	$1.79 \times 10^{-11} e^{-770/T}$	Hoobler & Leone (1997)	262 – 360
R509	$C_3N + H + M$	→	$HC_3N + M$	$k_0 = 1.26 \times 10^{-18} T^{-3.1} e^{-721/T}$ $k_\infty = 3.0 \times 10^{-10}$	Est. as k_0($H + C_2H + M$) 〃	
R510	$C_3N + H_2$	→	$HC_3N + H$	$1.2 \times 10^{-11} e^{-998/T}$	Est. as k($C_2H + H_2$)	
R511	$C_3N + CH_4$	→	$HC_3N + CH_3$	$1.11 \times 10^{-10} e^{-998/T}$	Clarke & Ferris (1995)	Relative to R510
R512	$C_3N + C_2H_2$	→	Products + H	1.3×10^{-10}	Est. as k($C_2H + C_2H_2$)	
R513	$C_3N + C_2H_4$	→	Products + H	1.4×10^{-10}	Est. as k($C_2H + C_2H_4$)	
R514	$C_3N + C_2H_6$	→	$HC_3N + C_2H_5$	$7.56 \times 10^{-10} e^{-998/T}$	Clarke & Ferris (1995)	Relative to R510
R515	$C_3N + C_3H_8$	→	$HC_3N + C_3H_7$	$7.56 \times 10^{-10} e^{-998/T}$	Est. as k($C_3N + C_2H_6$)	
R516	$C_3N + C_4H_2$	→	Products + H	1.3×10^{-10}	Est. as k($C_2H + C_4H_2$)	
R517	$C_3N + C_4H_{10}$	→	HC_3N + Products	$7.56 \times 10^{-10} e^{-998/T}$	Est. as k($C_3N + C_2H_6$)	
R518	$HC_3N + H + M$	→	$H_2C_3N + M$	$k_0 = 1.0 \times 10^{-27} e^{-740/T}$ $k_\infty = 1.1 \times 10^{-12} e^{-500/T}$	Est. based on Parker et al. (2004) Parker et al. (2004)	 200 – 298
R519	$HC_3N + CH_3 + M$	→	Product + M	$k_0 = 3.3 \times 10^{-28} e^{-740/T}$ $k_\infty = 1.1 \times 10^{-12} e^{-3880/T}$	Est. as k($CH_3 + C_2H_2$) 〃	
R520	$H_2C_3N + H$	→	$C_2H_2 + HCN$	$6.86 \times 10^{-11} e^{23/T}$	Est. as k($H + C_2H_3$)	
R521	$C_2H_3CN + C_2$	→	$C_2H_3 + C_3N$	4.4×10^{-10}	Reisler et al. (1980)	300
R522	$C_2H_3CN + C_2H_5$	→	Products	$1.02 \times 10^{-13} e^{-1710/T}$	Kerr & Parsonage (1972)	323 – 454
R523	$C_2N_2 + C$	→	$C_2N + CN$	3.0×10^{-11}	Whyte & Phillips (1983)	300
R524	$C_4N_2 + C_2H$	→	Products + CN	1.3×10^{-10}	Est. as k($C_2H + C_2H_2$)	

2.3.3 Vertical transport

The vertical transport of the produced species in the 1D simulated atmosphere is defined by the molecular and turbulent (eddy) diffusion. The former is controlled by the properties of each species and can be well reproduced by the evaluation of the diffusion coefficient for each molecule or atom, while the latter provides a representation for the impact of the atmospheric advection in the vertical profile of each species. This can only be reproduced by the validation of the model simulations against measurements. The combined contribution of the two diffusion processes can be described by the total diffusive flux at each region of the atmosphere, for each species i:

$$\Phi_i = \frac{Dn}{H}\left(1 - \frac{M_i}{M} - \alpha_T \frac{H}{T}\frac{\partial T}{\partial z}\right) f_i - (D+K)n\frac{\partial f_i}{\partial z} \tag{2.13}$$

with D and K the molecular and eddy diffusion coefficients respectively, α_T the thermal diffusion coefficient, H the atmospheric scale height, M_i the molecular weight of species i, n and M the number density and the mean molecular weight of the atmosphere and f_i the mole fraction of species i.

For the molecular diffusion, measurements of the binary coefficients have been performed only for some of the species included in the model. These are

given in the form:

$$D_{ij} = A_{ij}\frac{T^s}{n} \tag{2.14}$$

where A_{ij} and s are parameters that depend on the pair of diffusing species and are presented in Table 2.4. For the rest of the species for which no measurements exist, the diffusion coefficients can be calculated using the formula (Banks & Kockarts, 1973):

$$D_{ij} = 1.52 \times 10^{18}\left(\frac{1}{M_i} + \frac{1}{M_j}\right)^{1/2}\frac{T^{1/2}}{n} \tag{2.15}$$

with i corresponding to the diffusing minor species and j to the bath molecule. In order to take into account the variation of the atmospheric composition with altitude due to the changes in methane's vertical profile in the upper atmosphere for Titan's case, the bath gas molecular weight can be replaced by the atmospheric mean molecular weight.

The eddy mixing coefficient, K, can be retrieved by fitting the vertical profiles of tracer species. These are species which exhibit a very long photochemical life time compared to the characteristic for transport and in this way their structure dependents on the dynamical processes. Such species are the noble gases (from which only Ar is present in Titan) while in the past HCN and CH_4 have been used for the derivation of the eddy coefficient at different altitudes inTitan's atmosphere. The tracer species used here and the derived mixing profile are discussed in the following chapter along with the chemical composition of the simulated atmosphere.

2.3.4 Condensation

For most of the hydrocarbons and nitriles found in the lower stratosphere - troposphere of Titan, their saturation vapor pressure for the prevailing temperature conditions is smaller than their partial pressure allowed by photochemistry (Sagan & Thompson, 1984). This means that their saturation ratio, S, exceeds unity and that these species can condense. Under such conditions and provided that the atmosphere contains enough nucleation sites on the surface of

Table 2.4: Binary and thermal diffusion coefficients used in the model calculations. A is given in cm^2s^{-1}.

Pair	$Ax10^{17}$	s	α_T	Reference
H-N_2	4.87	0.698	-0.38	Banks & Kockarts (1973)
H_2-N_2	2.80	0.740	-0.38	Banks & Kockarts (1973)
N-N_2	0.969	0.770		Mason & Marreno (1970)
Ar-N_2	0.362	0.833	0.17	Mason & Marreno (1970)
CH_4-N_2	0.734	0.750		Banks & Kockarts (1973)
C_2H_6-N_2	0.561	0.730		Wakeham & Slater (1973)
C_3H_8-N_2	0.653	0.660		Wakeham & Slater (1973)
C_4H_{10}-N_2	0.734	0.610		Wakeham & Slater (1973)

which condensation proceeds readily (heterogeneous nucleation), the nucleation rate reaches very high values that lead to rapid loss of the condensing species (Pruppacher & Klett, 1978). In order to take into consideration the effects of this process in the final vertical profiles of the calculated species, a loss rate is included of the form:

$$L_c = -A_c(S-1)\frac{\exp\left(-0.5/\ln\left(S+1\right)^2\right)}{\ln\left(S+1\right)^2}, \quad S>1 \tag{2.16}$$

where A_c is constant in units of s^{-1}. The last part of the expression resembles the dependence of the heterogeneous nucleation rate of spherical nuclei on the saturation ratio, while the $(S-1)$ term forces the calculated volume mixing ratio to converge close to the saturated value. As can be seen in Fig. 2.11, the above expression provides increasing loss rates with increasing saturation ratios. Also shown for comparison, is a loss rate of the form $\sim -(S-1)/S$ which is similar to the ones used in previous photochemical models (Yung et al., 1984). This expression must provide a smooth transition between the condensing and non-condensing regions which is necessary in order to avoid the oscillation of the simulation between the two. Typical values used for A_c are of the order (0.1 - 1)$\times 10^{-7}\mathrm{s}^{-1}$. For the calculation of the saturation vapor pressure curves for each condensing species we used the data from Vargaftik (1975) and the NIST web database (http://webbok.nist.gov/chemistry/). The vapor pressure curves are usually parameterized in the function form of the Antoine equation:

$$log_{10}(P_S(T)) = A - \frac{B}{T+C} \tag{2.17}$$

were A, B and C are constants characteristic of each species. Values for the species found in Titan's atmosphere are presented in Table 2.5.

2.3.5 Simulation method

The model solves the time-dependent continuity equation in 1D for spherical geometry :

$$\frac{\partial n_i}{\partial t} = -\frac{1}{r^2}\frac{\partial(r^2\Phi_i)}{\partial r} + P_i - L_i \tag{2.18}$$

for each species i at each altitude z with $r = R_T + z$, R_T being Titan's radius. In the above, n_i is the number density of species i, Φ_i is the vertical flux and P_i and L_i describe production (photochemistry) and loss (photochemistry, condensation, surface deposition) processes, respectively.

This approach of spherical geometry is necessary for Titan's case because the atmosphere, due to the low gravity, is extended to high altitudes above the surface that are comparable with the size of the satellite. This makes the inclusion of the spherical correction necessary in order to take into account the dilution of the atmosphere as we move to higher altitudes. The importance of the spherical correction is manifested in Fig. 2.12 where the vertical profiles of some hydrocarbon and nitrile species are presented, calculated under spherical

Table 2.5: Vapor pressure parameters for the Antoine equation in the specified temperature range for the main species in Titan's atmosphere. Also shown is the heat of formation for each species in kJ/mol.

Species	$\Delta_f H^0$	A	B	C	Temperature
Methane, CH_4	-74.87	3.98950	443.03	-0.49	90.99-189.99
Ethane, C_2H_6	-83.8	4.50706	791.30	-6.422	91.33-144.13
		3.93835	659.74	-16.719	135.74-199.91
Ethylene, C_2H_4	54.47				
Acetylene, C_2H_2	226.73	4.19598	699.53	-21.47	192.59-206.3
Methylacetylene, CH_3C_2H	185.4	4.95219	1226.12	-1.926	161.5-254.27
Propylene, C_3H_6	20.41	3.97488	795.82	-24.884	165.81-225.98
Propane, C_3H_8	-104.7	4.01158	834.26	-22.763	166.02-231.41
Diacetylene, C_4H_2	464.0	3.05288	570.27	-95.334	190.6-282.8
Vinylacetylene, C_4H_4	295.0	4.04028	954.83	-41.838	179.9-278.4
1,3-Butadiene, C_4H_6	108.8	3.99798	941.66	-32.753	197.6-271.6
n-Butane, C_4H_{10}	-125.6	4.70812	1200.48	-13.01	135.42-212.89
Benzene, C_6H_6	82.93	4.01814	1203.84	-53.23	287.7-354.07
Hydrogen Cyanide, HCN	135.14	4.67417	1340.79	-11.59	256.73-319.38
Acetonitrile, CH_3CN	74.04	5.93296	2345.83	43.815	280.41-300.53
Cyanoacetylene, HC_3N	354.0				
Acrylonitrile, C_2H_3CN	179.7	4.06661	1255.94	-41.853	222-351
Cyanogen, C_2N_2	309.07	4.51661	1041.52	-21.288	252-391.3
Ammonia, NH_3	-45.94	3.18757	506.71	-80.78	164 - 239.5
Methylamine, CH_3NH_2	-22.97	4.51990	1034.98	-37.57	190-266
Hydrazine, N_2H_4		5.01105	1724.78	-41.83	288-343
Water, H_2O	-241.83	4.65430	1435.26	-64.848	255.8-373.
Carbon Dioxide, CO_2	-393.51	6.81228	1301.68	-3.494	154.26-195.89

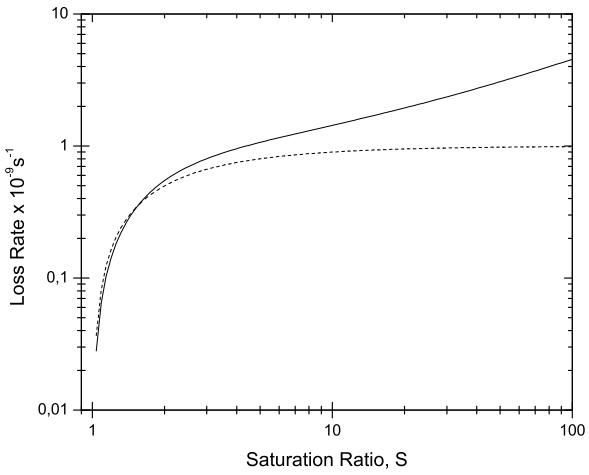

Figure 2.11: Loss rate for condensing species as a function of their saturation ratio from the function used in this work (solid line) and used in previous photochemical models (dashed line).

and plane-parallel geometry. The general trend is as follows. For species produced in the upper atmosphere and diffused downwards, the spherical solution requires that as the species move to lower altitudes the equivalent surface of the atmosphere becomes smaller. Hence their abundance must increase.

Using the hydrostatic equilibrium approximation in order to transform 2.18 to a pressure dependent form, the flux divergence term takes the form:

$$-\frac{1}{r^2}\frac{\partial(r^2\Phi_{i,k})}{\partial r} = \frac{p}{H}\frac{\partial\Phi_{i,k}}{\partial p} - \frac{2}{r}\Phi_{i,k} \tag{2.19}$$

where k refers to the pressure level and H is the atmospheric pressure scale height. In the same way, the vertical flux can be written in a compact form as:

$$\Phi_{i,k} = C_1(p,T)f_{i,k} + C_2(p,T)\frac{\partial f_{i,k}}{\partial p} \tag{2.20}$$

with (see equation 2.13)

$$C_1(p,T) = \frac{Dp}{k_B T H}\left(1 - \frac{M_i}{M} + \alpha_T\frac{p}{T}\frac{\partial T}{\partial p}\right)$$
$$C_2(p,T) = (D+K)\frac{p^2}{k_B T H} \tag{2.21}$$

Under this form, 2.19 can be expressed as:

$$-\frac{1}{r^2}\frac{\partial(r^2\Phi_{i,k})}{\partial r} = D_1(p,T)f_{i,k} + D_2(p,T)\frac{\partial f_{i,k}}{\partial p} + D_3(p,T)\frac{\partial^2 f_{i,k}}{\partial p^2} \tag{2.22}$$

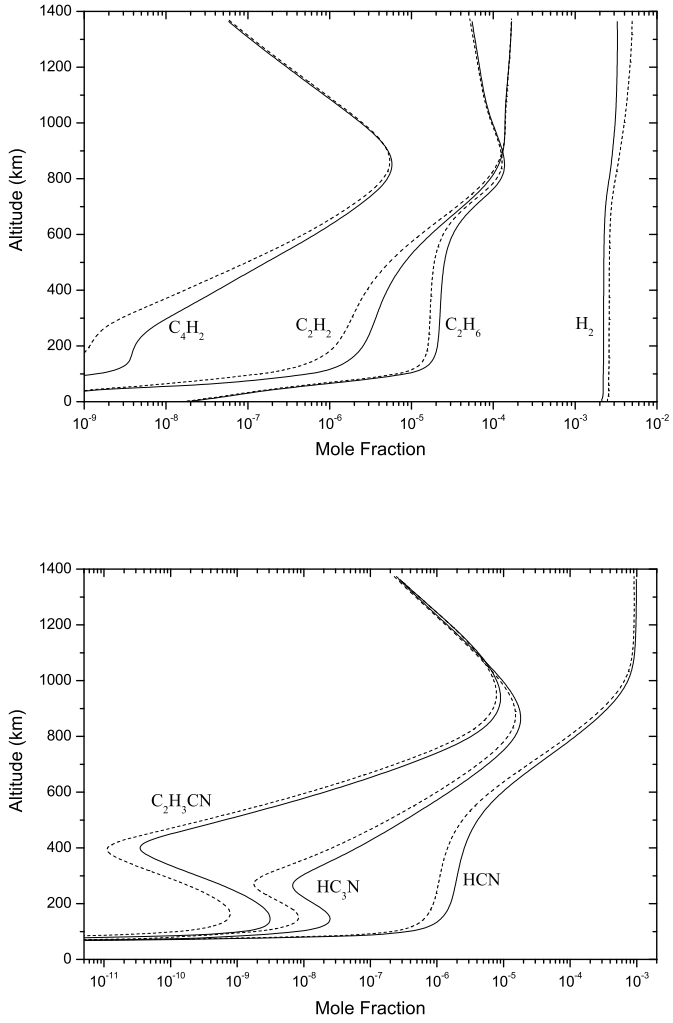

Figure 2.12: Impact of geometry assumed in the vertical species profiles. Solid lines describe the mole fractions calculated under spherical geometry and dashed lines the ones under plane-parallel geometry.

with:

$$\begin{aligned} D_1(p,T) &= \frac{p}{H}\frac{\partial C_1}{\partial p} - \frac{2}{r}C_1 \\ D_2(p,T) &= \frac{p}{H}(C_1 + \frac{\partial C_2}{\partial p}) - \frac{2}{r}C_2 \\ D_3(p,T) &= \frac{p}{H}C_2 \end{aligned} \tag{2.23}$$

On the other hand, the time derivative of the number density of each species can be written as:

$$\frac{\partial n_{i,k}}{\partial t} = \frac{\partial (n f_{i,k})}{\partial t} = n\frac{\partial f_{i,k}}{\partial t} + B(p,T) f_{i,k}, B(p,T) = -\frac{p}{k_B T^2}\frac{\partial T}{\partial t} \tag{2.24}$$

Substituting the above in 2.20, the continuity equation can be written as:

$$\frac{\partial f_{i,k}}{\partial t} + a_k f_{i,k} + b_k \frac{\partial f_{i,k}}{\partial p} + c_k \frac{\partial^2 f_{i,k}}{\partial p^2} = u_{i,k} - v_{i,k} \tag{2.25}$$

where

$$\begin{aligned} a_k &= \frac{1}{n_k}(B(p,T) + D_1(p,T)) \\ b_k &= \frac{D_2(p,T)}{n_k}, \quad c_k = \frac{D_3(p,T)}{n_k} \\ u_{ik} &= P_{i,k}/n_k, \quad v_{i,k} = L_{i,k}/n_k \end{aligned} \tag{2.26}$$

Grid transformation and boundary conditions

In view of the discrete pressure grid in the model, the continuity equation at each pressure level k and for each species i takes the form:

$$\frac{\partial f_{i,k}}{\partial t} = H_{i,k}(f_{1,i}, f_{2,k}, ..., f_{I,k}; f'_{i,k}; f''_{i,k}, p_k, T_k, t) \tag{2.27}$$

where

$$H_{i,k} = -\alpha_k f_{i,k} - w_{i,k} + u_{i,k} - v_{i,k} \tag{2.28}$$

and

$$w_{i,k} = b_k f'_{i,k} + c_k, f''_{i,k} \tag{2.29}$$

with

$$f'_{i,k} = \frac{\partial f_i}{\partial p} \; and \; f''_{i,k} = \frac{\partial f_i^2}{\partial p^2} \tag{2.30}$$

Introducing finite differences, the two derivatives can be written as:

$$f'_{i,k} = (f_{i,k+1} - f_{i,k})/sp_k \tag{2.31}$$

$$f''_{i,k} = g\frac{2}{sp_k}\left(\frac{f_{i,k+1} - f_{i,k}}{\Delta p_k} - \frac{f_{i,k} - f_{i,k-1}}{\Delta p_{k-1}}\right) \tag{2.32}$$

where

$$\begin{aligned} \Delta p_k &= p_{k+1} - p_k \\ sp_k &= \Delta p_k + \Delta p_{k+1} \\ g &= \left(\frac{2\Delta p_k \Delta p_{k-1}}{\Delta p_k^2 + \Delta p_{k-1}^2} \right) \end{aligned} \tag{2.33}$$

so that $w_{i,k}$ can be expressed as:

$$w_{i,k} = \alpha_k f_{i,k-1} + \beta_k f_{i,k} + \gamma_k f_{i,k+1} \tag{2.34}$$

with

$$\begin{aligned} \alpha_k &= \frac{b_k}{sp_k} + \frac{2gc_k}{\Delta p_k sp_k} \\ \beta_k &= -\frac{2gc_k}{\Delta p_k \Delta p_{k-1}} \\ \gamma_k &= -\frac{b_k}{sp_k} + \frac{2gc_k}{\Delta p_k sp_k} \end{aligned} \tag{2.35}$$

At the boundaries the first and second derivatives in the three term approximation introduced above, include an imaginary point. For the surface we consider that the value of the mixing ratio for the imaginary point under the surface is the same with the surface value. The physical meaning of this condition is that there is no loss or gain through the surface boundary by transport. Under this condition, the parameters of $w_{i,1}$ take the values:

$$\alpha_1 = 0, \beta_1 = \frac{b_1}{2\Delta p_1} - \frac{c_k}{\Delta p_1^2}, \gamma_1 = -\beta_1. \tag{2.36}$$

At the top of the atmosphere (TOA) the adopted condition is that of a continues first derivative. Under this approximation the value of the imaginary point can be calculated from the nullification of the second derivative and the $w_{i,TOA}$ parameters take the form:

$$\alpha_{TOA} = \frac{b_{TOA}}{\Delta p_{TOA}}, \beta_{TOA} = -\alpha_{TOA}, \gamma_{TOA} = 0. \tag{2.37}$$

Method of solution

The continuity equation (2.27) can not be directly integrated because the characteristic time of change of each species mixing ratio at each altitude, can differ by many orders of magnitude. This explains the characterization 'stiff' used for this type of equations. In order to overcome this obstacle an integration method with varying integration step (time in our case) must be used, such as the Newton-Raphson iteration method (e.g. Vardavas (1984)):

$$f_{i,k}(t_{m+1}) = f_{i,k}(t_m) + \Delta t_m H_{i,k}(t_m) \tag{2.38}$$

where Δt_m is the integration time step chosen with the criterion to be smaller than the smallest characteristic time for change in any species concentration at any altitude:

$$\Delta t_m < \tau_{ikm} = |f_{i,k,m}/(\partial f_{i,k}/\partial t)_m| \tag{2.39}$$

As shown in Vardavas (1984), for most cases $\Delta t_m = 0.1\tau_{ikm}$ is sufficient. As a species approaches chemical equilibrium, $\tau_{ikm} \to \infty$, the continuity equation reduces to $H_{i,k} = 0$, its steady state form. Setting $Q_{i,k} = u_{i,k} - v_{i,k}$ the H function takes the form:

$$H_{i,k} = -a_{i,k} f_{i,k} - w_{i,k} + Q_{i,k} \tag{2.40}$$

and the continuity equation for species i at level k can be written in the functional form:

$$G_{i,k}(f_{1,k}, f_{2,k}, ..., f_{I,k}; f'_{i,k}; f''_{i,k}, p_k, T_k, t) = 0 \tag{2.41}$$

where

$$G_{i,k}(\tau_{m+1}) = f_{i,k}(t_{m+1}) - f_{i,k}(t_m) - \Delta t_m H_{i,k}(t_m). \tag{2.42}$$

The last equation can be solved with Newton-Raphson iteration for the mixing ratio of each species i, at a level k. If we know the mixing ratios at a time t_m, $f_{i,k,m}$, then an estimation for the mixing ratio at the next time step, $f_{i,k,m+1}$ is performed, say $f^{(1)}_{i,k,m+1}$. This estimation is accompanied with an error $\epsilon^{(1)}_{i,k}$ for each species i at level k, which is defined by:

$$\begin{aligned} \epsilon^{(1)}_k &= f^{(1)}_{i,k,m+1} - f_{i,k,m+1} = \\ & f^{(1)}_{i,k,m+1} - f_{i,k,m} - \Delta t_m H_{i,k}(f^{(1)}_{i,k-1}; \mathbf{f}^{(1)}_k; f^{(1)}_{i,k+1}) \end{aligned} \tag{2.43}$$

with the vector $\mathbf{f}^{(1)}$ defined as:

$$\mathbf{f}^{(1)}_k = (f_{1,k}, f_{2,k}, ..., f_{I,k}). \tag{2.44}$$

The minimization of these errors is performed by imposing a correction $\Delta \mathbf{f}^{(1)}_k$ to the initial guess $\mathbf{f}^{(1)}$. The corrections are defined by equation (2.41), which when expanded in a Taylor series around the initial guess, takes the form:

$$G^{(1)}_{i,k} + (\partial G_{i,k}/\partial f_{j,l})_{(1)} \, \Delta f^{(1)}_{j,l} = 0 \tag{2.45}$$

with the j and l indices covering the total number of species and levels. Using the previous definitions, the last is reduced to the form:

$$\Delta t_m \left[\alpha_k \Delta f_{i,k+1} + \beta'_k \Delta f_{i,k} + \gamma \Delta f_{i,k-1} - \sum q_{i,l,k} \Delta f_{i,k} \right] = - \epsilon_{i,k} \tag{2.46}$$

with

$$q_{i,l,k} = \frac{\partial Q_{i,k}}{f_{i,k}} \beta'_k = 1/\Delta t_m + \alpha_k + \beta_k \tag{2.47}$$

The above system can be written in a matrix representation as:

$$\begin{pmatrix} A_1 & C_1 & 0 & \cdots & \cdots & 0 \\ B_2 & C_2 & A_2 & 0 & \cdots & \vdots \\ 0 & B_3 & C_3 & A_3 & \cdots & \vdots \\ \vdots & & & \ddots & & 0 \\ \vdots & & & & \ddots & C_{K-1} \\ 0 & \cdots & \cdots & 0 & B_K & A_K \end{pmatrix} \begin{pmatrix} \Delta\mathbf{f}_1 \\ \vdots \\ \vdots \\ \vdots \\ \vdots \\ \Delta\mathbf{f}_K \end{pmatrix} = \begin{pmatrix} \text{-}\epsilon_1 \\ \vdots \\ \vdots \\ \vdots \\ \vdots \\ \text{-}\epsilon_K \end{pmatrix} \tag{2.48}$$

with the elements of the I x I matrices A, B and C given by:

$$\begin{array}{lll} \mathrm{a}_{ilk} & = \text{-}\mathrm{q}_{ilk}\Delta\mathrm{t}_m + \beta_k^{'}\Delta\mathrm{t}_m & \text{, for l=i} \\ & = \text{-}\mathrm{q}_{ilk}\Delta\mathrm{t}_m & \text{, for l}\neq\text{i} \\ \mathrm{b}_{ilk} & = \Delta\mathrm{t}_m\gamma_k & \text{, for l=i} \\ & = 0 & \text{, for l}\neq\text{i} \\ \mathrm{c}_{ilk} & = \Delta\mathrm{t}_m\alpha_k & \text{, for l=i} \\ & = 0 & \text{, for l}\neq\text{i} \end{array} \tag{2.49}$$

for K levels and I species. Once the corrections $\Delta f_k^{(1)}$ are known an improved vector $f_k^{(2)}$ can be calculated and the procedure is repeated until the mixing ratios converge and the errors are negligible.

2.4 Microphysics

The chemical interaction of the haze precursors in Titan's atmosphere with the bulk gas phase species has a specific limit beyond which the growth of the precursors due to addition of new molecules is negligible. At this point the coalescence between the produced structures (the monomers), controls the evolution of their size and from this point and on the laws of microphysics apply. The basic equation describing the evolution of size and density of an initial monomer population in 1D is provided by the Smoluchowski description which in discrete form can be written as:

$$\begin{aligned} \frac{\partial n(v_k)}{\partial t} &= -\frac{\partial \Phi(v_k)}{\partial z} \\ &+\tfrac{1}{2}\sum_{i=1}^{k-1} K(u_i, v_k - u_i)n(u_i), n(v_k - u_i) \\ &-n(v_k)\sum_{i=1}^{\infty} K(u_i, v_k)n(u_i) + p(v_k). \end{aligned} \tag{2.50}$$

This is no more than a continuity equation saying that the evolution of the number density of volume v_k spherical particles is controlled by the flux of particles of this volume, $\Phi(v_k)$, the production of size v_k particles from smaller ones (first sum), the loss of size v_k particles to bigger ones (second sum) and the chemical

production of this size particles (only for the monomers) and/or loss due to precipitation or other processes. K is the coagulation kernel which describes the efficiency of the process between different size particles at different temperature and pressure conditions. These parameters are described analytically in the following sections.

2.4.1 Radial grid

Microphysical models provide a description for the evolution of an initial population of particles with a specified size distribution, over time. In order to simulate the production of bigger and bigger size particles due to coalescence between the initial population and new particles, a discrete radial grid must be used. Each bin of this grid will correspond to an average volume for the particles inside it. Because the range of values between the size of the initial population and that of the final particles could cover many orders of magnitude, the use of a linear grid is not favored. This would require a large number of bins that would lead to very large computational time. A different approach is used in which the size of each bin increases geometrically as the particles get bigger. The most well known technic applied in grid division is the volume-ratio size grid in which the average volume of each bin is equal to the volume of the previous bin multiplied with a constant value called the volume ratio, V_r :

$$v_{i+1} = V_r v_i \tag{2.51}$$

where v is the average volume of each bin i. V_r can take any value greater than unity and the choice depends on the resolution needed in the calculations. Due to the form of the grid the boundaries of each grid are related through the volume-ratio:

$$v_i^{high} = V_r v_i^{low}. \tag{2.52}$$

Combining the last with:

$$v_i = \frac{1}{2}(v_i^{high} + v_i^{low}) \tag{2.53}$$

provides the following two expressions for the lower and upper limits of each bin:

$$v_i^{low} = \frac{2v_i}{1+V_r}, \quad v_i^{high} = \frac{2V_r v_i}{1+V_r} \tag{2.54}$$

In the calculations that follow the volume-ratio has been set to:

$$\mathrm{V}_r = 2.$$

The resulting bin structure is shown in Table 2.4.1. There are 35 bins used ranging from the monomers size (0.735 Å) up to ∼2 microns. Higher size values are not necessary due to the electrostatic repulsion between the particles that constrain their final size to small values, as will be shown later.

Since, due to the discrete shape of the volume spectrum division, each bin corresponds to a range of volume values, the coagulation between two particles

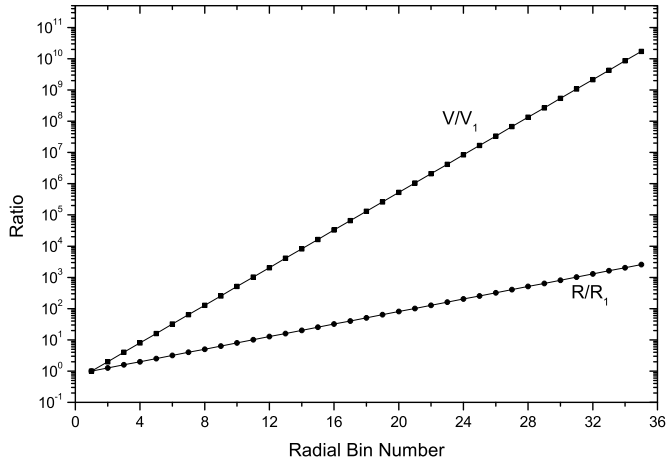

Figure 2.13: Evolution of average bin volume and the corresponding radius with bin number. Values are given in terms of the initial volume and radius.

can lead to the production of new bigger particles whose volume can range between adjacent bins. This requires the incorporation in the calculations of the volume fraction that the new particle has in each domain of the grid. The parameterization for the calculation of the volume fractions can be described by a simple form (see e.g. Jacobson (2005)). If i and j are the bins from which particles coagulate and the produced particle ranges in size between bins k and $k+1$, then the volume fraction, $F_{i,j,k}$ of the new particle over each bin will be:

$$F_{i,j,k} = \begin{cases} \frac{v_{k+1}-V_{i,j}}{v_{k+1}-v_k}\frac{v_k}{V_{i,j}} & v_k \leq V_{i,j} < v_{k+1} \quad k < N \\ 1 - f_{i,j,k-1} & v_{k-1} \leq V_{i,j} < v_k \quad k > 1 \\ 1 & V_{i,j} \geq v_k \quad k = N \\ 0 & Other \end{cases} \tag{2.55}$$

where $V_{i,j} = v_i + v_j$ and N is the number of bins used in the calculations.

2.4.2 Physical parameters

Before describing the basic concepts of microphysical processes an introduction to the physical parameters used is necessary. These parameters describe the properties of the atmosphere as a medium and also the properties of the particles moving in the atmospheric medium.

Thermal Velocity, $\mathbf{V}_T$ (cm/s) Based on the Boltzmann distribution for the velocities of the molecules at a specific temperature, the average thermal

Table 2.6: The radial grid used in the microphysical model. There are totally 35 size bins considered ranging between the monomers size (0.735 Å) and ∼2 microns. V_{min} and V_{max} are the range of volumes for each size bin, V_{mid} is the average volume of each bin and R_{mid} the corresponding average radius. Volumes are in units of the initial bin volume, $V_1=4\pi R_1^3/3$, and radii in microns.

Bin	V_{min}	V_{max}	V_{mid}	R_{mid}
1	0.667D+00	0.133D+01	0.100D+01	0.73500D-03
2	0.133D+01	0.267D+01	0.200D+01	0.92604D-03
3	0.267D+01	0.533D+01	0.400D+01	0.11667D-02
4	0.533D+01	0.107D+02	0.800D+01	0.14700D-02
5	0.107D+02	0.213D+02	0.160D+02	0.18521D-02
6	0.213D+02	0.427D+02	0.320D+02	0.23335D-02
7	0.427D+02	0.853D+02	0.640D+02	0.29400D-02
8	0.853D+02	0.171D+03	0.128D+03	0.37042D-02
9	0.171D+03	0.341D+03	0.256D+03	0.46670D-02
10	0.341D+03	0.683D+03	0.512D+03	0.58800D-02
11	0.683D+03	0.137D+04	0.102D+04	0.74083D-02
12	0.137D+04	0.273D+04	0.205D+04	0.93339D-02
13	0.273D+04	0.546D+04	0.410D+04	0.11760D-01
14	0.546D+04	0.109D+05	0.819D+04	0.14817D-01
15	0.109D+05	0.218D+05	0.164D+05	0.18668D-01
16	0.218D+05	0.437D+05	0.328D+05	0.23520D-01
17	0.437D+05	0.874D+05	0.655D+05	0.29633D-01
18	0.874D+05	0.175D+06	0.131D+06	0.37336D-01
19	0.175D+06	0.350D+06	0.262D+06	0.47040D-01
20	0.350D+06	0.699D+06	0.524D+06	0.59267D-01
21	0.699D+06	0.140D+07	0.105D+07	0.74671D-01
22	0.140D+07	0.280D+07	0.210D+07	0.94080D-01
23	0.280D+07	0.559D+07	0.419D+07	0.11853D+00
24	0.559D+07	0.112D+08	0.839D+07	0.14934D+00
25	0.112D+08	0.224D+08	0.168D+08	0.18816D+00
26	0.224D+08	0.447D+08	0.336D+08	0.23707D+00
27	0.447D+08	0.895D+08	0.671D+08	0.29869D+00
28	0.895D+08	0.179D+09	0.134D+09	0.37632D+00
29	0.179D+09	0.358D+09	0.268D+09	0.47413D+00
30	0.358D+09	0.716D+09	0.537D+09	0.59737D+00
31	0.716D+09	0.143D+10	0.107D+10	0.75264D+00
32	0.143D+10	0.286D+10	0.215D+10	0.94827D+00
33	0.286D+10	0.573D+10	0.429D+10	0.11947D+01
34	0.573D+10	0.115D+11	0.859D+10	0.15053D+01
35	0.115D+11	0.229D+11	0.172D+11	0.18965D+01

velocity of the molecules in the medium is given by the expression:

$$V_T = \sqrt{\frac{8RT}{\pi m}} \tag{2.56}$$

where R is the universal gas constant, T the local temperature and m the atmospheric mean molecular weight.

Dynamic Viscosity, η ($\mathbf{gcm^{-1}s^{-1}}$) Viscosity is a measure of a fluid's internal friction. The higher the viscosity the higher the resistance to the flow. In the atmospheric viscosity is calculated from:

$$\eta = \frac{5}{16 N_A d^2}\sqrt{\frac{mRT}{\pi}} \tag{2.57}$$

with N_A the Avogadro number and d the average molecular diameter. The last can be estimated for Titan's atmosphere from:

$$d = \frac{d_{N_2} x_{N_2} + d_{CH_4} x_{CH_4}}{x_{N_2} + x_{CH_4}} \tag{2.58}$$

with x the mole fraction of each species. The values of the individual molecular diameters are taken from Allen (1976) ($d_{N_2} = 3.282\mathring{A}$, $d_{CH_4} = 3.5\mathring{A}$). A parameter related to viscosity is the kinematic viscosity, ν ($\mathrm{cm^2/s}$):

$$\nu = \frac{\eta}{\rho} \tag{2.59}$$

with ρ ($\mathrm{g/cm^3}$) the atmospheric mass density. Note that the units of ν are the same as for the molecular diffusion coefficient, so that the kinematic viscosity is an average molecular diffusion coefficient for the atmosphere.

Atmospheric Mean Free Path, λ (cm) This parameter expresses the average distance a molecule can move before colliding with another molecule. It can be calculated through:

$$\lambda = \frac{2\eta}{\rho V_T} = \frac{2\nu}{V_T} \tag{2.60}$$

The last three parameters along with the atmospheric scale height for Titan's atmosphere are presented in Fig. 2.14.

Knudsen, Reynolds & Schmidt Numbers These dimensionless parameters are defined as:

$$Kn = \frac{\lambda}{r},\ Re = \frac{2 r v_s}{\nu},\ Sc = \frac{\nu}{D} \tag{2.61}$$

where v_s is the particle's settling speed and D the diffusion coefficient defined below. The first parameter, provides an estimate of the relative importance of different processes impacting on a particle's flow. For small values ($<< 1$), the size of the particle is very big compared to the mean free path of the molecules, hence the particles' environment is a continues fluid (continuum regime). For

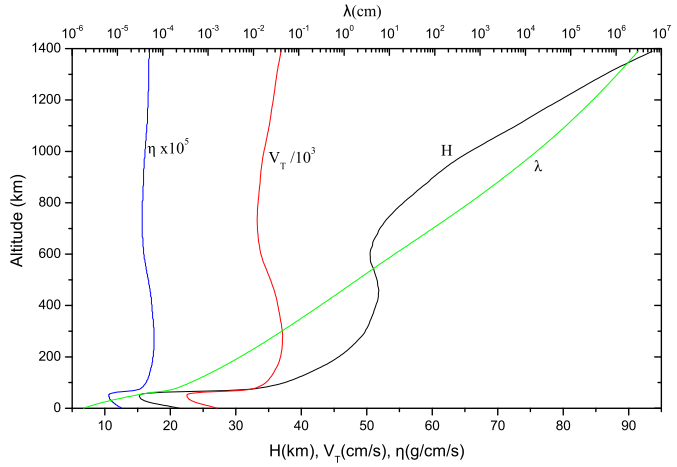

Figure 2.14: The vertical variation of thermal speed, dynamic viscosity and scale height (bottom scale) along with the atmospheric mean free path (top scale) for Titan's atmospheric conditions.

large values (> 10) the size of the particle is smaller than the mean free path of the atmospheric molecules and its motion is controlled by statistical laws of random collisions between particles and the atmospheric molecules (free-molecular regime, slip flow). Between the two limiting cases there is a transition regime. The Reynolds number provides another parameter for defining the type of flow the particles are experiencing. It provides an estimate for the importance of inertial forces (in this case the gravitational settling) acting on a particle relative to the force due to the viscosity of the medium. For $Kn < 1$ and $0.01 < Re < 1$ the Navier-Stokes equation can be analytically solved. This is the case of the Stokes flow. For larger Reynolds numbers the flow approaches the continuum regime while for smaller values the Stokes flow approaches the slip flow. Similarly to the Reynolds number, the Schmidt number is a measure of the importance of the viscous forces relative to the diffusive forces acting on the particle.

Particle Settling Speed, $\mathbf{V}_s$ (cm/s) The settling speed of a particle with radius r due to the gravitational acceleration can be calculated from:

$$V_s = \frac{2\rho_p g r^2}{9\eta} \tag{2.62}$$

where ρ_p is the mass density of the particle and g is the gravity acceleration. This formula results by equating the drag force on the particle by the medium under Stokes flow conditions, to the gravity force. In order to correct this expression as the flow approaches the slip limit, a multiplication correction factor has been

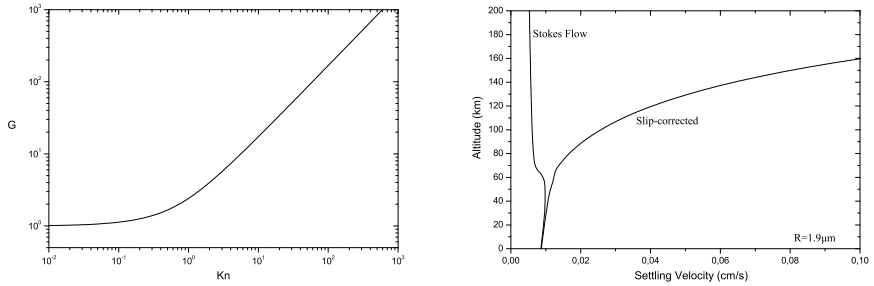

Figure 2.15: The effect of the slip correction introduced with the Cunningham-Millikan expression. The left panel presents the variation of the G factor with the Knudsen number while the right panel the effect of the slip correction on the settling speed of a 1.9μm radius particle in Titan's atmosphere. The sharp variation of the Stokes velocity above 50 km is due to the rapid increase in Titan's atmospheric temperature observed at this region.

introduced by Cunningham (1910):

$$G_r = 1 + Kn\left[A + Be^{-C/Kn}\right]. \tag{2.63}$$

This is known as the Cunningham-Millikan slip flow correction. The three parameter can be deduced from experiments (A=1.257, B=0.4 and C=1.1 as reported by Davies (1945)). When the flow is characteristic of Stokes conditions, the Knudsen number is very small and therefore $G_r = 1$. As Kn increases and the flow attains a slip character, G_r also increases as expected since the particle's resistance to motion decreases (Fig. 2.15).

Diffusion Coefficient, $\mathbf{D}_r$ ($\mathbf{cm^2/s}$) The diffusion coefficient for a particle under Stokes flow conditions is described by:

$$D_r = \frac{k_B T}{6\pi r_i \eta} \tag{2.64}$$

where k_B is the Boltzmann's constant. As for the case of the settling speed, the correction for the slip flow has to be included with a multiplication by G_r. The diffusion coefficients of different size particles in Titan's atmosphere are presented in Fig.2.16 along with their corresponding settling velocities.

2.4.3 Coagulation kernels

The most important contribution in the coagulation comes from the Brownian kernel which describes the random collisions among particles. The last, considering the coagulating particles to have a spherical shape, can be described in terms of their radii r and s:

$$K_B(r,s) = 4\pi(D_r + D_s)(r+s)\beta \tag{2.65}$$

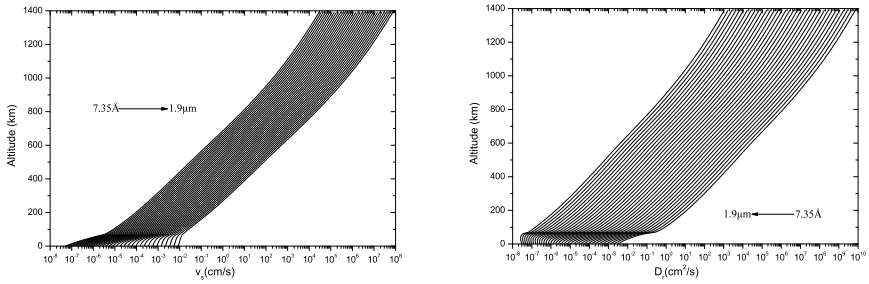

Figure 2.16: Upper panel: Settling speeds for different size particles in Titan's atmosphere. The arrow presents the direction of radial increase from the minimum (7.35Å) to maximum (1.9μm) sizes presented. Lower panel: The same for the diffusion coefficient.

The term β:

$$\beta^{-1} = \frac{r+s}{r+s+\sqrt{\delta_r^2+\delta_s^2}} + \frac{4(D_r+D_s)}{(r+s)\sqrt{\bar{V}_r^2+\bar{V}_s^2}} \tag{2.66}$$

with

$$\delta_r = \frac{(2r+\lambda_r)-(4r^2+\lambda_r^2)^{3/2}}{6r\lambda_r} - 2r \tag{2.67}$$

is an interpolation formula (Fuchs, 1964) that connects the continuum regime (where $\beta = 1$) with the free-molecular regime where the Brownian kernel is given by:

$$K_B(r,s) = \pi(r+s)^2\sqrt{\bar{V}_r^2+\bar{V}_s^2} \tag{2.68}$$

In the above, $\bar{V}_r$ is the particle's thermal velocity and λ_r is the particle's mean free path. These two parameters can be calculated from:

$$\bar{V}_r = \sqrt{\frac{8k_BT}{\pi\bar{M}_r}},\ \lambda_r = \frac{8D_r}{\pi\bar{V}_r} \tag{2.69}$$

An enhancement to the Brownian kernel comes from the increased diffusion produced by eddies created in the wake of large falling particles. The effect of the process can be described in terms of the Reynolds, Re, and Schmidt, Sc, particle numbers. The convective Brownian diffusion enhancement kernel can be parameterized as:

$$K_D(r,s) = \begin{cases} K_B(r,s)0.45Re_s^{1/3}Sc_r^{1/3} & Re_s \le 1,\ s \ge r \\ K_B(r,s)0.45Re_s^{1/3}Sc_r^{1/2} & Re_s > 1,\ s \ge r \end{cases} \tag{2.70}$$

Another contribution in the total coagulation kernel comes from the varying settling velocities among different size particles. This is the gravitational coagulation and it can be described in terms of the relative settling velocities among particles (Pruppacher & Klett, 1978):

$$K_G(r,s) = E(r,s)\pi(r+s)^2|V_s(r) - V_s(s)| \tag{2.71}$$

with E the collision efficiency between particles. The last can be parameterized as (Jacobson, 2005):

$$E(r,s) = \frac{60E_V(r,s) + E_A(r,s)Re_s}{60 + Re_s}, \quad s \geq r \tag{2.72}$$

with

$$E_V(r,s) = \begin{cases} \left[1 + \frac{0.75ln(2St(r,s))}{St(r,s)-1.214}\right]^{-2} & St(r,s) > 1.214 \\ 0 & St(r,s) \leq 1.214 \end{cases} \tag{2.73}$$

and

$$E_A(r,s) = \frac{St^2(r,s)}{(St(r,s)+0.5)^2} \tag{2.74}$$

where

$$St(r,s) = \frac{V_s(r)|V_s(s) - V_s(r)|}{sg}, \quad s \geq r \tag{2.75}$$

The total coagulation kernel is then given by:

$$K(r,s) = \alpha_c \left[K_B(r,s) + K_D(r,s) + K_G(r,s)\right] \tag{2.76}$$

with α_c the coalescence efficiency which describes the probability that two colliding particles will remain stuck to each other after the collision. In the calculations, α_c, was restrained only by the electrostatic repulsion between the particles, which are described by (Toon et al., 1980):

$$\alpha_c(r,s) = e^{-\tau} \tag{2.77}$$

with

$$\tau(r,s) = \frac{(r\chi e)(s\chi e)}{(r+s)k_B T} \tag{2.78}$$

In the above, χ, is the particles charging rate (number of electrons per radius) which is considered to be constant with altitude and e is the unit charge. When the particles are small their total charge and hence their electrostatic repulsion is small, hence the affect in the coagulation rate, minimal. As the size increases, the electrostatic forces between the particles become stronger and the sticking efficiency drops rapidly to very small values. Fig.2.17 presents the coagulation kernel between different size particles with and without the inclusion of the charging effect. Without the electrostatic repulsion the coagulation kernel approaches large values for different size particles and small values for similar size ones. With the inclusion of the charging effect, the coagulation rate is reduced as particles become big.

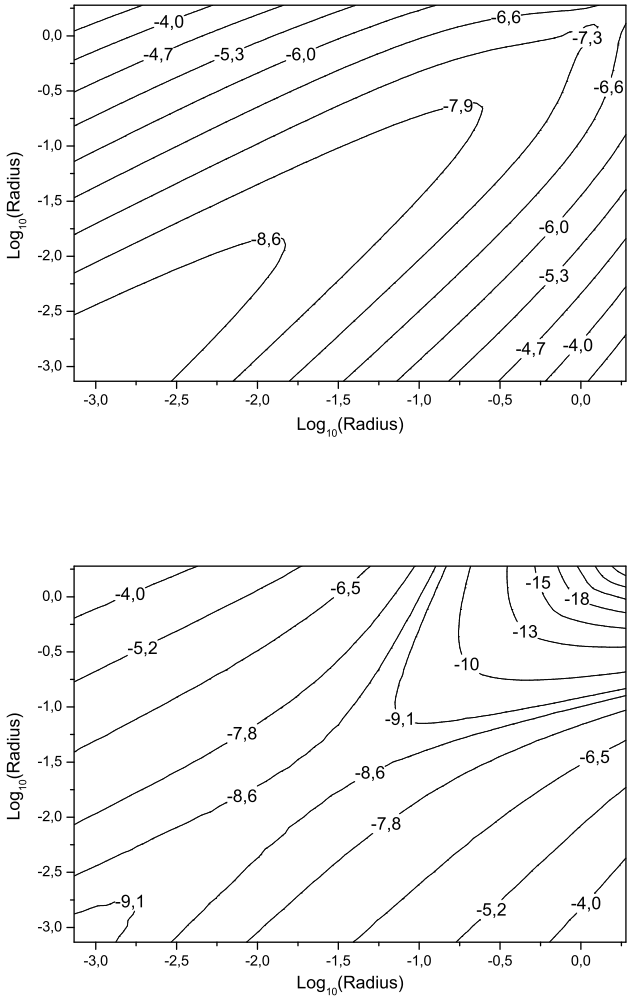

Figure 2.17: Variation of sticking efficiency between particles due to their mutual electrostatic repulsion. The charging rate is set at 30 e^-/μm. Size values are in microns.

2.4.4 Method of solution

The flux of particles with volume v, comprises two terms, one originating from the settling of the particles in the atmosphere and the other describing the mixing of the particles due to eddy:

$$\Phi(v) = -n(v)V_S(v) - Kn(v)\frac{\partial f_v}{\partial z} \tag{2.79}$$

where K is the eddy diffusion coefficient, V_S the settling speed of particles of volume v and f_v the volume mixing ratio of the particles with volume v. The particles for each size bin are considered as another species of the photochemical model that is described by equation(2.18) but with modified parameters for expressions (2.20):

$$\begin{aligned} C_1'(p,T) &= \tfrac{D}{k_B T} V_S(v) \\ C_2'(p,T) &= K \tfrac{p^2}{k_B T H} \end{aligned} \tag{2.80}$$

and the production and loss rates which are defined by the coagulation rate multiplied by the volume fraction for each colliding pair of particles.

Bibliography

Ackermann, L., Hippler, H., Pagsberg, P., Reihs, C., Troe, J., 1990. Pulse radiolysis, flash photolysis, and shock wave study of the recombination H + benzyl → toluene at 300 and 1300-1650 K. J. Phys. Chem. 94, 5247-5251.

Adam, L., Hack, W., Zhu, H., Qu, Z.-W., Schinke, R., 2005. Experiment and theoretical investigation of the reaction $NH(X^3\Sigma^-) + H(^2S) \rightarrow N(^4S) + H_2(X^1\Sigma_g^+)$. J. Chem. Phys. 122, 114301-114307.

Adachi, H., Basco, N., James, D.G.L., 1980. Mutual interaction of the methyl and methylperoxy radicals studied by flash photolysis and kinetic spectroscopy. Int. J. Chem. Kinet. 12, 949-977.

Ahmed, M., Peterka, D.S., Suits, A.G., 1999. The photodissociation of the vinyl radical (C_2H_3) at 243 nm studied by velocity map imaging. J. Chem. Phys. 110, 4248-4253.

Aleksandrov, E. N., Arutyunov, V.S., Dubrovina, I.V., Kozlov, S.N., 1980. Study of the reaction of atomic hydrogen with allene. Kinet. Catal. 21, 1323-1326.

Aleksandrov, E. N., Vedeneev, V.I., Kozlov, S. N., Obvivalneva, A.A., Pryakhin, G.A., 1990. Rate constants and mechanism of the reactions of $N(^4S)$ atoms with methane and ethane. Bull. Acad. Sci. URSS, Div. Chem. Sci. 39, 625.

Aleksandrov, E.N., Basevich, V.Y., Vedeneev, V.I., 1994. Initial act of nitrogen atoms interaction with H_2 in gas phase. Khim. Fiz. 13, 90-93.

Allen C.W., 1976. Astrophysical Quantities. The Athlone Press, University of London.

Arrington, C.A., Ramos, C., Robinson, A.D., Zwier, T.S., 1998. Aromatic ring-forming reactions of metastable diacetylene with 1,3-Butadiene. J. Phys. Chem. A 102, 3315-3322.

Atakan, B., Wolfrum, J., 1992. Kinetic studies of the reactions of CN radicals with alkanes in the temperature range between 294 and 1260 K. Chem. Phys. Lett. 186, 547-552.

Atkinson, D. B., Hudgens, J. W., 1999. Rate coefficients for the propargyl radical self-reaction and oxygen addition reaction measured using ultraviolet cavity ring-down spectroscopy. J. Phys. Chem. 103, 4242-4252.

Au, J.W., Cooper, G., Burton, G.R., Olney, T.N., Brion, C.E., 1993. The valence shell photoabsorption of the linear alkanes, C_nH_{2n+2} (n=1,8): Absolute oscillator strengths (7-220 ev). Chem. Phys. 173, 209-239.

Ausloss, P., Gorden, R.Jr., Lias, S.G., 1964. Effect of pressure in the radiolysis and photolysis of methane. J. Chem. Phys. 40, 1854-1860.

Back, R.A., Winkler, C.A., 1954. The reaction of active nitrogen with butanes. Can. J. Chem 32.

Backx, C., Wight, G.R., Van der Wiel, M.J., 1976. Oscillator strengths (10 - 70eV) for absorption, ionization and dissociation in H_2, HD and D_2, obtained by an electron-ion coincidence method. J. Phys. B: Atom. Mol. Phys. 9, 315-331.

Balucani, N., Asvany, O., Chang, A.H.H., Lin, S.H., Lee, Y.T., Kaiser, R.I., Bettinger, H.F., Schleyer, P.v.R., Schaefer H.F., 1999. Crossed beam reaction of cyano radicals with hydrocarbon molecules. I. Chemical dynamics of cyanobenzene (C_6H_5CN; X^1A_1) and perdeutero cyanobenzene (C_6D_5CN; X^1A_1) formation from reaction of CN ($X^2\Sigma^+$) with benzene C_6H_6 (X^1A_{1g}) and d_6-benzene C_6D_6 (X^1A_{1g}). J. Chem. Phys. 111, 7457-7471.

Balucani, N., Cartechini, L., Alagia, M., Casavecchia, P., Volpi, G. G., 2000. Observation of nitrogen-bearing organic molecules from reactions of nitrogen atoms with hydrocarbons: A crossed beam study of N(^{2}D) + ethylene. J. Phys. Chem. 104, 5655-5659.

Balucani, N., Mebel, A.M., Lee, Y.T., Kaiser, R.I., 2001. A combined crossed molecular beam and *ab initio* study of the reactions $C_2(X^1\Sigma_g^+,a^3\Pi_u)$ + C_2H_4 → *n*-$C_4H_3(X^2A')$ + H($^2S_{1/2}$)., J. Phys. Chem. A 105, 9813-9818.

Banks, P.M., Kockarts, G., 1973. Aeronomy, Academic Press.

Baulch, D. L., Cobbs, C. J., Cox, R.A., Esser, C., Frank, P., Just, Th., Kerr, J.A., Pilling, M.J., Troe, J., Walker, R.W., Warnatz, J., 1992. Evaluated kinetic data for combustion modeling. J. Phys. Chem. Ref. Data 21, 411-734.

Baulch, D. L., Cobbs, C.J., Cox, R.A., Esser, C., Frank, P., Just, Th., Kerr, J.A., Pilling, M.J., Troe, J., Walker, R.W., Warnatz, J., 1994. Evaluated kinetic data for combustion modeling. Supplement I. J. Phys. Chem. Ref. Data 23, 847-1033.

Bénilan Y., Andrieux, D., Khlifi, M., Bruston, P., Raulin, F., Guillemin, J.-C., Cossart-Magos, C., 1996. Temperature dependence of HC_3N, C_6H_2, and C_4N_2 mid-UV absorption coefficients: Application to the interpretation of Titan's atmospheric spectra. Astrophys. Space Sci., 236, 85-95.

Bénilan Y., Smith, N., Jolly, A., Raulin, F., 2000. The long wavelength range temperature variations of the mid-UV acetylene absorption coefficient. Planet. Space Sci. 48, 463-471.

Bergmann, K., Demtröder, W., 1968. Mass-spectrometric investigation of the primary processes in the photodissociation of 1,3-butadiene. J. Chem. Phys. 48, 18-22.

Bézard, B., Feuchtgruber, H., Moses, J.I., Encrenaz, T., 1998. Detection of methyl radicals (CH_3) on Saturn. Astron. Astrophys. 334, L41-L43.

Bézard, Romani, P.N., Feuchtgruber, H., Encrenaz, T., 1999. Detection of methyl radicals on Neptune. Astrophys. J. 515, 868 - 872.

Blitz M.A., Beasley, M.S., Pilling, M.J., Robertson, S.H., 2000. Formation of the propargyl radical in the reaction of $^1CH_2$ and C_2H_2: experiment and modelling. Phys. Chem. Chem. Phys., 2, 805-812.

Bocherel, P., Herbert, L.B., Rowe, B.R., Sims, I.R., Smith, I.W.M., Travers, D., 1996. Ultralow-temperature kinetics of CH(X2II) reactions: rate coefficients for reactions with O_2 and NO (T = 13-708 K), and with NH_3 (T = 23-295 K). J. Phys. Chem. 100, 3063-3069.

Böhland, T., Temps, F., Wagner, H.Gg., 1985a. The contributions of intersystem crossing and reaction in the removal of $CH_2(\tilde{a}\ ^1A_1)$ by hydrocarbons studied with the LMR. Ber. Bunsenges. Phys. Chem. 89, 1013-1018.

Böhland, T., Temps, F., Wagner, H.Gg., 1985b. Kinetics of the reactions between $CH_2(X\ ^3B_1)$ radicals and saturated hydrocarbons in the temperature range 296-707 K. Ber. Bunsenges. Phys. Chem. 89, 1110.

Böland, T., Temps F., Wagner, H.Gg., 1988. Kinetics of the reactions of CH2 (X 3B1)-radicals with C_2H_2 and C_4H_2 in the temperature range 296 K < T < 700 K. Symp. Int. Combust. Proc. 21, 841-850.

Braun,W., McNesby, J.R., Bass, A.N., 1967. Flash photolysis of methane in the vacuum ultraviolet. II. Absolute rate constants for reactions of CH with methane, hydrogen and nitrogen. J. Chem. Phys. 46, 2071-2080.

Brown R.L. (1973). A measurement of the rate of the reaction N + H + M → NH + M. Int. J. Chem. Kinet. 5, 663-668.

Brownsword, R. A., Gatenby, S.D., Herbert, L.B., Smith, I.W.M., Stewart, D.W.A., Symonds, A.C., 1996. Kinetics of reactions between neutral free radicals. Rate constants for the reaction of CH radicals with N atoms between 216 and 584 K. J. Chem. Soc. Faraday Trans. 92, 723-727.

Brownsword, R. A., Canosa, A., Rowe, B.R., Sims, I.R., Smith, I.W.M., Stewart, D.W.A., Symonds, A.C., Travers, D., 1997a. Kinetics over a wide range of temperature (13-744 K): Rate constants for the reactions of CH(n = 0) with H_2 and D_2 and for the removal of CH(n = 1) by H_2 and D_2. J. Chem. Phys. 106, 7662-7677.

Brownsword, R.A., Hillenkamp, M., Laurent, T., Vatsa, R.K., Volpp, H.R. and Wolfrum, J., 1997b. Quantum yield for H atom formation in the methane dissociation after photoexcitation at the Lyman α (121.6 nm) wavelength. Chem. Phys. Lett. 266, 259-266.

Burton, G.R., Chan, W.F., Cooper, G., Brion, C.E., 1993. The electronic absorption spectrum of NH_3 in the valence shell discrete and continuum regions. Absolute oscillator-strengths for photoabsorption (5-200 eV). Chem. Phys. 177, 217-231.

Butler, J.E, Fleming, J.W., Goss, L.P., Lin, M.C., 1981. Kinetics of CH radical reactions with selected molecules at room temperature. Chem. Phys. 56, 355-365.

Butterfield, M. T., Yu, T., Lin, M.C., 1993. Kinetics of CN reactions with allene, butadiene, propylene and acrylonitrile. Chem. Phys. 169, 129-134.

Canosa, A., Sims, I.R., Travers, D., Smith, I.W.M., Rowe, B.R., 1997. Reactions of the methylidiyne radical with CH_4, C_2H_2, C_2H_4, C_2H_6, and but-1-ene studied between 23 and 295 K with a CRESU apparatus. Astron. Astrophys. 323, 644-651.

Capone, L.A., Dubach, J., Prasad, S.S., Whitten, R.C., 1983. Galactic cosmic rays and N_2 dissociation on Titan. Icarus 55, 73-82.

Carty, D., LePage, V., Sims, I.R., Smith, I.W.M., 2001. Low temperature rate coefficients for the reactions of CN and C_2H radicals with allene (CH_2=C=CH_2) and methylacetylene (CH_3C=CH). Chem. Phys. Lett. 344, 310•316.

Chan W.F., Cooper, G., Sodhi, R.N.S., Brion, C.E., 1993. Absolute optical oscillator strengths for discrete and continuum photoabsorption of molecular nitrogen (11-200 eV). Chem. Phys. 170, 81-97.

Chang, Y.W., Wang, N.S., 1994. Rates of the reactions CN + H_2CO and NCO + H_2CO in the temperature range 294 - 769 K. Chem. Phys. 200, 431-437.

Chang, A.H.H., Mebel, A.M., Yang, X.M., Lin, S.H., Lee, Y.T., 1998. Ab initio/RRKM approach toward the understanding of ethylene photodissociation. J. Chem. Phys. 109, 2748-2761.

Chastaing, D., James, P.L., Sims, I.R., Smith, I.W.M., 1998. Neutral-neutral reactions at the temperatures of interstellar clouds. Rate coefficients for reactions of C_2H radicals with O_2, C_2H_2, C_2H_4 and C_3H_6 down to 15 K. Faraday Disc. 109, 165-181.

Chastaing D., Le Picard, S.D., Sims, I.R., Smith, I.W.M., 2001. Rate coefficients for the reactions of $C(^3P_J)$ atoms with C_2H_2, C_2H_4, CH_3C_2H and CH_2CCH_2 at temperatures down to 15 K. A&A 365, 241-247.

Chen F.Z., Wu, C.Y.R, 2004. Temperature-dependent photoabsorption cross sections in the VUV-UV region. I. Methane and ethane. J. Quant. Spectrosc. Radiat. Transfer, 85, 195-209.

Chen, F.Z., Judge, D.L., Wu, C.Y.R., Caldwell, J., 1999. Low and room temperature photoabsorption cross sections of NH_3 in the UV region. Planet. Space Sci. 47, 261-266.

Chen, F.Z., Judge, D.L., Wu, C.Y.R., 2000. Temperature dependent photoabsorption cross sections of allene and methylacetylene in the VUV-UV region. Chem. Phys. 260, 215-223.

Clarke, D.W., Ferris, J.P., 1995. Photodissociation of cyanoacetylene: Application to the atmospheric chemistry of Titan. Icarus 115, 119-125.

Clyne, M.A.A., Stedman, D.H., 1967. Rate of recombination of nitrogen atoms. J. Phys. Chem. 71, 3071-3073

Cody R.J., Romani, P.N., Nesbitt, F.L., Iannone, M.A., Tardy, D.C., Stief, L.J., 2003. Rate constant for the reaction $CH_3 + CH_3 \rightarrow C_2H_6$ at T = 155 K and model calculation of the CH_3 abundance in the atmospheres of Saturn and Neptune. J. Geophys. Res. 108,doi:10.1029/2002JE002037.

Collin G.J., 1988. Photochemistry of simple olefines: Chemistry of electronically excited states or hot ground state? Adv. Photochem. 14, 135-176.

Connors, R.E., Roebber, J.L., Weiss, K., 1974. Vacuum ultraviolet spectroscopy of cyanogen and cyanoacetylenes. J. Chem. Phys. 60, 5011-5024.

Cooper, G., Burton, G.R., Brion, C. E., 1995a. Absolute UV and soft X-ray photoabsorption of acetylene by high resolution dipole (e,e) spectroscopy. J. Electron Spectrosc. 73, 139-148.

Cooper G., Olney, T.N., Brion, C.E., 1995b. Absolute UV and soft X-ray photoabsorption of ethylene by high resolution dipole (e,e) spectroscopy. Chem. Phy. 194, 175-184.

Courtin, R., Wagener, R., McKay, C.P., Caldwell, J., Fricke, K.-H., Raulin, F., Bruston, P., 1991. UV spectroscopy of Titan's atmosphere, planetary organic chemistry and prebiological synthesis II. Interpretation of new IUE observations in the 220•335 nm range. Icarus 90, 43-•56.

Coustenis, A., Bézard, B., Gautier, D., Marten, A., Samuelson, R., 1991. Titan's Atmosphere from Voyager Infrared Observations. III. The vertical distributions of hydrocarbons and nitriles near Titan's north pole. Icarus 89, 152-167.

Cunningham, E., 1910. Proc. Roy. Soc., London A83, 357.

Davies, C.N., 1945. Proc. Phys. Soc., London 57, 259.

Derecskei-Kovacs, A., North, S.W., 1999. The unimolecular dissociation of vinylcyanide: A theoretical investigation of a complex multichannel reaction. J. Chem. Phys. 110, 2862•-2871.

Diau, E.W., Lin, M.C., 1994. A theoretical study of the $CH_3 + C_2H_2$ reaction. J. Chem. Phys. 101, 3923-3927.

Dobe, S., Oehlers, C., Temps, F., Wagner, H.Gg., Ziemer, H., 1994. Observations of an H/D-isotope exchange channel in the reaction D + H_2CO. Ber. Bunsenges. Phys. Chem. 98, 754-757.

Dransfeld, P., Wagner, H.Gg., 1987. Investigation of the gas phase reaction N + NH_2 → N_2 + 2 H at room temperature. Z. Phys. Chem. (Munich) 153.

Duràn, R.P., Amorebieta, V.T., Colussi, A.J., 1988. Is the homogeneous thermal dimerization of acetylene a free-radical chain reaction? Kinetic and thermochemical analysis. J. Phys. Chem. 92, 636-640.

Eden S., Limão-Vieira, P., Kendall, P., Mason, N.J., Hoffmann, S.V., Spyrou, S.M., 2003. High resolution photo-absorption studies of acrylonitrile, C_2H_3CN, and acetonitrile, CH_3CN. Eur. Phys. J. D 26, 201-210.

Eshleman, V.R., Lindal, G.F., Tyler, G.L., 1983. Is Titan wet or dry?. Science 22, 53-55.

Fagerstrom, K., Jodkowski, J.T., Lund, A., Ratajczak, E., 1995. Kinetics of the self-reaction and the reaction with OH of the amidogen radical. Chem. Phys. Lett. 236, 103-110.

Fahr, A., 2003. Ultraviolet absorption spectrum and cross-sections of ethynyl (C_2H) radicals, J. Molec. Spectr. 217, 249-254.

Fahr, A., Nayak, A.K., 1994. Temperature dependent ultraviolet absorption cross sections of 1,3-butadiene and butadiyne. Chem. Phys. 189, 725-731.

Fahr, A., Nayak, A., 1996. Temperature dependent ultraviolet absorption cross section of propylene, methylacetylene and vinylacetylene. Chem. Phys. 203, 351-358.

Fahr, A., Stein, S.E., 1989. Reactions of vinyl and phenyl radicals with ethyne, ethene, and benzene. In 22nd International Symposium on Combustion, p. 1023. The Combustion Institute, Pittsburgh.

Fahr, A., Laufer, A., Klein, R., Braun, W., 1991. Reaction rate determinations of vinyl radical reactions with vinyl, methyl, and hydrogen atoms. J. Phys. Chem. 95, 3218-3224.

Fahr, A., Hassanzadeh, P., Laszlo, B., Huie, R.E., 1997. Ultraviolet absorption and cross sections of propargyl (C_3H_3) radicals in the 230-300 nm region. Chem. Phys. 215, 59-66.

Fahr, A., Hassanzadeh, P., Atkinson, D.B., 1998. Ultraviolet absorption spectrum and cross-sections of vinyl (C_2H_3) radical in the 225-238 nm region. Chem. Phys. 236, 43-51.

Fennelly J.A., Torr, D.G., 1992. Photoionization and photoabsorption cross sections of O, N_2, O_2, and N for aeronomic calculations. Atom. D. Nucl. D. Tables 51, 321-363.

Flasar, F.M., and 44 co-authors, 2005. Titan's atmospheric temperatures, winds, and composition. Science 308, 975•978.

Frederick, J.E., Rusch, D.W., 1977. On the chemistry of metastable atomic nitrogen in the F region deducted from simultaneous satellite measurements of the 5200 Åairglow and atmospheric composition. J.Geophys. Res. 82, 3509-3517.

Fröhlich, C. 2006. Solar irradiance variability since 1978. Space Science Reviews, DOI: 10.1007/s11214-006-9046-5.

Fuchs, N.A., 1964. The mechanics of aerosols (translated by R.E. Daisley and M. Fuchs). New York, Pergamon Press.

Fulcignoni, M. and 42 coworkers (2005). In situ measurements of the physical characteristics of Titan's environment. Nature, doi:10.1038/nature04314.

Fulle D., Hippler, H., 1996. The high-pressure range of the reaction of CH($^2\Pi$) with N_2. J. Chem. Phys. 105, 5423-5430.

Fulle, D., Hippler, H., 1997. The temperature and pressure dependence of the reactions CH + H_2 ⇔ CH_3 ⇔ CH_2 + H. J. Chem. Phys. 106, 8691-8698.

Gardner, E.P., McNesby, J.R., 1982. Vacuum-Ultraviolet photolysis of methylamine. J. Phys. Chem 86, 2646-2651.

Garland, L.J., Bayes, K.D., 1990. Rate constants for some radical-radical cross sections and the geometric rule. J. Phys. Chem. 94, 4941-4945.

Garrett, B.C., Koszykowski, M.L., Melius, C.F., Page, M., 1990. Theoretical calculations of the thermal rate constants for the gas-phase chemical reactions H + NH_3 → H_2 + NH_2 and D + ND_3 → D_2 + ND_2. J. Phys. Chem. 94, 7096-7106.

Ge, S.-H., Cheng, X.-L., Yang, X.-D., Liu, Z.-J., Wang, W., 2006. Calculations of the thermochemistry of six reactions leading to ammonia formation in Titan's atmosphere. Icarus 183, 153-158.

von Gehring, M., Hoyermann, K., Wagner, H.Gg., Wolfrum, J., 1971. Die reaktion von atomaren wasserstoff mit hydrazin. Ber. Bunsenges. Phys. Chem. 75.

Gladstone, G. R., Allen, M., Yung, Y.L., 1996. Hydrocarbon photochemistry in the upper atmosphere of Jupiter. Icarus 119, 1-52.

Glicker, S., Okabe, H., 1987. Photochemistry of diacetylene. J. Phys. Chem. 91, 437-440.

Guadagnini, R., Schatz, G.C., Walch, S.P., 1998. Ab initio and RRKM studies of the reactions of C, CH, and $^1CH_2$ with acetylene. J. Phys. Chem. 102, 5857-5866.

Gueymard, C.A., 2004. The sun's total and spectral irradiance for solar energy applications and solar radiation models. Solar Energy 76, 423-453.

Hack, W., Wagner, H.Gg., Zaspypkin, A., 1994. Elementary reactions of NH($a^1\Delta$) and NH($X\ ^3\Sigma$) with N, O and NO. Bunsenges. Phys. Chem. 98, 156-164.

Haider, N., Husain, D., 1993. Absolute rate data for the reactions of ground-state atomic carbon, C[2p2(3PJ)], with alkenes investigated by time-resolved atomic resonance absorption spectroscopy in the vacuum ultraviolet. J. Chem. Soc. Faraday Trans. 89, 7-14.

Halberstadt, M. L., Crump, J., 1973. Insertion of methylene into the carbonhydrogen bonds of the C_1 to C_4 alkanes. J. Photochem. 1, 295.

Halpern, J.B., Miller, G.E., Okabe, H., 1989. The reaction of CN radicals with cyanoacetylene. Chem. Phys. Lett. 155, 347•350.

Hampson, R.F., McNesby, J.R., 1965. Vacuum-ultraviolet photolysis of ethane at high temperature. J. Chem. Phys. 42, 2200-2208.

Hanning-Lee, M.A., Pilling, M.J., 1992. Kinetics of the reaction between H atoms and allyl radicals. Int. J. Chem. Kinet. 24, 271-278.

Harding, L.B., Georgievskii, Y., Klippenstein, S.J., 2005. Predictive theory for hydrogen atom - hydrocarbon radical association kinetics. J. Phys. Chem. A. 109, 4646-4656.

Harding, L.B., Guadagnini, R., Schatz, G.C., 1993. Theoretical studies of the reactions H + CH → C + H_2 and C + H_2 → CH_2 using an ab initio global ground-state potential surface for CH_2. J. Phys. Chem. 97, 5472-5481.

Hartmann, J-M., Boulet, C., Brodbeck, C., van Thanh, N., Fouchet, T., Drossart, P., 2002. A far wing lineshape for H_2 broadened CH_4 infrared transitions. JQSRT 72, 117-122.

Heck, A.J.R., Zare, R.N., Chandler, D.W., 1996. Photofragment imaging of methane. J. Chem. Phys. 104, 4019-4030.

Heckmann, E., Hippler, H., Troe, J., 1996. High-temperature reactions and thermodynamic properties of phenyl radicals. Symp. Int. Combust. Proc. 26, 543-550.

Herron, J.T., 1999. Evaluated Chemical Kinetics Data for Reactions of $N(^2D)$, $N(^2P)$, and $N_2(A\ ^3\Sigma_u^+)$ in the Gas Phase. J. Phys. Chem. Ref. Data 28, 1453-1483.

Hess, W. P., Durant, J.L. Jr., Tully, F.P., 1989. Kinetic study of the reactions of CN with ethane and propane. J. Phys. Chem. 93, 6402-6407.

Ho, G.H., Lin, M.S., Wang, Y.L., Chang, T.W., 1998. Photoabsorption and photoionization of propyne. J. Chem. Phys. 109, 5868-5879.

Holland, D.M.P., Shaw, D.A., Hayes, M.A., Shpinkova, L.G., Rennie, E.E., Karlsson, L., Baltzer, P., Wannberg, B., 1997. A photoabsorption, photodissociation and photoelectron spectroscopy study of C_2H_4 and C_2D_4. Chem. Phys. 219, 91-116.

Hoobler, R.J., Leone, S.R., 1997. Rate coefficients for reactions of ethynyl radical (C_2H) with HCN and CH_3CN: Implications for the formation of complex nitriles on Titan. J. Geophys. Res. 102, 28717-28723.

Hoobler, R.J., Opansky, B.J., Leone, S.R., 1997. Low-temperature rate coefficients for the reactions of ethynyl radical (C_2H) with propane, isobutane, n-Butane, and neopentane. J. Phys. Chem. A 101, 1338-1342.

Hoobler, R. J., and S. R. Leone, 1999. Low temperature rate coefficients for reactions of the ethynyl radical (C_2H) with C_3H_4 isomers methylacetylene and allene. J. Phys. Chem. 103, 1342-1346.

Horne, D.G., Norrish, R.G.W., 1970. The photolysis of acyclic azines and the electronic spectra of R_1R_2CN radicals, Proc. R. Soc. London A 315.

Huang, L.C.L., Lee, Y.T., Kaiser, R.I., 1999. Crossed beam reaction of the cyanogen radical, $CN(X^2\Sigma^+)$, with acetylene, $C_2H_2(X^1\Sigma_g^+)$: Observation of cyanoacetylene, $HCCCN(X^1\Sigma^+)$. J. Chem. Phys. 110, 7119•7122.

Huang, C.S., Zhu, Z.Q., Xin, Y., Pei, L.S., Chen, C.X., Chen, Y., 2004. Kinetics of $C_2(a^3\Pi_u)$ radical reactions with alkanes by LIF. J. Chem. Phys. 120, 2225-2229.

Hubin-Franskin, M.-J., Delwiche, J., Giuliani, A., Ska, M.-P., Motte-Tollet, F., Walker, I.C., Mason, N.J., Gingell, J.M., Jones, N.C., 2002. Electronic excitation and optical cross sections of methylamine and ethylamine in the UV-VUV spectral region. J. Chem. Phys. 116, 9261-9268.

Hudson, R.D., 1971. Critical review of ultraviolet photoabsorption cross sections for molecules of astrophysical and aeronomic interest. Rev. Geophys. Space Phys. 9, 305-406.

Husain, D., Kirsch, L.J., 1971. Reactions of atomic carbon by kinetic absorption spectroscopy in the vacuum ultraviolet. Trans. Faraday Soc. 67, 2025.

Husain, D., Ioannou, A.X., 1997. Reactions of atomic carbon, C[2p2(3PJ)], with dienes and diynes investigated by time-resolved atomic resonance absorption spectroscopy in the vacuum ultraviolet. J. Chem. Soc. FaradayTrans. 93, 3625-3629.

Husain, D., Young, A.N., 1975. Kinetic investigation of ground-state carbon atoms. J. Chem. Soc. Faraday Trans. 71, 525.

Ivin, K.J., Steacie, E.W.R., 1951. The disproportionation and combination of ethyl radicals: the photolysis of mercury diethyl. Proc. R. Soc. London A 208, 25.

Jackson, W.M., Anex, D.S., Continetti, R.E., Balko, B.A., Lee, Y.T., 1991. Molecular beam studies of the photolysis of allene and the secondary photodissociation of the C_3H_x fragments. J. Chem. Phys. 95, 7327-7336.

Jacobs, T.A., Giedt, R.R., Cohen, N., 1965. Kinetics of decomposition of HF in shock waves. J. Chem. Phys. 43.

Jacobson, M.Z., 2005. Fundamentals of atmospheric modeling. Second Edition, Cambridge University Press.

Jamieson J.W.S., Brown, G.R., Tanner, J.S., 1970. The reaction of atomic hydrogen with methyl cyanide. Can. J. Chem. 48, 3619 - 3622.

Jodkowski, J.T., Ratajczak, E., Fagerstrom, K., Lund, A., Stothard, N.D., Humpfer, R., Grotheer, H-H., 1995. Kinetics of the cross reaction between amidogen and methyl radicals. Chem. Phys. Lett. 240, 63-71.

Joseph, J. H., Wiscombe, W. J., Weinman, J. A., 1976. The Delta-Eddington approximation or radiative flux transfer. J. Atmos. Sci. 33, 2452-2459.

Kameta, K., Machida, S., Kitajima, M., Ukai, M., Kouchi, N., Hatano, Y., Ito, K., 1996. Photoabsorption, photoionization, and neutral-dissociation cross sections of C_2H_6 and C_3H_8 in the extreme-uv region, J. Electron Spectrosc. 79, 391-393.

Kameta, K., Kouchi, N., Ukai, M., Hatano, Y., 2002. Photoabsorption, photoionization and neutral-dissociation cross sections of simple hydrocarbons in the vacuum ultraviolet range. J. Quant. Spectrosc. Radiat. Transfer 123, 225-238.

Kassner Ch., Stuhl, F., 1994. The VUV photodissociation $CH_3 \rightarrow CH(A\ ^2\Delta$ and B $^2\Sigma^-) + H_2$. Chem. Phys. Lett. 222, 425-430.

Keller, C.N., Cravens, T.E., Gan, L., 1992. A model of the ionosphere of Titan. J. Geophys. Res. 97, 12117-12135.

Kerr, J. A., Parsonage, M.J., 1972. Evaluated Kinetic Data on Gas-Phase Addition Reactions: Reactions of atoms and radicals with alkenes, alkynes, and aromatic compounds. Butterworth, London.

Kinsman, A. C., Roscoe, J.M., 1994. A kinetic analysis of the photolysis of mixtures of acetone and propylene. Int. J. Chem. Kinet. 26, 191-200.

Kley, D., Washida, N., Groth, W., 1974. Mechanism of CN^* production in flames of active nitrogen with cyanogen. Ber. Bunsenges. Phys. Chem. 78, 205.

Kloster-Jensen E., Haink, H.-J., Christen, H., 1974. The electronic spectra of unsubstituted mono- to penta- acetylene in the gas phase and in solution in the range 1100 to 4000 Å. Helvetica Chimica Acta 57, 1731-1744.

Koizumi H., Yoshimi, T., Shinsaka, K., Ukai, M., Morita, M., Hatano, Y., Yagishita, A., Ito, K., 1985. VUV-optical oscillator strength distributions of C_3H_6 and C_4H_8 isomers. J. Chem. Phys. 82, 4856-4861.

Knyazev, V. D., Bencsura, A., Stoliarov, S.I., Slagle, I.R., 1996. Kinetics of the $C_2H_3 + H_2 \leftrightarrows H + C_2H_4$ and $CH_3 + H_2 \leftrightarrows H + CH_4$ reactions. J. Phys. Chem. 100, 11346-11354.

Knyazev V.D., Slagle, I.R., 2001a. Kinetics of the reaction of allyl and propargyl radicals with CH_3. J. Phys. Chem. A 105, 3196-3204.

Knyazev V.D., Slagle, I.R., 2001b. Kinetics for the reactions of n-alkyl (C_2H_5, n-C_3H_7, and n-C_4H_9) radicals with CH_3. J. Phys. Chem. A 105, 6490-6498.

Knyazev, V.D., Slagle, I.R., 1996. Unimolecular decomposition of n-C4H9 and iso-C4H9 radicals. J. Phys. Chem. 100, 5318-5328.

Kraus, H., Oehlers, C., Temps, F., Wagner, H. Gg., Wolf, M., 1993. Rate constants for the reactions of $CH_2(X^3B_1)$ with selected alkenes at temperatures between 296 and 728 K. Ber. Bunsenges. Phys. Chem. 97, 545-553.

Langford, A.O., Petek, H., Moore, C.B., 1983. Collisional removal of $CH_2(^1A_1)$: Absolute rate constants for atomic and molecular collisional partners at 295 K. J. Chem. Phys. 78, 6650•-6659.

Lara, L.M., Lellouch, E., Lopez-Moreno, J., Rodrigo, R., 1996. Vertical distribution of Titan's atmospheric neutral constituents. J. Geophys. Res. 101, 23261•23283.

Laufer, A.H., McNesby, J.R., 1968. Photolysis of methane at 1236 Å: Quantum yield of hydrogen formation. J. Chem. Phys. 49, 2272-2278.

Laufer, A.H., Fahr, A., 2004. Reactions and kinetics of unsaturated C_2 hydrocarbon radicals. Chemical Reviews 104, 2813-2832.

Laufer, A.H., Gardner, E.P., Kwok, T.L., Yung, Y.L., 1983. Computations and estimates of rate coefficients for hydrocarbon reactions of interest to the atmospheres of the outer solar system. Icarus 56, 560-567.

Lebonnois, S. (2005). Benzene and aerosol production in Titan and Jupiter's atmospheres: a sensitivity study. Planet. Space Sci. 53, 486-497.

Lebonnois, S., Toublanc, D., Hourdin, F., Rannou, P., 2001. Seasonal variations of Titan's atmospheric composition. Icarus 152, 384-406.

Lee A.Y.T., Yung, Y.L., Cheng, B., Bahou, M., Chung, C., Lee, Y., 2001, Enhancement of deuterated ethane on Jupiter. Astrophys. J. 551, 93-96.

Lee, L.C., 1980. $CN(A^2\Pi_i \rightarrow X^2\Sigma^+)$ and $CN(B^2\Sigma^+ \rightarrow X^2\Sigma^+)$ yields from HCN photodissociation. J. Chem. Phys. 72, 6414-6421.

Lee, S.-H., Lee, Y.T., Yang, X., 2004. Dynamics of photodissociation of ethylene and its isotopomers at 157 nm: Branching ratios and kinetic-energy distributions. J. Chem. Phys. 120, 10983-10991.

Lellouch, E., Romani, P.N., Posenqvist, J., 1994. The vertical distribution and origin of HCN in Neptune's atmosphere. Icarus 108, 112-136.

Lemaire, P., Emerich, C., Vial, J.-C., Curdt, W., Schühle, U., Wilhelm, K., 2005. Variation of the full Sun hydrogen Lyman profiles through solar cycle 23. Adv. Space Res. 35, 384-387.

Lias, S.G., Collin, G.J., Rebbert, R.E., Ausloos, P., 1970. Photolysis of ethane at 11.6-11.8 eV. J. Chem. Phys. 52, 1841-1851.

Lindal, G.F., Wood, G.E., Hotz, H.B., Sweetnam, D.N., Eshleman, V.R., Tyler, G.L., 1983. The atmosphere of Titan: An analysis of the Voyager 1 radio occultation measurements. Icarus 53, 348-363.

Lungard, R., Heicklen, J., 1984. Pyrolysis of vinylacetylene between 300 and 450°C. Int. J. Chem. Kinet. 16, 125-148.

Magee, E.M. 1963. Photolysis of methane by vacuum-ultraviolet light. J. Chem. Phys. 39, 855-858.

Mahan, B.H., Mandal, R., 1962. Vacuum ultraviolet photolysis of methane. J. Chem. Phys. 37, 207-211.

Manabe, S., Wetherland, R.T., 1967. Thermal equilibrium of the atmosphere with a given distribution of relative humidity. J. Atmos. Sci. 24, 241-259.

Mantei, K.A., Bair, E.J., 1968. Reactions of nitrogen-hydrogen radicals. III. Formation and disappearance of NH radicals in the photolysis of ammonia. J. Chem. Phys. 49, 3248-3256.

Marston, G., Nesbitt, F.L., Stief, L.J., 1989. Branching ratios in the N + CH_3 reaction: formation of the methylene amidogen (H_2CN) radical. J. Chem. Phys. 91, 3483-3491.

Martinotti, F.F., Welch, M.J., Wolf, A.P., 1968. The reactivity of thermal carbon atoms in the gas phase. Chem. Commun. 3, 115.

Mason, E.A., Marreno, T.R., 1970. The diffusion of atoms and molecules, in: Bates, D.R, Esterman, I. (Eds.), Advances in atomic and molecular physics, Academic, San Diego, Calif., 155-232.

McEwan, M.J, Phillips, L.F., 1975. Chemistry of the atmosphere. Edward Arnold,ISBN: 0713124776.

McKay, C.P., Pollack, J.B., Courtin, R., 1989. The thermal structure of Titan's atmosphere. Icarus 80, 23-53.

McKay, C.P., Pollack, J.B., Courtin, R., 1991. The greenhouse and antigreenhouse effects on Titan. Science 253, 1118-1121.

McKellar, A.R.W., 1989. The spectrum of gaseous methane at 77 K in the 1.1-2.6 μm region: A benchmark for planetary astronomy. Can. J. Phys. 67, 1027-1035.

Mebel, A.M., Lin, M.C., Yu, T., Morokuma, K., 1997. Theoretical study of potential energy surface and thermal rate constants for the C_6H_5 + H_2 and C_6H_6 + H reactions. J. Phys. Chem. A 101, 3189-3196.

Mebel, A.M., Lin, M.C., 1999. Prediction of absolute rate constant for the reaction of NH_2 with alkanes from ab initio G2M/TST calculations. J. Phys. Chem. A 103, 2088-2096.

Mebel, A.M., Hayashi, M., Jackson, W.M., Wrobel, J., Green, M., Xu, D., Lin, S.H., 2001. Branching ratios of C_2 products in the photodissociation of C_2H at 193 nm. J. Chem. Phys. 114, 9821-9831.

Monks, P.S., Romani, P.N., Nesbitt, F.L., Scanlon, M., Stief, L.J., 1993. The kinetics of the formation of nitrile compounds in the atmosphere of Titan and Neptune. J. Geophys. Res. 98, 17115-17122.

Monks, P.S., Nesbitt, F.L., Payne, W.A., Scanlon, M., Stief, L.J., Shallcross, D.E., 1995. Absolute rate constants and product branching ratios for the reaction between H and C_2H_3 at T = 213 and 298 K. J. Phys. Chem. 99, 17151-17159.

Mordaunt, D.H., Lambert, I.R., Morley, G.P., Ashfold, N.R., Dixon, R.N., Western, C.M., Schnieder, L., Welge, K.H., 1993. Primary product channels in the photodissociation of methane at 121.6 nm, J. Chem. Phys. 98, 2054-2065.

Morter, C.L., Farhat, S.K., Adamson, J.D., Glass, G.P., Curl, R.F., 1994. Rate constant measurement of the recombination reaction C_3H_3 + C_3H_3. J. Phys. Chem. 98, 7029-7035.

Moses, J.I., Bézard, B., Lellouch, E., Gladstone, G.R., Feuchtgruber, H., Allen, M., 2000. Photochemistry of Saturn's Atmosphere: I. Hydrocarbon Chemistry and Comparisons with ISO Observations. Icarus 143, 244-298.

Moses J.I., Fouchet, T., Bézard, B., Gladstone, G.R., Lellouch, E., Feuchtgruber, H., 2005. J. Geophys. Res. 110, E08001, doi:10.1029/2005JE002411

Mullen, C., Smith, M.A., 2005. Low temperature H radical reactions with NO, saturated and unsaturated hydrocarbons studied in a pulsed supersonic Laval nozzle flow reactor between 53 and 188 K. J. Phys. Chem. 109, 1391-1399.

Munk, J., Pagsberg, P., Ratajczak, E., Sillesen, A., 1986a. Spectrokinetic studies of ethyl and ethylperoxy radicals. J. Phys. Chem. 90,2752-2757.

Munk, J., Pagsberg, P., Ratajczak, E., Sillesen, A., 1986b. Spectrokinetic studies of i-C_3H_7 and i-$C_3H_7O_2$ radicals. Chem. Phys. Lett. 132.

Münzel, N., Schweig A., 1988. UV/VIS absorption spectrum, geometry and electronic structure of transient *o*-Benzyne, Chem. Phys. Lett. 147, 192-194.

Murhpy J.E., Vakhtin, A.B., Leone, S.R., 2003. Laboratory kinetics of C_2H radical reactions with ethane, propane, and n-butane at T=96-296 K: implications for Titan. Icarus 163, 175-181.

Nakayama, T., Watanabe, K., 1964. Absorption and photoionization coefficients of acetylene, propyne and 1-butyne. J. Chem. Phys. 40, 558-561.

Nava, D.F., Mitchell, M.B., Stief, L.J., 1986. The reaction H + C_4H_2: Absolute rate constant measurement and implication for atmospheric modeling of Titan. J. Geophys. Res. 91, 4585-4589.

Nesbitt, F.L., Marston, G., Stief, L.J., 1990. Kinetic studies of the reactions of H_2CN and D_2CN radicals with N and H. J. Phys. Chem. 94, 4946-4951.

Nguyen, M.T., Sengupta, D., Ha, T.-K., 1996. Another look at the decomposition of methyl azide and methanimine: How is HCN formed?. J. Phys. Chem. 100, 6499-6503.

Nicholas, J.E., Spiers, A.I., Matin, N.A., 1986. Kinetics and mechanism in the decomposition of NH_3 in a radio-frequency pulse discharge. Plasma Chem. Plasma Process. 6.

Nicolas, C., Alcaraz, C., Thissen, R., Vervloet, M., Dutuit, O., 2003. Dissociative photoionization of N_2 in the 24-32 eV photon energy range. J. Phys. B: At. Mol. Phys. 36, 2239-2251.

Nizamov, B., Dagdigian, P.J., 2003. Spectroscopic and kinetic investigation of methylene amidogen by cavity ring-down spectroscopy. J. Phys. Chem. A 107, 2256-2263.

Nizamov B., Leone, S.R., 2004. Kinetics of C_2H reactions with hydrocarbons and nitriles in the 104-296 K temperature range. J. Phys. Chem. A. 108, 1746-1752.

North S.W., Blank, D.A., Chu, P.M., Lee, Y.T., 1995. Photodissociation dynamics of the methyl radical 3s Rydberg state. J. Chem. Phys. 102, 792-798.

Nuth, J.A., Glicker, S., 1982. The vacuum ultraviolet spectra of HCN, C_2N_2, and CH_3CN. J. Quant. Spectrosc. Radiat. Transfer 28, 223-231.

Obi K., Akimoto, H., Ogata, Y., Tanaka, I., 1971. Photolyses of propane, n-Butane, and Cyclobutane at Xe and Kr resonance lines. J. Chem. Phys. 55, 3822-3828.

Okabe, H. 1978. Photochemistry of small molecules. Wiley New York.

Okabe, H. 1981. Photochemistry of acetylene at 1470 A. J. Chem. Phys. 75, 2772-2778.

Okabe, H. 1983. Photochemistry of acetylene. Can. J. Chem 61, 850-855.

Okabe, H., Becker, D.A., 1963. Vacuum ultraviolet photochemistry. VII. Photolysis of n-butane. J. Chem. Phys. 39, 2549-2555.

Onyszchuk, M, Breitman, L., Winkler, C.A., 1953. The reaction of active nitrogen with propane. Can. J. Chem. 32.

Opansky, B.J., Leone, S.R., 1996a. Low-temperature rate coefficients of C_2H with CH_4 and CD_4 from 154 to 359 K. J. Phys. Chem. 100, 4888-4892.

Opansky, B.J., Leone, S.R., 1996b. Rate coefficients of C_2H with C_2H_4, C_2H_6, and H_2 from 150 to 359 K. J. Phys. Chem. 100, 19904-19910.

Pagsberg, P.B., Eriksen, J., Christensen, H.C., 1979. Pulse Radiolysis of Gaseous Ammonia-Oxygen Mixtures. J. Phys. Chem. 83, 582-590.

Parker, J.K., Payne, W.A., Cody, R.J., Stief, L.J., 2004. Kinetics of the reaction of atomic hydrogen with cyanoacetylene from T=200 to 298 K. J. Phys. Chem A 108, 1938-1945.

Payne, W.A., Monks, P.S., Nesbitt, F.L., Stief, L.J., 1996. The reaction between N(^{4}S) and C_2H_3: Rate constant and primary reaction channels. J. Chem. Phys. 104, 9808-9815.

Peeters, J., Boullart, W., Langhans, I., 1994. Branching ratio of the C_2H_2 + O reaction at 290 K from kinetic modelling of relative methylene concentration versus time profiles in C_2H_2/O/H systems. Int. J. Chem. Kinet. 26, 869-886.

Petrie, S., Osamura, Y., 2004. NCCN and NCCCCN formation in Titan's atmosphere: 2. HNC as a viable precursor. J. Phys. Chem. A 108, 3623-3631.

Petrishchev, V.A., Sapozhkov, A.Yu, 1981. Rate constant of the N + H_2 reaction. Kinet. Catal. 22.

Pilling, M.J., Bass, A.M., Braun, W., 1971. Oscillator strengths of CH_2 and CH_3 in the vacuum ultraviolet. Chem. Phys. Lett. 9, 147-148.

Pitts, W.M., Pasternack, L., McDonald, J.R., 1982. Temperature dependence of the C_2(X $^1\Sigma_g^+$ and a $^3\Pi_u$ equilibrated states) with O_2. Chem. Phys. 68, 417-422.

Pruppacher, H.R., Klett, J.D., 1978. Microphysics of clouds and precipitation. Reidel Publishing Company, Dordrecht.

Ramanathan, V., Coakley, J.A., 1978. Climate modeling through radiative-convective models. Rev. Geophys. Space Phys. 16, 465-490.

Rebbert, R.E. and Ausloos, P., 1973. Photolysis of methane: Quantum yield of C(^{1}D) and CH. J. Photochem. 1, 171-176.

Redondo, P., Pauzat, F., Ellinger, Y., 2006. Theoretical survey of the NH + CH_3 potential energy surface in relation to Titan atmospheric chemistry. Planet. Space Sci. 54, 181-187.

Reisler, H., Mangir, M.S., Wittig, C., 1980. Kinetics of free radicals generated by IR laser photolysis.IV. Intersystem crossings and reactions of $C_2(X^1\Sigma_g^+)$ and $C_2(\alpha^3\Pi_u)$ in the gaseous phase. J. Chem. Phys. 73, 2280-2286.

Rennie, E.E., Johnson, C.A.F., Parker, J.E., Holland, D.M.P., Shaw, D.A., Hayes, M.A., 1998. A photoabsorption, photodissociation and photoelectron spectroscopy study of C_6H_6 and C_6D_6, Chem. Phys., 229, 107-123.

Romani, P.N., 1996. Recent rate constant and product measurements of the reactions C_2H_3 + H_2 and C_2H_3 + H•Importance for the photochemical modeling of hydrocarbons on Jupiter. Icarus 122, 233•241.

Romanzin C. and 8 co-authors, 2005. Methane photochemistry: A brief review in the frame of a new experimental program of Titan's atmosphere simulations. Adv. Space Research, 36, 258-267.

Sagan, C., and W. R. Thompson, 1984, Production and condensation of organic gases in the atmosphere of Titan. Icarus 59, 133•-161.

Samson, J.A.R., Marmo, F.F., Watanabe, K., 1962. Absorption and photoionization coefficients of propylene and butene-1 in the vacuum ultraviolet. J. Chem. Phys. 36, 783-786.

Samson, J.A.R., Haddad, G.N., Masuoka, T., Pareek, P.N., Kilcoyne, D.A.L., 1989. Ionization yields total absorption and dissociative photoionization cross sections of CH_4 from 110 to 950 Å. J. Chem. Phys. 90, 6925-6932.

Samuelson, R.E., 1983. Radiative equilibrium model of Titan's atmosphere. Icarus 53, 364-387.

Samuelson, R.E., Mayo, L.A., Knuckles, M.A., Khanna, R.J., 1997. C_4N_2 ice in Titan's north polar stratosphere. Planet. Space Sci. 45, 941-948.

Sato, K., Misawa, K., Kobayashi, Y., Matsui, M., Tsunashima, S., Kurosaki, Y., Takayanagi, T., 1999. Measurements of thermal rate constants for the reactions of $N(^2D,^2P)$ with C_2H_4 and C_2D_4 between 225 and 292 K. J. Phys. Chem. A 103, 8650-8656.

Scala, A.A., Salomon, D., 1976. The gas phase photolysis and γ radiolysis of ethylenimine. J. Chem. Phys. 65, 4455-4461.

Scherzer, K., Claus, P., Karwath, M., 1985. Untersuchungen sur kinetik und zum mechanismus der addition von methylradicalen an vinylacetylen. Z. Chem. Phys. (Leipzig) 266, 321.

Schiavello, M., Volpi, G.G., 1962. Reaction of hydrogen atoms with hydrazine, ammonia and nitrous oxide. J. Chem. Phys. 37, 1510-1513.

Schofield, K., 1973. Evaluated chemical kinetic rate constants for various gas phase reactions. J. Phys. Chem. Ref. Data 2, 25-84.

Schwanebeck,W., Warnatz, J., 1975. Reaktionen des butadiins. I. Die reaction mit wasserstoffatomen. Ber. Bunsenges. Phys. Chem. 79, 530-535.

Seki, K., Nakashima, N., Nishi, N., Kinoshita, M., 1986. Photochemistry of acetylene at 193 nm: Two pathways for diacetylene formation. J. Chem. Phys. 85, 274-279.

Seki, K., Okabe, H., 1992, Photodissociation of methylacetylene at 193 nm. J. Phys. Chem. 96, 3345-3349.

Seki, K., Okabe, H., 1993, Photochemistry of acetylene at 193.3 nm. J. Phys. Chem. 97, 5284-5290.

Seki, K., Yagi, M., He, M.Q., Halpern, J.B., Okabe, H., 1996. Reaction rates of the CN radical with diacetylene and dicyanoacetylene. Chem. Phys. Lett. 258, 657-662.

Shettle, E.P., Weinman, J.A., 1970. The transfer of solar irradiance through inhomogeneous turbid atmospheres evaluated by Eddington's approximation. J. Atmosp. Sci. 27, 1048-1055.

Shindo F., Benilan, Y., Guillemin, J.-C., Chaquin, P., Jolly, A., Raulin, F., 2005. Ultraviolet and infrared spectrum of C_6H_2 revisited and vapor pressure curve in Titan's atmosphere. Planet. Space Sci. 51, 9-17.

Sillesen, A., Ratajczak, E., Pagsberg, P., 1993. Kinetics of the reaction H + C_2H_4 $\rightarrow$ C_2H_5, H + C_2H_5 $\rightarrow$ 2 CH_3, CH_3 + C_2H_5 $\rightarrow$ products studied by pulse radiolysis combined with infrared diode lase spectroscopy. Chem. Phys. Lett. 201, 171-177.

Sims, I.R., Queffelec, J.-L., Travers, D., Rowe, B., Herbert, L.B., Karthäuser, J., Smith, I.W.M., 1993. Rate constants for the reactions of CN with hydrocarbons at low and ultra-low temperatures. Chem. Phys. Lett. 211, 461-468.

Sims, I.R., Queffelec, J.L., Defrance, A., Rebrion-Rowe, C., Travers, D., Bocherel, P., Rowe, B.R., Smith, I.W.M., 1994. Ultralow temperature kinetics of neutral-neutral reactions. The technique and results for the reactions CN + O_2 down to 13 K and CN + NH_3 down to 25 K. J. Chem. Phys. 100, 4229-4241.

Slack, M.W., 1976. Kinetics and thermodynamics of the CN molecule. III. Shock tube measurement of CN dissociation rates. J. Chem. Phys. 64, 228-236.

Slanger, T.G., Black, G., 1982. Photodissociative channels at 1216 $\AA$ for H_2O, NH_3 and CH_4.J. Chem. Phys. 77, 2432-2437

Smith, G.P., 2003, Rate theory of methyl recombination at the low temperatueres and pressures of planetary atmospheres. Chem. Phys. Lett, 376, 381-388.

Smith N.S., Bénilan, Y., Bruston, P., 1998. The temperature dependent absorption cross-sections of C_4H_2 at mid ultraviolet wavelengths. Planet. Space Sci. 46, 1215-1220.

Smith, N.S., Raulin, F., 1999. Modeling of methane photolysis in the reducing atmospheres of the outer solar system. J. Geophys. Res. 104, 1873•1876.

Smith, P.L., Yoshino, K., Parkinson, W.H., 1991. High-resolution, VUV (147-201 nm) photoabsorption cross sections for C_2H_2 at 195 and 195 K. J. Geophys. Res. 96, 17529-17533.

Sromovsky, L.A., Irwin, P.G.J., Fry, P.M., 2006. Near-IR methane absorption in the outer planet atmospheres: Improved models of temperature dependence and implications for Uranus cloud structure. Icarus 182, 577-593.

Stark, G., Huber, K.P., Yoshino, K., Chan, M.-C., Matsui, T., Smith, P.L., Ito, K., 2000. Line oscillator strength measurements in the 0-0 band of the $c_4'^1\Sigma_u^+ \leftarrow X^1\Sigma_g^+$ transition of N_2. ApJ 531, 321-328.

Stewart, P.H., Larson, C.W., Golden, D.M., 1989. Pressure and temperature dependence of reactions proceeding via a bound complex. II. Application to 2 CH_3?C_2H_5CH. Combust. Flame 75, 25.

Stief, L.J., 1970. Ratio of disproportionation to combination of N_2H_3 radicals. J. Chem. Phys. 52, 4841-4845.

Stief, L.J., Nesbitt, F.L., Payne, W.A., Kuo, S.C., Tao, W., Klemm, R.B., 1995. Rate constant and reaction channels for the reaction of atomic nitrogen with the ethyl radical. J. Chem. Phys. 102, 5309-5316.

Sun, Q., Yang, D.L., Wang, N.S., Bowman, J.M., Lin, M.C., 1990. Experimental and reduced dimensionality quantum rate coefficients for $H_2(D_2)$ + CN → H(D)CN + H(D). J. Chem. Phys. 93, 4730-4739.

Sun, W., Yokoyama, K., Robinson, J.C., Suits, A.G., Neumark, D.M., 1999. Discrimination of products isomers in the photodissociation of propyne and allene at 193 nm. J. Chem. Phys. 110, 4363-4368.

Suto, M., Wang, X., Lee, L.C., 1985. Fluorescence from VUV excitation of formaldehyde. J. Chem. Phys. 85, 4228-4233.

Suto M., Wang, X., Shan, J., Lee, L.C., 1992. Quantitative photoabsorption and fluorescence spectroscopy of benzene, naphthalene and some derivatives at 106-295 nm. J. Quant. Spectrosc. Radiat. Transfer 48, 79-89.

Takahashi S., Miyazaki S., 1977. The reactions of the nitrogen atom with ethylene and ethylene-d4. Bull. Chem. Soc. Jpn. 50, 1627-1628.

Teng, L., Jones, W.E., 1972. Kinetics of the reactions of hydrogen atoms with ethylene and vinyl fluoride. J. Chem. Soc. Faraday Trans. 68, 1267-1277.

Teslja, A., Nizamov, B., Dagdigian, P.J., 2004. The electronic spectrum of methyleneimine. J. Phys. Chem. 108, 4433-4439.

Toon, O.B., Turco, R.P., Pollack, J.B., 1980. A physical model of Titan's clouds. Icarus 43, 260-282.

Toon, O.B., McKay, C.P., Griffith, C.A., Turco, R.P., 1992. A physical model of Titan's aerosols. Icarus 95, 24-53.

Toublanc, D., Parisot, J.P., Brillet, J., Gautier, D., Raulin, F., McKay, C.P., 1995. Photochemical modeling of Titan's atmosphere. Icarus 113, 2•26.

Tsang, W., 1988, Chemical kinetic data base for combustion chemistry. III. Propane. J. Phys. Chem. Ref. Data 17, 887-951.

Tsang, W., 1990, Chemical kinetic data base for combustion chemistry. Iv. Isobutane., J. Phys. Chem. Ref. Data 17, 887-951.

Tsang, W., 1991. Chemical kinetic data base for combustion chemistry. V. Propene. J. Phys. Chem. Ref. Data 20, 221-274.

Tsang W., 1992, Chemical kinetic data base for propellant combustion. II. Reactions involving CN, NCO, and HNCO. J. Phys. Chem. Ref. Data 21, 753

Tsang, W., Hampson, R.F., 1986. Chemical kinetic data base for combustion chemistry. Part 1. Methane and related compounds. J. Phys. Chem. Ref. Data 15, 1087-1279.

Tsang, W., Herron, J.T., 1991. Chemical kinetic data base for propellant combustion. I. Reactions involving NO, NO_2, HNO, HNO_2, HCN and N_2O 20. J. Phys. Chem. Ref. Data 20, 609-663.

Vakhtin A.B., Heard, D.E., Smith, I.W.M., Leone, S.R., 2001. Kinetics of reactions of C_2H radical with acetylene, O_2, methylacetylene, and allene in a pulsed Laval nozzle apparatus at T=103 K. Chem. Phys. Lett., 344, 317-324

Vakhtin A.B., Heard, D.E., Smith, I.W.M., Leone, S.R., 2001. Kinetics of C_2H radical reactions with ethene, propene and l-butene measured in a pulsed Laval nozzle apparatus at T=103 and 296 K. Chem. Phys. Lett. 348, 21-26.

Vaghjiani, G.L., 1993. Ultraviolet absorption cross section for N_2H_4 vapor between 191-291 nm and H(^{2}S) quantum yield in 248 nm photodissociation at 296 K. J. Chem. Phys. 98, 2123-2132.

Vaghjiani, G.L., 1995. Laser photolysis studies of hydrazine vapor: 193 and 222-nm H-atom primary quantum yields at 296 K, and the kinetics of H + N_2H_4 reaction over the temperature range 222 - 657 K. Int. J. Chem. Kinet. 27,777-790.

Vardavas, I.M., 1984. Modelling reactive gas flows within shock tunnels. Aust. J. Phys. 37, 157-177.

Vardavas, I.M., Carver, J.H., 1984a. Comments on the Newton-Raphson method for obtaining temperature profiles from radiative-convective models. Planet. Spac. Sci. 32, 803-807.

Vardavas, I.M., Carver, J.H., 1984b. Solar and terrestrial parameterizations for radiative-convective models. Planet. Spac. Sci. 32, 1307-1325.

Vardavas, I.M., Taylor, F.W., 2007. Radiation and Climate, Oxford University Press.

Vargaftik, N.B., 1975. Tables on the thermophysical properties of liquids and gases in normal and dissociated states. John Wiley & Sons, INC.

Vuitton, V., Gée, C., Raulin, F., Bénilana, Y., Crépin, C., Gazeau, M.-C., 2003. Intrinsic lifetime of metastable excited C_4H_2: implications for the photochemistry of C_4H_2 in Titan's atmosphere. Plan. Space Sci. 51, 847-852.

Vuitton V., Yelle, R.V., Anicich, V.G., 2006a. The nitrogen chemistry of Titan's upper atmosphere revealed. Ap. J. 647, L175-L178

Vuitton V., Yelle, R.V., Anicich, V.G., 2006b. Detection of complex molecules in Titan's upper atmosphere. DPS meeting, #38, #36.03.

Vuitton, V., Doussin, J.-F., Bènilan, Y., Raulin, F., Gazeau, M.-C., 2006c. Experimental and theoretical study of hydrocarbon photochemistry applied to Titan stratosphere, Icarus 185, 287-300.

Wakeham, W.A., Slater, D.H., 1973. Diffusion coefficients for n-alkanes in binary gaseous mixtures with nitrogen. J. Phys. B: Atom. Molec. Phys. 6, 886-896.

Wang, H., Frenklach, M., 1994. Calculations of rate coefficients for the chemically activated reactions of acetylene with vinylic and aromatic radicals. J. Phys. Chem. 98, 1465•1489.

Wang, H., Frenklach, M., 1997. A detailed kinetic modeling study of aromatics formation in laminar premixed acetylene and ethylene flames. Combust. Flame 110, 173-221.

Wang, J-H., Liu, K., 1998. VUV photochemistry of CH_4 and isotopomers. I. Dynamics and dissociation pathway of the H/D-atom elimination channel. J. Chem. Phys. 109, 7105-7112.

Wang, B., Hou, H., Gu, Y., 2000. Mechanism and rate constant of the reaction of atomic hydrogen with propyne. J. Chem. Phys. 112, 8458-8465

Wang, J-H, Liu, K., Min, Z., Su, H., Bersohn, R., Preses, J., Larese, Z., 2000. Vacuum ultraviolet photochemistry of CH_4 and isotopomers. II. product channel fields and absorption spectra. J. Chem. Phys. 113, 4146-4152.

Warnatz, J., 1984. Rate coefficients in the C/H/O system, in : Combustion Chemistry,ed. W.C. Gardiner,Jr., Springer-Verlag, NY

Weissman, M.A., Benson, S.W., 1988. Rate parameters for the reactions of C_2H_3 and C_4H_5 with H_2 and C_2H_2. J. Phys. Chem. 92, 4080-4084.

Westmoreland, P.R., Dean, A.M., Howard, J.B., Longwell, J.P., 1989. Forming benzene in flames by chemically activated isomerization. J. Phys. Chem. 93, 8171-8180.

Waite, J.H. Jr., and 21 co-authors, 2005. Ion neutral mass spectrometer results from the first flyby of Titan. Science 308, 982-986.

White, O.R., 1978. The Solar Output and its variation. Colorado Associated University Press, Boulder, Colorado.

Whyte, A.R., Phillips, L.F., 1983. Rate of reaction of N with CN(v = 0, 1). Chem. Phys. Lett. 98, 590-593.

Whytock, D.A., Payne, W.A., Stief, L.J., 1976. Rate of reaction of atomic hydrogen with propyne over an extended pressure and temperature range. J. Chem. Phys. 65, 191-195.

Wilson, E.H., Atreya, S.K., 2000. Sensitivity studies of methane photolysis and its impact on hydrocarbon chemistry in the atmosphere of Titan. J. Geophys. Res. 105, 20263•20273.

Wilson, E.H., Atreya, S.K., Coustenis, A., 2003. Mechanisms for the formation of benzene in the atmosphere of Titan. J. Geophys. Res. 108, doi:10.1029/2002JE001896.

Wilson, E.H., Atreya, S.K., 2004. Current state of modeling the photochemistry of Titan's mutually dependent atmosphere and ionosphere. J. Geophys. Res. 109, doi:10.1029/2003JE002181.

Wilson, S.H.S, Howe, J.D., Rosser, K.N., Ashfold, M.N.R., Dixon, R.N., 1994. A reinvestigation of the near-ultraviolet photodissociation dynamics of the methyl radical. Chem. Phys. Lett. 227, 456-460.

Woods, T.N., Tobiska, W.K., Rottman, G.J., Worden, J.R. 2000. Improved solar Lyman α irradiance modeling from 1947 through 1999 based on UARS observations. J. Geophys. Res. 105, A12, 27195-27215.

Woods, T.N., Rottman, G.J., 2002. Solar ultraviolet variability over time periods of aeronomic interest. In: Mendillo, M. et al. (Eds.), Comparative aeronomy in the solar system. American Geophysical Union Monograph.

Xu, Z-F., Fang, D.-C., Fu, X.-Y., 1998. Ab initio study on the reaction 2 $NH_2 \rightarrow$ NH + NH_3. Int. J. Quantum Chem. 70, 321-329.

Xu, Z.-F., Li, S.-M., Yu, Y.-X., Li, Z.-S., Sun, C.-C., 1999. Theoretical studies on the reaction path dynamics and variational transition-state theory rate constants of the hydrogen-abstraction reactions of the NH($X^3\Sigma$-) radical with methane and ethane. J. Phys. Chem. A 103, 4910-4917.

Yang, D.L., Yu, T., Lin, M.C., Melius, C.F., 1992a. CN radical reactions with hydrogen cyanide and cyanogen: comparison of theory and experiment. J. Chem. Phys. 97, 222-226.

Yang, D. L., Yu, T., Wang, N.S., Lin, M.C., 1992b. Temperature dependence of cyanogen radical reactions with selected alkanes: CN reactivities towards primary, secondary and tertiary C-H bonds. Chem. Phys. 160, 307-315.

Yelle R.V., Strobel, D.F., Lellouch, E., Gautier, D., 1997. Engineering models for Titan's atmosphere, ESA SP-1177, 243-256, European Space Agency, Noordwijk

Yokoyama A., Zhao, X., Hintsa, E.J., Continetti, R.E., Lee, Y.T., 1990. Molecular beam studies of the photodissociation of benzene at 193 and 248 nm. J. Chem. Phys. 92, 4222-4233.

Young, E.F., Rannou, P., McKay, C.P., Griffith, C.A., Noll, K., 2002. A three dimensional map of Titan's tropospheric haze distribution based on HST imaging. Astron. J. 123, 3473•3486.

Yung, Y. L., 1987. An update of nitrile photochemistry on Titan. Icarus 72, 468-472.

Yung, Y. L., Allen, M., Pinto J.P., 1984. Photochemistry of the atmosphere of Titan: Comparison between model and observations. Astrophys. J. Supp. 55, 465-506.

Zabarnick, S., Fleming, J.W., Lin, M. C., 1988. Kinetics of $CH(X^2\pi)$ radical reactions with cyclopropane, cyclopentane, and cyclohexane, J. Chem. Phys. 88.

Zabarnick, S., Lin, M.C., 1989. Kinetics of $CN(X^2\Sigma^+)$ radical reactions with HCN, BrCN, and CH_3CN. Chem. Phys. 134, 185-191.

Zabarnick S., Fleming, J.W., Lin, M.C., 1991. Direct measurement of rate constants for the reactions of CH and CD with HCN and DCN. Chem. Phys. 150, 109-115.

Zelikoff, M., Watanabe, K., 1953. Absorption coefficients of ethylene in the vacuum ultraviolet. J. Opt. Soc. Am. 43, 756-759.

Zetzsch, C., Stuhl, F., 1981. Formation and fate of $NH(X^3\Sigma^-)$ in the pulsed vacuum UV photolysis of NH_3. Ber. Bunsenges. Phys. Chem. 85.

Zipf, E.C., Espy, P.J., Boyle, C.F., 1980. The excitation and collisional deactivation of metastable $N(^2P)$ atoms in auroras. J. Geophys. Res. 85, 687-694.

Zhu R.S., Xu, Z.F., Lin, M.C., 2004. *Ab initio* studies of alkyl radical reactions: Combination and disproportionation reactions of CH_3 with C_2H_5, and the decomposition of chemically activated C_3H_8. J. Chem. Phys. 120, 6566-6573.

Zhu, Z., Zhang, Z., Huang, C., Pei, L., Chen, C., Chen, Y., 2003. Kinetics of CCN radical reactions with a series of normal alkanes. J. Phys. Chem. A 107, 10288-10291.

Zu, Z-F., Fang, D.-C., Fu, X.-Y. 1997. Ab initio study on the reaction 2 $NH(X\ ^3\Sigma\text{-}) \rightarrow NH_2(X\ ^2B_1) + N(^4S)$. Chem. Phys. Lett. 275, 386-391.

Zwier, T.S., Allen, M., 1996. Metastable diacetylene reactions as routes to large hydrocarbons in Titan's atmosphere. Icarus 123, 578-583.

Chapter 3

Pathways of Haze Formation

The chemical reactions in Titan's atmosphere, lead to increasingly complex species from which the formation of haze particles is believed to emerge. Laboratory experiments have been performed in order to derive information about how this gas-to-particle transformation happens, while further theoretical estimations have been suggested. In this chapter a description of the laboratory results is given and the pathways tested in the model are presented.

3.1 Laboratory measurements

Based on the idea of photochemical origin for the haze particles, many laboratory attempts for simulating this production were performed. The main idea of the simulation is to irradiate a specific mixture of nitrogen, methane and possibly other hydrocarbons (in amounts equivalent with those present in the atmosphere of Titan) with an energy source analogous to those in Titan (UV radiation, magnetospheric electrons and protons, cosmic rays). The energy sources usually chosen are electric discharge, cold plasma discharge and UV radiation. The results of such experiments were the production of complex organic solids, which were baptized tholins (Sagan & Khare, 1979).

The most well established laboratory simulation of tholins is the one made by Khare et al. (1984a) using a mixture of 90% N_2 - 10% CH_4 with DC electrical discharge. This is because they provided for the first time measurements of the complex refractive index that exhibited the correct wavelength dependence of the imaginary part, necessary to fit the geometric albedo. As it was shown by Rages & Pollack (1980), haze is the main absorber in the UV region responsible for the sharp decrease in the geometric albedo below 0.6μm and the slope of the geometric albedo is directly correlated with the slope of the refractive index's imaginary part in this region. All radiation transfer models published so far use the above refractive index values scaled by a (wavelength dependent)

Table 3.1: Laboratory Haze Simulations

Reference	**T (K)**	**P (mb)**	**Composition**	**C/N**	**C/H**	**Method**
Khare et al. (1984a)	300	0.2	90% N_2–10% CH_4	-	-	Spark
Bar-Nun et al. (1988)	300	270	5% C_2H_2/ 5% C_2H_4 / 5% HCN in Ar	-	-	UV light
Thompson et al. (1991)	300	17	90% N_2 –10% CH_4	-	-	Cold Plasma
Scattergood et al. (1992)	300	73	2%C_2H_2/ 2% C_2H_4 in N_2	-	-	UV light
			2% HCN in He	-	-	
McDonald et al. (1994)	300	1	90% N_2 –10% CH_4	1.5	0.6	Cold Plasma
Coll et al. (1995)	150	900	90% N_2 –10% CH_4	11	1	Spark
McKay (1996)	300	1000	90% N_2 – 10% CH_4	5.5	1	Spark
Clarke & Ferris (1997)	300	330	90% C_2H_2– 10% HC_3N	6.4	1.6	
Coll et al. (1999)	150	2	98% N_2 – 2%CH_4	2.8	0.8	Cold Plasma
Khare et al. (2002)	300	71	90% N_2 –10% CH_4	-	-	Spark
Ramirez et al. (2002)	300	1	98% N_2 –2% CH_4	-	-	Cold Plasma
Tran et al. (2003)	300	933	98% N_2-1.8% CH_4 - 0.2% H_2	17.6	-	UV light
Imanaka et al. (2004)	300	0.13-23	90%N_2– 10% CH_4	1.5-3	-	Cold Plasma

multiplication factor in order to achieve the best possible fit to the geometric albedo.

Other simulations for the production of haze analogs had as primary mixture photochemical products of a N_2 - CH_4 atmosphere. Bar-Nun et al. (1988) used acetylene (C_2H_2), ethylene (C_2H_4) and hydrogen cyanide (HCN) in Ar while Scattergood et al. (1992) used C_2H_2 and C_2H_4 in N_2, HCN in He and also mixtures of them in different amounts. They both obtained spherical particles, which were sticky and hence formed clusters giving in this way credit to the suggestion of West & Smith (1991) of non - spherical final particles in Titan's atmosphere. The disadvantage of these simulations was that they didn't correspond to the mixtures found in Titan's atmosphere.

With the interest in Titan's organic chemistry increasing, laboratory researchers tried to simulate better the conditions prevailing in Titan's atmosphere. Coll et al., in a series of publications (1995, 1998, 1999), pointed out the significance of low temperature conditions in the experiments, close to the ones in Titan's atmosphere, and the possible contamination of previous simulations by terrestrial gases; many of the species formed in the reactor vessels were found to be unstable at standard room temperature and the solid products were of low stability in the presence of O_2 and H_2O. McKay (1996) investigated the effect of different initial methane amounts in the mixture on the optical properties of the produced particles. He concluded that increasing the methane content of the mixture, produces tholins which are darker in the UV and violet compared to the visible and near-IR. Clarke & Ferris (1997) studied the possible formation of haze analogs from cyanoacetylene (HC_3N) and cyanoacetylene-acetylene copolymers. They concluded that HC_3N is much more reactive in polymerization than HCN and that the optical properties of the produced HC_3N/C_2H_2 copolymers could fit Titan's haze properties better than the pure polymers. Khare et al. (2002) studied the time evolution of laboratory produced tholins and observed the formation of aromatic rings almost immediately after the glow discharge in their initial mixture. Ramirez et al. (2002) used a N_2/CH_4 mixture closer to the one in Titan's atmosphere and without the possible effects of terrestrial contamination; the refractive index of their produced tholins exhibited a wavelength variation similar to the one of Khare et al. (1984a) but of smaller absolute value. Tran et al. (2003) used mixtures of CH_4, H_2, C_2H_2, C_2H_4 and HC_3N in N_2, and produced haze analogs using as energy source direct UV light. They also retrieved similar slope for the $k(\lambda)$ plot as previous investigators, but the absolute value of their imaginary refractive index varied depending on the composition of the mixture and the conditions of the experiment.

Many methods have been used for the chemical analysis and elemental composition of the produced tholin particles (Khare et al., 1984b; Ehrenfreund et al., 1995; McKay, 1996; Coll et al., 1999; Khare et al., 2002; Tran et al., 2003). Their structure was found to be a complex mixture of hydrocarbon and nitriles including aromatic compounds and polycyclic aromatic hydrocarbons (PAH), but the results between different experiments were not always similar. The parameters commonly used for the elemental composition of the particles are their C/N and C/H ratios. These are important not only because they provide an

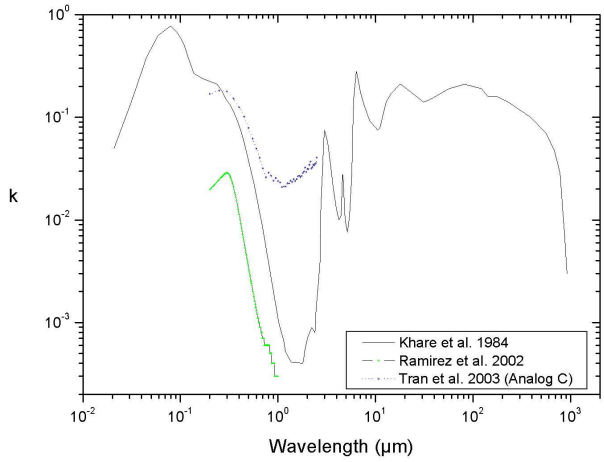

Figure 3.1: Imaginary part of refractive index of laboratory produced-haze analogs.

estimate of the bulk mass of the haze particles, but also an estimate of the role of the haze particles as a possible sink for atmospheric gases. Again, as for the optical properties, the derived ratios depend on the experimental conditions and the energy sources used: C/N ratios were found to range from 0.75 (McDonald et al., 1994) to 17.6 (Tran et al., 2003) and C/H ratios between 0.6 (Khare et al., 1984a) and 1.6 (Clarke & Ferris, 1997) (see Table 3.1).

Motivated by the different results between the published simulations, Imanaka et al. (2004) performed a systematic study, with experiments covering a wide range of pressures that represent different altitude regions in Titan's atmosphere. They found that the pressure is a critical parameter in the chemical and hence optical properties of the derived analogs, with nitrogen being more efficiently incorporated in the particles in low deposition pressures (increasing C/N ratio with increasing pressure). In addition the presence of aromatic compounds and nitrogen-containing polycyclic aromatic compounds (N-PACs) was found to increase with decreasing pressure, making in this way the derived tholins more absorbing in the UV/Visible region due to the delocalized π electrons of these structures. These conclusions explained the differences observed between the previous experiments and proved that the haze particles found in Titan's atmosphere, by and large will have different properties at different pressure regions, as was suggested in the past (Chassefiere & Cabane, 1995).

3.2 Huygens in situ measurements

The ACP instrument on board the Huygens probe, provided the first results regarding the chemical composition of the haze particles in Titan's atmosphere (Israel et al., 2005). The pyrolysis of the refractory core of the particles, provided indications for the presence of HCN and NH_3 in their structural form, although the results were preliminary and as the authors say, the poor resolution of the mass spectrometer did not allow for a clear verification of the above conclusions. If correct, they suggest that there is a strong incorporation of nitrogen in the haze particles which could act as a significant sink for this atmospheric component. In addition to the above, the two different altitude sample collections have shown that the aerosol composition is homogeneous below 130 km which suggests that the production region must be situated above this altitude.

In view of the low temperature conditions prevailing in the interstellar medium, and the formation of complex organic structures in it, possible pathways in which haze could be formed in Titan's atmosphere can be suggested. The presence of polyaromatics (PAH) in the interstellar clouds has been known for long time (Allamandola et al., 1989), while recently Hudgins (2005) have found that N-PACs to be also abundant in the universe and produced around dying stars. These are considered to be much more important than simple PAHs due to their connection with the chemistry of life. Chlorophyll for example is such a compound. Although it was believed that the formation of these complexes was related to ion chemistry, recent results (Ricca et al., 2001) suggest that they are produced by neutral radical reactions which proceed even at the very low temperatures found in these regions of the universe. Similar mechanisms could also lead to the production of haze in Titan's atmosphere.

3.3 Suggested pathways

Based on the laboratory measurements certain possible pathways for the transformation of gases to particles have been suggested (Lebonnois et al., 2002; Wilson & Atreya, 2003) but remain to be tested with regard to the formation of the haze from the photochemistry. In the present work these suggested pathways, along with new ones, are used to generate the vertical haze structure from the photochemistry, and are validated by comparing the model vertical temperature structure, spectral geometric albedo and vertical species distributions against measurements.

The reactions used along with their rates are given in Table 3.2. The particles are believed to form from the chemical growth of certain polymer structures. Allen et al. (1980) suggested that a possible mechanism for the production of these polymers could be the photolysis of acetylene, leading to polyyne ($C_{2n+2}H_2$) formation. The first step of this process, as was described in the previous section, is the production of diacetylene from the reaction of ethyl radical with acetylene. The process continues giving higher order polyacetylenes (C_6H_2, C_8H_2, etc.):

Table 3.2: Reactions used for the gas-to-particle transformation

Reaction				ε	Rate	Reference	T(K)
Polyynes							
R525	$C_4H + C_6H_2$	→	*Polymer*	17.9	1.3×10^{-10}	Est. as k($C_2H + C_2H_2$)	
R526	$C_6H + C_4H_2$	→	*Polymer*	17.5	1.3×10^{-10}	Est. as k($C_2H + C_2H_2$)	
R527	$C_6H + C_6H_2$	→	*Polymer*	11.7	1.3×10^{-10}	Est. as k($C_2H + C_2H_2$)	
Aromatics							
R528	$C_6H_5 + C_2H_2$	→	*Polymer*	34.5	$k_0 = 4.96 \times 10^{-19} T^{-4.08} e^{403/T}$	Wang & Frenklach (1994)	500 – 2500
					$k_\infty = 6.64 \times 10^{-17} T^{1.56} e^{-1912/T}$	〃	300 – 2500
R529	$C_6H_5 + C_6H_6$	→	*Polymer*	11	$1.6 \times 10^{-12} e^{-2168/T}$	Park et al. (1999)	298 – 1330
R530	$C_6H_5 + HC_3N$	→	*Polymer*	17.1	$k_0 = 4.96 \times 10^{-19} T^{-4.08} e^{403/T}$	Est. as k($C_2H_2 + C_6H_5$)	
					$k_\infty = 6.64 \times 10^{-17} T^{1.56} e^{-1912/T}$	〃	
Pure Nitriles							
R531	$H_2CN + HCN$	→	*Polymer*	35	$1.1 \times 10^{-12} e^{-900/T}$	Est. as k($C_2H_3 + HCN$)	
R532	$H_2CN + CH_2NH$	→	*Polymer*	33.7	$1.1 \times 10^{-12} e^{-900/T}$	Est. as k($C_2H_3 + HCN$)	
R533	$CN + C_2H_3CN$	→	*Polymer*	35.4	$3.02 \times 10^{-11} e^{103.6/T}$	Butterfield et al. (1993)	297 – 528
R534	$CN + C_2N_2$	→	*Polymer*	35.5	$2.2 \times 10^{-21} T^{2.7} e^{-325/T}$	Yang et al. (1992a)	300 – 740
R535	$CN + C_4N_2$	→	*Polymer*	35.5	5.4×10^{-13}	Seki et al. (1996)	300
Copolymers							
R536	$C_4H + HC_3N$	→	*Polymer*	18.4	$8.6 \times 10^{-16} T^{1.80} e^{474/T}$	Est. as k($C_2H + C_2H_2$)	
R537	$C_3N + C_4H_2$	→	*Polymer*	18	$8.6 \times 10^{-16} T^{1.80} e^{474/T}$	Est. as k($C_2H + C_2H_2$)	
R538	$C_4H_3 + HC_3N + M$	→	*Polymer*	17.6	$k_0 = 3.3 \times 10^{-30} e^{-740/T}$	Est. as k_0($H + C_2H_2 + M$)	
					$k_\infty = 5.53 T^{-3.89} e^{-4635/T}$	Est. as k($C_2H_2 + C_4H_3$), Wang & Frenklach (1994)	

$$C_{2n}H_2 + C_2H \rightarrow C_{2n+2}H_2 + H.$$

In addition to the above, the photolysis of the polyynes formed leads to the production of polyyne radicals (C_4H, C_6H, C_8H) which also enhance the polymerization. On the other hand, the production of polyynes is constrained by the acetylenic recycling of the C_2H and other polyyne radicals through reactions with the saturated hydrocarbons in the atmosphere from which the main contribution comes from methane:

$$C_2H + CH_4 \rightarrow C_2H_2 + CH_3.$$

Due to the high number densities of the saturated species, this recycling is very efficient and the contribution of increasing order polyynes will have a decreasing effect on the total haze production (Wilson & Atreya, 2003). According to laboratory measurements, (Opansky & Leone, 1996a; Chastaing et al., 1998; Vakhtin et al., 2001a), the reaction of the ethyl radical with acetylene proceeds readily even at very low temperatures. Since the reaction rates for the higher order polyyne radicals have not been measured at low temperatures, these were estimated from their equivalent reactions with the C_2H radical. All reactions leading to the formation of hydrocarbons with more than ten carbon atoms are considered to lead to the formation of haze. Based on this, the reactions used in the model as haze pathways in Titan's atmosphere from this process, are:

$$C_4H + C_6H_2 \rightarrow \textit{polymer}$$
$$C_6H + C_4H_2 \rightarrow \textit{polymer}$$
$$C_6H + C_6H_2 \rightarrow \textit{polymer}.$$

Similar to polyynes, cyanopolyynes are also possible haze precursors. These are formed in the same way as polyynes but with the ethynyl radical replaced by its isoelectronic nitrile equivalent, the cyanogen, CN. The process is initiated with the reaction of the CN radical with unsaturated hydrocarbons and nitriles giving cyanoacetylene, acrylonitrile and dicyanoacetylene, as described in the chemistry section. The polymerization is considered to proceed with further addition of the CN radical on the produced polyynes and nitriles. In the model calculations, the reaction used is:

$$CN + C_6H_2 \rightarrow \textit{polymer}.$$

The above pathways lead to the production of polymers which due to their structural form, are characterized by large C/N and C/H ratios, which are not supported by the laboratory results. This suggests that if indeed the haze in Titan's atmosphere is similar to the analogs produced in the laboratories, these polymers must have a small contribution to the total haze production.

Polymers of HCN could lead to C/N ratios closer to those observed in the laboratory. In these, the polymerization starts with the production of an $(HCN)_2$ dimer and subsequent addition of HCN molecules leads to poly-HCN structures (Rettig et al., 1992). Even though HCN structures were defined in the haze analogs produced (Coll et al., 1999), the optical properties of pure poly-HCN

structures do not exhibit the correct wavelength dependence inferred from Titan's geometric albedo (Khare et al., 1994) and hence they are not expected to have a major contribution to bulk haze production. Thompson & Sagan (1989) suggested the possible formation of heteropolymeric structures from the addition of R-CN structures and CN radicals on nitriles. In order to take into consideration the R-CN type process, the following pathway was suggested:

$$H_2CN + HCN \rightarrow \textit{polymer}.$$

The rate for this reaction has not been measured and in previous works it was estimated with the rate of the C_2H_3 + HCN reaction (Monks et al., 1993), due to the similarity observed for the rates of reaction between H_2CN and C_2H_3 with H and N. Wilson & Atreya (2003) suggested that the measured rate, is strongly overestimated based on their calculated vertical profiles for C_2H_3CN and HC_3N, which were above the observed values. In addition, using the measured rate for the H_2CN + HCN reaction, led to large haze production in the lower atmosphere, which was above the magnitude defined by microphysical models. Hence they estimated the rate of the latter reaction to be 1000 times smaller than that of Monks et al. (1993).

This requirement for a lower rate could possibly originate from the presence of the CN radical on the two reactants. Seki & Okabe (1993) have measured the rates for the reaction of CN radicals with diacetylene and dicyanoacetylene and reported the first to be about 500 times faster than the second, while Butterfield et al. (1993) found that the rate of reaction between CN and acrylonitrile is significantly smaller that the rate for reaction with ethylene. This decrease in the rate of CN reaction between hydrocarbons and their equivalent H/CN replaced nitriles is attributed to a significant electron withdrawing effect of the cyanogen group. It could be possible that the same process reduces the rate of the H_2CN + HCN reaction relative to its C_2H_3 equivalent.

A sensitivity test of the model results for different values of the above reaction rate was performed (see Chapter 5). The results suggest that the chemical loss of atmospheric molecules in the growth of the polymer structures described here, to the monomer size beyond which microphysics takes over, has an important role in the total haze production. The way this loss is included in the model calculations is described in the following section.

Pathways based on the CN addition process on nitrile species are described by:

$$CN + C_2N_2 \rightarrow \textit{polymer}$$
$$CN + C_4N_2 \rightarrow \textit{polymer}$$
$$CN + C_2H_3CN \rightarrow \textit{polymer}.$$

The rates for the last two reactions have been measured, as discussed above, while the rate for the CN reaction with cyanogen was measured by Yang et al. (1992b). Although these measurements were performed at temperature conditions higher than in Titan's atmosphere, the radical character of the reactions with the small negative temperature dependence suggests that these reactions can take place at very low temperatures with rates close to the above.

Clarke & Ferris (1997) suggested a pathway for HC_3N/C_2H_2 copolymer mixtures. HC_3N was found to be much more reactive in polymerization than HCN and that the copolymers formed could exhibit the necessary wavelength dependence, something which the pure polymers of either case did not do. For this case the reactions used are:

$$C_4H_2 + C_3N \rightarrow \textit{polymer}$$
$$HC_3N + C_4H \rightarrow \textit{polymer}.$$

The rates for these reactions are also not measured, however, based on the relative rates of abstraction between C_2H and C_3N radicals with hydrocarbons (Clarke & Ferris, 1995), they can be estimated with their C_2H equivalent. Lebonnois et al. (2002) have included also a possible pathway based on:

$$HC_3N + C_4H_3 \rightarrow \textit{polymer}$$

This is a pressure-dependent reaction and we have used the rate expression of Wang & Frenklach (1994).

Pathways including aromatic hydrocarbons have also been suggested. PAHs are well known to exist in the low temperatures of the interstellar medium (Allamandola et al., 1989) in significant amounts. Since benzene, C_6H_6, the simplest aromatic hydrocarbon, has been detected on Titan (Coustenis et al., 2003), PAH could also be a possible pathway for haze formation. The production of PAHs is considered to proceed through the reaction of benzene molecules with acetylene (Bauschlicher & Ricca, 2000):

$$C_2H_2 + C_6H_5 \rightarrow \textit{polymer}.$$

The rate for this reaction has been measured but, as in the case of benzene formation, the measurements were performed at high temperatures. Yu et al. (1994) measured the rate in the temperature range 297 - 523 K, while Wang & Frenklach (1994) preformed theoretical simulations for the rate in the range 300 - 2500 K. Both studies suggest that the overall reaction rate is pressure-independent while the products (either stabilized adduct which leads to the formation of PAHs or dissociation of the initially vibrationally excited adduct) have a strong temperature and pressure dependance, with the adduct becoming increasingly more important as the pressure increases and the temperature decreases. Another pathway considered in previous works is the one of the direct addition of phenyl radical on a benzene molecule:

$$C_6H_5 + C_6H_6 \rightarrow \textit{polymer}$$

with the rate for this reaction measured by Park et al. (1999).

For the case of the N-PACs, Ricca et al. (2001) investigated the possible incorporation of nitrogen atoms in the PAH structures. Considering reactions between C_6H_5, HCN and C_2H_2 they found that the formation of a second ring with a nitrogen atom in the skeleton through radical reactions, is strongly prohibited by high energy barriers unless the aromatic molecules are vibrationally excited. Yet once such a ring is formed, the presence of the nitrogen atom

promotes the formation of the next ring. On the other hand reactions with cyanoacetylene and acetylene which lead to the formation of rings with CN as a side group, have barriers which are very close to those for the case of pure PAHs and hence can proceed in Titan's low temperatures. Thus the following reaction has been included as a possible pathway in the model:

$$HC_3N + C_6H_5 \rightarrow \textit{polymers}$$

and the rate was estimated with that of acetylene reaction with phenyl.

Finally, another pathway with methyleneimine, based on the suggestions of Redondo et al. (2006) has been included in the simulation. CH_2=NH is a suitable compound for polymerization and could be a precursor for haze production. The same component was also found in the low pressure tholins produced in the Imanaka et al. (2004) experiments. The growth of this polymer could be initiated by the addition of the H_2CN radical, as for the case of the HCN polymerization:

$$H_2CN + CH_2{=}NH \rightarrow \textit{polymer}.$$

Some of the above pathways have been used in photochemical models in order to test their validity (Lebonnois et al., 2002; Wilson & Atreya, 2003). Even though their results showed that the suggested reactions lead to column haze production rates which are close to those needed by microphysical models for the reproduction of the geometric albedo, the effects of the derived haze production rates on the radiation field and the temperature structure were not tested, as done in the present work.

3.3.1 Monomer size

The above pathways describe the production and chemical growth of the haze precursors by means of polymerization. This growth is considered to proceed until the precursors reach a specific size beyond which the chemical growth ceases and the laws of microphysics control their evolution. This is the monomer stage in our work. It should be made clear that the monomers in this work do not correspond to the monomers used in other microphysical models of fractal-type particles where the monomers define the transition region between spherical growth of particles and fractal growth (Rannou et al., 2003). In the present work, the monomers correspond to the lower size limit of haze particles from which all others are produced through coagulation. The size of the monomers was set to 7.35 Å. This choice was based on laboratory results which showed that nucleation of polymers to particles starts at masses between 600 - 2000 amu depending on the chemical composition of the particles and the environment in which they nucleate (Dimitrov & Bar-Nun, 1994; Richter & Howard, 2000). Taking as a typical value the mass for the monomers to be of the order of 1000 amu and considering the mass density of the particles to have the typical value of 1 gm/cm^3 (an assumption used in all microphysical models) we obtain the above radius for the spherical monomers.

3.3.2 Chemical loss to haze

The impact of haze formation on the chemical loss of species is also an important issue for atmospheric composition. The production of haze monomers discussed above, does not include the chemical growth of the polymers but only the production of an initial dimer. From the monomer point of view this is realistic because the chemical growth of these dimers provides the final monomer population. The chemical addition of molecules to these structures will only change their size and not their number density. Yet, for the atmospheric composition there is a sink for the gas molecules lost during the chemical growth of the dimers that has to be taken into account. This loss was estimated based on the assumed mass of the haze monomers and that the chemical growth of the dimers for each suggested pathway is based on the smallest mass molecule. That is, the growth of the initially formed dimers proceeds with the addition of the smallest of the two molecules that form it. Under this condition the chemical loss for atmospheric gases can be estimated from:

$$\frac{\partial n_i}{\partial t} = -\varepsilon_i Pr_i \tag{3.1}$$

were n_i is the number density of the gas molecule which is lost during the chemical growth of the dimer described through pathway i, Pr_i is the production rate of dimers for this pathway and ε_i is the number of molecules that have to be added onto the dimer in order to reach the mass of the monomer. The ε factors are presented in Table 3.2 for each pathway. Their values range between 11 and 35.5, which means that the total chemical loss is significantly larger than the loss due to the dimer formation.

Bibliography

Allamandola, L.J., Tielens, A.G.G.M., Barker, J.R., 1989. Interstellar polycyclic aromatic hydrocarbons: the infrared emission bands, the excitation/emission mechanism, and the astrophysical implications. Astrophys. J. Suppl. 71, 733-775.

Allen, M., Pinto, J.P., Yung, Y.L., 1980. Titan: aerosol photochemistry and variations related to the sunspot cycle. Astrophys. J. 242, L125-L128.

Bar-Nun, A., Kleinfeld, I., Ganor, E., 1988. Shape and optical properties of aerosols formed by photolysis of acetylene, ethylene and hydrogen cyanide. J. Geophys. Res. 93, 8383-8387.

Bauschlicher Jr, C.W., Ricca, A. Mechanisms for polycyclic aromatic hydrocarbon (PAH) growth. Chem. Phys. Lett. 326, 283-287.

Butterfield, M. T., Yu, T., Lin, M.C., 1993. Kinetics of CN reactions with allene, butadiene, propylene and acrylonitrile. Chem. Phys. 169, 129-134.

Chassefiere, E., Cabane, M., 1995. Two formation regions for Titan's hazes: indirect clues and possible synthesis mechanism. Planet. Space Sci. 43, 91•103.

Chastaing, D., James, P.L., Sims, I.R., Smith, I.W.M., 1998. Neutral-neutral reactions at the temperatures of interstellar clouds. Rate coefficients for reactions of C_2H radicals with O_2, C_2H_2, C_2H_4 and C_3H_6 down to 15 K. Faraday Disc. 109, 165-181.

Clarke, D.W., Ferris, J.P., 1995. Photodissociation of cyanoacetylene: Application to the atmospheric chemistry of Titan. Icarus 115, 119-125.

Clarke, D.W., Ferris, J.P., 1997. Titan Haze: Structure and properties of the cyanoacetylene and cyanoacetylene-acetylene photopolymers. Icarus 127, 158-172.

Coll, P., Coscia, D., Gazeau, M.-C., de Vanssay, E., Guillemin, J.C., Raulin, F., 1995. Organic chemistry in Titan's atmosphere: new data from laboratory simulations at low temperature. Adv. Space Res. 16, 93-103.

Coll, P., Coscia, D., Gazeau, M.-C., Guez, L., Raulin, F., 1998. Review and latest results of laboratory investigations of Titan's aerosols. Origins Life Evol. Biosphere 28, 195-213.

Coll, P., Coscia, D., Smith, N., Gazeau, M.-C., Ramirez, S.I., Cernogora, G., Israël, G., Raulin, F., 1999. Experimental laboratory simulation of Titan's atmosphere: aerosols and gas phase. Planet. Space Sci. 47, 1331•1340.

Coustenis, A., Salama, A., Schulz, B., Ott, S., Lellouch, E., Encrenaz, Th., Gautier, D., Feuchtgruber, H., 2003. Titan's atmosphere from ISO mid-infrared spectroscopy. Icarus 161, 383-403.

Dimitrov, V., Bar-Nun, A., 2002. Aging of Titan's aerosols. Icarus 156, 530-538.

Ehrenfreund, P., Boon, J.J., Commandeur, J., Sagan, C., Thompson, W.R., Khare, B., 1995. Analytical pyrolysis experiments of Titan aerosol analogues in preparation for the Cassini•Huygens mission. Adv. Space Res. 15, 335•342.

Hudgins, D.M., Bauschlicher, C.W., Allamandola, L.J., 2005. Variation in the peak position of the 6.2 μm interstellar emission future: a tracer of N in the interstellar polycyclic aromatic hydrocarbon population. Astrophys. J. 632, 316-332.

Imanaka, H., Khare, B.N., Elsila, J.E., Bakes, E.L.O., McKay, C.P., Cruikshank, D.P., Sugita, S., Matsui, T., Zare, R.N., 2004. Laboratory experiments of Titan tholin formed in cold plasma at various pressures: implications for nitrogen-containing polycyclic aromatic compounds in Titan haze. Icarus 168, 344-366.

Israël G. and 21 coworkers, 2005. Complex organic matter in Titan's atmospheric aerosols from in situ pyrolysis and analysis. Nature, doi:10.1038/nature04349

Khare, B.N., Sagan, C., Arakawa, E.T., Suits, F., Calcott, T.A., Williams, M.W., 1984a. Optical constants of organic tholins produced in a simulated Titanian atmosphere: from soft X-ray to microwave frequencies. Icarus 60, 127-137.

Khare, B.N., Sagan, C., Thompson,W.R., Arakawa, E.T., Suits, F., Callcott, T.A., Williams, M.W., Shrader, S., Ogino, H., Willingham, T.O., Nagy, B., 1984b. The organic aerosols of Titan. Adv. Space Res. 4, 59-68.

Khare, B.N., Sagan, C., Thompson, W.R., Arakawa, E.T., Meese, C., Tuminello, P.S., 1994. Optical properties of poly-HCN and their astronomical applications. Can. J. Chem. 72, 678-694.

Khare, B.N., Bakes, E.L.O., Imanaka, H., McKay, C.P., Cruikshank, D.P., Arakawa, E.T., 2002. Analysis of the time-dependent chemical evolution of Titan haze tholin. Icarus 160, 172•182.

Lebonnois, S., Bakes, E.L.O., McKay, C.P., 2002. Transition from gaseous compounds to aerosols in Titan's atmosphere. Icarus 159, 505-517.

McDonald, G.D., Thompson, W.R., Heinrich, M., Khare, B.N., Sagan, C., 1994. Chemical investigation of Titan and Triton tholins. Icarus 108, 137-145.

McKay, C.P., 1996. Elemental composition, solubility and optical properties of Titan's organic haze. Planet. Space Sci. 44, 741-747.

Monks, P.S., Romani, P.N., Nesbitt, F.L., Scanlon, M., Stief, L.J., 1993. The kinetics of the formation of nitrile compounds in the atmosphere of Titan and Neptune. J. Geophys. Res. 98, 17115-17122.

Opansky, B.J., Leone, S.R., 1996a. Low-temperature rate coefficients of C_2H with CH_4 and CD_4 from 154 to 359 K. J. Phys. Chem. 100, 4888-4892.

Park, J., Burova, S., Rodgets, A.S., Lin, M.C., 1999. Experimental and theoretical studies of the C_6H_5 + C_6H_6 reaction. J. Phys. Chem. 103, 9036-9041.

Rages, K., Pollack, J.B., 1980. Titan aerosols: Optical properties and vertical distribution. Icarus 41, 119-130.

Ramirez, S.I., Coll, P., da Silva, A., Navarro-Gonzalez, R., Lafait, J., Raulin, F., 2002. Complex refractive index of Titan's aerosol analogues in the 200•900 nm domain. Icarus 156, 515•529.

Rannou, P., McKay, C.P., Lorenz, R.D., 2003. A model of Titan's haze of fractal aerosols constrained by multiple observations. Planet. Space Sci. 51, 963-976.

Redondo, P., Pauzat, F., Ellinger, Y., 2006. Theoretical survey of the NH + CH_3 potential energy surface in relation to Titan atmospheric chemistry. Planet. Space Sci. 54, 181-187.

Rettig, T.W., Tegler, S.C., Pasto, D.J., Mumma, M.J., 1992. Comet outbursts and polymers of HCN. Astrophys. J. 398, 293-298.

Richter, H., Howard, J.B., 2000. Formation of polycyclic aromatic hydrocarbons and their growth to soot- a review of chemical reaction pathways. Prog. Energy Combust. Sci. 26, 565-608.

Ricca, A., Bauschlicher Jr., C.W., Bakes, E.L.O., 2001. A computational study of the mechanisms for the incorporation of a nitrogen atom into polycyclic aromatic hydrocarbons in the Titan haze. Icarus 154, 516•521.

Sagan, C., Khare, B.N., 1979. Tholins: organic chemistry of interstellar grains and gas. Nature 277, 102-107.

Scattergood, T.W, Lau, E.Y, Stone, B.M., 1992. Titan's aerosols. I. Laboratory investigations of shapes, size distributions, and aggregation of particles produced by UV photolysis of model Titan atmospheres. Icarus 99, 98-105.

Seki, K., Okabe, H., 1993, Photochemistry of acetylene at 193.3 nm. J. Phys. Chem. 97, 5284-5290.

Thompson, W.R., Sagan, C., 1989. Atmospheric formation of organic heteropolymers from N_2 + CH_4: Structural suggestions for amino acid and oligomer precursors. Origins of Life 19, 503-504.

Thompson, W.R., Henry, T.J., Schwartz, J.M., Khare, B.N., Sagan, C., 1991. Plasma discharge in N_2+CH_4 at low pressures: Experimental results and application to Titan. Icarus 90, 57-73.

Tran, B.N., Joseph, J.C., Ferris, J.P., Persans, P.D., Chera, J.J., 2003. Simulation of Titan haze formation using a photochemical flow reactor: the optical constants of the polymer. Icarus 165, 379•390.

Vakhtin A.B., Heard, D.E., Smith, I.W.M., Leone, S.R., 2001. Kinetics of reactions of C_2H radical with acetylene, O_2, methylacetylene, and allene in a pulsed Laval nozzle apparatus at T=103 K. Chem. Phys. Lett., 344, 317-324

Wang, H., Frenklach, M., 1994. Calculations of rate coefficients for the chemically activated reactions of acetylene with vinylic and aromatic radicals. J. Phys. Chem. 98, 1465•1489.

West, R.A., Smith, P.H., 1991. Evidence for aggregate particles in the atmospheres of Titan and Jupiter. Icarus 90, 330•333.

Wilson, E.H., Atreya S.K., 2003. Chemical sources of haze formation in Titan's atmosphere. Planet. Space Sci. 51, 1017-1033.

Yang, D. L., Yu, T., Wang, N.S., Lin, M.C., 1992b. Temperature dependence of cyanogen radical reactions with selected alkanes: CN reactivities towards primary, secondary and tertiary C-H bonds. Chem. Phys. 160, 307-315.

Yu, T., Lin, M.C., Melius, C.F., 1994. Absolute rate constant for the reaction of phenyl radical with acetylene. Int. J. Chem. Kin. 26, 1095-1104.

Chapter 4

Chemical Composition

This chapter presents the results of the photochemical modelling. These provide the basis for the description of the haze-formation pathways presented in the following chapter. The species vertical profiles that will be presented in turn implicitly include the effects of the haze structure on the radiation field and on the temperature structure. The calculated spectrally-resolved geometric albedo that corresponds to the radiation field that determines the species vertical profiles presented hereafter and the corresponding vertical temperature profile, are discussed in Chapter 6. The species vertical profiles are validated against the latest measurements from the Cassini/Huygens mission and previous observations. Upper atmospheric neutral abundances were retrieved from neutral (Waite et al., 2005) and ion (Vuitton et al., 2006a,b) spectra of the INMS instrument, while stratospheric vertical profiles and abundances were retrieved from the CIRS limb (Vinatier et al., 2006) and nadir (Coustenis et al., 2007) spectra, respectively. In addition, ground-based observations for some of the nitrile species from Marten *et al.* (2002) are presented.

4.1 Eddy mixing profile

One dimensional photochemical models, rely on the eddy mixing coefficient for the inclusion of turbulent diffusion effects on the simulated species vertical distribution. As discussed previously (see 2.3.3), this parameter is usually derived by fitting the measured profiles of species whose vertical structure is controlled only by transportation (inert species). Previous photochemical models have used methane (CH_4) and hydrogen cyanide (HCN) for this purpose. This of course does not mean that these species are inert; after all the complex chemistry of Titan's atmosphere is initiated from methane photodissociation. Their characteristic time for transport in some regions of the atmosphere is considerably smaller than the characteristic times of photochemical variation and this allows the use of the above molecules as mixing tracers.

Methane is expected to become diffusively separated in the upper atmosphere,

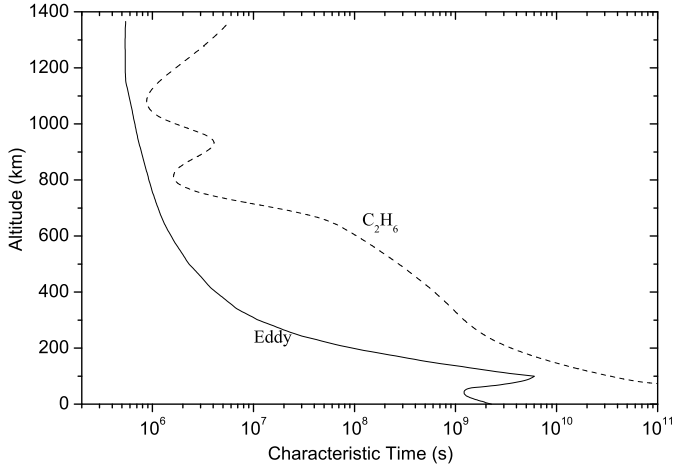

Figure 4.1: Characteristic life time of C_2H_6 relative to characteristic time of transport due to eddy mixing.

above the homopause, while in the lower atmosphere, above the tropopause, its mole fraction is constant and hence no conclusions about the effects of turbulence can be retrieved from there. On the other hand, HCN is produced in the upper atmosphere and as it settles towards the surface, its chemical lifetime increases compared to the diffusion characteristic time, due to its low reactivity with other species. Hence the CH_4 vertical profile and the location of the homopause and slope of its increase due to diffusive separation was used to retrieve information on the extent of turbulent mixing in the thermosphere, while HCN was used for the determination of the mixing in the lower atmosphere.

After the success of the Cassini/Huygens mission, the above approach has become equivocal. Methane's abundance in the upper atmosphere has been measured by Cassini, putting an end to the controversy originating from the initially retrieved value by the Voyager UVS observations (Smith et al., 1982) and their later re-analysis by Vervack et al. (2004). The analysis of the INMS measurements (Waite et al., 2005; Yelle et al., 2006), showed that methane's mole fraction is 2.71 $\pm$ 0.1 % at 1174 km. Based on a diffusion model and an isothermal temperature structure they inferred an eddy mixing coefficient of about $4^{+4}_{-3}\times10^9$ cm^{-2}s^{-1}, assuming that it is constant in the region between 1200 and 1550 km and that methane does not escape. Yet, allowing methane to escape, the above measured methane mole fraction can be reproduced using a lower eddy mixing coefficient that moves the location of the homopause to lower altitudes (Yelle et al., 2005, 2006).

As was shown by Vinatier et al. (2006), a problem arises if a single mix-

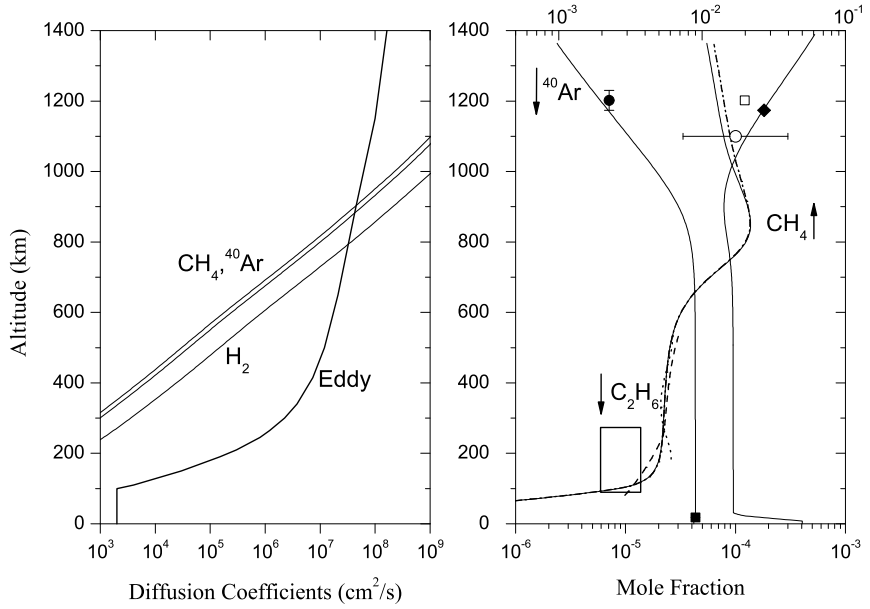

Figure 4.2: The retrieval of the eddy diffusion coefficient used in the model calculations. The left panel presents the derived vertical eddy mixing profile that provided the best fit to the calculated vertical profiles of the simulated species, along with the molecular diffusion coefficients for argon, methane and molecular hydrogen. The altitude at which the argon molecular diffusion coefficient intersects the eddy mixing profile, provides an estimation of the region where the homopause is placed. The right panel presents the model calculated vertical profiles of the species used for the retrieval of the mixing profile. The filled circle and square correspond to the argon measurements from INMS (Waite et al. 2005) and GCMS (Niemann et al., 2005) measurements, respectively. The open square and circle are the INMS measurements for ethane (Waite et al., 2005, Vuitton et al., 2006a) and the filled diamond is the INMS measurement for methane (Yelle et al., 2006). The box represents the CIRS-retrieved range of abundances for C_2H_6 at 33°N (Coustenis et al., 2007) and the dashed and dotted lines correspond to the CIRS-inferred profiles of ethane at 15°S and 80°N, respectively (Vinatier et al., 2006). Solid lines correspond to the model results, while the dashed-dotted line represents the sensitivity of the model ethane profile to the N_2 dissociative photoionization scheme.

ing profile is used to fit the vertical distributions of HCN and C_2H_6. The modelling of the HCN profile requires the use of strong eddy mixing in the lower atmosphere, which when applied leads to the rapid destruction of ethane. This occurs because the large downward fluxes, generated by the strong mixing, rapidly transport C_2H_6 towards the lower stratosphere where it condenses and is irreversibly lost. This problem was initially reported by Lara *et al.* (1996), who also found difficulties in matching at the same time the HCN profile and the C_2H_X hydrocarbons with a single mixing profile for all species. This led to the conclusion that, possibly, a loss mechanism for HCN is present in the lower atmosphere, efficient enough to constrain the HCN vertical profile without the use of a large eddy mixing coefficient.

From a different point of view, the recent analysis of ion spectra from INMS (Vuitton et al., 2006a) has identified the presence of methyleneimine (CH_2NH) along with other new nitrile species and also provided an abundance measurement for HCN, with a mole fraction of 2×10^{-4} at 1200 km, which is smaller than the abundances given in this region by previous photochemical models. CH_2NH is an intermediate species in HCN production, the photochemical evolution of which has not been followed by previous models. Its inclusion could possibly explain the overestimation of the HCN abundance in the upper atmosphere and also provide a loss mechanism in the lower atmosphere through its polymerization. These issues are addressed in the following paragraphs, describing the results of the photochemistry.

Based on the above discussion, it is evident that there are processes that control the HCN vertical profile, and also the nitrile chemistry in general, that are not clear yet and have to be investigated. Hence, in the current work the eddy mixing profile retrieval was not based on HCN but was used as a secondary validation parameter. Ethane was used in its place. As a saturated hydrocarbon it is characterized by low chemical reactivity, while due to the overlap of its absorption cross section in the UV region with that of methane, its photochemical life time is significantly large. As shown in Fig. 4.1, where the characteristic times for mixing and photochemical changes are presented, ethane's vertical profile is mainly controlled by mixing below 700 km making it appropriate as a tracer species.

In addition to the above tracers, we also have now information for the mixing in Titan's atmosphere from a really inert species, argon (Ar). INMS (Waite et al., 2005) has detected ^{40}Ar at a $7.1 \pm 0.1\times10^{-6}$ mixing ratio in the upper atmosphere, while the GCMS instrument onboard the Huygens probe has given 4.32 ± 0.1 x 10^{-5} in the lower atmosphere, close to the tropopause (Niemann et al., 2005). Argon's vertical profile is constant since it does not react with other species in the atmosphere and varies only as it moves into the diffusive separation region. Hence its variation with altitude provides realistic information about the turbulence effects and can set constraints on the minimum and maximum values of eddy mixing in the atmosphere.

The eddy mixing coefficient used in the calculations is presented in Fig. 4.2 along with the calculated vertical profiles of the above species used for its derivation. Using only argon as a tracer for the atmospheric eddy mixing is not

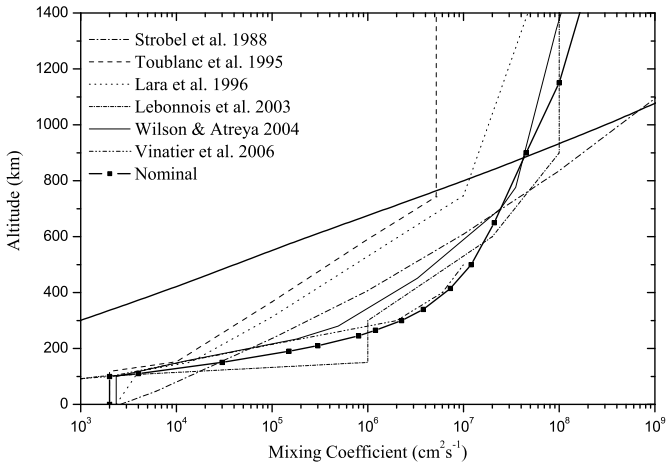

Figure 4.3: Eddy diffusion profiles used in previous photochemical models. The solid line traversing all mixing profiles is the methane diffusion coefficient.

sufficient, because its vertical profile, defined by the above two altitude measurements, can be fitted with different altitude variations of the mixing profile. That is why at least one more tracer species is necessary. In order to keep the simulated ethane vertical profile close to the CIRS observed values, which suggest a rather constant variation with altitude in the region between 200 and 500 km (Vinatier et al., 2006), a strong eddy mixing profile must be considered. In the lower atmosphere, the magnitude of the mixing profile controls the flow of species towards the condensation region. The values of the eddy profile in this region affect the ethane profile, shifting the whole distribution towards larger (smaller) mole fractions for smaller (larger) values of the mixing coefficient. Having this region constrained, the upper atmosphere mixing profile was varied until a good fit to the argon measurement was achieved.

A comparison with the eddy mixing profiles used in previous photochemical models is provided in Fig. 4.3. It is obvious that the current mixing profile is significantly larger in the lower atmosphere, between 250 and 650 km than the previously suggested profiles in order to constrain the ethane profile to a vertical variation similar to the observed one. The new profile follows very closely the profile suggested by Vinatier et al. (2006) which was calculated based on the CIRS retrieved ethane profile for the region below 500 km. Above this region, our mixing profile is close to the Wilson & Atreya (2004) profile but slightly larger in the upper atmosphere above 1000 km, in order to fit the argon measurement. Between 150 and 250 km, Hourdin et al. (2004) derived an estimate for the eddy mixing profile based on GCM simulations. They suggested a ver-

tical mixing between 10^6 and 5×10^7 cm^2s^{-1}. The lower limit of this range is close to the magnitude of the current mixing profile at 250 km but the structure of the latter suggests a rapid decrease of the mixing coefficient at lower altitudes in order to constrain the loss of the species due to condensation. It should be kept in mind that transport in other directions than the vertical can significantly affect the species profiles and explain the differences in the mixing profiles derived by GCM simulations and 1D models.

The position of the homopause, based on the argon molecular diffusion coefficient (which is very close to that of methane used in previous models) and the calculated vertical temperature profile and number density, is near 900 km, which is close to the 850 km retrieved by Wilson & Atreya (2004). Apart from the use of different photochemical schemes and reaction rates, the variability observed between previous photochemical models for the shape of the mixing profile and the position of the homopause, is related to the fact that the methane stratospheric abundance was not well constrained at that time but varied significantly among different simulations, while the thermospheric abundance was overestimated. Now, from the Cassini/Huygens mission there are significantly better constraints for the methane profile, as discussed in §1.2.3.

In addition, it becomes apparent that in order to provide a match to the INMS measured methane abundance in the upper atmosphere (Yelle et al., 2006), a strong eddy coefficient cannot be applied, since this would lead to a large overestimation of the argon profile. This leaves us with the second choice, that of methane escape. In the profile presented in Fig. 4.2 methane was allowed to escape from the top of the simulated atmosphere with a flux equal to 70% of the diffusive flux at that level, with the latter reaching at these altitudes its diffusion limited value. Under this condition the simulated methane mole fraction is very close to the observed one. The sensitivity of the thermospheric methane profile on the escaping flux used is presented in Fig. 4.4.

4.2 Validation with Cassini/Huygens

The model vertical profiles for the main hydrocarbons, and nitriles are described in the following paragraphs and compared with the measurements of the instruments on board Cassini. Before comparing them with the observations, it is important to note that the model solves for a solar zenith angle of 60°, which corresponds to mid-latitude conditions, so that the derived profiles should, in principle, lie between the equatorial and northern vertical profiles retrieved from CIRS limb spectra (Vinatier et al., 2006). The polar profiles are affected by the downwelling of air masses, i.e. the Hadley cell. The subsiding cell at the winter North pole, enhances the transport of species formed in the upper atmosphere towards the lower layers, which explains the latitudinal variations observed. Such a process is not described under the 1D character of our simulation. We furthermore compare with the 33°N values of the CIRS retrieved stratospheric abundances from nadir spectra (Coustenis et al., 2007), which represent mid-latitude conditions (keeping in mind the large obliquity of Titan's rotational

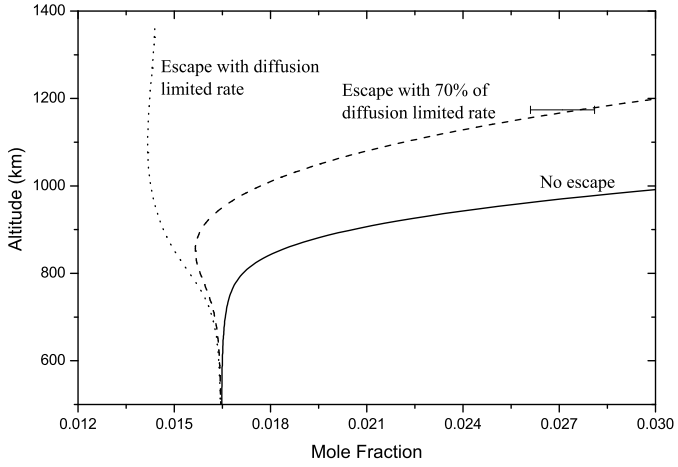

Figure 4.4: Sensitivity of methane's thermospheric profile to the escape rate assumed. The measurement is the Yelle et al. (2006) derived abundance from INMS measurements.

axis, 27°). In addition, it must be noted that the INMS derived abundances correspond to a specific flyby (T5) that represents a specific location and solar illumination conditions on Titan's disk. Although the atmosphere at the probed altitudes is expected to be well mixed (due to the observed super-rotation of the atmosphere and also suggested by the convergence of the vertical temperature profiles from different latitudes above 400 km (see Fig. 1.7), possible variations can not be excluded when comparing the global average results of the model with the local observations. Unless stated otherwise, the upper atmosphere will correspond to the INMS probed altitude region (thermosphere), while the lower atmosphere corresponds to the CIRS probed region (stratosphere).

4.2.1 Hydrocarbons

$\boldsymbol{C_2H_6}$ Ethane production is dominated by the methyl radical (CH_3) recombination rate. This is a pressure-dependent reaction and the rate used in the model description for the low-pressure limit has a major impact, not only to the final ethane profile in the upper atmosphere, but also to the profiles of ethylene, acetylene and methane. This happens because the methyl radical is related to the formation of all C_2H_X species. The efficiency of the recombination reaction at low pressures, controls the population of methyl radicals that are available for the production of ethylene through reaction with excited methylene:

$$^1CH_2 + CH_3 \rightarrow C_2H_4 + H$$

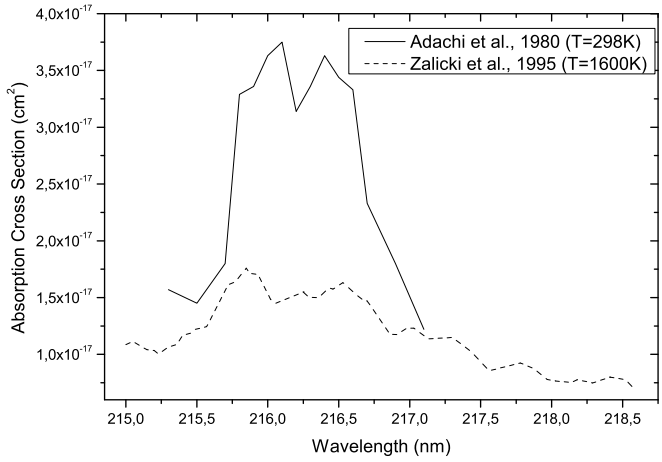

Figure 4.5: Comparison of CH_3 absorption cross section at different temperatures.

while the photolysis of ethylene is the main production pathway for acetylene in the upper atmosphere. Hence, the efficiency of recombination at low pressures controls the relative magnitudes of acetylene and ethane. In addition, CH_3 radical photolysis at 216 nm, is a significant source of excited methylene radicals:

$$CH_3 + h\nu \rightarrow {}^1CH_2 + H$$

that enhances methane's catalytic destruction and hence affects the production of all hydrocarbons.

The importance of methyl photolysis was originally noted by Yung et al. (1984) and included in all photochemical models for Titan's atmosphere since then. The absorption cross section used is the one in a very narrow region around 216 nm, which has been reported over a large range of temperatures. For room temperature, which is the lowest temperature we found in the literature, we used the Adachi et al. (1980) high resolution measurements that cover the 215.3 - 217.1 nm region. It is important to note the strong temperature dependence of the cross section (with increasing absorptivity for decreasing temperature) that can be readily seen if these cross sections are compared with the Zalicki et al. (1995) high resolution cross sections reported for the same spectral region but at 1600 K (Fig.4.5). Previous models have included the photolysis of CH_3 in this region but used the cross section of Parks et al. (1973).

The Callear & Metcalfe (1976) measurements have shown that the electronic transitions in this region overlay a continuum, which extends down to 204 nm and although it is of a smaller cross section, it could also contribute to the total photodissociation due to its broad character. Absorption peaks have also been

observed around 150 nm (Pilling et al., 1971). Photolysis at these wavelengths follow a different pathway giving (Kassner &Stuhl, 1994):

$$CH_3 + h\nu \rightarrow CH + H_2 \ .$$

Due to the significant role of CH_3 in Titan's photochemistry, it is important to have a better understanding of its absorption spectrum, which at the moment doesn't exist. The current calculations include along with the 216 nm absorption feature, the absorption cross sections at 150 nm but not the absorption continuum reported in the region between 204 and 216 nm, since there are no clear measurements of the latter.

For the methyl recombination rate, laboratory measurements have provided some results for the high-pressure limit rate over a range of temperatures, with most recent, the results of Cody et al. (2003), which were obtained for low temperature conditions, appropriate to Titan. The low-pressure limit is difficult to measure and the contribution of theoretical descriptions based on measurements at the fall-off region and at the high-pressure limit, was necessary in order to retrieve a rate. The suggested rates found in the literature depend also on the bath gas responsible for the deactivation of the energized complex, which is usually taken to be one of either H_2, He, Ar or N_2. The extrapolation though, of the suggested low-pressure limit rates to Titan's conditions leads to results that can vary by orders of magnitude and hence produce significantly different C_2H_6 profiles (Fig. 4.6).

In the current calculations the high and low pressure rate limits given in the Cody et al. (2003) work have been initially used. Although the latter have used He as a bath gas, which could lead to smaller rates compared to those for N_2, we have used their results since they are the only ones published for low temperature conditions. A correction to the rate due to the N_2 bath in Titan's atmosphere can be performed through the theoretical estimation of Smith (2003) who calculated the ratio of the low pressure limits due to different bath gases. For the case of He and N_2 the ratio is $k_0(N_2)/k_0(He)=1.714$ although this, in general, is temperature dependent. Nevertheless using this low pressure limit for the methyl recombination produces an ethane profile that is significantly lower than what is observed. The same has been noticed by Wilson & Atreya (2004) who multiplied their low pressure limit (they used the low pressure limit rate suggested by Slagle et al. (1988), which is of similar magnitude with the Cody et al. (2003) rate) by a factor of 10. This is also suggested by ISO observations of CH_3 on Saturn (Bézard et al., 1998; Atreya et al., 1999). In view of these results this conclusion of under-estimation was adopted for the low pressure limit of methyl recombination and multiplied the above rate by 10. The model profile for ethane, with the above described rate, was presented in Fig. 4.2. In the upper atmosphere, the calculated mole fraction at 1200 km is 6.8×10^{-5} compared to the 1.2×10^{-4} retrieved by the INMS neutral spectra (Waite et al., 2005) and within the range reported based on the ion spectra (Vuitton et al., 2006a).

A different approach to this need for an enhanced low pressure limit of methyl recombination is that the population of methyl radicals is under-estimated. The

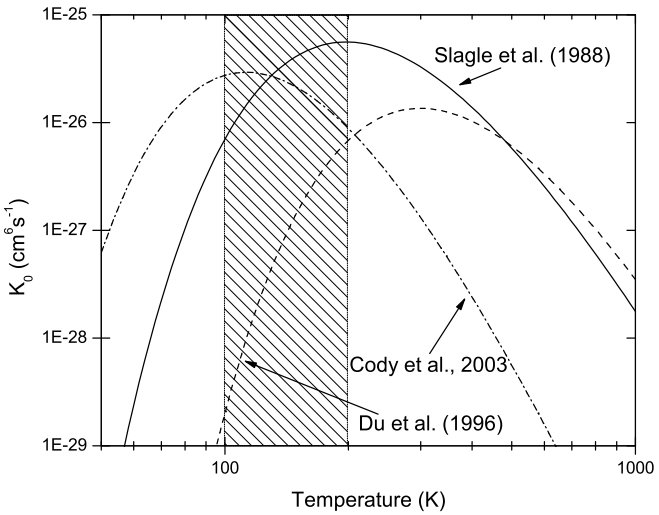

Figure 4.6: Low pressure limit rates for methyl recombination derived by different measurements and theoretical estimations. The shaded area marks the range of temperatures found in Titan's atmosphere.

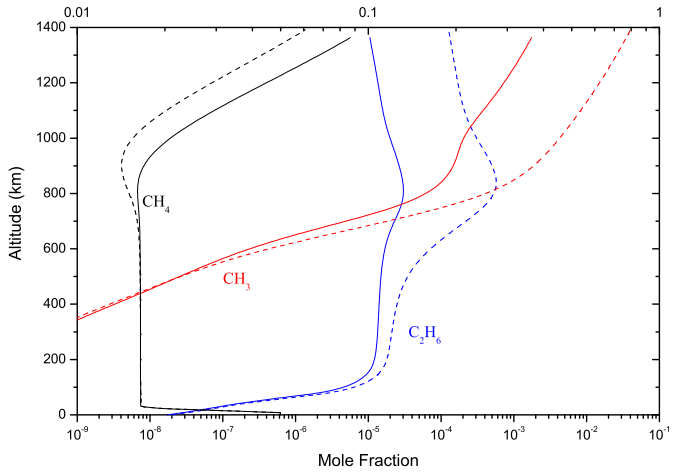

Figure 4.7: Vertical profiles of methane (top scale), ethane & methyl radical (bottom scale) with (solid line) and without (dashed line) the $^1CH_2$ collisional de-excitation included. When the $^1CH_2$ population is not de-excited, methane's destruction is enhanced with the production of a minimum around 900 km and the methyl radical's population is increased leading to an increase on the ethane's abundance. The rate of methyl recombination is set to the Cody et al. (2003) rate for both cases.

population of CH_3 radicals in the upper atmosphere can be significantly affected by the presence of excited methylene radicals ($^1CH_2$). The latter are produced in methane's photolysis (see §2.3.1) and further catalytically dissociate it giving:

$$^1CH_2 + CH_4 \rightarrow 2\ CH_3.$$

The population of $^1CH_2$ is controlled by the collisional de-excitation with N_2. If the rate for this reaction is decreased then the abundance of methyl radicals is rapidly increased leading to an increased ethane abundance in the upper atmosphere without the need for an enhanced low pressure rate relative to the one suggested by Cody et al. (2003). Further, the enhanced destruction of methane, leads to the production of a minimum to its vertical profile, situated at about 900 km. These features are presented in Fig. 4.7 where the $^1CH_2$ collisional de-excitation by N_2 has been switched off.

The dissociative ionization scheme used (see discussion in 2.3.1) has a rather small but observable impact on ethane's abundance in the thermosphere. When the N_2 dissociative ionization is assumed to yield ground state nitrogen atoms, as was done in previous models, the loss of ethane is decreased and its mole fraction at the same altitude increases to 7.8×10^{-4} (see dash-dotted line in Fig. 4.2).

C_2H_4 Ethylene has been a source of surprise in photochemical models, due to the low abundance predicted by them in the lower atmosphere, compared to the observed one. Voyager's IRIS measurements have placed the stratospheric C_2H_4 mole fraction at 1.5×10^{-7} at the equator, increasing up to 1.5×10^{-6} at the winter pole (North at that time), while ISO retrieved a disk-average value of 1.2×10^{-7} (Coustenis et al., 2003). The above values are in agreement with the mid-latitude mole fraction of 1.5×10^{-7} retrieved by CIRS nadir spectra (Coustenis et al., 2007), although this time there is a hint for a reversed latitudinal variation. The latest results from the limb spectra (Vinatier et al., 2006) have shown that ethylene's vertical profile increases monotonically below 300 km, with the difference of the two latitude profiles becoming smaller towards the surface. From previous works, only Lara *et al.* (1996) provided a vertical profile which matched the observed stratospheric abundance, by forcing the surface mole fraction to a fixed value, which is equivalent to assuming a surface emission of C_2H_4. The current model simulation, suffers from the same low estimation of the ethylene abundance (Fig. 4.8a) although it provides a mole fraction in the upper atmosphere which is in close agreement with the INMS retrieved one (Vuitton et al., 2006b).

The loss processes for ethylene in the lower atmosphere are dominated by photolysis and reaction with atomic hydrogen leading to the formation of the ethyl radical (C_2H_3). Recent results from 2-D photochemical models and GCMs have provided a possible solution for this underestimation, by suggesting that the enhancement of ethylene could be due to circulation effects (S. Lebonnois, personal communication). The downwelling flux of C_2H_4 due to the Hadley cell circulation, could lead to an enhancement in the lower atmosphere, since ethylene does not condense at the low temperature conditions found in this part of Titan's atmosphere, while most of the other species do condense. In view of

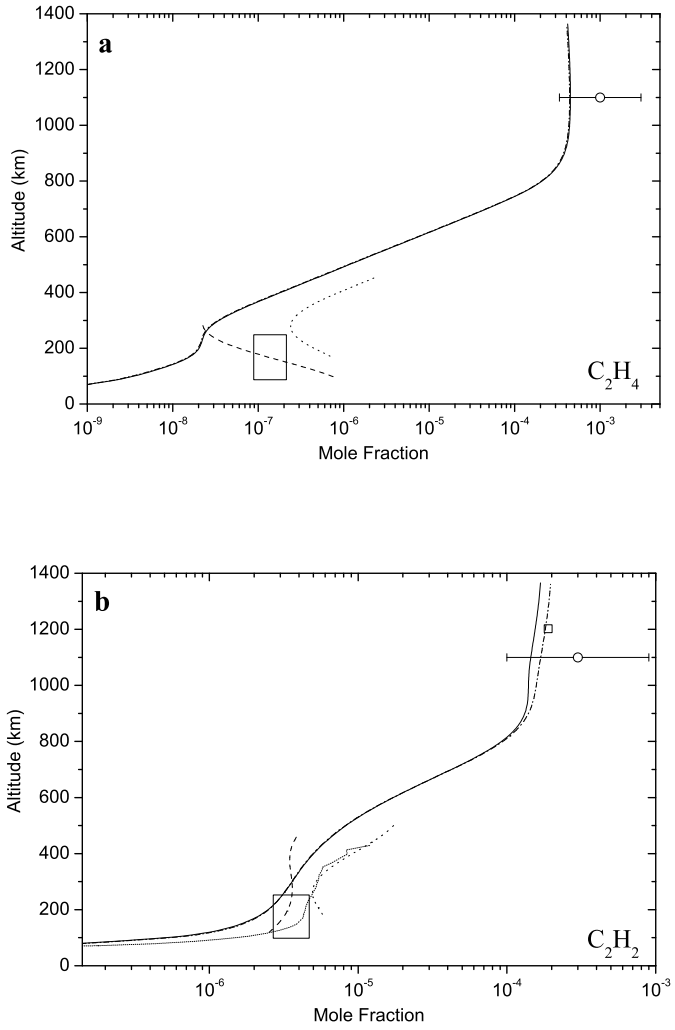

Figure 4.8: Model results for the mixing ratio of ethylene (a) and acetylene (b) in Titan's atmosphere and comparison with the latest measurements from the Cassini/Huygens mission. Solid lines correspond to model results, dashed and dotted lines correspond to the CIRS retrieved profiles for 15°S and 80°N, respectively (Vinatier et al., 2006) based on limb spectra, while open squares and circles represent the INMS measurements for the upper atmosphere from Waite et al. 2005 and Vuitton et al. 2006a,b, respectively). CIRS abundances from nadir spectra at 33°N are also shown in boxes (Coustenis et al., 2007) and the short-dotted line corresponds to the Hourdin et al. (2004) acetylene profile generated by a 2-D photochemical/dynamical model that was found to provide a good fit to the CIRS nadir spectra for the equator. The dash-dotted line presents the sensitivity of the model to the N_2 dissociative ionization scheme.

the relatively good agreement of our model and that of previous models with measurements regarding the other hydrocarbons in this region, the dynamical solution seems to be a possible scenario. Whether this process can account for the total abundance of ethylene in the lower atmosphere or there is a need for photochemical adjustments to obtain an abundance comparable with the observed one, is something which must be tested by future simulations.

C_2H_2 Acetylene's vertical profile is presented in Fig. 4.8b. The simulated profile is close to the upper atmosphere retrieved abundance by INMS (Waite et al., 2005; Vuitton et al., 2006a). The structure observed in this region, with the small minimum at about 1100 km is related to the N_2 photolysis scheme and the reaction of the produced $N(^2D)$ atoms with acetylene. The new scheme used in the current calculations regarding the products of the N_2 photodissociative ionization, increases the production of excited nitrogen atoms and enhances their role in the destruction of hydrocarbons in the upper atmosphere. The scheme used in previous models, where only $N(^4S)$ atoms are formed yields the dash-dotted line in Fig. 4.8b.

In the mesosphere, the model results provide a reasonable profile which is in between the equatorial and polar vertical profiles retrieved by CIRS (Vinatier et al., 2006). Only in the lower atmosphere, below 300 km do the results underestimate the acetylene abundance. At 200 km the calculated abundance is smaller by a factor of 1.33 and 1.48 from the CIRS equatorial value and mid-latitude value (Coustenis et al., 2007), respectively. Due to the broad pressure-range probed by the ν_5 band of acetylene, the latter authors managed to retrieve information about the vertical structure of its profile from the CIRS nadir spectra. They concluded that the vertical profile generated through the 2-D photochemical-dynamical model of Hourdin et al. (2004) (see description in Coustenis et al. (2007) and short-dotted line in Fig. 4.8b) provided the best fit to the observed spectra relative to previous photochemical results. Although the profile gives a similar altitude variation with their suggested profile above 250 km, it decreases faster at lower altitudes. The observed difference could be corrected by adjusting the mixing efficiency in the lower stratosphere, but such a treatment would lead to an increase in other hydrocarbons and nitriles in this region that are well simulated by the current eddy mixing profile. Further, decreasing the eddy mixing in the mesosphere provides an acetylene profile which is closer to the CIRS observed one, but in this way the fit to C_2H_6 and Ar that are used as tracers, is destroyed. Possibly, dynamical effects are able to adjust the acetylene mole fraction closer to the observed one.

C_3H_4 Methylacetylene (CH_3C_2H) and its isomer allene (CH_2CCH_2) are presented in Fig. 4.9. INMS (Waite et al., 2005) has provided a mole fraction of $3.86\pm0.22\times10^{-6}$ for the C_3H_4 mass channel, a value close to that of the model profile for the combined contribution (2.7×10^{-6}). Allene is converted to methylacetylene in the presence of atomic hydrogen, as described in §2.3.2, which explains its decrease relative to the CH_3C_2H abundance as we move towards lower altitudes. Yet, in the lower atmosphere the CH_3C_2H profile is underestimated compared to the CIRS lower limit retrieved abundance for the equator (Vinatier et al., 2006) and the CIRS mid-latitude abundance (Coustenis et al.,

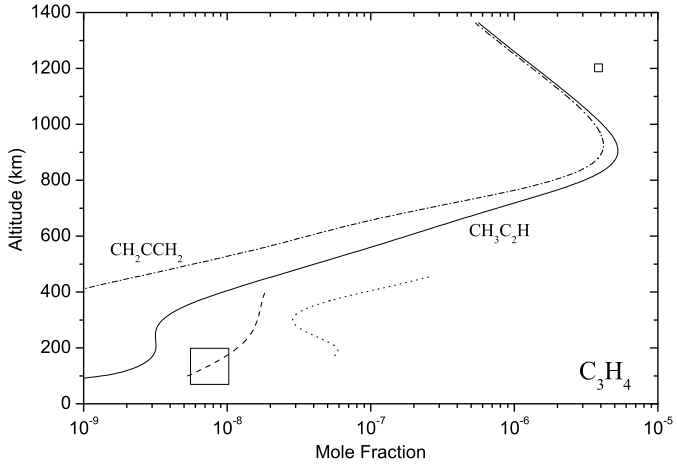

Figure 4.9: Model calculated vertical profile of methylacetylene and its isomer allene. The symbols are the same as those used in Fig. 4.8.

2007). At 300 km our profile is five times smaller than the equatorial value and also it presents a vertical structure significantly different from the observed one. Previous photochemical models also tend to underestimate the methylacetylene abundance relative to that observed by CIRS, with the exception of Toublanc et al. (1995) although this is probably related to their use of a significantly smaller eddy mixing coefficient (see Fig. 4.3) rather than due to differences in the photochemical scheme.

The possible reasons for this underestimation are open to discussion. The main loss mechanisms for methylacetylene are photolysis and the three body reaction with atomic hydrogen that leads to the production of C_3H_5. From the good agreement between the observed and modelled geometric albedo in the UV region (see Fig. 6.7), and the structure of the modelled haze extinction profile (Fig. 6.5 & 6.6), which is in reasonable agreement with that retrieved by the HASI instrument on board the Huygens probe, the possibility of an enhanced photolysis due to a possible underestimation of the haze or gas opacities, is probably not the answer to our problem. For the hydrogen population, the model provides a realistic simulation as will become apparent in the discussion for the diacetylene profile later on. Hence the underestimation is probably related to a lack of production in the lower atmosphere. An enhanced production in the lower atmosphere could be related to the local enhancement observed for ethylene but not reproduced by the model calculations. Another possible source for the low abundance of CH_3C_2H could be the overestimation of the propane profile in the lower atmosphere discussed later.

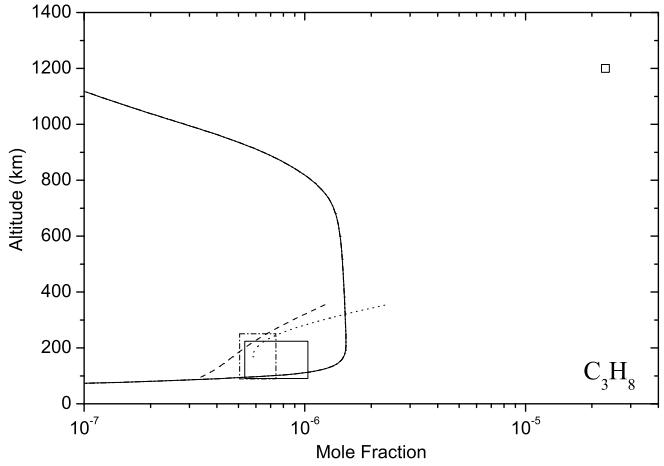

Figure 4.10: Model calculated vertical profile of propane. The symbols are the same as those used in Fig. 4.8 and the dashed-dotted box corresponds to the range of values set by the Roe et al. (2003) measurements for the propane stratospheric abundance.

C_3H_8 Propane's production is dominated by the combination reaction between methyl and ethyl radicals. The high-pressure limit rate for this reaction has been measured for elevated temperatures and theoretically investigated for lower ones. Most recent laboratory measurements are those of Sillesen et al. (1993) and Knyazev & Slagle (2001), while previous measurements are reviewed in Tsang & Hampson (1986) and Baulch et al. (1992). The rates measured in these reports, include also the hydrogen abstraction channel:

$$CH_3 + C_2H_5 \rightarrow C_2H_4 + CH_4$$

which was not possible to isolate. Theoretical investigations have attempted to provide some information about the relative importance of the two channels and the transition through which they proceed. Zhu et al. (2004) reported rates for the two main energetically possible channels (association/abstraction). Their results are in good agreement with the latest measurements and other theoretical investigations and are those used in the current calculations. Based on these reports, for temperatures below 600 K the reaction rate presents a negative temperature dependence and the association rate appears to be dominant and pressure independent for the measured pressure range (1 - 21 Torr). This suggests that for Titan, propane production can proceed readily even at low pressures compared to other three-body reactions. For the low pressure limit the rate was estimated from the methyl radical recombination rate.

The resulting propane profile (fig. 4.10) is significantly different from what is suggested by the observations. In the upper atmosphere the model suggests an abundance that is more than two orders of magnitude smaller than that measured by INMS (Waite et al., 2005). This suggests that other processes, not included in the model, are responsible for the production of propane in the upper atmosphere.

In the lower atmosphere the modelled profile is larger and has a significantly different altitude variation than the CIRS retrieved vertical profiles (Vinatier et al., 2006) and stratospheric abundance (Coustenis et al., 2007). The observed profiles suggest a decreasing abundance with altitude, with the two latitude profiles converging towards the condensation region. In contrast, the model suggests a constant vertical mole fraction, before the abundance starts to decrease towards the condensation region. In previous photochemical models, Lara *et al.* (1996) have provided a vertical profile which increased with altitude in the above region similar to the observed altitude variation, while Wilson & Atreya (2004) suggested that the absence of the C_3H_7 radical in the former photochemical model, led to this altitude variation. The recycling induced by the following scheme:

$$\begin{gathered} C_3H_8 + h\nu \rightarrow C_3H_6 + H_2 \\ H + C_3H_6 + M \rightarrow C_3H_7 + M \\ 2\ C_3H_7 \rightarrow C_3H_6 + C_3H_8 \end{gathered}$$

conserves propane and provides the constant mole fraction in the lower atmosphere observed in their model results, as in ours. Hence, one would expect that if this process was for some reason reduced, then the abundance of C_3H_6 would increase and by its photolysis an enhancement in the methylacetylene profile would be observed. Yet, based on the current calculations, removing the above scheme, did not have any significant effect on the structure and abundance of propane or methylacetylene, rendering the above scheme not important in our simulation. The reason for this is that propane's production is dominated by the methyl - ethyl addition reaction in the total vertical range of Titan's atmosphere, with any secondary production mechanisms having a negligible contribution. Since C_3H_8 is not affected, C_3H_6 also remains the same and hence there is no significant change in C_3H_4.

Photochemical loss processes for propane are limited. Due to the overlap of propane's absorption cross section with that of methane, which is present in significantly larger amounts, propane photodissociation is small. On the other hand, as a saturated hydrocarbon it presents limited reactivity with other species, of which the most important is that with C_2H. Hence, its vertical profile is balanced by diffusion and loss to condensation. Reducing the eddy mixing coefficient in the stratosphere - mesosphere, in order to provide a better match, destroys the agreement with ethane and argon, which are used as mixing tracers. Increasing the mixing in the lower atmosphere, below the stratopause, in order to increase the condensation flux, leads to a strong underestimation of ethane and acetylene in the lower atmosphere, since the condensation fluxes of these species (along with all other condensing species) increases also. Hence, we are

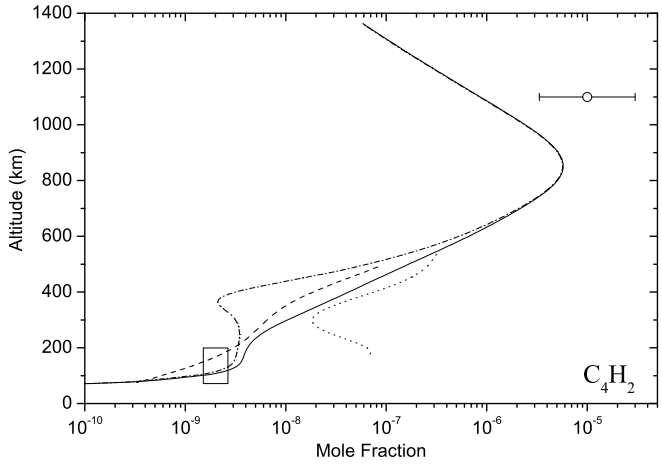

Figure 4.11: Model calculated vertical profile of diacetylene. The symbols are the same as those used in Fig. 4.8 and the solid and dashed-dotted lines correspond to model results with and without the inclusion of the PRM heterogeneous process, respectively.

currently left with the possibility of an enhanced production of propane in the lower atmosphere to explain the model overestimated abundance in this region.

C_4H_2 & ***H, H_2*** Diacetylene is an important species because it is directly related to haze production pathways. In addition, since in the lower atmosphere the chemical loss of C_4H_2 is dominated by reaction with atomic hydrogen, the vertical profile of diacetylene can be used as a tracer for the maximum abundance of atomic hydrogen allowed in this part of the atmosphere. INMS (Vuitton et al., 2006b) has measured the upper atmospheric abundance at 1×10^{-5} mole fraction, while the CIRS retrieved vertical profiles have constrained the mole fraction to $\sim10^{-8}$ in the vicinity of the stratopause (Vinatier et al., 2006). At about 110 km, where the contribution function from nadir spectra for this species peaks at mid-latitudes, CIRS gave a mole fraction of $1.8^{+0.6}_{-0.5}\times10^{-9}$ (Coustenis et al., 2007). In Fig. 4.11 the dashed dotted line presents the calculated vertical profile of C_4H_2. It is obvious that in the region of 400 km where the calculated atomic hydrogen abundance presents a broad maximum (see Fig. 4.13b), C_4H_2 exhibits a significant decrease below the lower limit set by the CIRS equatorial profile (Vinatier et al., 2006), while for higher and lower altitudes the agreement with the observed abundances is better. The vertical profile of diacetylene presents a dependence on the used eddy profile, something which was also reported by Wilson & Atreya (2004). Yet, having the mixing profile set with the above described method and assuming a single mixing profile for all gas species, there

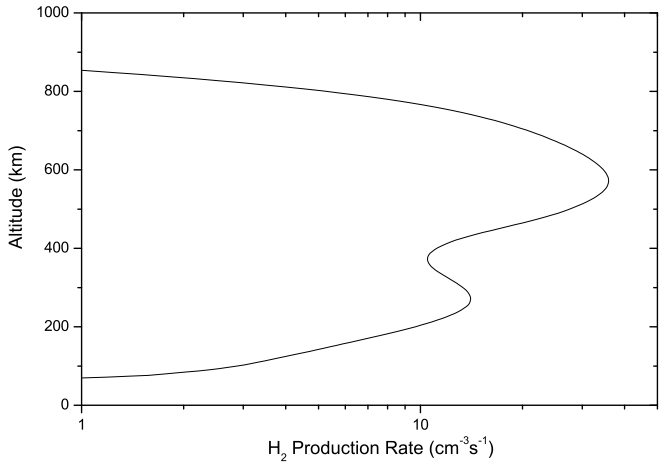

Figure 4.12: The calculated production rate of H_2, or equivalently loss rate for atomic H due to heterogeneous transformation of atomic to molecular hydrogen at the surface of the aerosol particles. The rate has two pronounced peaks related to the number density of atomic hydrogen and size distribution of the aerosol particles (see text).

is not much that can be done by changing the mixing profile in order to correct the C_4H_2 profile, without destroying the fit to the tracers used. At the same time, the calculated H_2 profile (Fig. 4.13a) is lower than the INMS retrieved abundance in the upper atmosphere (Yelle et al., 2006). These two facts hint at the possibility of an underestimation in the conversion of atomic hydrogen to molecular.

The underestimation of the conversion of H to H_2 was initially noted by Yung et al. (1984) who suggested that heterogeneous processes at the surface of the aerosol particles could possibly enhance this process. Bakes et al. (2003) and Lebonnois *et al.* (2003) were the first to describe and model this process for Titan's haze particles based on the prompt-reaction model (PRM) of Duley (1996). In this model, atomic hydrogen from the gas medium reacts readily with H atoms that are bonded at the surface of the particles giving H_2, which is released to the atmosphere. They concluded that this was an important process for the H and H_2 abundances, but also for other hydrocarbon species in the stratospheric region. In their calculations, they used the Toon et al. (1992) size distribution for the haze particles and estimated the activation energy for hydrogen abstraction based on the Sugai (1989) measurements, which were performed at room temperature. Recently, Sekine et al. (2006) have reported measurements for the activation energy at low temperatures, appropriate

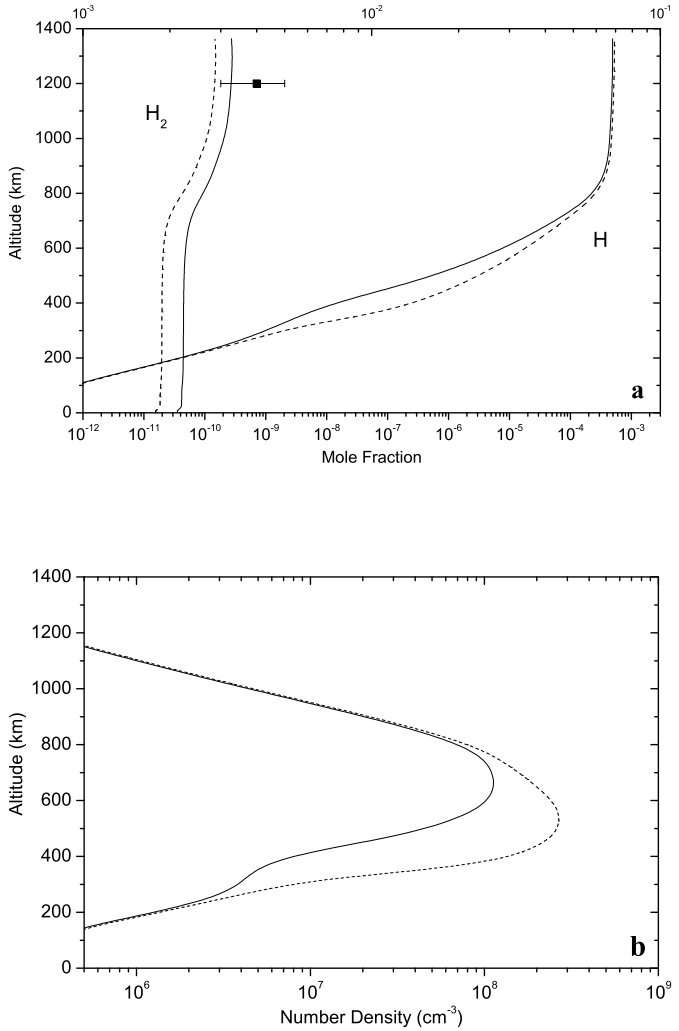

Figure 4.13: The effects of heterogeneous transformation of atomic to molecular hydrogen at the surface of the aerosol particles. The impact of the PRM process on the resulting mixing ratios of atomic (bottom scale) and molecular hydrogen (top scale) of the model (a) is significant with a decrease in the H abundance between 300 and 800 km, which is more evident when viewed in terms of number density (b), and an increase in the H_2 mole fraction, giving better agreement with the observed abundance in the upper atmosphere from Yelle et al. (2006).

for Titan's conditions and found that the activation barrier for abstraction is significantly smaller than previous estimates, making this process even more efficient. Based on their results, the probability of reaction of atomic hydrogen with the surface of an aerosol particle is given by:

$$p_b = 1.9 \times 10^{-3} \mathrm{e}^{-300/T}$$

for the temperature range 160 - 300 K, which means that the cross section for bonded hydrogen abstraction will be given by:

$$\sigma_b = 4\pi \mathrm{r}^2 p_b$$

with r the radius of the aerosol particle.

We have included this process in our calculations following the description given in Lebonnois *et al.* (2003) and using the size distribution for the haze particles calculated in our microphysical model, presented in the next chapter (see Fig. 6.2). The impact of the process on the vertical profiles is found to be important. The production rate of H_2 molecules and hence loss rate of atomic H, is presented in Fig. 4.12. The shape of the profile is different from that shown in Bakes et al. (2003) due to the significant differences between the size and number density profiles used in the two calculations. There are two production peaks observed, which are related to the fact that the production rate is proportional to the number density of atomic hydrogen and to the number density and surface area of the particles. The upper peak is related to the region where the H number density reaches its maximum value due to production by photochemical processes, while the lower peak comes from the fact that as we move towards the surface the size and hence the surface area of the particles upon which abstraction of H atoms can take place becomes larger due to the coagulation process. At the same time though, larger size particles are present in smaller densities, which explains the decreased contribution of the secondary peak to the overall production rate.

The resulting model atomic hydrogen and molecular hydrogen mole fractions are presented in Fig. 4.13a. A sharp decrease in the H profile in the region between 300 and 800 km is evident as shown in Fig. 4.13b in terms of the number density. The molecular hydrogen formed, increases the initial abundance calculated by the model and provides a mole fraction in the upper atmosphere that is closer to one retrieved from the INMS measurements (Yelle et al., 2006). The escaping hydrogen fluxes at the top of the simulated atmosphere are presented

Table 4.1: Mole fractions at 1200 km and escaping H & H_2 fluxes (molecules $cm^{-2}s^{-1}$) at the top of the simulated atmosphere.

	Mole Fraction at 1200 km		Escaping Flux	
	w/o PRM	with PRM	w/o PRM	with PRM
H	5.2×10^{-4}	4.9×10^{-4}	1.0×10^{9}	9.3×10^{8}
H_2	2.9×10^{-3}	3.3×10^{-3}	3.7×10^{9}	4.2×10^{9}

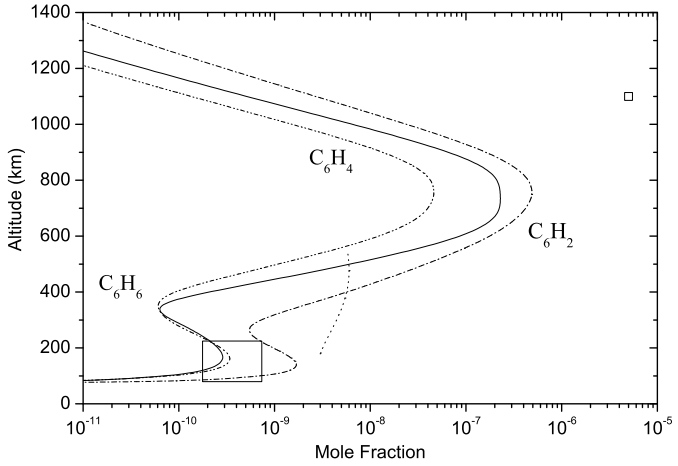

Figure 4.14: Model calculated vertical profile for C_6H_X species. The upper atmosphere measurement corresponds to an upper limit for the benzene abundance retrieved during the first flyby of Cassini. The lines correspond to the model profiles for benzene (solid line), triacetylene (dash-dotted line) and benzyne (dash-double-dotted line).

in Table 4.1 for the two cases. The total escaping flux in terms of H_2 molecules when the PRM process is included is 4.7×10^9 molecules/cm^2/s. The decrease in the atomic hydrogen population, allows for more diacetylene, in the above region, with the new simulated profile (solid line in Fig. 4.11) being in good agreement with the CIRS retrieved vertical profiles (Vinatier et al., 2006).

C_6H_6 Benzene was initially detected by ISO with a mole fraction of $4\pm3\times10^{-10}$ in the stratosphere (Coustenis et al., 2003). From limb spectra, CIRS have managed to retrieve a vertical profile only for high latitudes, which represents an average between 65 and 80°N, while for equatorial regions the derived upper limit was 1.1×10^{-9} mole fraction (Vinatier et al., 2006). From nadir spectra, a significantly improved retrieval for the abundance of this species was possible; Coustenis et al. (2007) suggested a mole fraction of $4.3^{+3.0}_{-2.5}\times10^{-10}$ at 120 km for 33°N, while a strong latitudinal variation was observed with more than an order of magnitude increase in the stratospheric abundance when moving from 70°S to 70°N. In the upper atmosphere, the INMS detected abundance at 1200 km was of ppm order of magnitude (Waite et al., 2005), which is significantly larger than the model-derived abundances at that level.

The pathways of benzene formation at low temperatures are far from being well defined due to the fact that the suggested processes correspond to laboratory and theoretical work at high temperatures, as discussed also in 2.3.2. The

main production process for benzene in the upper atmosphere under the scheme used is the recombination of two propargyl radicals (C_3H_3). The high-pressure limit for this reaction has been measured (Morter et al., 1994) but the low pressure one is not know and hence must be estimated. A common approach among photochemical modellers is the use of the low pressure limit of methyl recombination multiplied by a factor of 10. Yet, the problem is far from being resolved since the rates for the methyl recombination at the low pressure limit are also not well established, as discussed previously for the case of ethane. Hence, the use of different rates can lead to mole fractions in the upper atmosphere that can vary by a few orders of magnitude. In view of the large abundances observed in the upper atmosphere, the low pressure limit suggested by Moses et al. (2000) and also by Lebonnois (2005), which is significantly larger than the rate suggested by Cody et al. (2003), has been used.

The resulting vertical profile, under the scheme used in the model produces the profile presented in Fig. 4.14. The model abundance in the upper atmosphere is still significantly smaller than the INMS derived one. This probably enhances the idea that the benzene formation could be related with the ion chemistry in that region. The model vertical profile satisfies, the CIRS upper limit from limb spectra (Vinatier et al., 2006), the above described ISO disk-average observations in the stratosphere and it is well within the CIRS reported abundance at the same altitude region for mid-latitude conditions based on nadir spectra (Coustenis et al., 2007). Yet, the resulting abundance shows a different vertical variation from previous models with a minimum near 350 km. Previous photochemical models have managed to produce benzene profiles of higher abundance in the stratosphere, relative to the one reported here. Yet, these results could be over-estimated as discussed in the following paragraph. Further, the observed vertical structure from CIRS (Vinatier et al., 2006) corresponds to high latitude regions in which the enhancement due to the circulation descending cell, could enhance the mesosphere with benzene molecules produced in the upper atmosphere and remove the minimum observed in our result. In other words, the possibility that the minimum observed in the profile is present to some extent in the benzene profiles at lower latitudes, can not be excluded. In any case, the C_6H_6 production in Titan's atmosphere still suffers from large uncertainties and the possibility of other photochemical/ion-chemistry pathways, which could lead to its production must be investigated.

C_6H_4 & C_6H_2 Also presented in Fig. 4.14, are the vertical profiles of benzyne and triacetylene, respectively. The former is a direct product of benzene photolysis. Previous models have not included its photolysis. Yet based on the current calculations, if it is not photodissociated, larger abundances of this species would occur in the atmosphere that would have been observed. In addition, the abundances of other species related to the C_6H_X formation are underestimated since they are effectively lost to C_6H_4. Similarly, benzyne is not efficiently lost to its precursors resulting in an increased benzene abundance, which although closer to the observed abundance it is artificial. Hence, we have decided to estimate the benzyne photolysis; Münzel & Schweig (1988) reported that electronically, C_6H_4 is similar to benzene with an additional σ bond. Hence,

we have estimated benzyne photolysis with the absorption cross section of benzene and a similar photochemical scheme. With this description, a significant photolysis product of C_6H_4 is triacetylene, which explains the larger abundance obtained by our calculations for this species relative to previous photochemical models (Wilson & Atreya, 2003, 2004).

4.2.2 Nitriles

HCN & ***CH_2NH*** The HCN vertical profile has been retrieved by ground-based millimeter (Tanguy et al., 1990; Hidayat et al., 1997; Marten *et al.*, 2002) and submillimeter (Gurwell, 2004) observations, while the stratospheric abundances have been inferred by the Voyager IRIS disk-resolved measurements (Coustenis & Bézard, 1995), which showed the latitudinal variability due to seasonal effects, and by the ISO disk-average observations (Coustenis et al., 2003). The Cassini CIRS results have shown again that HCN has a strong latitudinal variation (Teanby et al., 2006), with stratospheric abundances increasing towards the north pole, which is entering the winter season at this time. The vertical profiles inferred at different latitudes from CIRS (Vinatier et al., 2006; Coustenis et al., 2007), depict this variation of the HCN abundance but also show that the vertical variation of the mole fraction is not with a steady slope but similar to the Marten *et al.* (2002) measurements, although not as steep.

The production of hydrogen cyanide is directly related to the production of atomic nitrogen from the photolysis of N_2. The latter is rapidly transformed to H_2CN and CH_2NH, which eventually provide HCN on reaction with H and photolysis, respectively. As discussed in 2.3.2, previous photochemical models have not included or followed the production of CH_2NH in their schemes, since there is a lack of information about its photochemical properties. The main problem is the absence of reaction rates and pathways regarding the loss of methyleneimine to other species. The main production and loss mechanisms included in the model calculations are presented in Table 4.2.

In the calculations CH_2NH is mainly produced by:

$$\begin{aligned} N(^2D) + CH_4 &\rightarrow CH_2NH + H \\ NH + CH_3 &\rightarrow CH_2NH + H. \end{aligned}$$

The rate for the first reaction is taken from Herron (1999) where a yield of 80% was suggested for this pathway with the remaining 20% attributed to the NH + CH_3 pathway. Recent results by Balucani & Casavecchia (2006) at low temperatures appropriate for Titan, also suggest that the production of CH_2NH in the above reaction is the main process, possibly with a larger yield. For the second reaction, which was recently suggested to provide methyleneimine (Redondo et al., 2006), the rate was estimated based on a comparison with other radical-radical reactions (10^{-11} cm^3s^{-1}). The same approach was followed by Lellouch et al. (1994) for this reaction. For the photolysis products I have assumed a single pathway leading to HCN formation directly:

$$CH_2NH + h\nu \rightarrow HCN + 2\ H$$

Table 4.2: Production and loss processes for methyleneimine used in the model calculations.

Reaction			Rate	Reference	T(K)
			Production		
$N(^2D) + CH_4$	$\rightarrow$	$CH_2NH + H$	$3.84 \times 10^{-11} e^{-750/T}$	Herron (1999)	232 – 292
$NH + CH_3$	$\rightarrow$	$CH_2NH + H$	1.0×10^{-11}	Redondo et al. (2006)	Est.
$2\ H_2CN$	$\rightarrow$	$CH_2NH + HCN$	5.13×10^{-12}	Horne & Norrish (1970); Nizamov & Dagdigian (2003)	296
$CH + NH_3$	$\rightarrow$	$CH_2NH + H$	$4.1 \times 10^{-9} T^{-0.56} e^{-28/T}$	Bocherel et al. (1996)	23 – 295
$CH_3NH_2 + h\nu$	$\rightarrow$	$CH_2NH + 2\ H$		See table 3 in Part I	
			Loss		
$CH_2NH + H$	$\rightarrow$	$H_2CN + H_2$	4.0×10^{-14}	Est. as k(CH_2O + H)	
$CH_2NH + C_2H$	$\rightarrow$	Products + H	1.4×10^{-10}	Est. as k(C_2H_4 + C_2H)	
$CH_2NH + CN$	$\rightarrow$	$H_2CN + HCN$	$6.71 \times 10^{-11} e^{-412/T}$	Est. as k(CH_2O + CN)	
$CH_2NH + N(^2D)$	$\rightarrow$	Products	$2.3 \times 10^{-10} e^{-503/T}$	Est. as k(C_2H_4 + $N(^2D)$)	
$CH_2NH + N$	$\rightarrow$	$H_2CN + H$	$3.32 \times 10^{-14} e^{-352/T}$	Est. as k(C_2H_4 + N)	
$CH_2NH + H_2CN$	$\rightarrow$	polymer	$1.1 \times 10^{-12} e^{-900/T}$	Est. as k(C_2H_3 + HCN)	
$CH_2NH + h\nu$	$\rightarrow$	$HCN + 2\ H$		See Table 2.2	

based on the results of Nguyen et al. (1996). Assuming as a photolysis product the H_2CN radical, there were no significant changes in the HCN profile, since the former readily provides the latter in reaction with H.

According to the present literature, only recently there has been some investigation of methyleneimine's UV spectrum by Teslja et al. (2004) who measured the absorption cross section in the 235 - 260 nm region and found it to range between 2-4$\times 10^{-19}$cm^2. No published measurements of the CH_2NH absorption cross section in any other part of the spectrum was found. The possible chemical loss mechanisms for CH_2NH remain another open question. Basiuk (2001) has investigated theoretically the reactions of methyleneimine with CN and HCN, water and OH. Between CN and HCN he found that although reaction with HCN is not allowed to occur, due to the presence of three high energy transition states, reaction with CN is without a barrier and can proceed readily in the gas phase. In addition, CH_2NH is isoelectronic with formaldehyde (CH_2O) and ethylene for which rates for reaction with some of the important radicals present in Titan's atmosphere have been measured. Hence, reactions of methyleneimine with H, C_2H, N, N(^{2}D) and CN have been included and their products were estimated based on the equivalent reactions with the above two species. Finally, another possible loss mechanism could be related to the polymerization of methyleneimine, a process which is known to proceed readily for CH_2O. No published laboratory or theoretical investigation, regarding the process which could lead to the production of this polymer under the conditions found in Titan's atmosphere was found. Hence, it was assumed that it is initiated by the addition of H_2CN radicals similar to the process assumed from the HCN polymerization:

$$H_2CN + CH_2NH \rightarrow \textit{polymer}.$$

The resulting profiles of CH_2NH and HCN are presented in Fig. 4.15. In order to have a view of the impact of the different processes in the final profiles, the calculated vertical profiles at different steps are presented. For the methyleneimine the solid curve corresponds to the case were all production reactions presented in Table 4.2 are included and for the photochemical loss, there is only photolysis (case A). In case B (dashed line) the rest of the chemical reactions suggested are included. The large decrease in the profile observed above 400 km is due to the reaction with atomic hydrogen, which is the most important among those included. The N_2 dissociative ionization has also a significant impact in the upper atmosphere abundance of methyleneimine. In the previous two cases the N_2 dissociative photoinization was assumed to provide excited state N atoms. In case C (dotted line), the production of ground state N atoms is assumed. Due to the smaller abundance of N(^{2}D) atoms in this case, the production is significantly decreased, leading to a vertical profile which is 2 times smaller than that of case B at 1100 km.

Yet in all cases the calculated abundance is larger than the one retrieved by the INMS measurements (Vuitton et al., 2006b) suggesting that the loss processes for CH_2NH in the model calculations are underestimated. In view of the narrow region of the spectrum for which we have information about the

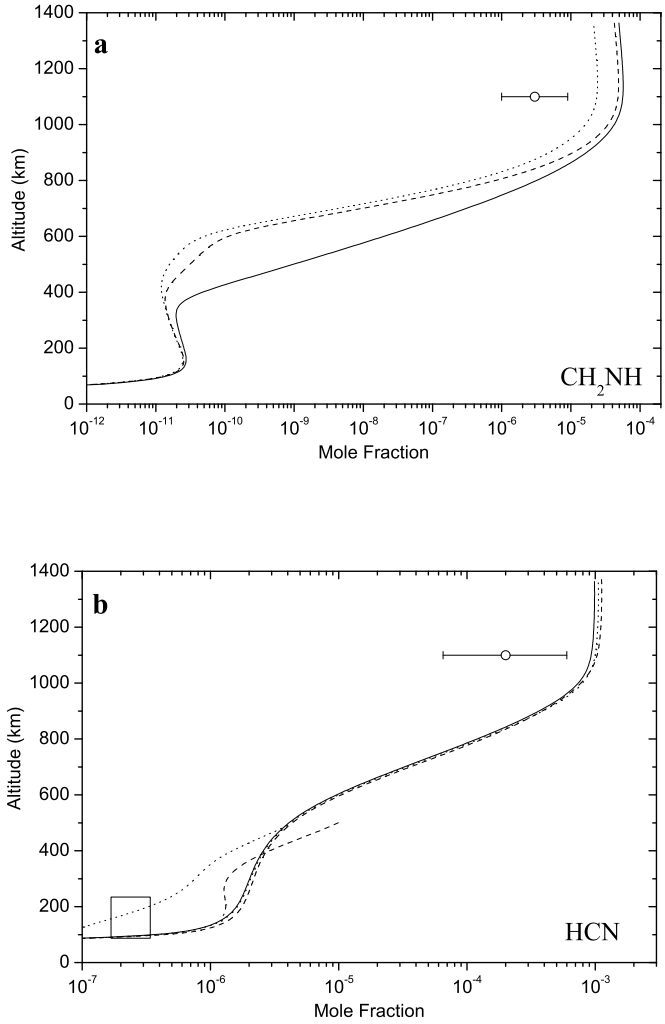

Figure 4.15: Model calculated vertical profiles for methyleneimine (a) and hydrogen cyanide (b). The references for the measurements are the same as those in Fig. 4.8. In (a) for the solid line only photolysis is included as a loss process for CH2NH (case A in text). For the dashed line all chemical loss processes considered are included (case B) and for the dotted line the N_2 dissociative ionization is set to yield ground state nitrogen atoms. In (b) the solid line corresponds to case B discussed above, the dashed line corresponds to the case were the evolution of CH_2NH is not followed and the dotted line presents the sensitivity of the profile on the N_2 dissociative ionization scheme.

absorption cross section, it is realistic to expect that there has to be some contribution to the photodissociation by the rest of the spectrum. On the other hand, reactions with other hydrocarbons and nitriles could also contribute to reducing the abundance in the upper atmosphere closer to the observed one. It is important to note that for most of the reactions assumed here, the ones that have an important role, produce either HCN directly or H_2CN that eventually yields HCN. This means that the inclusion of methyleneimine under the current scheme can not have any important effect on the HCN profile. This is shown in Fig. 4.15b. with the solid and dashed lines. The latter corresponds to the case assumed in previous models where the CH_2NH was produced but its evolution was not followed. This effectively corresponds to its removal from the system. The former, represents case B discussed above, where the evolution of methyleneimine is followed. It is obvious that there are no significant changes in the HCN profile, since processes which could transform methyleneimine to other channels than HCN are of low efficiency.

As discussed previously, in the retrieval of the eddy mixing coefficient, previous works have reported the difficulty of simulating the HCN and C_2H_X stratospheric abundances with a unique mixing profile. The resulting HCN profile presents the same problem with the mole fraction being significantly bigger than the observed abundances by CIRS measurements in the lower atmosphere. Compared to the mid-latitude stratospheric abundance retrieved by Coustenis et al. (2007) our profile is 3.3 times larger at 120 km (where the contribution function peaks), while compared to the CIRS observations at 15°S and 80°N, retrieved by Vinatier et al. (2006) (although the polar profile is affected by circulation effects) our profile is larger by 5 and 1.2 times, respectively, at 200 km.

In the upper atmosphere, the calculated mole fraction is well above the retrieved abundance by INMS (Vuitton et al., 2006a), a characteristic common in all previous photochemical models. The inclusion of the new N_2 dissociative ionization scheme produces only a very small reduction in the abundance at 1100 km relative to that with the ground state N atoms scheme (dotted line in Fig. 4.15b) and the calculated mole fraction (1×10^{-3}) is well above the measured 2×10^{-4}. This over-estimated production of HCN in the upper atmosphere is probably responsible for the enhanced abundance resulting in the lower atmosphere. It is evident that there is something missing in the photochemical models with regard to the description of HCN evolution. From current knowledge and estimates performed here for the properties of CH_2NH, it seems that its role is limited. Yet in order to come to a clear conclusion, new laboratory measurements regarding the reactivity of CH_2NH are needed.

NH_3 Ammonia has only been observed in Titan's thermosphere. The INMS measurements in the upper atmosphere (Vuitton et al., 2006b) retrieved a mole fraction of 4×10^{-6} at 1100 km while the model calculated mole fraction at the same altitude is about 2.1×10^{-7} (Fig. 4.16). Although this result is about 10 times larger than previous estimates from photochemical models (Wilson & Atreya, 2004), there is another issue. The calculated vertical profile of ethylenimine, the photolysis of which is the main source of the enhanced NH_3

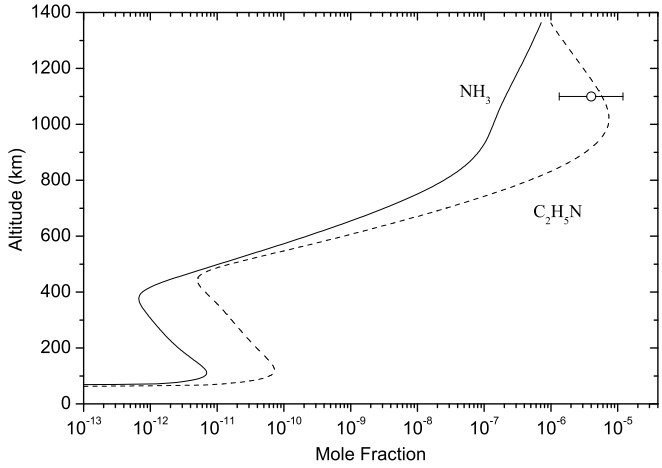

Figure 4.16: Calculated vertical profiles of NH_3 and C_2H_5N from the model. The open circle corresponds to the ammonia abundance retrieved by the INMS instrument (Vuitton et al., 2006b).

production, shows a significant abundance in the upper atmosphere that has not been observed by any INMS measurements. No published measurements for the UV absorption cross section of C_2H_5N have been found and it was estimated from that of $C_2H_5NH_2$. Possibly, the over prediction of the abundance of the former by the model, is not due to the possible underestimation of its cross section, but due to the overestimation of its production from the reaction between $N(^2D)$ and ethane. It has been assumed that the only product of this reaction is ethylenimine, in order to investigate the maximum contribution to ammonia production. This is probably not the case with other products being more stable. From the above, it is concluded that ethylenimine's production in Titan's atmosphere is smaller than that provided by the simulation, hence its role in the production of ammonia should be of secondary importance relative to the processes which allow its abundance to be closer to the observed.

CH_3CN Acetonitrile's production is dominated by the reaction of $N(^2D)$ with C_2H_4, while its loss is controlled by photolysis. This description is based on the latest measurements by Sato et al. (1999), Balucani et al. (2000a) and Payne et al. (1996), as was described by Wilson & Atreya (2004). For this species, the effects of the N_2 dissociative-ionization possible products have the most pronounced effect due to its dependence on the $N(^2D)$ population. In the model results shown in Fig. 4.17, the two vertical profiles correspond to N (solid line) and $N(^2D)$ (dotted line) production by N_2 dissociative photoionization. When the nitrogen atoms are assumed to be in their ground state, the result-

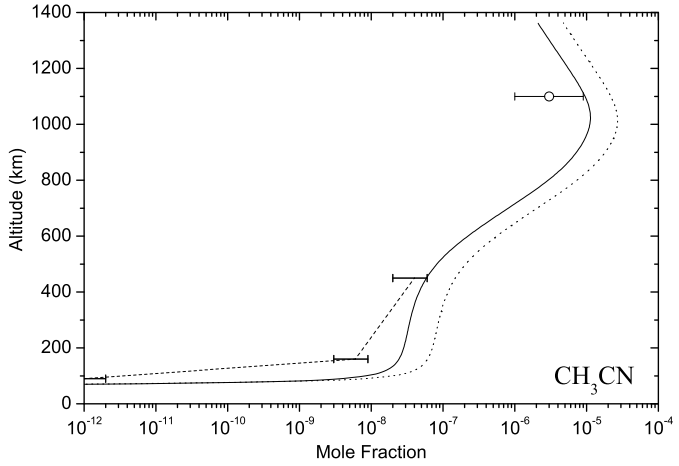

Figure 4.17: Model vertical profile for acetonitrile. Upper atmosphere measurement is from Vuitton et al. (2006a) and the horizontal error bars connected with dashed lines represent the Marten *et al.* (2002) ground-based observations. The solid and dotted lines present the sensitivity of the profile on the N_2 dissociative ionization scheme.

ing acetonitrile mole fraction is about 2.4 times smaller than the one when the atoms are produced in their excited state, at 1010 km, where the maximum is observed. Assuming the production of ground state nitrogen atoms, a vertical profile is produced that is closer to the observations. Although for both cases the upper atmosphere abundance calculated by the model is overestimated relative to the INMS derived mole fraction (Vuitton et al., 2006b), the agreement is significantly improved in the lower atmosphere relative to the Marten *et al.* (2002) retrieved abundance at 400 km for the case of $N(^4S)$ production. The model profile suggests a larger abundance of acetonitrile in the region below, compared to the observations. It is important to note that the above disk-average observations, as the authors report, are representative of low latitude regions. This could explain the different slope observed between the measurements and model in the region between 150 and 400 km since the current calculations are representative of mid-latitude regions, which are expected to have an enhanced nitrile abundance.

C_2H_3CN The production of acrylonitrile in the upper atmosphere is controlled by the reaction of CN radicals with ethylene. Although the rate for this reaction has been measured down to very low temperatures (Sims et al., 1993), the possible products have been a subject of debate for some time. Monks et al. (1993) measurements suggested a yield of 20% for acrylonitrile with the rest 80% attributed to the C_2H_3 + HCN formation. This branching ratio is used in most

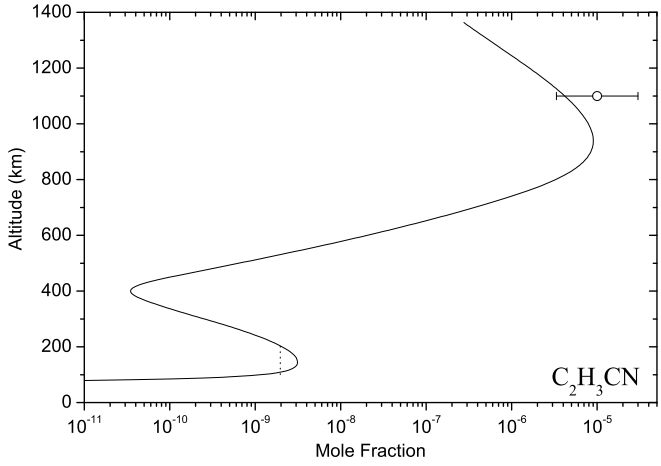

Figure 4.18: Model vertical profile for acetonitrile. Upper atmosphere measurement is from Vuitton et al. (2006b) and the vertical dotted line is the stratospheric detection limit from Marten *et al.* (2002).

of the published photochemical models of Titan's atmosphere. More recently, Balucani et al. (2000b) have reported the production of C_2H_3CN but were unable to detect HCN and C_2H_3 due to the high background signal at m/e=27 in their experiment. The RRKM theoretical investigation by Vereecken et al. (2003) suggested that the major product is acrylonitrile with the HCN pathway becoming important only at high temperatures (T > 1000 K). Recently Choi *et al.* (2004) suggested a branching ratio of 1 for acrylonitrile production, by measuring the H atom branching ratio at room temperature. The recent results from INMS for the composition of the upper atmosphere (Vuitton et al., 2006a), also show that the mole fraction of acrylonitrile is about an order of magnitude higher than those suggested by previous photochemical models, assuming the Monks et al. (1993) branching ratio. Based on the above, in the current calculations the products of the CN + C_2H_4 reaction were attributed solely to acrylonitrile production. The model calculated profile (Fig. 4.18) is in very good agreement with the observed abundance in the upper atmosphere.

Until now there has been no observation of C_2H_3CN in Titan's lower atmosphere. There, its production depends on the reaction of hydrogen cyanide with vinyl radical (C_2H_3). The rate of this reaction has also been measured by Monks et al. (1993) at room temperature, with the reported temperature dependence assumed based on similar reactions of C_2H_3 with acetylene and ethylene. The reaction was suggested to lead to the formation of acrylonitrile based on thermochemical considerations, although C_2H_3CN was detected only

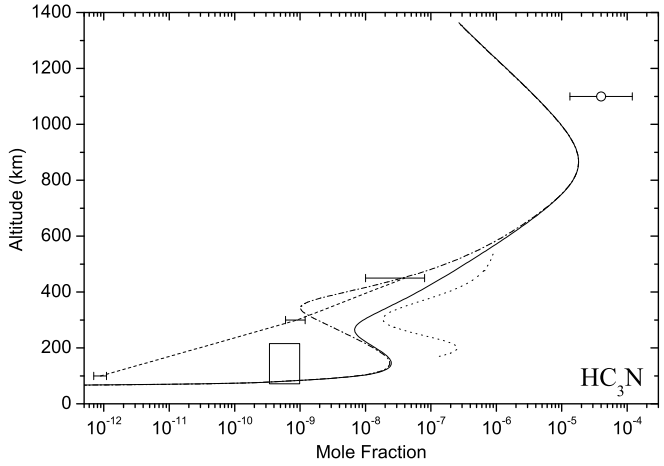

Figure 4.19: Model vertical profile for cyanoacetylene. Upper atmosphere measurement is from Vuitton et al. (2006a), the horizontal error bars connected with dashed lines represent the Marten *et al.* (2002) ground-based observations and the box represents the CIRS observations from Coustenis et al. (2007). The solid and dash-dotted lines correspond to the model results with and without the PRM process, respectively.

in trace amounts. Previous photochemical models concluded that the inclusion of this pathway with the suggested rate, leads to excessive production of acrylonitrile in the lower atmosphere, well above the detection limit placed by ground-based observations ($\sim 2\times10^{-9}$, Marten et al. 2002) with mole fraction values reaching above 10^{-8} in Wilson & Atreya (2004). The current results provide a stratospheric abundance for C_2H_3CN that is just above the upper defined limit. This improved agreement, is mainly related to chemical loss to haze, which is specifically described in the current work (see next chapter). In addition, the larger mixing profile in the lower atmosphere, constrains the mole fractions of species in this region to smaller values, since it increases their flow towards the condensation region where they are irreversibly lost.

HC_3N The photolysis of the produced acrylonitrile is the main source for the formation of cyanoacetylene. This is enhanced in the upper atmosphere by the reaction of CN radicals with acetylene, while the main loss mechanisms are photolysis and reaction with atomic hydrogen:

$$H + HC_3N + M \rightarrow H_2C_3N + M.$$

The high pressure limit of the latter has been recently measured for the first time by Parker et al. (2004) down to 200 K and was found to be about 4 times faster at this temperature, than that of the equivalent reaction with acetylene:

$$H + C_2H_2 + M \rightarrow C_2H_3 + M$$

which was used in previous models for the estimation of this rate. In addition, based on their measurements at different pressures, the authors concluded that the pressure dependence for this reaction is smaller than that of the equivalent reaction with C_2H_2, which means that the reaction proceeds with a significant rate even at small pressures.

The model vertical profile of cyanoacetylene is presented in Fig. 4.19. Although the calculated profile for acrylonitrile is in good agreement with the INMS derived abundance in the thermosphere (Vuitton et al., 2006a), the model cyanoacetylene in the upper atmosphere is below the retrieved abundance. The contribution of the acetylene based pathway:

$$CN + C_2H_2 \rightarrow HC_3N + H$$

has a comparable magnitude at these altitudes with that of C_2H_3CN photolysis. But, in view of the reasonably good agreement of the model with the C_2H_2 profile, we cannot expect a significant enhancement of the model acrylonitrile by improving the match to this species either. This probably suggests that other processes not included in the model enhance the production of HC_3N in the upper atmosphere.

In the stratosphere it is important to note the effects of the heterogeneous process described previously, on the model HC_3N vertical profile. When the heterogeneous hydrogen scavenging is not included, the large atomic hydrogen population that is allowed to survive in the mesosphere, leads to a large chemical loss through the formation of H_2C_3N discussed above. This loss brings the calculated mesospheric mole fraction (dashed-dotted line in Fig. 4.19) below the retrieved mole fraction from the ground-based observations in the region between 350 and 450 km (Marten *et al.*, 2002). When the atomic hydrogen population is strongly reduced by the inclusion of the heterogeneous process (solid line in Fig. 4.19), the HC_3N profile increases towards the polar profile retrieved by the CIRS observations (Vinatier et al., 2006).

Yet in both cases the calculated mole fractions below 350 km increase due to the contribution of the photolyzed C_2H_3CN in this region. This brings the model abundance in the stratosphere closer to the mole fractions reported by CIRS for higher latitudes compared to the mid-latitude reported abundance (Coustenis et al., 2007), shown in Fig. 4.19. It is important to note that the model abundance for C_2H_3CN, which has not been detected in Titan's stratosphere, is very close to the upper detection limit defined by the observations. Hence, the possibility of an enhanced production for this species by the model calculations compared to that actually present (but not detectable) in Titan's stratosphere, leading eventually to an increased HC_3N abundance in this region, can not be excluded.

C_2N_2 & C_4N_2 Cyanogen and dicyanogen are presented in Fig. 4.20. CIRS observations (Teanby et al., 2006) have managed to retrieve an upper limit of 5×10^{-10} for the low latitude regions increasing to a mole fraction of $\sim9\times10^{-10}$ at 50°N, both at 3 mbar ($\sim$150 km). No information for gaseous C_4N_2 has been published so far. The calculated profile for C_2N_2 is well below the previous upper

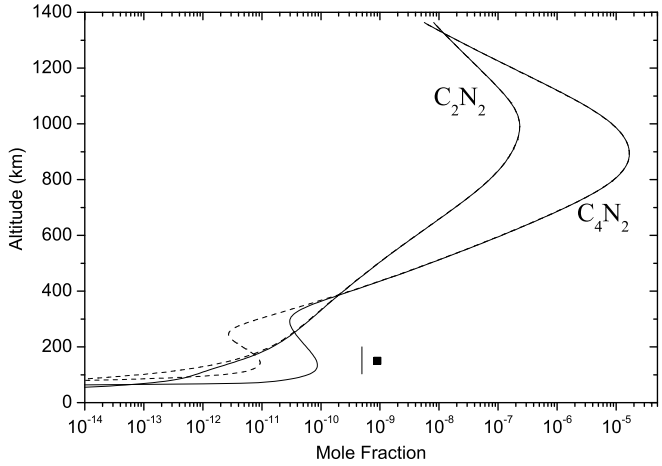

Figure 4.20: Model vertical profiles for cyanogen and dicyanogen. The vertical line and the filled square correspond to the upper limit-low latitude and high northern latitude retrieved abundance, respectively, for C_2N_2 from CIRS measurements by Teanby et al. (2006).

limit, with a mole fraction of 3.9×10^{-12} at 150 km. As reported by previous works also, the vertical profiles of these two species demonstrate the significant impact of the GCR process with an increase observed when the enhanced N_2 destruction is included. This is presented with the dashed lines in Fig. 4.20, which correspond to the model calculated profiles if the galactic cosmic rays are not included. Yet the contribution of GCR, based on the results is significantly smaller than the one reported by Wilson & Atreya (2004). The latter, reported an increase of the C_2N_2 abundance in the stratosphere larger than 6 orders of magnitude with the mole fraction reaching very close to the reported upper limit from CIRS. The reasons for this disagreement between the two model results is not clear.

In Table 4.3 the model calculated photochemical column production and loss rates along with the net production for the major species in Titan's atmosphere are presented. For N_2 and CH_4, which are the only species (along with argon) for which their surface abundances are kept fixed, assuming there is a constant supply from the surface, the net production is negative demonstrating the fact that these species are destroyed and so provide the rest of the chemical composition that is observed. For all other long-lived species the net production is positive, since these are present in the atmosphere after the convergence to a steady state. Their vertical profiles are determined by a balance between diffusion, loss due to escape to space and/or condensation and surface deposition.

From the above results it is concluded that the model successfully reproduces the observed abundances for the upper atmosphere, retrieved by INMS for most of the hydrocarbons. C_2H_6, C_2H_4, C_2H_2 and C_3H_4 are well reproduced, while C_4H_2 is just below the observed lower limit, and only C_3H_8 and C_6H_6 are significantly under-estimated. For the nitrile species, the model results are again close to observed abundances but the agreement is not as good as that observed for the hydrocarbons. The resulting HCN abundance is above the observed upper limit, which is also the case for CH_3CN and CH_2NH, while the case reverses for HC_3N and NH_3 for which the calculated abundances are below the lower defined limit. The calculated abundance for C_2H_3CN provides an excellent fit to the observed one. In the region of the INMS observations (thermosphere) the atmosphere is expected to be well mixed, thus dynamical effects are not expected to have a significant impact on the observed abundances. This means that the observed difference should be attributed to the photochemical description (rates and yields used). Further, the large number of new nitrile species observed by INMS in the upper atmosphere (Vuitton et al., 2006b), which are not included in the current calculations, could possibly have an impact on the above species, leading to the observed abundances.

In the region of the CIRS observations (stratosphere) dynamical processes are expected to have a stronger effect. This is more well observed for the case of C_2H_4 as discussed above. The model results for C_2H_6, C_4H_2 and C_6H_6 are in close agreement with the observed abundances, while C_2H_2 is slightly below the observed profiles below 300 km. For CH_3C_2H and C_3H_8 the model underestimates and over-estimates their abundances, respectively. A possible reason for this discrepancy is presented in the last chapter, regarding the role of the methyl radicals. For nitriles, the simulated HCN is above the observed range of abundances. For the rest of the observed nitriles in this region (CH_3CN, HC_3N, C_2H_3CN), the model is in agreement with the abundances and upper limits set by CIRS and ground-based observations.

4.3 Solar cycle effects

The variability of the incoming solar flux, due to the 11-yr solar cycle (SC), at the top of Titan's atmosphere can induce significant temporal changes in the species vertical profiles. This happens because the photolysis rates are directly dependent on the incoming solar flux (c.f. Eq. 2.12). For SC minimum (maximum) methane's photolysis is reduced (enhanced) and this leads to a reduced (increased) production for the rest of hydrocarbon species (Fig. 4.21. Between solar minimum and solar maximum the difference in the photolysis rates relative to the average:

$$R_{SC} = \frac{J_{Maximum} - J_{Minimum}}{J_{average}} \tag{4.1}$$

suggests a 43% increase in methane's photolysis at 1300 km and 68% increase for N_2 photolysis. Keep in mind that the solar cycle variability is spectrally de-

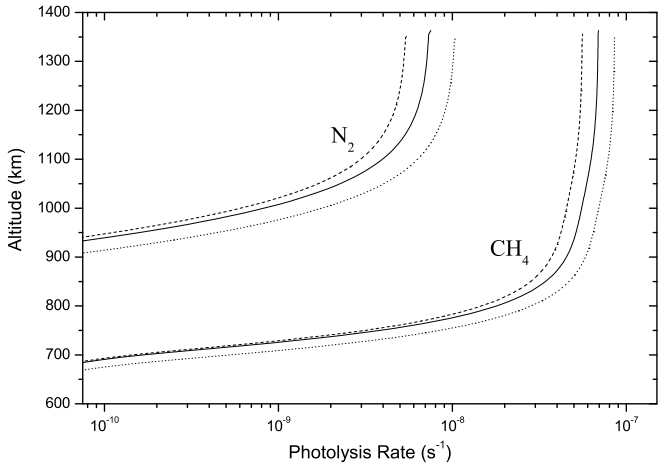

Figure 4.21: Variation of photolysis rates for N_2 and CH_4 due to variability of the incoming solar flux during the solar cycle. The solid line corresponds to solar average conditions, the dashed to solar minimum and the dotted to solar maximum.

Table 4.3: Column photochemical production and loss rates for the main hydrocarbon and nitrile species in Titan's atmosphere ($cm^{-2}s^{-1}$).

Species	Production	Loss	Net Production
H	1.6×10^{10}	1.2×10^{10}	3.8×10^{9}
H_2	8.5×10^{9}	3.0×10^{9}	8.2×10^{9}
CH_4	7.5×10^{8}	1.4×10^{10}	-1.3×10^{10}
C_2H_6	4.7×10^{9}	6.0×10^{8}	4.1×10^{9}
C_2H_4	1.9×10^{9}	1.8×10^{9}	6.0×10^{7}
C_2H_2	1.2×10^{10}	1.1×10^{10}	3.2×10^{8}
CH_3C_2H	9.7×10^{7}	9.5×10^{7}	2.3×10^{6}
C_3H_8	4.8×10^{8}	1.1×10^{8}	3.7×10^{8}
C_4H_2	2.6×10^{9}	2.6×10^{9}	4.6×10^{6}
C_6H_6	3.8×10^{8}	3.8×10^{8}	2.1×10^{5}
N_2	1.1×10^{8}	4.7×10^{8}	-3.6×10^{8}
HCN	2.3×10^{9}	1.9×10^{9}	3.2×10^{8}
CH_2NH	5.3×10^{7}	5.3×10^{7}	3.7×10^{4}
NH_3	2.7×10^{6}	2.6×10^{6}	6.7×10^{4}
CH_3CN	2.7×10^{7}	1.0×10^{7}	1.7×10^{7}
C_2H_3CN	1.6×10^{9}	1.6×10^{9}	2.8×10^{5}
HC_3N	1.2×10^{9}	1.1×10^{9}	9.2×10^{6}
C_2N_2	3.5×10^{5}	3.3×10^{5}	2.6×10^{4}
C_4N_2	1.1×10^{8}	1.1×10^{8}	1.9×10^{6}

pendent (c.f. section 2.1.1) with the difference between minimum and maximum increasing towards shorter wavelengths. This explains the stronger sensitivity of N_2 photolysis on the SC since its cross section is located at smaller wavelengths relative to methane's.

Similar variability is observed for nitriles. The model vertical profiles for solar average, solar minimum and solar maximum conditions are presented in Figs. 4.22 and 4.23 for hydrocarbons and nitriles, respectively. In the upper atmosphere the observed variability for hydrocarbons is small. Propane is the only species, after methane, for which at solar minimum conditions the calculated mole fraction profile is larger than that for solar maximum conditions. This happens because its destruction is dominated by the photolysis and not by the rest of the chemistry, which is the case for the other species. At lower altitudes the differences between solar minimum and maximum increases. For nitriles, due to the larger impact of the SC variability on the N_2 photolysis, the differences between solar minimum and solar maximum are larger that those for hydrocarbons.

It should be kept in mind that the differences in the profiles at low altitudes would be in principle smaller, due to the mixing of the atmosphere over the SC period. The impact of solar cycle effects, is higher in the upper atmosphere where the photolysis rates have large values and hence their effect is rapid. Moving towards the surface the response of the atmospheric composition to the solar flux has a larger characteristic time due to the competition between photochemistry and atmospheric mixing. Furthermore, the differences in the atmospheric composition induced by the SC variability, has an impact on the haze production profile that eventually translates to a different radiation field and vertical temperature profile. These are already included in the presented profiles and are discussed in the following chapters.

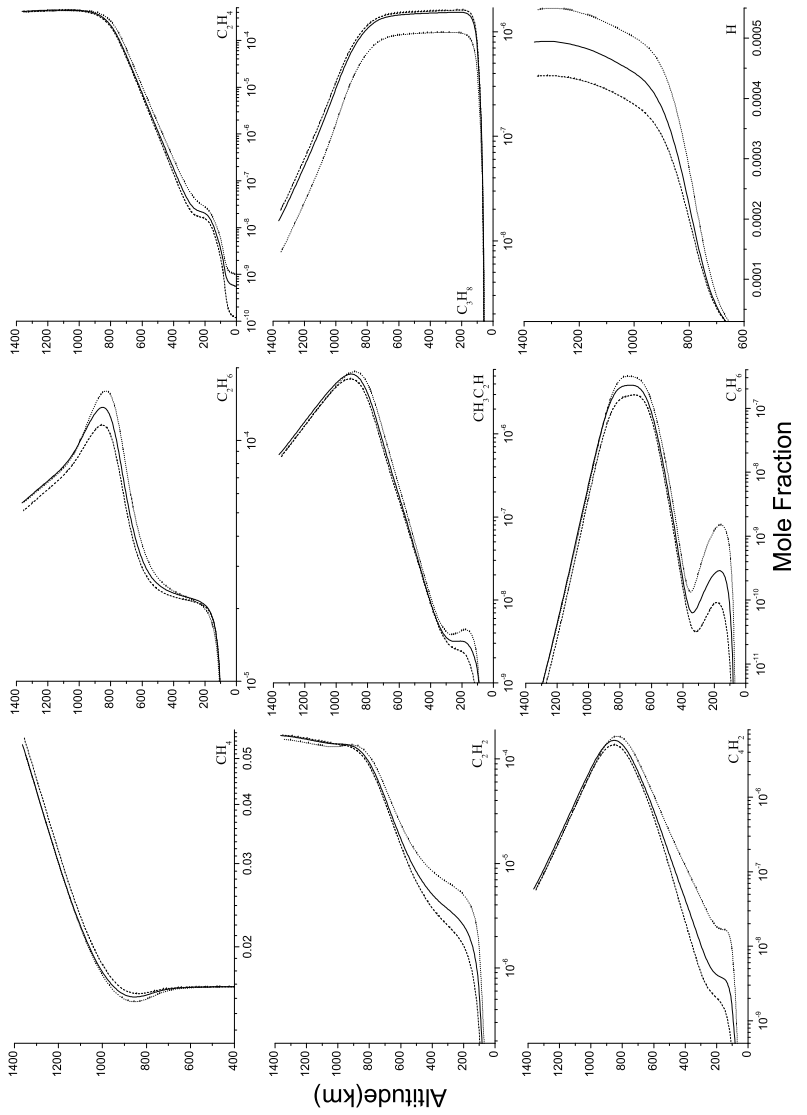

Figure 4.22: Sensitivity of hydrocarbon species vertical profiles on the solar cycle. The solid line corresponds to solar average conditions, the dashed to solar minimum and the dotted to solar maximum.

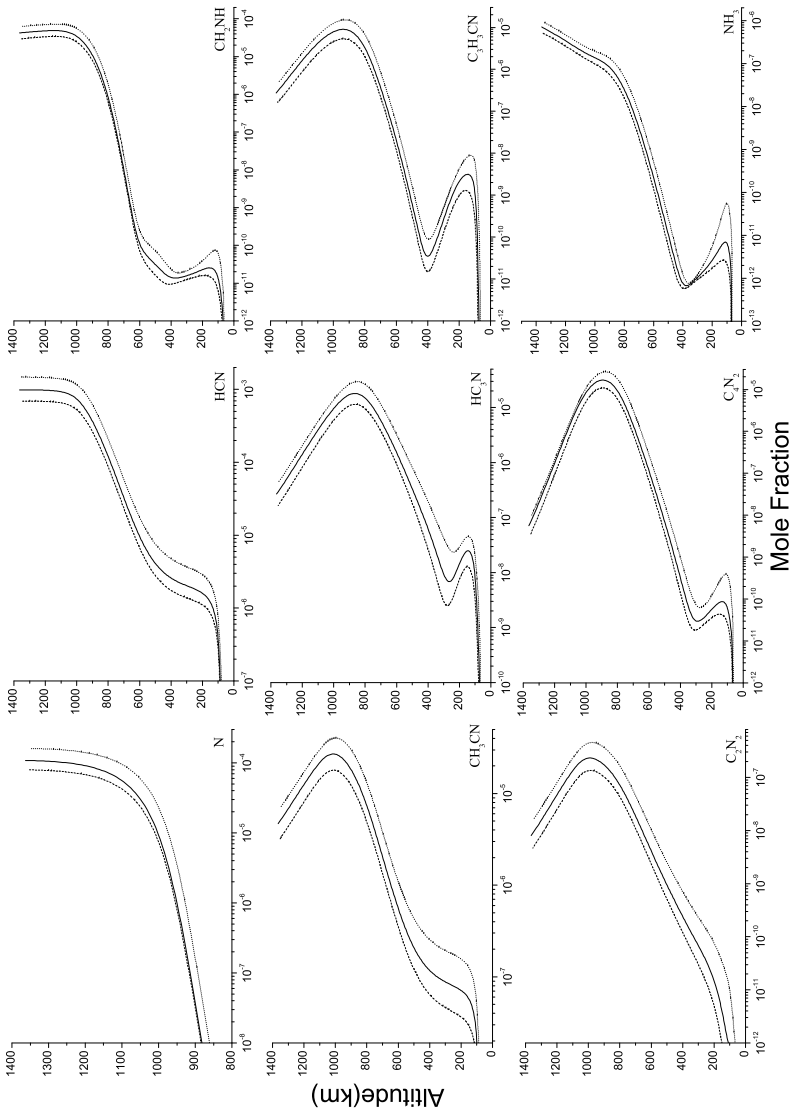

Figure 4.23: Sensitivity of nitrile species vertical profiles on the solar cycle. The solid line corresponds to solar average conditions, the dashed to solar minimum and the dotted to solar maximum.

Bibliography

Adachi, H., Basco, N., James, D.G.L., 1980. Mutual interaction of methyl and methylperoxy radicals studied by flash photolysis and kinetic spectroscopy,Int. J. Chem. Kinet. 12, 949-977.

Atreya, S.K., Edgington, S.G., Encrenaz, T., Feuchtgruber, H., 1999. ISO observations of C_2H_2 on Uranus and CH_3 on Saturn: Implications for atmospheric vertical mixing in the Voyager and ISO epochs, and a call for relevant laboratory measurements, Eur. Space Agency Spec. Publ., ESA SP-427, 149-152.

Bakes, E.L.O., Lebonnois, S., Bauschlicher Jr., C.W., McKay, C.P., 2003. The role of submicrometer aerosols and macromolecules in H_2 formation in the Titan haze. Icarus 161, 468-473.

Balucani, N., Cartechini, L., Alagia, M., Casavecchia, P., Volpi, G.G., 2000a. Observation of nitrogen-bearing organic molecules from reactions of nitrogen atoms with hydrocarbons: A crossed beam study of N(^{2}D) + ethylene. J. Phys. Chem. 104, 5655-5659.

Balucani, N., Asvany, O., Chang, A.H.H., Lin, S.H., Lee, Y.T., Kaiser, R.I., Osamura, Y., 2000b. Crossed beam reaction of cyano radicals with hydrocarbon molecules. III. Chemical dynamics of vinylcyanide (C_2H_3CN; X ^{1}A') formation from the reaction of CN(X $^2\Sigma^+$) with ethylene, C_2H_4(X ^1A_g), J. Chem. Phys. 113, 8643-8655.

Balucani, N., Casavecchia, P., 2006. Laboratory studies on N(^{2}D) reactions of relevance to the chemistry of planetary atmospheres. 1st. European Planetary Science Congress 2006, P0162, EPSC2006-A-00079.

Basiuk V.A., 2001. Formation of amino acid precursors in the interstellar medium. A DFT study of some gas-phase reactions starting with methyleneimine. J. Phys. Chem A. 105, 4252-4258.

Baulch, D. L., Cobbs, C.J., Cox, R.A., Esser, C., Frank, P., Just, Th., Kerr, J.A., Pilling, M.J., Troe, J., Walker, R.W., Warnatz, J., 1992. Evaluated kinetic data for combustion modeling. J. Phys. Chem. Ref. Data 21, 411-734.

Bézard, Feuchtgruber, H., Moses, J.I., Encrenaz, T., 1998. Detection of methyl radicals (CH_3) on Saturn. Astron. Astrophys. 334, L41-L44.

Bocherel, P., Herbert, L.B., Rowe, B.R., Sims, I.R., Smith, I.W.M., Travers, D., 1996. Ultralow-temperature kinetics of CH(X2II) reactions: rate coefficients for reactions with O_2 and NO (T = 13-708 K), and with NH_3 (T = 23-295 K). J. Phys. Chem. 100, 3063-3069.

Callear, A.B., Metcalfe, M.P., 1976. Oscillator strengths of the bands of the $\tilde{B}^2A_1'$-$\tilde{X}A_2''$ system of CD_3 and a spectroscopic measurement of the recombination rate. Comparison with CH_3. Chem. Phys. 14, 275-284.

Choi, N., Blitz, M.A., McKee, K., Pilling, M.J., Seakins, P.W., 2004. H atom branching ratios from the reactions of CN radicals with C_2H_2 and C_2H_4, Chem. Phys. Let. 384, 68-72.

Cody R.J., Romani, P.N., Nesbitt, F.L., Iannone, M.A., Tardy, D.C., Stief, L.J., 2003. Rate constant for the reaction $CH_3 + CH_3 \rightarrow C_2H_6$ at T = 155 K and model calculation of the CH_3 abundance in the atmospheres of Saturn and Neptune. J. Geophys. Res. 108,doi:10.1029/2002JE002037.

Coustenis, A., Bézard, B., 1995. Titan's atmosphere from Voyager infrared observations. IV. Latitudinal variations of temperature and composition. Icarus 115, 126-140.

Coustenis, A., Salama, A., Schulz, B., Ott, S., Lellouch, E., Encrenaz, Th., Gautier, D., Feuchtgruber, H., 2003. Titan's atmosphere from ISO mid-infrared spectroscopy. Icarus 161, 383-403.

Coustenis, A., and 24 co-authors, 2007. The composition of Titan's stratosphere from Cassini/CIRS mid-infrared spectra. Icarus, *in press.*

Duley, W.W., 1996. The formation of H_2 by H-atom reaction with grain surfaces. MNRAS 279, 591-594.

Gurwell, M., 2004. Submillimeter observations of Titan: Global measures of stratospheric temperature CO, HCN HC_3N and the isotopic ratios $^{12}C/^{13}C$ and $^{14}N/^{15}N$. Ap. J. 616, L7-L10.

Herron, J.T., 1999. Evaluated Chemical Kinetics Data for Reactions of $N(^2D)$, $N(^2P)$, and $N_2(A\ ^3\Sigma_u^+)$ in the Gas Phase. J. Phys. Chem. Ref. Data 28, 1453-1483.

Hidayat, T., Marten, A., Bézard, B., Gautier, D., Owen, T., Matthews, H.E., Paubert, G., 1997. Millimeter and submillimeter heterodyne observations of Titan: Retrieval of the vertical profile of HCN and the $^{12}C/^{13}C$ ratio, Icarus 126, 170•182.

Horne, D.G., Norrish, R.G.W., 1970. The photolysis of acyclic azines and the electronic spectra of R_1R_2CN radicals, Proc. R. Soc. London A 315.

Hourdin, F., Lebonnois, S., Luz, D., Rannou, P., 2004. Titan's stratospheric composition driven by condensation and dynamics. J. Geophys. Res. 109, doi:10.1029/2004JE002282

Kassner, Ch., Stuhl, F., 1994. The VUV photodissociation $CH_3 \rightarrow CH(A^2\Delta$ and $B^2\Sigma^-) + H_2$, Chem. Phys. Lett. 222, 425-430.

Knyazev, V.D., Slagle, I.R., 2001. Kinetics of the reactions of n-Alkyl (C_2H_5, n-C_3H_7, and n-C_4H_9)radicals with CH_3. J. Phys. Chem. A 105, 6490-6498.

Lara, L.-M., Lellouch, E., Lopez-Moreno, J., Rodrigo, R., 1996. Vertical distribution of Titan's atmospheric neutral constituents. J. Geophys. Res. 101, 23261•23283.

Lebonnois, S., 2005. Benzene and aerosol production in Titan and Jupiter's atmospheres: a sensitivity study. Planet. Space Sci. 53, 486-497.

Lebonnois, S., Bakes, E.L.O., McKay, C.P., 2003. Atomic and molecular hydrogen budget in Titan's atmosphere. Icarus 161, 474-485.

Lellouch, E., Romani, P.N., Posenqvist, J., 1994. The vertical distribution and origin of HCN in Neptune's atmosphere. Icarus 108, 112-136.

Marten, A., Hidayat, T., Biraud, Y., Moreno, R., 2002. New millimeter heterodyne observations of Titan: Vertical distributions of HCN HC_3N, CH_3CN, and the isotopic ratio $^{15}N/^{14}N$ in its atmosphere. Icarus 158, 532•544.

Monks, P.S., Romani, P.N., Nesbitt, F.L., Scanlon, M., Stief, L.J., 1993. The kinetics of the formation of nitrile compounds in the atmosphere of Titan and Neptune. J. Geophys. Res. 98, 17115-17122.

Morter, C.L., Farhat, S.K., Adamson, J.D., Glass, G.P., Curl, R.F., 1994. Rate constant measurement of the recombination reaction C_3H_3 + C_3H_3. J. Phys. Chem. 98, 7029-7035.

Moses, J.I., Bézard, B., Lellouch, E., Gladstone, G.R., Feuchtgruber, H., Allen, M., 2000. Photochemistry of Saturn's Atmosphere: I. Hydrocarbon Chemistry and Comparisons with ISO Observations. Icarus 143, 244-298.

Münzel, N., Schweig A., 1988. UV/VIS absorption spectrum, geometry and electronic structure of transient *o*-Benzyne, Chem. Phys. Lett. 147, 192-194.

Nguyen, M.T, Sengupta D., Ha, T.-K. 1996. Another look at the decomposition of methyl azide and methanimine: How is HCN formed? J. Phys. Chem 100, 6499-6503.

Niemann, H.B., and 17 co-authors, 2005. The abundance of constituents of Titan's atmosphere from the GCMS instrument on the Huygens probe. Nature doi:10.1038/nature04122.

Nizamov, B., Dagdigian, P.J., 2003. Spectroscopic and kinetic investigation of methylene amidogen by cavity ring-down spectroscopy. J. Phys. Chem. A 107, 2256-2263.

Parker, J.K., Payne, W.A., Cody, R.J., Stief, L.J., 2004. Kinetics of the reaction of atomic hydrogen with cyanoacetylene from T=200 to 298 K. J. Phys. Chem A 108, 1938-1945.

Parkes, D.A., Paul, D.M., Quinn, C.P., Robson, R.C., 1973. The ultraviolet absorption by alkylperoxy radicals and their mutual reactions. Chem. Phys. Lett. 23, 425-429.

Payne, W.A., Monks, P.S., Nesbitt, F.L., Stief, L.J., 1996. The reaction between N(^{4}S) and C_2H_3: Rate constant and primary reaction channels. J. Chem. Phys. 104, 9808-9815.

Pilling, M.J., Bass, A.M., Braun, W., 1971. Oscillator strengths of CH_2 and CH_3 in the vacuum ultraviolet. Chem. Phys. Lett. 9, 147-148.

Redondo, P., Pauzat, F., Ellinger, Y., 2006. Theoretical survey of the NH + CH_3 potential energy surface in relation to Titan atmospheric chemistry. Planet. Space Sci. 54, 181-187.

Sato, K., Misawa, K., Kobayashi, Y., Matsui, M., Tsunashima, S., Kurosaki, Y., Takayanagi, T., 1999. Measurements of thermal rate constants for the reactions of N(^{2}D,^{2}P) with C_2H_4 and C_2D_4 between 225 and 292 K. J. Phys. Chem. A 103, 8650-8656.

Sekine, Y., Imanaka, H., Lebonnois, S., Khare, B.N., Bakes, E.L.O., McKay, C.P., Sugita, S., Matsui, T., 2006. The role of organic haze in the hydrogen budget on Titan.1st. European Planetary Science Congress 2006, EPSC2006-A-00312.

Sillesen, A., Ratajczak, E., Pagsberg, P., 1993. Kinetics of the reaction H + C_2H_4 → C_2H_5, H + C_2H_5 → 2 CH_3, CH_3 + C_2H_5 → products studied by pulse radiolysis combined with infrared diode lase spectroscopy. Chem. Phys. Lett. 201, 171-177.

Sims, I.R., Queffelec, J.-L., Travers, D., Rowe, B., Herbert, L.B., Karthäuser, J., Smith, I.W.M., 1993. Rate constants for the reactions of CN with hydrocarbons at low and ultra-low temperatures. Chem. Phys. Lett. 211, 461-468.

Slagle, I.R., Gutman, D., Davies, J.W., Pilling, M., 1988. Study of the recombination reaction CH_3 + CH_3 → C_2H_6. I. Experiment. J. Phys. Chem. 92, 2455-2462.

Smith, G.R., Strobel, D.F., Broadfoot, A.L., Sandel, B.R., Shemansky, D.E., Holdberg, J.B., 1982. Titan's upper atmosphere: Composition and temperature from the EUV solar occultation results. J. Geophys. Res. 87, 1351-1359.

Smith, G., 2003. Rate theory of methyl recombination at the low temperatures and pressures of planetary atmospheres. Chem. Phys. Let. 376, 381-388.

Sugai, H., Yoshida, S., Toyoda, H., 1989. Hydrogen retention and release dynamics of amorphous carbon films exposed to a hydrogen plasma. Appl. Phys. Lett. 54, 1412-1414.

Tanguy, L., Bézard, B., Marten, A., Gautier, D., Gérard, E., Paubert, G., Lecacheux, A., 1990. Stratospheric profile of HCN on Titan from millimeter observations. Icarus 85, 43-57.

Teanby, N.A., and 11 co-authors, 2006. Latitudinal variations of HCN, HC_3N, and C_2N_2 in Titan's stratosphere derived from Cassini CIRS data. Icarus 181, 243-255.

Teslja. A., Nizamov, B., Dagdigian, P.J. 2004. The electronic spectrum of methyleneimine. J. Phys. Chem. A. 108, 4433-4439.

Toon, O.B., McKay, C.P., GriKth, C.A., Turco, R.P., 1992. A physical model of Titan aerosols. Icarus 95, 24•53.

Toublanc, D., Parisot, J.P., Brillet, J., Gautier, D., Raulin, F., McKay, C.P., 1995. Photochemical modeling of Titan's atmosphere. Icarus 113, 2•26.

Vereecken, L., De Groof, P., Peeters, J., 2003. Temperature and pressure dependent product distribution of the addition of CN radicals to C_2H_4. Phys. Chem. Chem. Phys. 5, 5070-5076.

Vervack, R.J., Sandel, B.R., Strobel,D.F., 2004. New perspectives on Titan's upper atmosphere from a reanalysis of the Voyager 1 UVS solar occultations. Icarus 170, 91-112.

Vinatier, S., et al., 2006. Vertical abundance profiles of hydrocarbons in Titan's atmosphere at 15°S and 80 °N retrieved from Cassini/CIRS spectra, *in press*.

Vuitton V., Yelle, R.V., Anicich, V.G., 2006a. The nitrogen chemistry of Titan's upper atmosphere revealed. Ap. J. 647, L175-L178

Vuitton V., Yelle, R.V., Anicich, V.G., 2006b. Detection of complex molecules in Titan's upper atmosphere. DPS meeting, #38, #36.03.

Waite J.H. Jr. and 21 coauthors, 2005. Ion neutral mass spectrometry results from the first flyby of Titan. Science 308, 982-986.

Wilson, E.H., Atreya S.K., 2003. Chemical sources of haze formation in Titan's atmosphere. Planet. Space Sci. 51, 1017-1033.

Wilson, E.H., Atreya, S.K., 2004. Current state of modeling the photochemistry of Titan's mutually dependent atmosphere and ionosphere. J. Geophys. Res. 109, doi:10.1029/2003JE002181.

Yelle, R.V., 1991. Non-LTE models of Titan's upper atmosphere. Astrophys. J. 383, 380-400.

Yelle, R.V., Waite, J.H., Cravens, T., Ip, W., Kasprzak, W., Ledvina, S., Luhmann, J., M*ü*eller-Wodarg, I., McNutt, R., Niemann, H., de la Haye, V., Borggren, N., 2005. Vertical structure of Titan's atmosphere from INMS observations. Titan Cassini/Huygens meeting: Titan after the Huygens and first Cassini encounters.

Yelle, R.V., Borggren, N., de la Haye, V., Kasprzal, W.T., Niemann, H.B., Müller-Wodarg, I., Waite, J.H., 2006. The vertical structure of Titan's upper atmosphere from the Cassini ion neutral mass spectrometer measurements. Icarus 182, 567-576.

Yung, Y. L., Allen, M., Pinto J.P., 1984. Photochemistry of the atmosphere of Titan: Comparison between model and observations. Astrophys. J. Supp. 55, 465-506.

Zalicki, P., Ma, Y., Zare, R.N., Wahl, E.H., Dadamio, J.R., Owano, T.G., Kruger, C.H., 1995. Methyl radical measurement by cavity ring-down spectroscopy. Chem. Phys. Lett 234, 269-274.

Zhu R.S., Xu, Z.F., Lin, M.C., 2004. *Ab initio* studies of alkyl radical reactions: Combination and disproportionation reactions of CH_3 with C_2H_5, and the decomposition of chemically activated C_3H_8. J. Chem. Phys. 120, 6566-6573.

Chapter 5

Haze Production

5.1 Haze pathways

In the previous chapter the results of the model calculations regarding the vertical chemical composition of Titan's atmosphere were described. The overall picture is in good agreement with the retrieved abundances from the latest measurements taken by the instruments of the Cassini/Huygens mission. This suggests that the model generated haze opacities, based on the suggested pathways described in Chapter 3, which affect the solar radiation fluxes responsible for the photolysis of the species and the vertical temperature profile, provide an adequate equivalent of the ones found in Titan's atmosphere. In this chapter, a description of the contribution of each pathway is presented.

5.1.1 Aromatics

The aromatics family includes both pure hydrocarbon and copolymer structures (see Fig. 5.1). The polymer structures initiated with the acetylene addition on phenyl radicals provide the major contribution for this family with a peak at 140 km and a rate of 2.3×10^{-2} particles $cm^{-3}s^{-1}$. As discussed in 3.3 also, the pressure-dependent rate of Wang & Frenklach (1994) has been used for this reaction, since the stabilized adduct is the one that leads to the formation of PAH structures. When this rate is compared with the high-pressure limit rate for the adduct formation reported by Yu et al. (1994) and not with the total reaction rate, which is pressure independent, it becomes apparent that the two rates, in the temperature range between 100 and 200 K, characteristic for Titan's conditions, are in much better agreement.

The aromatic copolymer structures based on the cyanoacetylene addition on phenyl radicals have a smaller contribution than the PAH formation pathway. It peaks at 135 km with a production rate of 3.7×10^{-4} particles $cm^{-3}s^{-1}$. The rate for this reaction was estimated with the pressure-dependent rate for the acetylene addition. Both the above two aromatic pathways, decrease with altitude due to their pressure dependence. The third aromatic pathway used, that

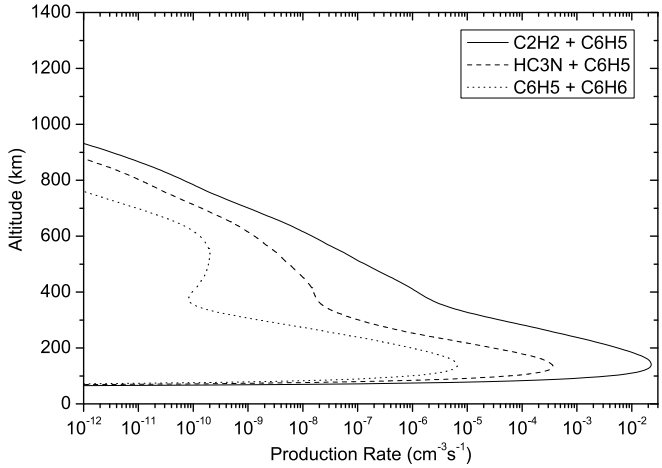

Figure 5.1: Haze vertical production profiles from aromatics.

of direct phenyl addition on benzene molecules has a very small contribution, due to the low abundances for both of the reacting species.

Although benzene formation, as discussed in Chapter 4, still suffers from large uncertainties in the upper atmosphere, the role of aromatic chemistry in haze formation based on these pathways is a first step towards an estimation of their contribution. Since, based on our calculations and those of others, their contribution is important only in the lower atmosphere, where the model resulting benzene profile is within the range of latitudinal values reported by CIRS, we have included them in the total haze production rate.

5.1.2 Polyynes

Polyyne formation is based on C_4H_2 and C_6H_2 species in the model description and proceeds with the addition of C_4H and C_6H radicals (Fig. 5.2). The main peak of the total polyyne contribution is situated at 620 km with a production rate of 9.2×10^{-4} particles/cm^3/s, which is very small compared to the total column production from all the pathways (Fig. 5.5). This is something which is expected, as discussed in §2.3.2, due to the decreasing abundance of polyynes with increasing size of these molecules. Compared to the production profile of polyynes reported in Wilson & Atreya (2003), the current monomer production profile is larger due to the increased abundance of C_4H_2 in my calculations compared to their profile. On the other hand, my calculated profile is very close to the lower boundary of the retrieved abundance by INMS, which means that possibly the contribution of polyynes is slightly larger in the upper atmosphere, than the one suggested by our calculations. Yet, the total production in this

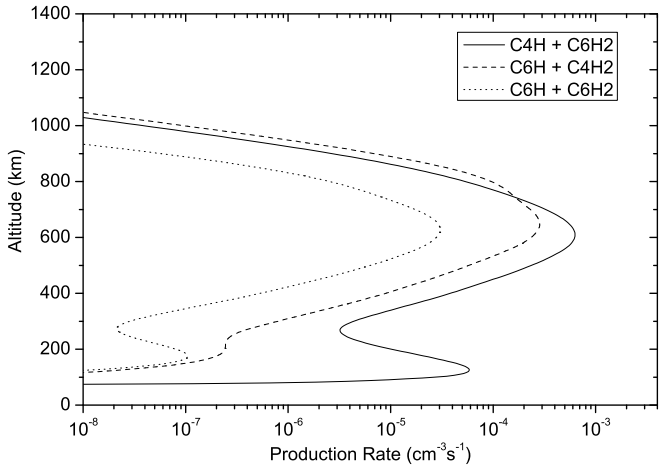

Figure 5.2: Haze vertical production profiles from polyynes.

region is dominated by the aliphatic copolymer contribution, which means that even if the current polyyne production is slightly underestimated, this will not be significant for the total haze production profile.

5.1.3 Aliphatic copolymers

Aliphatic copolymers are based on the Clarke & Ferris (1997) suggestion for HC_3N/C_2H_2 copolymers. Based on the pathways use here, their contribution dominates the total production rate above 300 km with a peak at ∼720 km of 3.1×10^{-2} particles/cm^3/s. The two different pathways included

$$C_3N + C_4H_2 \rightarrow \text{polymer}$$
$$C_4H + HC_3N \rightarrow \text{polymer}$$

have comparable contributions, with the first being slightly larger in the upper atmosphere (Fig. 5.3). The third pathway for this family, based on the

$$HC_3N + C_4H_3 \rightarrow \text{polymer}$$

pathway (Lebonnois et al., 2002), has a significantly smaller contribution due to the pressure dependence of the rate.

The aliphatic copolymer pathways have a main contribution in the upper atmosphere, which was not present in previous model results. The high altitude production of particles generated by this family is very important in the model calculations. This is because it provides a significant source of opacity in the upper atmosphere which is necessary in order to match the observed haze

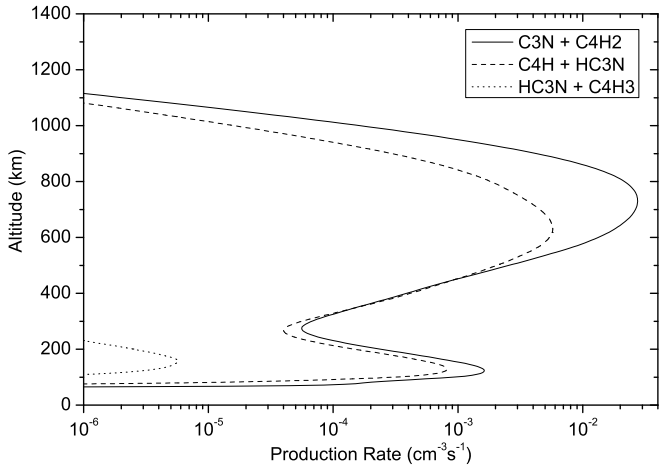

Figure 5.3: Haze vertical production profiles from copolymers.

extinction profiles (Tomasko et al., 2005) and as a consequence, the observed vertical temperature structure. These are discussed in more detail in the next section.

5.1.4 Pure nitriles

As discussed in 3.3, the nitrile species involved in the pathways of haze formation are HCN, H_2CN, CH_2NH, C_2H_3CN, C_2N_2 and C_4N_2. In the upper atmosphere the nitrile contribution is dominated by the reaction

$$CN + C_2H_3CN \rightarrow \textit{polymer}$$

due to the large observed abundance of C_2H_3CN in this region, while in the lower atmosphere, the largest contribution comes from the

$$H_2CN + HCN \rightarrow \textit{polymer}$$

pathway (see Fig. 5.4). This qualitative picture is similar to the one suggested by Wilson & Atreya (2003) although the quantitative details are different due to the different vertical profiles of the precursor species calculated by the two models. Our total nitrile contribution in the upper atmosphere peaks at 845 km with a production rate of 6.5×10^{-3} particles/cm^3/s, while Wilson & Atreya (2003) suggest a peak at about the same region but with more than an order of magnitude smaller production rate. This is due to the underestimation of the C_2H_3CN abundance in the upper atmosphere, in their pre-Cassini model results. The CN addition mechanism is also important for the case of C_4N_2, with this

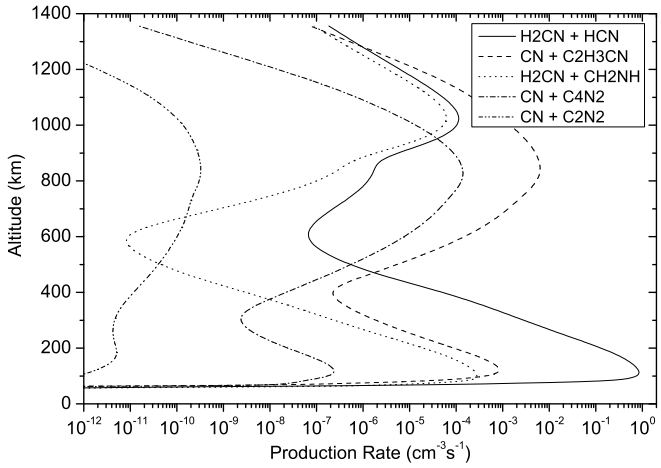

Figure 5.4: Haze vertical production profiles from pure nitriles.

pathway providing the second most important contribution of the pure nitrile pathways in the upper atmosphere, after the C_2H_3CN contribution, although of significantly smaller magnitude. Due to its small abundance, the C_2N_2 pathway has a negligible contribution.

On the other hand, in the lower atmosphere, their suggested contribution from the H_2CN pathway peaks at about 200 km, while the current results suggest a peak significantly lower, at ∼115 km. This difference is probably related to the different structure of the calculated HCN profiles in this region by the two models, with my more constant profile below 300 km, providing an enhanced contribution by this pathway below 200 km. Further, the pathway based on the the polymerization of CH_2NH (along with the acrylonitrile pathway) provides the second most important nitrile contribution in the lower atmosphere while its contribution becomes important again in the upper atmosphere, above 1000 km although the suggested production rate in this region could be overestimated due to the large abundance suggested by the model calculations for CH_2NH, relative to the observed one.

5.1.5 Haze production profile and the role of GCR

The total vertical production rate, along with the contribution of each family is presented in Fig. 5.5. From the above description it becomes evident that there are specific altitude regions where the contribution of each family is important. In the lower atmosphere, below 300 km, the production is controlled by the nitrile family along with the aromatics. At higher altitudes, the aliphatic copolymers dominate the production up to 1000 km, while at even higher levels,

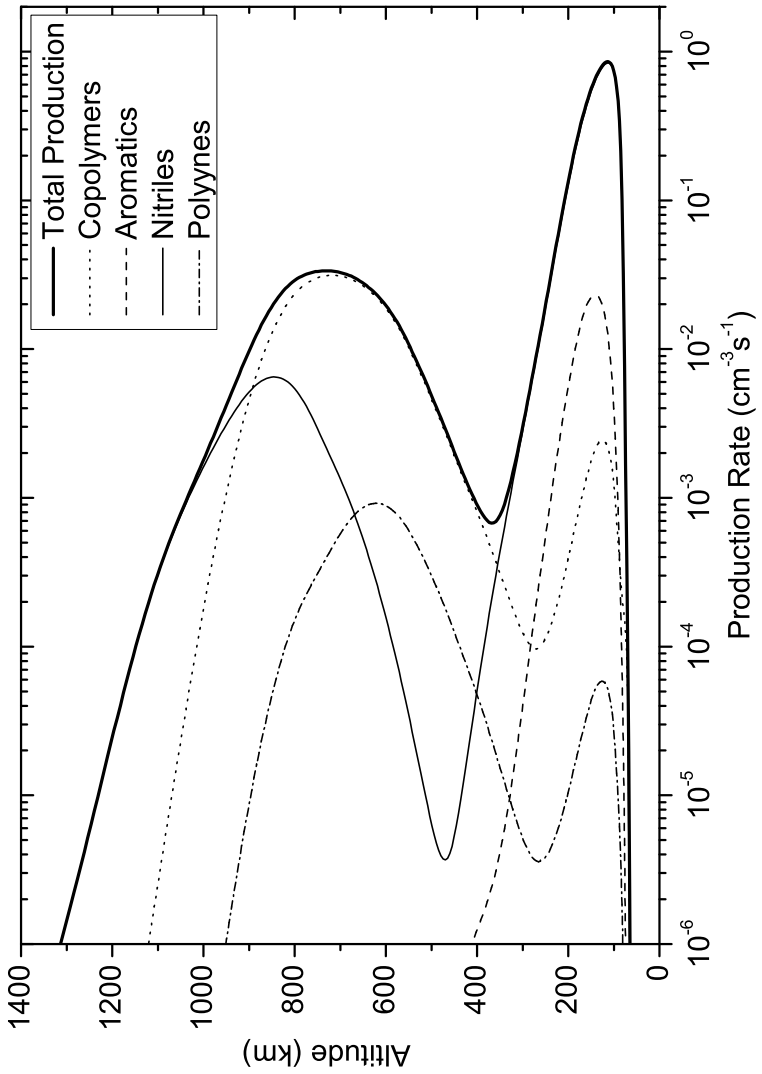

Figure 5.5: The vertical production profile of haze particles (monomers) according to the model calculations and based on the calculated chemical composition. Each one of the thin lines corresponds to the contribution of a different family of polymer structures, while the thick line corresponds to the total production rate.

the nitrile contribution dominates again. Polyynes are found to be of secondary importance compared to all other families.

This picture of varying production and composition with altitude is a representation of the photochemical background of haze formation, under the current description. Nitriles, are produced at very high altitudes, due to their dependence on the N_2 destruction. The last is possible only by high energy UV photons, which have their maximum deposition above 1000 km based on our calculations. Hydrocarbon production, which is initiated by methane photolysis, has its maximum at lower altitudes due to the absorption of these species at longer wavelengths with increasing carbon complexity (CH_4 photolysis has its maximum deposition at ∼800 km, see Figs. 2.8 & A.1). Hence, above 1000 km, nitrile pathways dominate haze production, while below the combined contribution of nitriles and hydrocarbons increases. Finally, at lower altitudes pure hydrocarbons start to have a larger contribution.

At this point it is important to note the significance of GCR impact in the haze production profile. In particular, H_2CN and CH_2NH exhibit a large variation in their stratospheric profile when galactic cosmic rays are included, with their abundances increasing significantly (Fig. 5.6a). This translates to a large contribution to the haze production profile in this region from the pathways that are based on them and explains why the nitrile family starts to become important again below 300 km. This effect is presented in Fig. 5.6b where the total vertical production rate for the haze monomers is shown with and without the GCR contribution. When it is removed, the decrease in the H_2CN and CH_2NH stratospheric abundance, practically removes the contribution of nitrile pathways in the lower atmosphere. From the above, it is clear that the temporal character of GCR could lead to temporal variations in total haze production.

Under this description, it is evident that the contribution of pure hydrocarbon pathways is only significant in the lower atmosphere, through the aromatic polymer pathway, since the contribution from polyynes is significantly smaller than that of all other families. Yet, even in the lower atmosphere, the total production, when the GCR are included, is dominated by the nitrile pathways. This small contribution of pure hydrocarbon pathways in the haze vertical production, seems to be in keeping with the measurements from the ACP instrument on board the Huygens probe (Israel et al., 2005). These measurements, as discussed also in §3.2, provide evidence of nitrogen incorporation in the haze particles, based on the pyrolysis products of the sampled aerosols. Neglecting the pathways of pure hydrocarbons in haze formation does not change significantly the vertical structure of the produced haze particles, since their contribution to the vertical production profile is in the same region as that of the other pathways. The difference will be only in the total haze opacity. For the current calculations we have included the pure hydrocarbon contribution.

The column production rate from all of the above pathways is 9.0×10^6 particles/cm^2/s, which corresponds to 1.27×10^{-14} g/cm^2/s for the 7.25 Å radius used for the monomers. This value is within the range 0.5-2$\times10^{-14}$ g/cm^2/s, reported in McKay et al. (2001) from previous photochemical and microphysical models along with laboratory simulations. Care should be taken when compar-

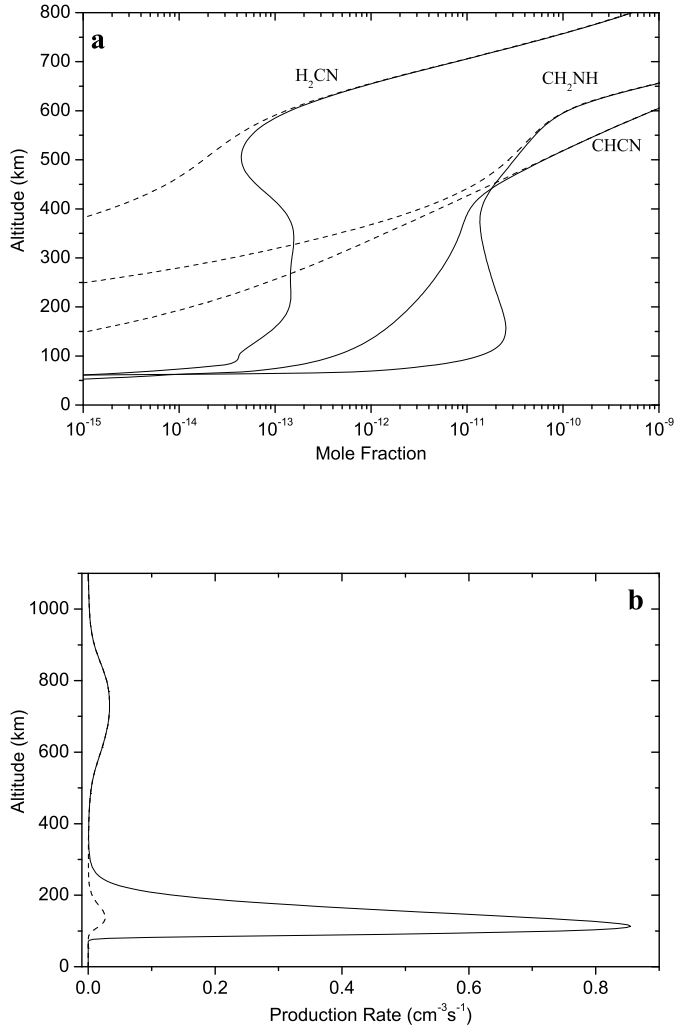

Figure 5.6: (a) The impact of GCR on the vertical profiles of CHCN, CH_2NH, and H_2CN. Solid lines include the GCR contribution while dashed lines correspond to no GCR impact.(b) GCR have a broad contribution in the haze vertical production profile in the lower atmosphere. The vertical production profile shown with the solid line is the same as that in Fig. 5.5, but on a linear scale. The dashed profile corresponds to the resulting production profile when GCR are not included. In this case the production in the lower atmosphere is controlled by the aromatic family. The two profiles converge at higher altitudes where the impact of GCR is negligible.

Table 5.1: Column production rates for the families studied at different regions of the atmosphere along with the total C, N and H lost in the chemical formation and growth of the haze monomers. Read a(b) as a$\times 10^b$. Units are in cm^{-2}s^{-1}.

Family	Column Production Rate			Total Chemical Loss		
	0 - 300 km	300 - 1400 km	Total	C	N	H
Aromatics	1.9(5)	1.1(2)	1.9(4)	1.5(7)	4.4(4)	1.4(7)
Polyynes	5.0(2)	2.5(4)	2.5(4)	2.0(6)	0	5.9(5)
Nitriles	7.1(6)	2.6(5)	7.4(6)	2.8(8)	2.7(8)	2.7(8)
Copolymers	2.0(4)	1.4(6)	1.4(6)	8.8(7)	2.2(7)	7.1(6)
Total	7.4(6)	1.6(6)	**9.0(6)**	**3.8(8)**	**3.0(8)**	**2.9(8)**

ing results from different works because the size of the monomers used is usually not the same and this can lead to slightly different results regarding the column production rate. In addition, the assumed shape of the particles (spherical or fractal), is known to lead to significantly different results for the column production rates, with the fractal aggregates usually requiring larger production rates than those with spherical shape (McKay et al., 2001). Nevertheless, the current column production is in good agreement with previous estimates based on spherical particle calculations. The contribution of each family to the total column production is presented in Table 5.1 along with the contributions in the upper (300 - 1500 km) and lower (0 - 300 km) atmosphere.

5.2 Chemical loss to haze

The total number of C, N and H atoms lost in the formation of the initial dimer and chemical growth to the size of the monomer, beyond which microphysical growth takes over, is presented in Table 5.1. Due to the dominance of the pure nitrile and copolymer pathways in the haze production, the total number of nitrogen atoms lost to the haze is significant. With the column atomic nitrogen production from N_2 destruction being 7.3×10^8 $cm^{-2}s^{-1}$ from our calculations, the loss to haze formation corresponds to $\sim$40% of the total N production. The importance of this nitrogen loss was initially suggested by McKay (1996) who estimated it to be about 12% of the total atomic nitrogen production in the upper atmosphere, based on the total C & N produced in the photolysis of CH_4 & N_2 and assuming a C/N ratio of 4, taken as an average from the laboratory derived ratios. The current results, which are specifically based on the chemical loss to haze and not the total production of C and N, suggest C/N and C/H ratios which are about 1.3 and hence approximately correspond to a stoichiometric formula of $C_4H_3N_3$ for the haze particles.

The initial chemical loss for the dimer formation is of significantly smaller magnitude than the total chemical loss for the growth to the size of the monomer (see ε factors presented in Table 3.2). This means that, if only the chemical loss for the formation of the dimer is included in the calculations, there will be an underestimation of the impact of haze formation in the atmospheric gas composition. This is presented in Fig. 5.7a, where the vertical profiles of the main hydrocarbons and nitriles are presented with and without the inclusion of the chemical loss through the chemical growth of the dimers to the monomer size. The impact of this process is more important for nitrile species than hydrocarbons. This is expected since the relative loss of carbon to haze is smaller than that of nitrogen.

Based on the possible importance of haze formation as a nitrogen sink, Lara *et al.* (1999), suggested that the loss of HCN through polymerization, could be a possible process for the reduction of the stratospheric HCN abundance and the correct representation of this species along with the C_2H_X carbons with the use of a single eddy mixing profile. They concluded that for the process to be efficient, a loss rate of the order (3-5)$\times10^8$ $cm^{-2}s^{-1}$ was necessary, while

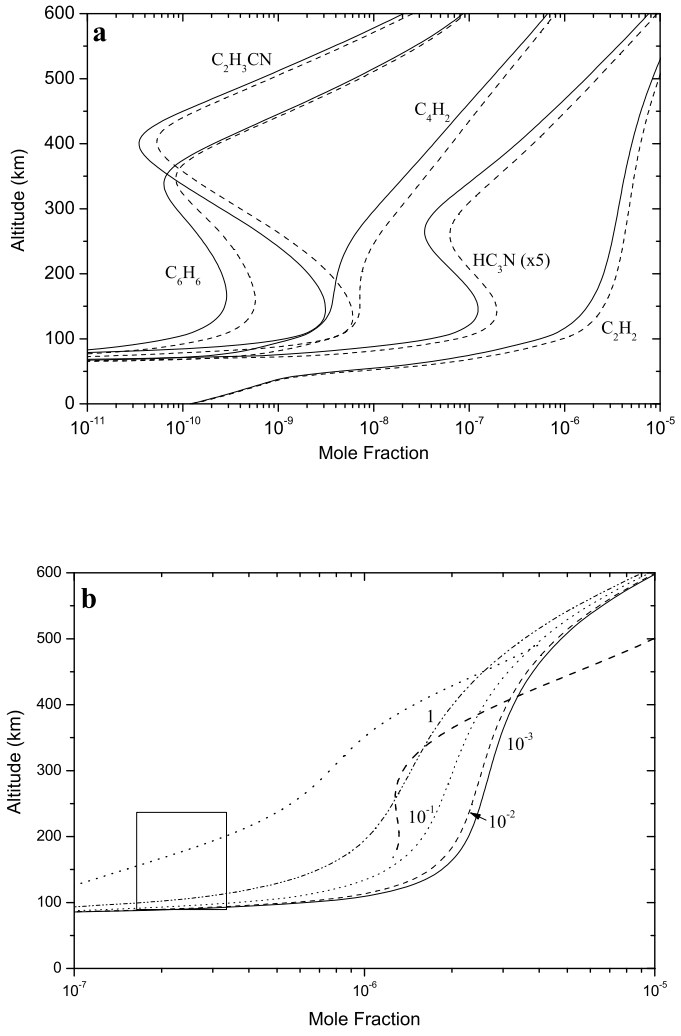

Figure 5.7: (a) The impact of chemical loss due to haze monomer production on the vertical profiles of species involved in the pathways. Solid and dashed lines correspond to the model results with and without the chemical growth of the initial dimers, respectively. Notice that the HC_3N vertical profiles are multiplied by a factor of 2 for clarity. (b) The impact of haze formation on the HCN vertical profile for different H_2CN + HCN reaction rates. For the solid line the rate was estimated with the Monks et al. (1993) measured rate for the reaction C_2H_3 + HCN rate, while dashed, dotted lines and dashed-dotted lines correspond to 10^{-1}, 10^{-2} and 10^{-3} times the Monks et al. (1993) rate. Also shown are the CIRS retrieved vertical profiles for equatorial and polar regions based on limb spectra (Vinatier et al., 2006) and the CIRS mid-latitude stratospheric abundance based on nadir spectra from (Coustenis et al., 2007).

Vinatier et al. (2006) reached a similar conclusion regarding the total loss rate of HCN needed to be used in their calculations to match the CIRS retrieved vertical profiles of C_2H_6 and HCN with a single mixing profile.

According to the description provided above, the major HCN loss (and nitrogen loss at the same time) due to haze formation is from the

$$HCN + H_2CN \rightarrow \text{polymer}$$

pathway. Yet, the magnitude of the process depends on the rate used for the formation of the initial dimer and as discussed in §3.3, the rate for this reaction is not measured but estimated based on the C_2H_3 + HCN reaction measured by Monks et al. (1993). Wilson & Atreya (2003) have used a reduced rate for this reaction based on their results regarding the C_2H_3CN and HC_3N profile along with the total haze production generated in their calculations, while in §3.3 a possible reason for the reduction of this reaction rate was discussed. Nevertheless, a sensitivity test for the effects of the rate used was performed. Fig. 5.7b presents the calculated vertical HCN profile from the model for four different estimations of the ratio

$$\gamma = \frac{k(H_2CN + HCN)}{k(Monks\ et\ al.\ 1993)} \tag{5.1}$$

ranging between one and a 1000 times smaller rate. From the presented results it is obvious that the higher the rate of the reaction, the stronger the decrease in the HCN profile observed. Setting γ to 1, provides a loss rate for the HCN molecules due to haze production that is sufficient to constrain the calculated profile within the bounds of the observations in the stratosphere. In terms of HCN molecules lost, the column rate is 4.2×10^8 $cm^{-2}s^{-1}$. Yet, in view of the over-estimation of the HCN abundance in the upper atmosphere, which leads to larger fluxes towards the lower atmosphere and the expected reduced rate of the reaction discussed, γ was kept at 0.1. All results presented so far are for this value of γ. The increased nitrile loss for increasing values of γ has also an impact on the resulting C/N ratio which decreases by a factor of 2.5 for γ values between 10^{-3} and 1 (Table 5.2).

Changing the rate for the H_2CN + HCN reaction changes the total haze production. Yet, the increase in the monomer production is counter-balanced by the loss of the precursors. This is presented in Fig. 5.8. There the model calculated column production of particles due to this pathway is presented along

Table 5.2: Variation of C/N and C/H ratios for different values of the γ ratio along with the column production rate (CPR) from all included pathways in $10^{-14}gcm^{-2}s^{-1}$.

γ	10^{-3}	10^{-2}	10^{-1}	1	No Chem. Loss, γ=10^{-1}
C/N	2.98	1.78	1.28	1.18	1.34
C/H	3.87	1.91	1.29	1.17	1.32
CPR	0.24	0.50	1.27	1.97	1.62

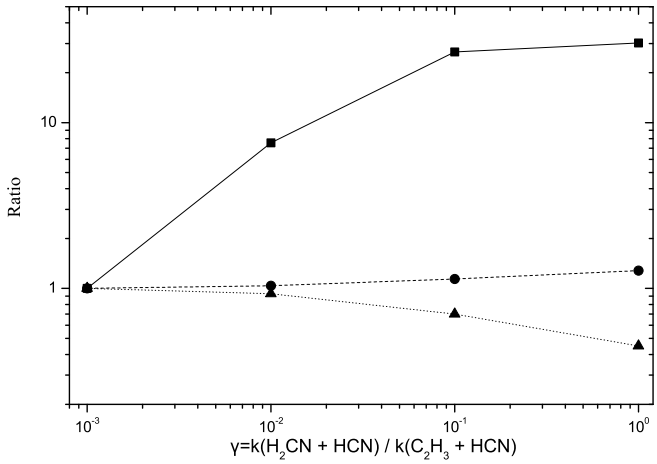

Figure 5.8: Variation of column haze production through the H_2CN + HCN pathway (squares), HCN mixing ratio at 200 km (triangles) and haze opacity at 530 nm (circles) for different values of the ratio γ. All values have been normalized to unity for γ=10^{-3}.

with the resulting HCN mole fraction at 200 km and haze column opacity at 530 nm, for different values of the γ ratio. All values have been normalized to unity for γ=10^{-3}. The chemical loss of HCN resulting from the above reaction constrains the increase in haze production. As γ increases from 10^{-3} to 1, the column production increases by a factor of $\sim$ 30, while the HCN mole fraction at 200 km decreases by 0.45. At the same time, because the increase in the production is located in the lower atmosphere, the change in the resulting haze opacity is minimal (for γ=1 the ratio of the opacities is $\sim$1.3). This happens because the large down-welling fluxes present in the lower atmosphere force the particles to flow fast towards the surface where they are irreversibly lost.

The above picture would be much different without the inclusion of the chemical loss in the growth of the dimers to the monomer size. As discussed above, the chemical loss due to the dimer formation is significantly smaller than the total chemical loss due to the haze production. Hence, if the latter is not included, the increased production will not be constrained by the loss of the precursors and the total haze produced will be too large to match the observed geometric albedo. Previous results from Wilson & Atreya (2003, 2004) do not specifically mention the inclusion of this process in their calculations although their HCN vertical profiles seems to be in agreement with the observed stratospheric abundances.

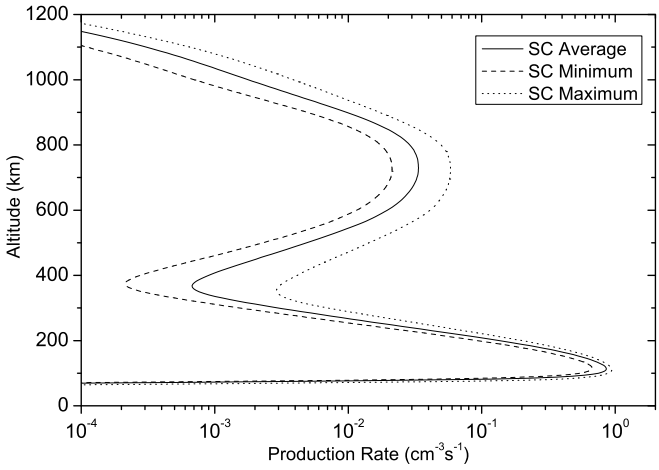

Figure 5.9: Vertical profiles of haze monomer production for solar average (solid line), solar minimum (dashed line) and solar maximum (dotted line) conditions.

5.3 Solar cycle effects

At shown in §4.3, the SC induces changes in the species vertical profiles. This variability of the gas composition has a direct impact in the haze monomer production . In Fig. 5.9 the vertical haze production at solar average, solar minimum and solar maximum conditions is presented. The variation of the monomer production is more prominent in the upper atmosphere with the production being larger at solar maximum than at solar minimum. This variability is mainly due to changes in the nitrile species vertical profiles over the SC. As discussed previously, the impact of the SC is larger on the nitrile compared to hydrocarbon species due to the stronger variation of the N_2 photolysis rate relative to methane's. In terms of column production, the model suggests an increase of about 60% from minimum to maximum relative to the column production at average solar conditions.

Bibliography

Clarke, D.W., Ferris, J.P., 1997. Titan Haze: Structure and properties of the cyanoacetylene and cyanoacetylene-acetylene photopolymers. Icarus 127, 158-172.

Coustenis, A., and 24 co-authors, 2007. The composition of Titan's stratosphere from Cassini/CIRS mid-infrared spectra. Icarus, *in press.*

Israël G. and 21 coworkers, 2005. Complex organic matter in Titan's atmospheric aerosols from in situ pyrolysis and analysis. Nature, doi:10.1038/nature04349

Lara, L.-M., Lellouch, E., Shematovich, V., 1999. Titan's atmospheric haze: the case for HCN incorporation. A&A 341, 312-317.

McKay, C.P., 1996. Elemental composition, solubility and optical properties of Titan's organic haze. Planet. Space Sci. 44, 741-747.

McKay, C.P., Coustenis, A., Samuelson, R.E., Lemmon, M.T., Lorenz, R.D., Cabane, M., Rannou, P., Drossart, P., 2001. Physical properties of the organic aerosols and clouds on Titan. Planet. Space Sci. 49, 79•99.

Monks, P.S., Romani, P.N., Nesbitt, F.L., Scanlon, M., Stief, L.J., 1993. The kinetics of the formation of nitrile compounds in the atmosphere of Titan and Neptune. J. Geophys. Res. 98, 17115-17122.

Tomasko, M.G., Lemmon, M., Roose, L.R., Smith, P.H., Eibl, A., West, R.A., 1997. Models of the penetration of sunlight into the atmosphere of Titan. ESASP-1177, 345•358.

Tomasko, M.G., and 39 co-authors, 2005. Rain, winds, and haze during the Huygens probe's descent to Titan's surface. Nature, doi:10.1038/nature04126.

Vinatier, S., et al., 2006. Vertical abundance profiles of hydrocarbons in Titan's atmosphere at 15°S and 80 °N retrieved from Cassini/CIRS spectra, *in press.*

Wilson, E.H., Atreya S.K., 2003. Chemical sources of haze formation in Titan's atmosphere. Planet. Space Sci. 51, 1017-1033.

Wilson, E.H., Atreya, S.K., 2004. Current state of modeling the photochemistry of Titan's mutually dependent atmosphere and ionosphere. J. Geophys. Res. 109, doi:10.1029/2003JE002181.

Wang, H., Frenklach, M., 1994. Calculations of rate coefficients for the chemically activated reactions of acetylene with vinylic and aromatic radicals. J. Phys. Chem. 98, 1465•1489.

Yu, T., Lin, M.C., Melius, C.F., 1994. Absolute rate constant for the reaction of phenyl radical with acetylene. Int. J. Chem. Kin. 26, 1095-1104.

Chapter 6

Haze Opacity & Atmospheric Structure

Having provided a description of the atmospheric chemical composition and of the pathways used to generate the haze particles, this chapter describes the results of the microphysical evolution of the haze monomers to the haze opacity and the impact of the latter on the observed geometric albedo and temperature structure. The last two observational parameters are used as validation data for the correctness of the atmospheric simulation.

6.1 Haze radiative properties

Using the previously described production profile for the haze particles, the microphysical part of the model provides a description for the evolution of the monomers to the observed particle size in Titan's atmosphere. The produced size distribution along with the resulting optical properties of the haze layer generated with the use of Mie theory are described in this section and are validated against the retrieved haze optical properties from the Cassini/Huygens mission and the observed geometric albedo.

6.1.1 Size distribution

The microphysical evolution of the produced monomers leads to the production of bigger size particles, the final size of which is constrained only by the electrostatic repulsion among them. The charging rate of the particles was kept constant during the calculations at 25 e^-/μm. Typical values for the charging rate, from previous microphysical models, range between 20 and 30 e^-/μm. Differences originate from the use of different shape particles, different production regions and different monomer sizes.

Based on the sensitivity analysis performed for this parameter, the above value gave the best results regarding the agreement between the model and

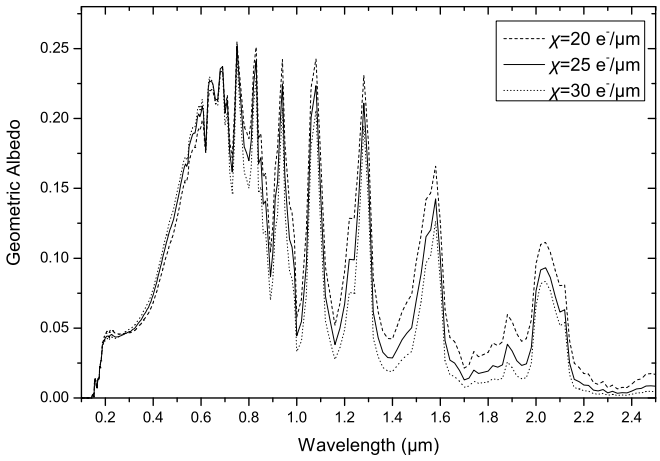

Figure 6.1: Calculated geometric albedo for different values of the charging rate between aerosol particles.

measured geometric albedo, while at the same time provided a spectral variation for the haze column opacity that is consistent with that observed by the DISR instrument (Tomasko et al., 2005), discussed later on. Higher (lower) values for the charging rate, constrain the final average size of the particles to smaller (bigger) values, which for a certain wavelength, decreases (increases) their efficiency factors, based on Mie theory. Hence, by decreasing the charging rate we increase the scattering of the aerosol particles and in this way enhance the geometric albedo above 0.6 μm, where the particles are mostly scattering rather than absorbing (Fig. 6.1). The size distribution of the produced particles is presented in the contour plot of Fig. 6.2.

Since the model generates the population for each size particle, an optically effective radius at each altitude can be calculated. This average size of particles corresponds to the size that has the maximum effect in the radiation transfer calculations and is weighted according to the surface, S_i, of each particle, i:

$$R_{\rm eff} = \frac{\sum_i n_i r_i S_i}{\sum_i n_i S_i} = \frac{\sum_i n_i r_i^3}{\sum_i n_i r_i^2}. \tag{6.1}$$

The resulting effective radius is presented also in Fig. 6.2 along with the range of values retrieved for this parameter by the Voyager measurements (Rages & Pollack, 1983). Below 200 km, $R_{\rm eff}$ approaches a constant value of 0.2 μm which is the lower limit value retrieved by these measurements. In addition this limiting optically effective size for the particles is identical with the equivalent sphere radius suggested by McKay et al. (2001) based on calculations performed with fractal particles.

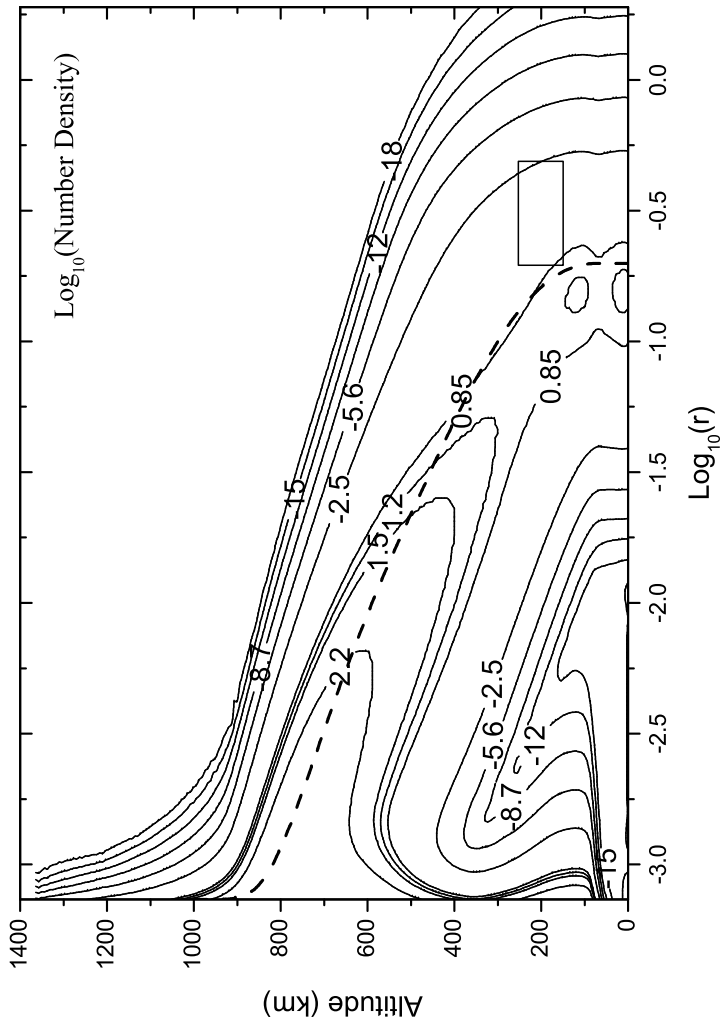

Figure 6.2: Contour plot of the model size distribution for the haze particles. Size is in microns and number density is in cm^{-3}. The dashed line corresponds to the optically effective average radius for this distribution of sizes and the rectangle gives the range of values for the effective size of the particles retrieved by Rages & Pollack (1983) from the Voyager I measurements.

6.1.2 Opacity and structure

Using the Khare et al. (1984) measurements for the refractive index, the opacity of the produced particles can be calculated with the use of Mie theory. The above measurements for the refractive index extend from UV to the IR and are the only ones published that cover such a long interval of the spectrum, which explains their use by all radiation transfer models so far. The application of a scaling factor to the spectral variation of this refractive index was found to be necessary in order to obtain a reasonable match to the spectrally resolved geometric albedo and the vertical temperature structure McKay et al. (1989). These scaling factors are used for the shortwave and thermal infrared haze properties involved in the radiation transfer. In the shortwave, the scaling controls the absorptivity of the particles and hence the match of the geometric albedo below 0.6 μm, where the refractive index shows significant absorption, and through this absorption the extent of the temperature rise in the stratosphere. In the thermal infrared it affects the efficiency of the cooling due to emission from the aerosol particles and hence directly the temperature structure. McKay et al. (1989) suggested a set of scaling factors (4/3 for solar and 1/2 for thermal), which were retrieved based on an optimum match to the observed geometric albedo using spherical aerosol particles. Using their values the agreement for the temperature and geometric albedo is significantly improved and hence are adopted in the calculations. In other microphysical models in which fractal particles are used, a larger scaling has to be considered in order to match the geometric albedo (e.g. 2 - 2.3 for the solar spectrum as in Rannou et al. (2003)). Fig. 6.3 presents a sensitivity test of the modelled geometric albedo on the solar scaling factor. Small variations on the scaling have an important impact on the modelled albedo, hence its value can be well constrained from the observations. The impact on the temperature profile is presented in a following section.

The produced haze particles are assumed to be irreversibly lost to the surface through deposition. Yet, if no other loss process is included, large opacities are maintained in the lower atmosphere in a steady state. A parameter that affects the flow of the particles in this region is the mixing profile used. If the particles are assumed to be mixed with the same eddy coefficient as the gas molecules, then the resulting flux of particles towards the surface is small and the haze opacity builds up in the lower atmosphere. This is significantly different from that measured by the DISR instrument on board the Huygens probe and also much larger than the opacity necessary to match the geometric albedo and the vertical temperature structure. Previous radiation transfer models have also noticed this problem and solved it by applying a cut-off in the haze extinction profile in order to match the observed geometric albedo. The shape and magnitude of this reduction varies among different models, between total removal of the haze opacity below a certain altitude (McKay et al., 1989; Tomasko et al., 1997) or decreased opacity in a certain region (Rannou et al., 2003). But the latest results of the DISR instrument have shown that the haze extends down to the surface with a rather constant opacity below 100 km.

In view of these results a different approach, that of an increased mixing

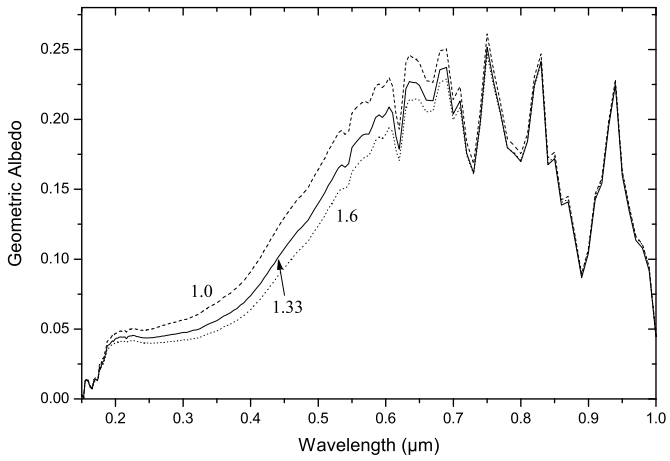

Figure 6.3: Impact of solar scaling factor for haze refractive index on the modelled geometric albedo.

coefficient for the haze particles below the stratopause relative to the one used for the gas species, was applied. This allows the particles to flow faster towards the surface where they are irreversibly lost. The mixing profile for the haze particles above the stratopause is considered to be the same as for the rest of the chemical species in the model. The magnitude of the mixing below the stratopause was increased until a good match to the geometric albedo was obtained. After scaling the mixing in this way we realized that the resulting mixing profile between 300 and 100 km was very close to the mixing profile obtained assuming an altitude dependence that follows the inverse square root of the density ($\rho^{-1/2}$) scaled to the mixing magnitude at 300 km. Due to the close agreement between the vertical mixing profile needed to match the geometric albedo and the scaling suggested by the above dependence it was adopted in the calculations. This approach for the scaling of the mixing profile of the particles was suggested by previous microphysical models (Rannou et al. (2003) and references therein), although the magnitude of the mixing coefficient varies among models.

Below 100 km the eddy mixing profile derived with the above process shows a sharp decrease due to the increase in the density below that level, which is related to the sharp decrease in the temperature observed in this region. Allowing for such a mixing profile still results in a haze opacity which is too large. Hence, the mixing was increased in the lower 80 km, relative to that following $\rho^{-1/2}$. The eddy mixing profile used in the calculations is presented in Fig. 6.4.

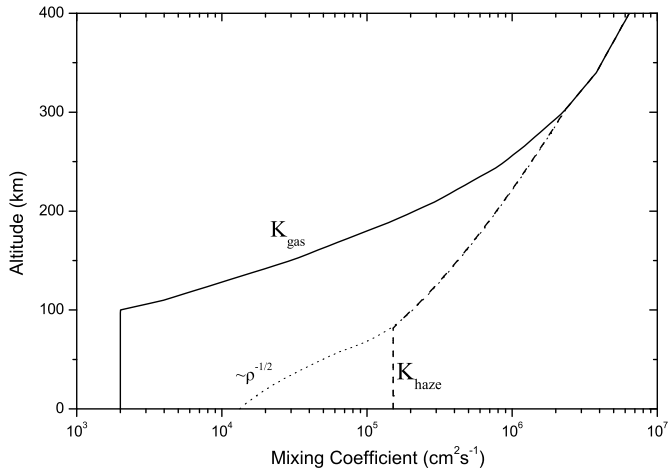

Figure 6.4: The eddy mixing profile used for the aerosol particles. The solid line corresponds to the mixing profile used for the gas species, while the dotted line presents the mixing profile assuming an altitude dependence that follows the $\rho^{-1/2}$ law starting at 300 km. The dashed line presents the final mixing profile used for the haze particles, where in the lower 100 km the mixing magnitude has been increased in order to enhance the loss of the particles to the surface.

This increased flux towards the surface sink is just a simulation of one loss process taking place in Titan's atmosphere. In the lower atmosphere below the stratopause, hydrocarbons and nitriles condense and are removed from the atmosphere. Cloud formation has been observed in specific locations on Titan's disk as discussed in §1.2.6, while Rannou et al. (2006) have shown that the production of clouds using the haze particles as nucleation sites, is possible in certain latitudinal regions, similar to the ones where clouds are observed. Hence, the condensation of atmospheric gases with the consequent cloud formation acts as a sink for the haze particles, which could explain the haze opacity in this region. Applying a large eddy mixing coefficient is just a way of representing this loss, by making the particles flow faster towards the surface sink. Further, the larger eddy mixing profile assigned for the haze particles in the lower atmosphere, below the stratopause, compared to that for the gas species, is found to be necessary irrespective of the value assumed for the γ parameter (Eq. 5.1). The results presented in Table 5.2 correspond to the eddy mixing profile shown in Fig. 6.4.

The resulting column haze opacity is presented in Fig. 6.5 and compared with the measured values retrieved by the DISR instrument (Tomasko et al., 2005). It must be kept in mind that the latter correspond to the location where the probe descended, while the model results correspond to the disk-average opacity that is necessary to provide a good match to the geometric albedo and

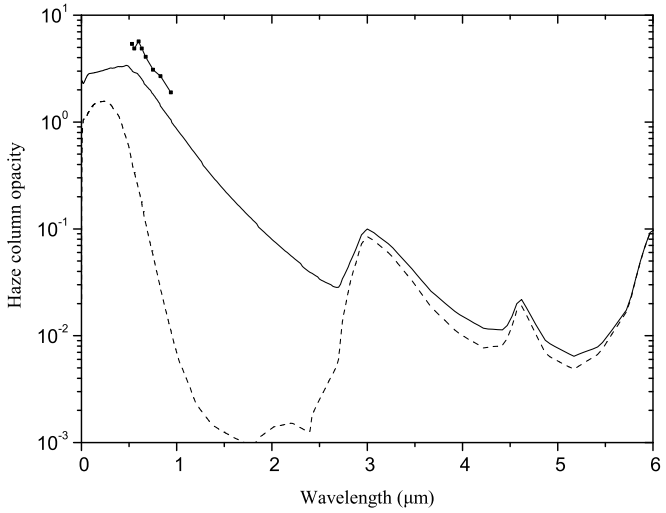

Figure 6.5: The column absorption (dashed line) and extinction (solid line) opacity for the produced haze particles based on the model calculations, along with the measured extinction by the DISR instrument on board the Huygens probe (Tomasko et al., 2005). The particles were considered to attain a spherical shape (Mie particles) and the refractive index required for the calculation of the efficiencies was taken from the laboratory simulations of Khare et al. (1984).

a realistic temperature profile corresponding to global average conditions. The model calculations suggest that a smaller total haze opacity than the measured one is more appropriate in order to match the observations. The measured column opacity by DISR at 750 nm, is 70% larger than the one retrieved by matching the observed geometric albedo (Fig. 6.7). Nevertheless, the measured spectral variation of the opacity between 531 and 938 nm, is similar to that of the model based on the refractive index assumed (Khare et al., 1984) and the charging rate value used in the calculations.

The DISR measurements have also provided results regarding the vertical variation of the haze opacity. The extinction profiles measured cover the above reported range and a comparison between the locally measured and disk-average model profiles, is presented in Fig. 6.6, for four wavelengths. Similar results were obtained for other wavelengths given by DISR. Although the DISR extinction profiles were retrieved assuming the particles to have a fractal structure, the resulting opacity is not depended on the shape of the particles. The DISR instrument measures the variation in the radiation intensity between layers of the atmosphere and hence retrieves the opacity necessary for the reproduction of this variation with altitude. Whether the particles are of spherical or fractal shape, this will have an impact on the resulting number density and size distribution of the particles.

The vertical variation of the opacity derived by the model calculations based

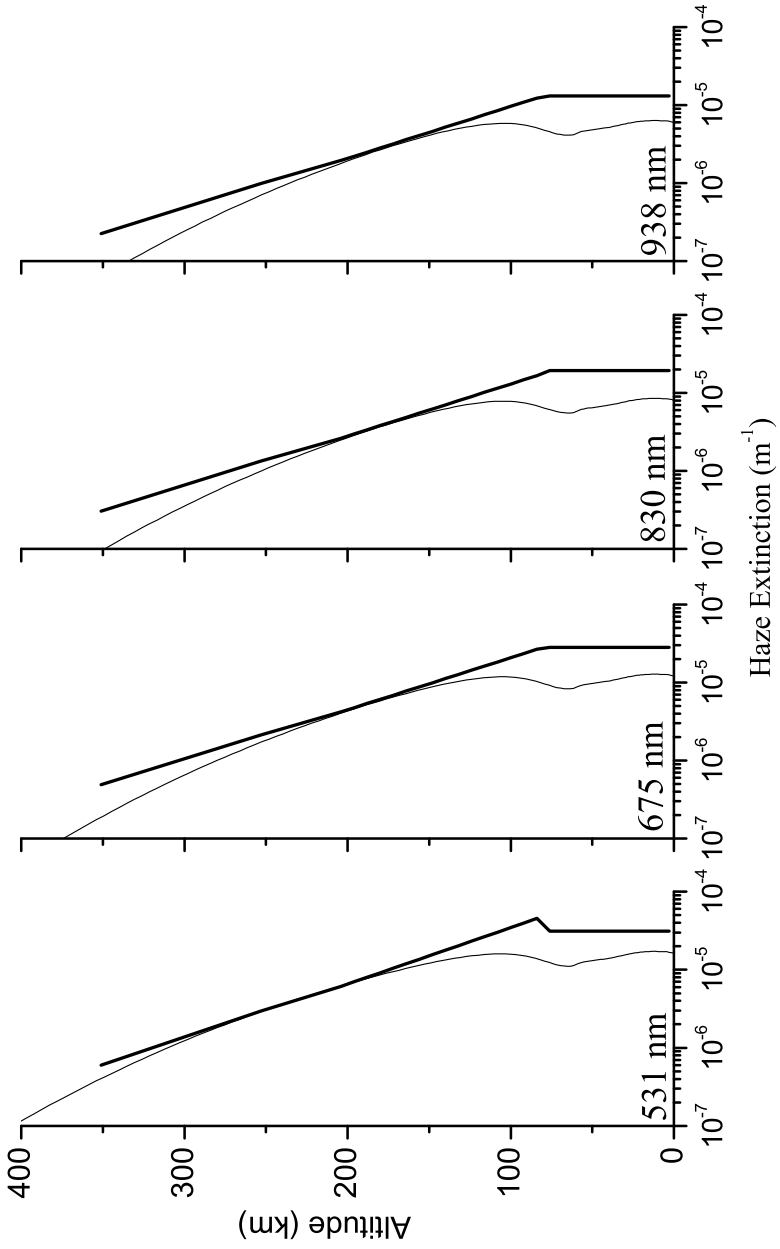

Figure 6.6: The model disk-average resulting extinction profiles of the haze particles at different wavelengths compared with the DISR retrieved profiles which are characteristic of the Huygens probe descent location.

on the suggested pathways is very close to that observed by the DISR measurements. The copolymer contribution in the upper atmosphere is mainly responsible for the production of particles, the evolution of which provides the opacity in the region above 300 km. Without the contribution from this family the haze structure would be significantly different with smaller extinction values. At lower altitudes the cumulative contribution from aromatics and nitriles produces the observed opacity, which is constrained by the enhanced mixing applied.

At higher altitudes the model-derived extinction profiles decrease faster than the observed profiles. This is the manifestation of dynamical effects, which become important in this region leading finally to the production of the observed detached haze layers. Under the current picture of haze formation, it is evident that the chemical composition of the detached haze layer will be mostly affected by the copolymer family than by the nitriles/aromatics, which are formed further below. This could lead to different optical properties for the particles formed in this region compared to the optical properties of the final particles in the lower atmosphere. Such a qualitative picture was obtained also by Rannou et al. (2000) in their investigation of the detached haze optical properties.

6.1.3 Geometric & surface albedo

The agreement between model and observed geometric albedo is an important validation requirement, since it provides a picture for the whole atmospheric structure and composition. Different energy photons reach different altitudes of the atmosphere, hence the spectrally resolved geometric albedo depends on the haze structure, the chemical composition and the surface albedo. The model geometric albedo is presented in Fig. 6.7 where it is compared with measurements from HST in the UV region between 1800 and 3300 Å (McGrath et al., 1998), the Neff et al. (1984) (0.35 - 1.05 μm) and Karkoscka (1994) (0.30 -1.0 μm) measurements in the visible and near infrared, along with the Negrão et al. (2006) (0.8 - 2.5 μm), Geballe et al. (2003) (2.9 - 3.5 μm) and Coustenis et al. (2003)(2.6 - 4.8 μm) measurements in the above intervals. Also in the lower panel of Fig. 6.7, the corresponding lowest altitude at which photons at each wavelength reach inside the atmosphere is presented. This is calculated in terms of the effective optical depth:

$$\tau_{\rm eff} = \tau\sqrt{(1-\omega)(1-\omega g)} \tag{6.2}$$

with ω the single scattering albedo and g the asymmetry factor. The effective optical depth, $\tau_{\rm eff}$, provides a better estimate for the penetration depth of photons inside the atmosphere since it includes the contribution of the forward scattered photons (Rannou et al., 2003).

The agreement between the model and observed geometric albedo in the UV region is significantly improved compared to previous radiation transfer models that used haze opacities derived for spherical particles. The reason for this better agreement is the more complete description of the atmospheric composition in the radiation transfer calculations, with the inclusion of the absorption

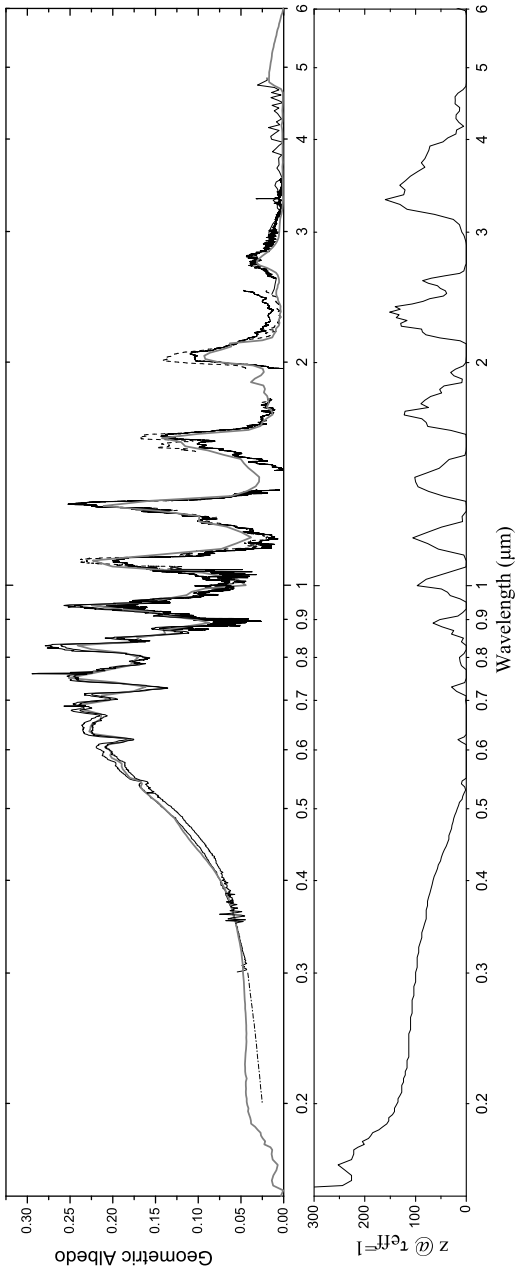

Figure 6.7: Top panel: Observed and modelled geometric albedo of Titan's atmosphere. References for the observations can be found in the text and in Table 1.2. Dashed and solid lines at similar wavelengths correspond to the leading and trailing hemispheres, respectively. Bottom panel: depth of penetration of photons inside the atmosphere.

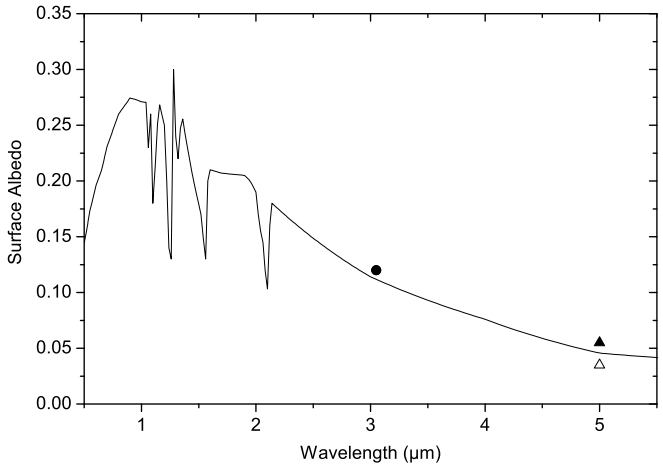

Figure 6.8: Spectral variation of the surface albedo used in the model. The circle at 3 μm is from Coustenis *et al.* (2006), while filled and empty triangles correspond to the surface albedo values from Lellouch *et al.* (2004) for the leading and trailing sides of Titan, respectively.

cross sections of all the photodissociated species used in the photochemical description. The altitude of penetration for UV photons decreases with increasing wavelength. Photons with energies below 100 nm are absorbed at altitudes above 1000 km, while between 100 and 200 nm the altitude of penetration exhibits a sharp decrease, reaching about 135 km at 200 nm. Between 200 and 300 nm the altitude of penetration has a small plateau. This is also observed in the geometric albedo in this region, which is approaching a constant value although measurements suggest that there is a steady decrease of the observed geometric albedo towards smaller wavelengths (McGrath et al., 1998). This could be an indication of missing gas absorption by species not included in the calculations, or of increased absorptivity of the haze particles in this spectral region, but most likely a signature of the contribution of the detached haze layer.

In the visible part of the spectrum the model provides a very good match to the observed geometric albedo. In this region the opacity is mainly controlled by haze absorption, which decreases as we move to larger wavelengths. Hence the altitude of penetration has an equivalent drop. In the region of 0.64 μm, the calculated geometric albedo, matches very well the observed minimum due to methane absorption. This is a common characteristic for spherical haze particles in contrast to fractal. The correct fit of the geometric albedo in the visible part of the spectrum, where the particles are mainly absorbing suggests a correct representation of the main haze layer by the model haze structure.

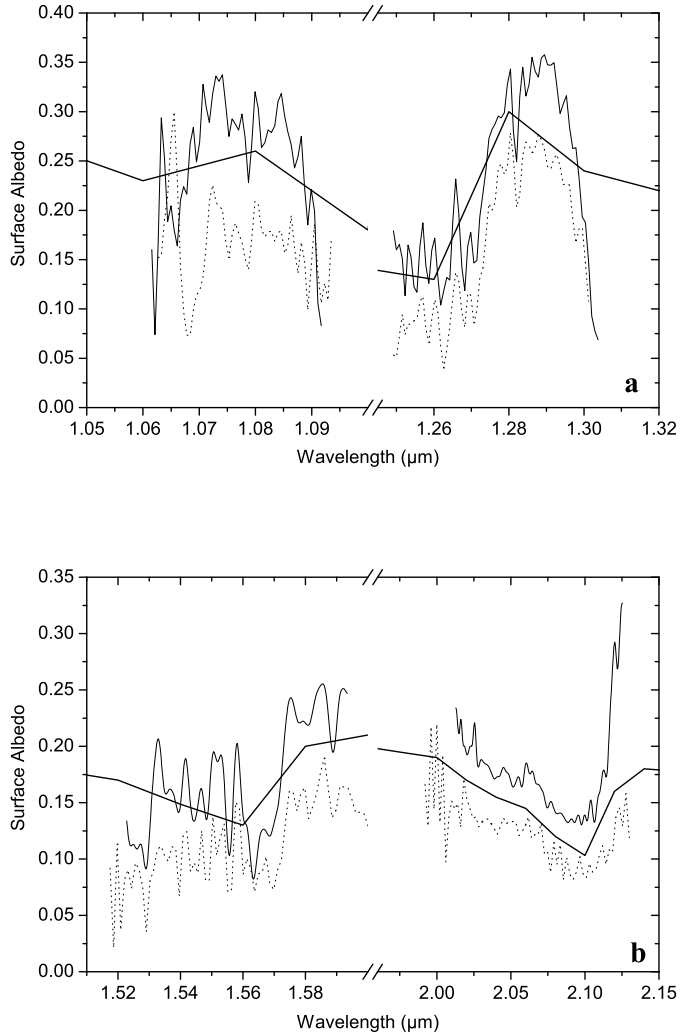

Figure 6.9: The model surface albedo (thick solid line) inside the methane windows in the range 1.0 - 2.5 μm, compared to the values retrieved by Negrão et al. (2006) (thin solid and dotted line for the leading and trailing side, respectively.)

At longer wavelengths, the spectrum is characterized by the strong minima produced by the methane absorption bands. The contribution of haze, which is mostly scattering now, mainly controls the magnitude of the geometric albedo inside and on the sides of the methane windows that correspond to the peaks. Inside the windows, photons can reach the surface where the reflected flux depends significantly on the surface albedo. The spectral variation of surface reflectivity used is shown in Fig. 6.8. and is in between the surface albedos reported by Negrão et al. (2006), in the interval 1.06 to 2.12 μm (see Fig. 6.9), for the leading and trailing sides of Titan's atmosphere. As discussed in §A.1.3, the Boudon et al. (2004) line-by-line absorption coefficients for methane in the near IR above 1.54 μm have been used, like in Negrão et al. (2006). This explains the agreement between the surface albedo values presented here and the ones reported by the latter authors, compared to previous results (Griffith *et al.*, 2003) based on different absorption calculations for methane. At longer wavelengths the values for the surface albedo were constrained to be close to those reported by Coustenis *et al.* (2006) at 3 μm and Lellouch *et al.* (2004) at 5 μm.

6.2 Atmospheric structure

Having provided a description of the haze optical properties generated by the model calculations based on the photochemical description of the atmosphere and the suggested pathways of haze formation, the resulting atmospheric structure that also controls the above processes is presented here. The calculated vertical temperature structure and atmospheric density are validated against the retrieved values by the CIRS (Cassini) and HASI (Huygens) measurements.

The resulting temperature profile, based on the above description of haze production and evolution, is presented in Fig. 6.10 for the lower (a) and upper (b) atmosphere. For comparison the retrieved vertical temperature profiles from HASI (F.Ferri, private communication) and CIRS (R. Achterberg and B. Conrath, personal communication) are given. The bundle of CIRS profiles present the variation of the temperature structure at different latitudes from pole to pole. As discussed in Chapter 1, the variation of the temperature is rather small, only a few degrees for most latitudes until we start to move towards the winter pole where the stratopause temperature increases and the stratosphere below cools. This is related to the seasonal variation of the atmospheric structure that enhances the production of haze particles in the winter pole and hence produces this temperature variation. At higher altitudes, above the stratopause, the temperature profiles converge again, indicating that the atmosphere above is well mixed. It is important to note the different location for the stratopause and the stratospheric temperatures retrieved by the two instruments. The in situ measurements of HASI (which correspond to a specific path of descent through Titan's atmosphere by the Huygens probe) suggest a hotter stratosphere compared to the average temperature retrieved by CIRS as described by the overlap of the mid-latitude and equatorial profiles in Fig. 6.10.a. The location of the stratopause for HASI is at about 250 km with a temperature slightly above

185 K, while the CIRS profile provides a higher stratopause situated at 320 km with a few degrees colder temperature (at equatorial regions). The differences between the profiles derived by the two instruments have yet to be explained. The calculated vertical profile, which corresponds to global average conditions, provides an intermediate temperature structure between the observed profiles. It is in better agreement with the HASI profile in the lower atmosphere where it follows it closely up to $\sim$ 170 km. Above that region it provides a colder stratopause of about 182 K but located at 280 km in the same region as the HASI profile. At higher altitudes the model temperature drops more slowly compared to the HASI and approaches the converging CIRS profiles above 375 km (Fig 6.10.b).

In the troposphere, as was shown by McKay et al. (1989), the greenhouse effect from the collision induced absorption controls the temperature structure. The thermal window in the region between 400 and 600 cm^{-1} which is controlled by the N_2-H_2 and H_2-CH_4 collision induced absorption, controls the thermal flux that can escape from the surface and troposphere to space. Hence, the correct simulation of the hydrogen budget affects the atmospheric temperature. In the lower atmosphere the H_2 mole fraction is constant. According to the calculations, increasing the H_2 mole fraction from 1×10^{-3} to 2×10^{-3} leads to an increase in the surface temperature by about 1/2 a degree. The convective region of the simulated atmosphere is constrained to the first 5 km with the lapse rate being 1.26 K/km. This is very close to the one ($\sim$ 1.1K/km retrieved from the observed temperature profiles from CIRS and HASI (§2.2.4).

The rapid increase of the temperature profile above the tropopause, depends mainly on the structure of the haze extinction profile (and the methane abundance) and hence on the correct representation of the main haze layer by the model. Above the stratopause, IR cooling by methane, acetylene and ethane defines the extent of the temperature drop. The scaling factors applied on the refractive index of the particles also have an important effect on the temperature structure. This is presented in Fig. 6.11. Starting with the nominal values, (1.33 for solar and 0.5 for thermal) the presented temperature profiles report the sensitivity of the thermal structure for smaller or bigger values. These profiles are only radiativelly converged and not photochemically, meaning that the impact of the varied temperature structure on the chemical composition and haze structure has not been included. The thermal scaling has a large impact on the temperature profile, providing a temperature increase of 40 K when the changing from 1 to 0.1. The solar scaling has a smaller impact on the temperature structure, increasing it by $\sim$5 K when increased from 1. to 1.6. Yet, as discussed previously the impact on the geometric albedo is more sensitive to the solar scaling parameter and allows a better constraining for its value.

The current calculations do not include corrections due to non-LTE effects. In the upper atmosphere, the HCN profile controls the thermospheric cooling due to transitions in the rotational degrees of freedom, which are in LTE under the conditions found in Titan's thermosphere (Yelle, 1991). Heating is provided by the UV photodissociation of the atmospheric species. As was shown, the model-generated HCN profile is above the measured abundance in the upper

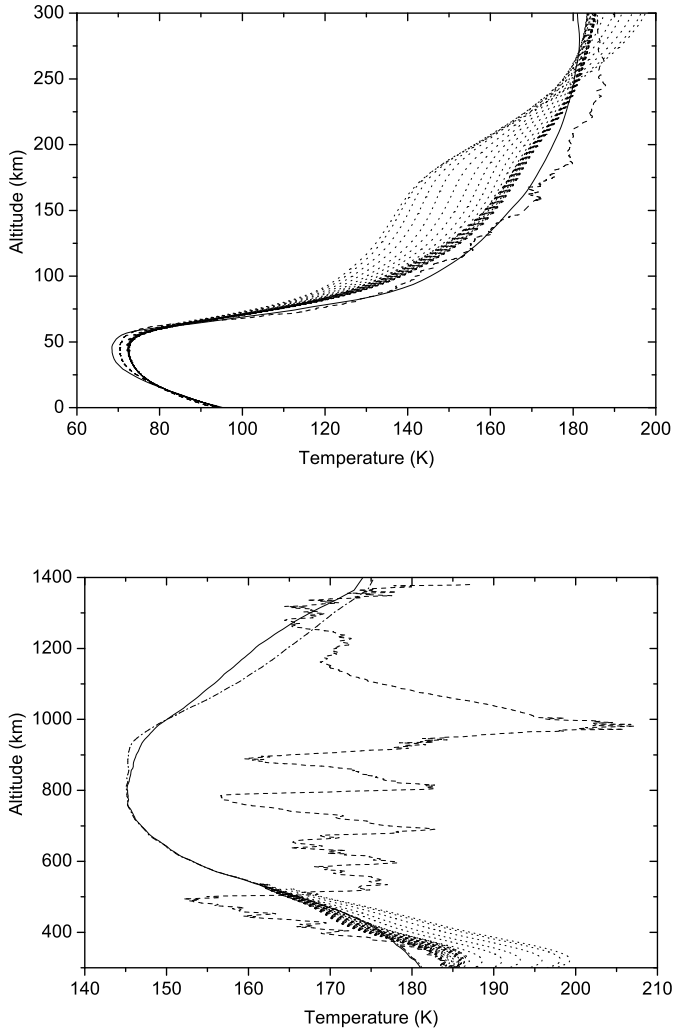

Figure 6.10: Calculated vertical temperature profile and the retrieved temperature profiles of the HASI (Huygens) and CIRS (Cassini) instruments presented with dashed and dotted lines, respectively. In the lower atmosphere(a), the model agrees better with the HASI observed profile and provides a stratopause located at 280 km. In the upper atmosphere (b), above 375 km, the calculated profile converges with the majority of the CIRS measurements that constitute the thicker solid line, which represents overlapping of many profiles from mid-latitude and equatorial regions.

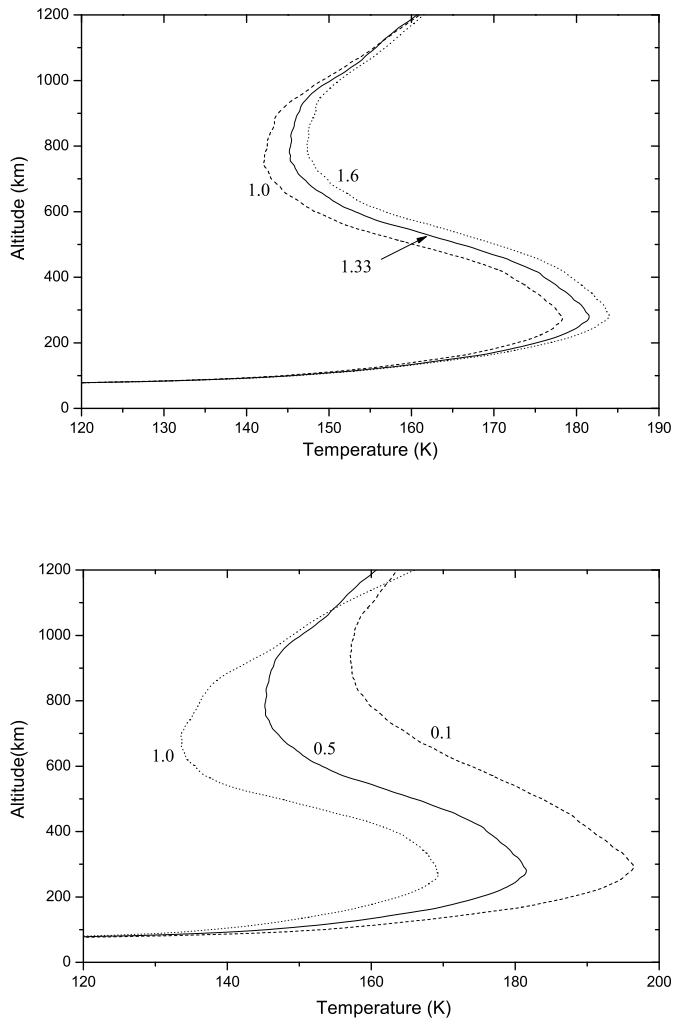

Figure 6.11: Sensitivity of vertical temperature profile on the scaling factors of the haze particles for solar (upper panel) and thermal (lower panel) wavelengths.

atmosphere, where the effect of the HCN cooling has its maximum impact. This means that the modelled temperature profile is colder than what it should be if the HCN abundance was correctly reproduced. This underestimation of the temperature is also presented in Fig. 6.10.b with the dashed-dotted line, where we have set an upper limit in the radiation transfer calculations for the calculated HCN mole fraction based on the derived values from the INMS measurements (2×10^{-4}, Vuitton et al. 2006a). The increase in the temperature is located above 900 km having reached a maximum of $\sim$5 K above 1200 km. This temperature difference did not provide any significant changes to the vertical profiles of the species in this region.

As discussed above, the model profile corresponds to a global average temperature structure. The observed profiles include the contribution of dynamical effects that produce variations in the vertical temperature structure. The latitudinal transport induced by the Hadley circulation allows the haze particles to remain in the atmosphere for a longer time until they are deposited in the polar regions, where the circulation fluxes attain a descending character. In our model we only simulate the vertical motion of the particles and hence we do not take into consideration this effectively smaller settling velocity of the particles, when viewed in a 1D picture. On the other hand, the observed oscillations in the vertical temperature structure of the upper atmosphere by the HASI instrument, suggest the presence of significant transient wave effects which are not simulated by the model.

Another validation parameter is the vertical profile of the mass density. This was measured by the HASI instrument on board the Huygens probe during its descent inside Titan's atmosphere (Fulchignoni et al., 2005). The measured and modelled vertical profiles for this quantity are presented in Fig. 6.12. Mass density depends on the vertical temperature structure, which defines the atmospheric density, and the chemical composition of the atmosphere. From the surface up to about 800 km the modelled and observed density and pressure profiles are very close. Above that level the divergence between the simulated and observed temperature profiles leads to divergence in the mass density.

6.3 Solar cycle effects

In §5.3 it was shown that the 11-year SC variability has an impact on the vertical haze production, due to the changes induced in the species vertical profiles. The haze structures that are eventually produced at solar minimum and maximum conditions are different and this has an impact on the geometric albedo and vertical temperature structure.

At solar maximum the haze production is increased due to the enhancement of nitrile production for this condition. As a result the optical depth of the haze structure is increased and this leads to an enhancement of the heating induced from the absorption of solar radiation by the particles. This is presented in Fig.6.13. The increased haze opacity, leads to a rise in the temperature above the stratopause up to the mesopause, while the atmosphere below is cooled since

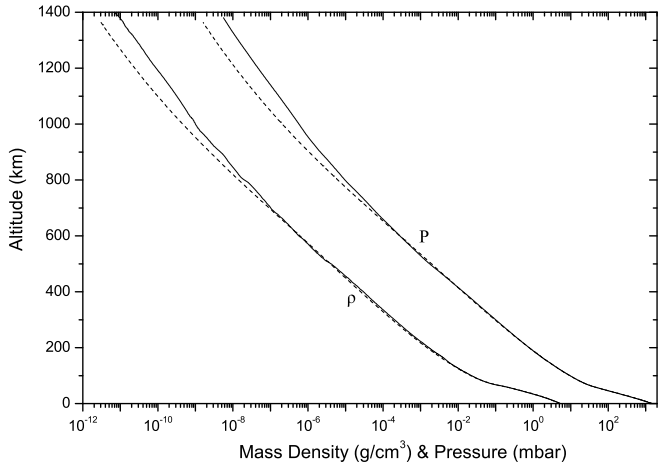

Figure 6.12: The model vertical mass density and pressure profiles (dashed lines) compared with the observed profiles (solid lines) by the HASI instrument on board the Huygens probe (Fulchignoni et al., 2005).

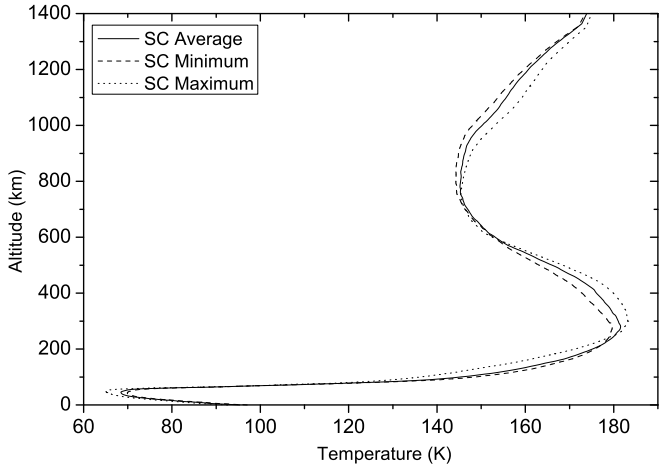

Figure 6.13: Impact of solar cycle variability on the calculated temperature structure.The solid line corresponds to solar average conditions, the dashed to solar minimum and the dotted to solar maximum.

less photons reach as deep in the atmosphere as for the solar average case. In fact the location of the stratopause is affected also with its altitude moving upwards by about 20 km from solar average to solar maximum conditions. In the upper atmosphere, the increased solar flux, induces an increase in the heating of the atmosphere from the absorption of atmospheric gases at short wavelengths were the SC variability has a major effect. It should be mentioned that non-LTE corrections would have an effect on the magnitude of the temperature variation at these altitudes. The results are reversed for solar minimum conditions but the magnitude of the temperature changes is smaller.

For the geometric albedo the impact of the SC is presented in Fig. 6.14. The calculated albedo at solar maximum is smaller than the one for solar average conditions for wavelengths below 0.6 μm and larger for bigger wavelengths. This is due to the optical properties of the haze particles which are strongly absorbing up to 0.6 μm and scattering at longer wavelengths (Fig. 3.1). This is more prominent when viewed in terms of the difference of the albedos between solar maximum and minimum relative to the solar average condition. As for the case of the vertical temperature structure, the impact of the SC is large for solar maximum than for solar minimum.

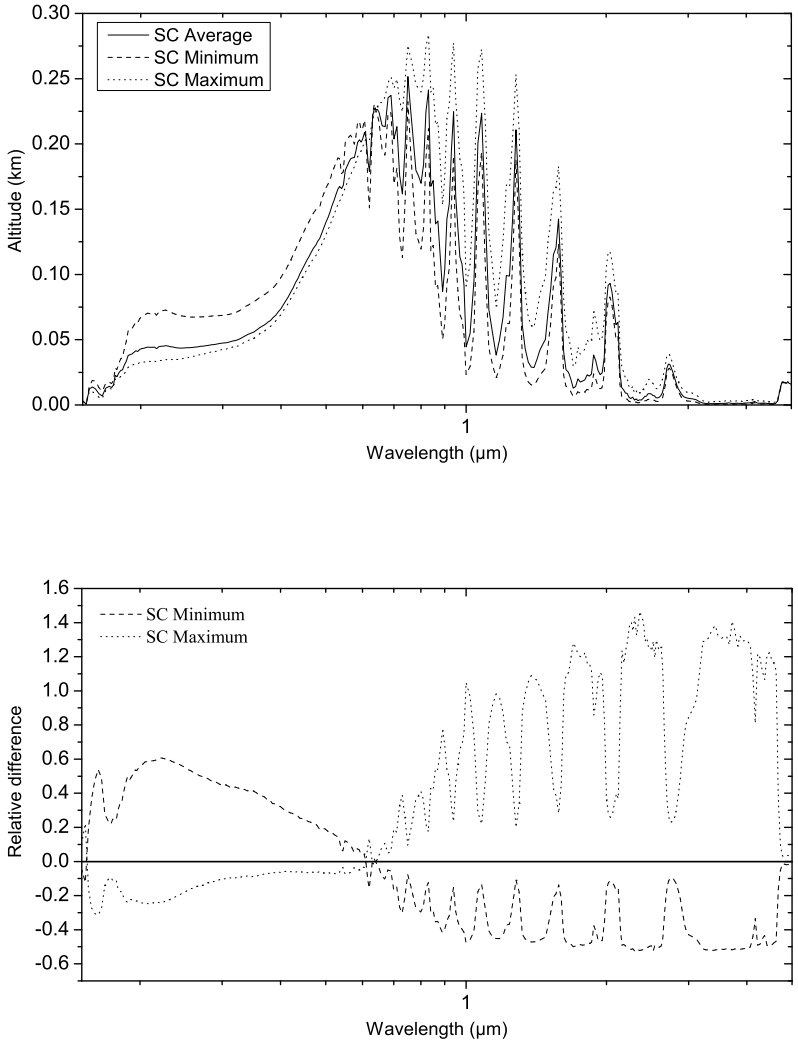

Figure 6.14: The effect of solar variability in the calculated geometric albedo due to the induced changes in the haze production (upper panel). The difference between solar maximum and solar minimum relative to the average conditions shows more clearly that the SC has a spectral signature with the difference changing sign as the particles change from absorbing to scattering (lower panel).

Bibliography

Boudon, V., Champion, J.-P., Gabard, T., Loëte, M., Michelot, F., Pierre, G., Rotger, M., Wenger, Ch., Rey, M., 2004. Symmetry-adapted tensorial formalism to model rovibrational and rovibronic spectra of molecules pertaining to various point groups. J. Mol. Spectrosc. 228, 620-634.

Coustenis, A., Negrão, A., Salama, A., Schulz, B., Lellouch, E., Rannou, P., Drossart, P., Encrenaz, T., Schmitt, B., Boudon, V., Nikitin, A., 2006. Titan's 3-micron spectral region from ISO high-resolution spectroscopy, Icarus 180, 176-185.

Fulcignoni, M. and 42 coworkers (2005). In situ measurements of the physical characteristics of Titan's enviroment. Nature,doi:10.1038/nature04314.

Griffith, C.A., Owen, T., Geballe, T.R., Rayner, J., Rannou, P., 2003. Evidence for the exposure of water ice on Titan's surface, Science 300, 628-630.

Khare, B.N., Sagan, C., Arakawa, E.T., Suits, F., Calcott, T.A., Williams, M.W., 1984. Optical constants of organic tholins produced in a simulated Titanian atmosphere: from soft X-ray to microwave frequencies. Icarus 60, 127-137.

Lellouch, E., Schmitt, B., Coustenis, A., Cuby, J.-G., 2004. Titan's 5-micron lightcurve, Icarus 168, 209-214.

McKay, C.P., Pollack, J.B., Courtin, R., 1989. The thermal structure of Titan's atmosphere. Icarus 80, 23-53.

Negrão, A., Coustenis, A., Lellouch, E., Maillard, J.-P., Rannou, P., Schmitt, B., McKay, C.P., Boudon, V., 2006. Titan's surface albedo variations over a Titan season from near-infrared CFHT/FTS spectra, Planet. Space Sci. 54, 1225-1246.

Rages, K., Pollack, J.B., 1983. Vertical distribution of scattering hazes in Titan's upper atmosphere. Icarus 55, 50-62.

Rannou, P., Ferrari, C., Rages, K., Roos-Serote, M., Cabane, M., 2000. Characterization of aerosols in the detached haze layer of Titan, Icarus 147, 267-281.

Rannou, P., McKay, C.P., Lorenz, R.D., 2003. A model of Titan's haze of fractal aerosols constrained by multiple observations. Planet. Space Sci. 51, 963-976.

Rannou, P., Montmessin, F., Hourdin, F., Lebonnois, S., 2006. The latitudinal distribution of clouds on Titan. Science 311, 201-204.

Tomasko, M.G., and 39 co-authors, 2005. Rain, winds, and haze during the Huygens probe's descent to Titan's surface. Nature, doi:10.1038/nature04126.

Yelle, R.V., 1991. Non-LTE models of Titan's upper atmosphere. Astrophys. J. 383, 380-400.

Chapter 7

Discussion & Conclusions

7.1 Discussion

The one-dimensional picture of Titan's atmospheric processes presented in this work has provided a realistic representation of the mean vertical atmospheric structure and composition. The haze pathways used provide a haze production profile which can reproduce the observed aerosol structure by the DISR measurements. At the same time, the interaction of the calculated haze structure with the radiation field provides a vertical temperature profile which is in very good agreement with observations, while the very good agreement between the model spectrally resolved geometric albedo and the observed one, suggests a realistic representation of radiation transfer through Titan's atmosphere. The solar fluxes calculated by the model, along with the temperature structure, drive the photochemical and thermochemical evolution of the simulated species, for most of which the model provides reasonably good vertical profiles compared with the observations. Under this self-consistent picture where each process is linked to the others, a more complete representation of Titan's atmosphere has been presented and the effect of the coupling between different processes has been investigated.

7.1.1 Haze pathways and chemical loss

Amongst the pathways included in the description of the photochemical production of the haze particles, nitriles and copolymers have the most important role. Copolymers have a dominant contribution in the upper atmosphere and are the main source for the opacity above the stratopause, which is necessary for the correct reproduction of the vertical temperature structure. When the impact of the galactic cosmic rays is included, nitriles contribute mainly in the lower atmosphere and are of secondary importance in the radiation transfer since the particles formed in this region are quickly lost to the surface. If the contribution of the GCR is removed, the haze production in the lower atmosphere is significantly reduced and is then controlled by the aromatics. The contribution from

polyynes at all altitudes and under all conditions, is significantly smaller than that of the other families. Hence, under the current description the omission of pure hydrocarbon pathways from the haze production, in accordance with the results of the ACP instrument, would not change the produced haze structure significantly. This altitude-dependent chemical composition of the haze particles is in agreement with the observed variation of the detached haze optical properties relative to the ones of the main haze layer, as reported by Rannou et al. (2000), although in the current calculation, a single refractive index for all altitudes was used.

The chemical loss of atmospheric gases through the formation of the haze monomers, is found to be important for the vertical profiles of the precursor species involved in the haze pathways used. The chemical growth of the initial dimer formed, to the size of a monomer, beyond which the particles become larger by their mutual coagulation, has the largest impact on the chemical composition. The increased contribution of hydrocarbon-nitrile copolymers and pure nitriles relative to the pure hydrocarbon pathways in the haze production results in a significant loss for nitrogen in all forms of nitrile species involved in the pathways.

The profiles of HCN, HC_3N and C_2H_3CN are reduced in the stratosphere, although the magnitude of this reduction depends mainly on the assumed rate for the reaction H_2CN + HCN. An important conclusion from the current work regarding this rate is that its variation, although affects significantly the HCN abundance and the total haze production in the stratosphere, has a very small impact on the resulting haze opacity. The calculated C/N and C/H ratios suggest a stoichiometric formula of $C_4H_3N_3$ for the haze particles.

7.1.2 N_2 dissociative photoionization and nitriles

Another sensitivity test from this work is the new dissociative ionization scheme for N_2 suggested by the work of Nicolas et al. (2003). Compared to previous suggestions that favored the production of ground state neutral and ionized nitrogen atoms for wavelengths smaller than 510 Å, the latter measurements suggest that the neutral atoms are in their excited state. The effect of this is to produce significantly larger CH_3CN abundance compared to the observed. For other species, such as HCN, CH_2NH, C_2H_6 and C_2H_2 the effect is smaller.

7.1.3 Heterogeneous chemistry

The current work has provided more insight into the effects of heterogeneous processes on the surface of aerosol particles. The scavenging of atomic hydrogen and its conversion to molecular hydrogen by aerosols results in a H_2 vertical profile closer to that retrieved by INMS in the upper atmosphere. It also produces a vertical diacetylene profile that is in much better agreement with the CIRS retrieved profiles. Further, it affects the radiation transfer; first, directly due to the higher abundance of diacetylene, and secondly indirectly, since C_4H_2 is a very important precursor for haze production based on the copolymer family.

Another important process is the increased thermal opacity inside the thermal window between 400 and 600 cm^{-1} because of H_2-N_2 and H_2-CH_4 collisionally induced absorption that arises from increased H_2 abundance. This allows less of the thermal radiation to escape to space and hence increases the surface temperature. It is clear that heterogeneous processes affect the temperature, radiation field, photochemistry and haze production.

7.1.4 The role of methyl radicals

Methyl radicals play an important role in the photochemical evolution of the atmosphere. As discussed in the previous sections, their recombination defines the production of C_2H_6, while reaction with atomic nitrogen is the main production mechanism for HCN and CH_2NH. In addition, their photolysis is a significant source of $^1CH_2$ that affects the rest of the hydrocarbon chemistry. Hence variations in the abundance of CH_3 will have an impact on all of the above species. Both hydrogen cyanide and methyleneimine are overestimated by the model in the upper atmosphere. The model ethane (along with argon) profile is used for the retrieval of the eddy mixing profile, which depends on the methyl radical abundance.

Methyl radicals, like atomic hydrogen, can react heterogeneously with hydrogen atoms on the surface of the aerosol particles to form CH_4. If this process is of comparable efficiency with that observed for the conversion of H to H_2, the population of CH_3 radicals would be reduced with the process having its maximum effect in the region between 300 and 600 km, as observed for atomic hydrogen. This is the region were the eddy mixing profile is controlled by ethane. The possible reduction of the methyl radical by a heterogeneous process would lead to a decrease in ethane production within this region and hence to a different characteristic life time for this species relative to the one given in Fig. 4.1. Hence, variations in the eddy mixing profile would occur, while the reduced CH_3 abundance will have a photochemical effect on those species directly affected by it.

7.1.5 Solar cycle effects

The temporal variability induced by the 11-year solar cycle affects the species photolysis rates. This eventually produces variations in the species vertical profiles which were found to be stronger for nitrile species compared to hydrocarbons. This variability is further imparted in the haze production that was found to increase by $\sim$60% between solar minimum to solar maximum relative to solar average conditions. As a result of the enhanced haze opacity the temperature profile changes with an increase of the temperature and the geometric albedo is significantly affected.

7.2 Conclusions

A 1D radiative / convective - photochemical - microphysical model to study the formation of Titan's haze from the chemical species formed in its atmosphere has been developed. The model results were validated against recent Cassini/Huygens mission measurements and other ground-based and space-borne observations. The model generates the radiation field, atmospheric composition, haze structure, geometric albedo and temperature/density structure in a self consistent manner.

More specifically, ethane and argon, along with methane escape to space, were used to constrain the eddy mixing coefficient for the gaseous species, while a separate eddy mixing coefficient for the haze particles was applied. The use of two different profiles was found to give better results with regard to the agreement between model and observed gaseous species vertical profiles of abundance and haze properties. Yet, the increased mixing profile assumed for the haze particles is just one way for constraining the produced haze abundance to the value that is necessary for the correct reproduction of the geometric albedo. The physical interpretation of this approach has to be clarified with further investigation. Possibly the loss of haze particles as nucleation sites upon which cloud formation can proceed can produce the same effect as the increased flow towards the surface sink applied here. Further, the latitudinal transport of particles could effectively act in the same way, depositing the particles in the polar regions. On the other hand this could also signify some lack in our understanding of the chemical processes that define haze formation in Titan's atmosphere.

The model calculations include the effects of the heterogeneous chemistry on aerosol surfaces that convert atomic hydrogen to molecular hydrogen. The resultant H_2 profile is found to be closer to the INMS measurements, while the vertical profile of the diacetylene formed, which is controlled by atomic hydrogen and the retrieved mixing profile, is found to be closer to that of the CIRS profile when this heterogenous chemistry is included. Both of these species play an important role in the radiative transfer; H_2 in collisionally induced absorption in the thermal infrared, and C_4H_2 in haze production based on the copolymer family.

Further, the photochemistry of methyleneimine in Titan's atmosphere have been investigated and included for the first time in photochemical model.

The pathways of haze formation included, reveals a new second major peak in the vertical profile of haze production rate between 500 and 900 km. This peak is produced by the copolymer family used and has important ramifications for the vertical atmospheric temperature profile and geometric albedo. In particular, the existence of this second peak determines the vertical profile of haze extinction. The model results regarding the haze extinction have been compared with the DISR retrieved profiles and are found to be in very good agreement, given that our results represent global mean values whereas the DISR represent profiles from the descent site of the Huygens probe. If this second peak is absent, then the model haze extinction profiles would decrease more rapidly above 100 km than indicated by the DISR measurements. Further, this peak controls

the atmospheric temperature decrease above 300 km.

The model temperature profile is found to be in agreement with the HASI measurements in the lower atmosphere below the stratopause. The latter, based on the calculations is placed at 280 km. Above 375 km, the calculated temperature profile agrees better with the mid-latitude CIRS profiles. At higher altitudes, where the profiles from all latitudes begin to converge, the simulated and observed profiles are in agreement.

Finally, the model geometric albedo, which represents an integration of radiative processes in Titan's atmosphere is in very good agreement with the observations. The peaks in the near infrared are primarily controlled by haze scattering and surface albedo, whilst the troughs are determined by methane absorption. The matching of the model peaks and troughs with the observations lends further support to the coupling of Titan's photochemistry to haze formation performed here.

Epilogue

The scientific investigation of the atmospheric processes in Titan's atmosphere described in this thesis, has provided a new insight into specific issues defining Titan's atmosphere. Answers and new suggestions have been given regarding the most intriguing aspect of the atmosphere: the pathways leading to the production of the observed haze structure from the complex photochemical background. The outcomes of this investigation were validated against the observed vertical temperature structure, spectrally resolved geometric albedo and atmospheric chemical composition as these have been inferred from the latest measurements performed by the Cassini/Huygens mission. The self-consistent approach which was followed has provided a comprehensive representation of the complex interaction between the main atmospheric processes, which can now be applied to any planetary atmosphere.

Yet, as was discussed previously, the issues addressed here are but a small fraction of our questions that we would like to answer about Titan's atmosphere and more generally the way atmospheric and geological processes define the evolution of a planetary atmosphere. Although the Huygens mission has ended, the Cassini mission is still ongoing and its success will probably guarantee the missions extension beyond the scheduled end in 2008. The data that are being gathered are making Titan more and more familiar by the day, illuminate our knowledge, amaze us with its resemblance to our home planet and excite us with new, never before seen aspects of planetary formation and evolution.

But, this is not the end of our quest. The planetary scientific community, buoyant by the success of the Cassini/Huygens mission and the new picture of Titan revealed, is planning for another space mission. This will bring us back in Titan with a new orbiter around Titan along with an aerial probe, probably a balloon, which will be able to float around at different latitudes and longitudes and gather information. This will provide a better, in situ insight regarding the surface composition and properties, the methane reservoir, the possibility of a sub-surface ocean, lake formation, haze particle formation, the atmospheric dynamics, the seasonal variability and many other issues that need to be understood.

Appendix A

Light Interaction with Matter

The radiation transfer process is based on the interaction of the radiation (Electromagnetic) field with matter. When a beam of light interacts with a medium it is attenuated in two ways. In the first interaction, part of the energy of the incident beam is transferred by the medium and transformed to other kinds of energy, mainly heat. This is what we call *absorption* and is present whether the medium is made of one or many materials, whether it contains small or big particles or whether the structure of the medium is random or not (for example a crystalline structure). In any of the above cases the absorption will be present and the variation of the medium's properties will only affect how weak or strong the attenuation of the incident beam will be.

The second interaction of light with matter is that of *scattering* which occurs whenever light transverses a medium with varying optical properties. When an incident beam reaches a 'surface' that defines a limit between two regions with different optical properties, part of the beam is radiated to directions different from the original. Pure scattering doesn't include any energy transformation. The integral of energy radiated in all directions is equal to the energy of the initial beam. The attenuation here is regarded only with respect to the energy left in the direction of the incident radiation. In the case of the atmosphere the importance of scattering is decisive in the way we observe our surrounding environment. All the light our eyes receive away from a source of light (e.g. the Sun) comes from radiation scattered by the atoms, molecules, aerosols and other particles of the atmosphere. This scattered radiation is responsible for the blue color of the morning sky, the rainbow and the halos in order to name few of the optical phenomena in the atmosphere produced by scattering.

In order to take into account the total attenuation of the beam, due to both scattering and absorption, the term *extinction* is used, which is defined as:

$$\text{Extinction} = \text{Absorption} + \text{Scattering}$$

The relative importance of the above two procedures depends mainly on the

optical properties of the medium and the relative ratio between the size of the scattering centers and the wavelength of the incident radiation. In the usual case where the scattering centers are considered to have spherical shape the scattering properties are calculated in terms of the size parameter x, defined as:

$$\mathrm{x} = \frac{2\pi r}{\lambda} \tag{A.1}$$

where, r is the radius of the scattering center and λ the wavelength of the incident radiation.

In order to describe the scattering problem with more tangible means, certain parameters have been introduced. Consider the scattering from a particle of arbitrary shape. The last is characterized by its geometric cross section, σ, that depends only on the shape the particle has (its geometrical shadow), and three more effective cross sections, one for every basic procedure (absorption, scattering & extinction). The cross section for scattering, σ_{sca}, is an area such that the total energy of the scattered wave in all directions is equal to the energy of the incident wave falling on this area. In a similar way, the cross section for absorption, σ_{abs}, refers to the energy absorbed in the particle and the cross section for extinction, σ_{ext} describes the total attenuation of the incident energy. Since the total attenuation is due to the combined effect of absorption and scattering, the conservation of energy requires that:

$$\sigma_{ext} = \sigma_{abs} + \sigma_{sca} \tag{A.2}$$

The dimensionless parameters:

$$\begin{array}{l} Q_{sca} = \frac{\sigma_{sca}}{\sigma} \\ Q_{abs} = \frac{\sigma_{abs}}{\sigma} \quad with \quad Q_{sca} + Q_{abs} = Q_{ext} \\ Q_{ext} = \frac{\sigma_{ext}}{\sigma} \end{array} \tag{A.3}$$

are called the efficiency factors for scattering, absorption and extinction respectively and are the ones that are usually used.

A.1 Absorption

The spectral variation of the absorption cross section in the UV region for most of the species used in the calculations are presented in Fig. A.1. At these wavelengths the absorption originates from the electronic transitions of the electrons in the atoms and molecules, which are induced by the high energy UV photons. The presence of unsaturated bonds with increasing size of the molecules allows them to absorb at increasingly longer wavelengths as shown in the plots. The units of cross sections can vary between different descriptions and laboratory measurements and are summarized in Table A.1.

As we move towards longer wavelengths in the near IR and thermal IR, the radiation excites the rotational and vibrational degrees of freedom of the molecules. In these wavelengths the effects of pressure and temperature start

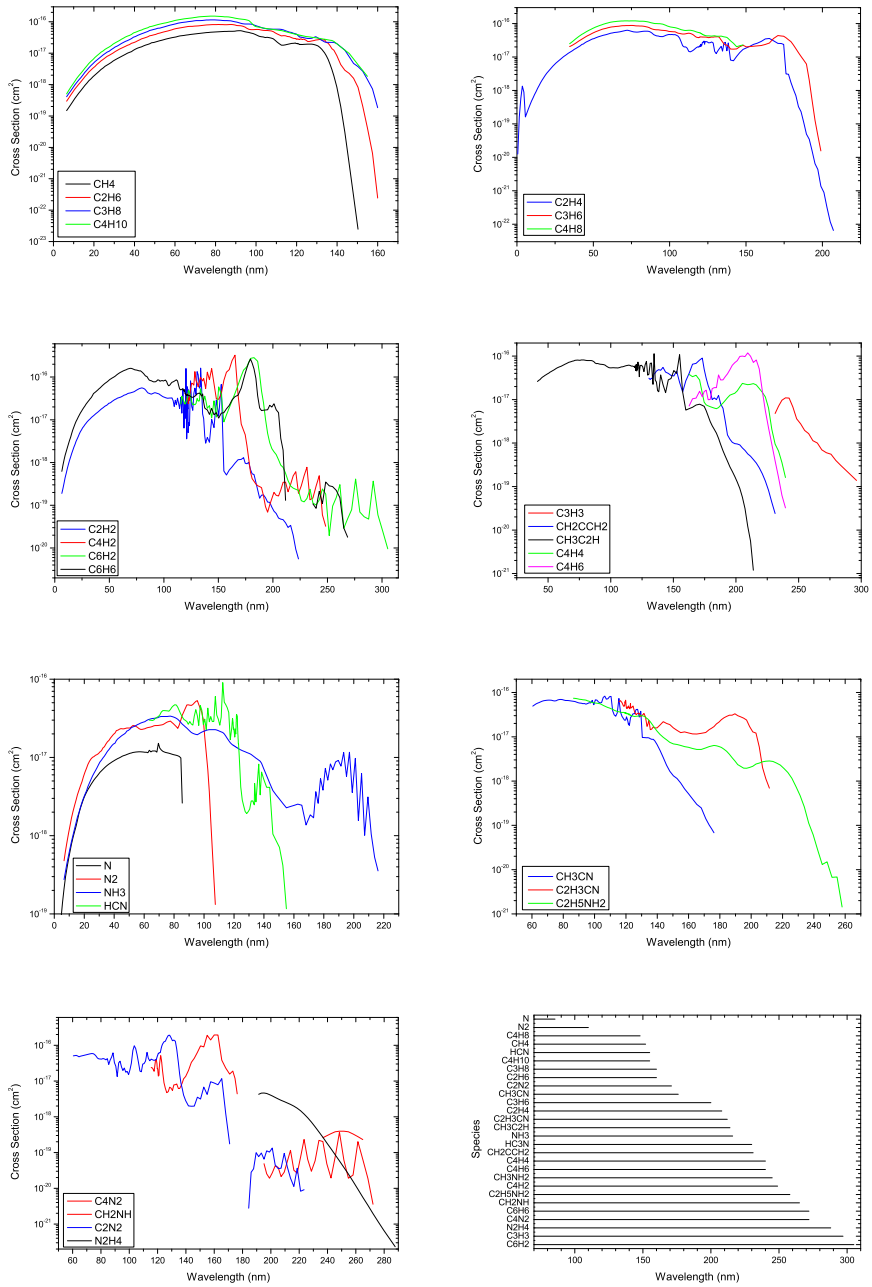

Figure A.1: UV cross sections for the main hydrocarbon and nitrile species in Titan's atmosphere. The spectral extent of UV absorption cross section of the different species depends on the structure of the molecules and the presence of different type of bond structures that give rise to certain absorption bands. Notice the shift to larger wavelengths for larger species with increasing number of unsaturated bonds in the lower right figure.

Table A.1: Different units for the absorption coefficient found in the literature.

	Volume	Molecular	Mass	S.T.P.
Units	cm^{-1}	cm^2	cm^2/g	$(cm\text{-}Amagat)^{-1}$

to have a significant impact on the absorption properties of the species and has to be included in the calculations. Further, the use of spectroscopic data is necessary for the calculation of the absorption cross sections.

A.1.1 Spectroscopic data

Spectroscopic databases (such as HITRAN or GEISA a.o.) provide a number of spectroscopic parameters, which are valuable for the theoretical calculation of molecular transmittances. For a given molecule and its isotopes, the database contains information for all the known transitions it can proceed to. The parameters necessary for the calculation of a molecule's absorption coefficient are:

- The position of each transition, ν_0 (cm^{-1}), that corresponds to the energy of the photon emitted or absorbed by the molecule in the transition between two quantum states.

- The spectral line intensity of the transition, S_0 ($cm^{-1}/(molecule\ cm^{-2})$). From radiation transfer theory the line intensity for a rotational/vibrational transition is given by:

$$S_0 = \frac{h\nu_{nn'}}{c}\frac{n_{n'}}{N}(1 - \frac{g_n n_{n'}}{g_{n'} n_n})B_{nn'} \tag{A.4}$$

  where h is the Planck's constant, c the speed of light, n and n' refer to the lower and upper state respectively, N is the molecular number density, n_n and $n_{n'}$ are the populations of each state, g are statistical weights which take into consideration the electronical, vibrational, rotational and nuclear degrees of freedom of the molecule and $B_{nn'}$ is the Einstein coefficient ($cm^3/(ergs\ s^2)$) for induced absorption. For LTE conditions the population of each state is defined by the Boltzmann statistics, which means that the line strength is temperature dependent.

- The air-broadened halfwidth at half maximum (HWHM), $\gamma_{air}(cm^{-1}/atm)$, of the line that depends on the temperature and pressure conditions.

With the above data the calculation of the monochromatic absorption coefficient, k_ν ($molecule^{-1}cm^{-2}$), at a specific wavenumber, ν, due to a single transition, ν_0, is straightforward, and it will be given by:

$$k_\nu = S_0 f(\nu - \nu_0)$$

where f($\nu - \nu_0$) is the line shape function (cm). The total contribution to wavenumber ν from all the transition lines, ν_0, will then be:

$$k_\nu = \sum_{\nu_0} S_0 f(\nu - \nu_0) \tag{A.5}$$

The spectroscopic databases usually provide data that correspond to standard temperature and pressure conditions (T_{ref} = 297 K and P_{ref} = 1 atm). This means that for different conditions, corrections to the line intensities and halfwidths must be performed before the calculation of the absorption coefficient. In order to correct for temperature variations in the line strength we need to know the dependence of the statistical weight and state populations on it. Based on the condition of LTE, the Boltzmann distribution provides this information:

$$\frac{g_n n_{n'}}{g_{n'} n_n} = exp(-c_2 \nu_{nn'}/T) \tag{A.6}$$

and

$$\frac{n_{n'}}{N} = \frac{g_n exp(-c_2 E_n/T)}{Q(T)} \tag{A.7}$$

In the above, $c_2 = hc/k_B$, with k_B the Boltzmann constant and E_n the energy of the lower state which is also provided in the HITRAN database. $Q(T)$ is the total partition function of the molecule that is given by the usual expression:

$$Q(T) = \sum_n g_n exp(-c_2 E_n/T) \tag{A.8}$$

Substituting the above in the line strength equation we get:

$$S_0 = \frac{h\nu_{nn'}}{c} \frac{g_n exp(-c_2 E_n/T)}{Q(T)} (1 - exp(-c_2 \nu_{nn'}/T)) B_{nn'} \tag{A.9}$$

From the last result it is clear that the temperature dependence of the line intensity relatively to a reference temperature will have the form:

$$S_0(T) = S_0(T) \frac{Q(T_{ref})}{Q(T)} \frac{exp(-c_2 E_n/T)}{exp(-c_2 E_n/T_{ref})} \frac{(1 - exp(-c_2 \nu_{nn'}/T))}{(1 - exp(-c_2 \nu_{nn'}/T_{ref}))} \tag{A.10}$$

In the last expression all parameters necessary for the calculations are directly provided from the database. Q(T) can calculated using the Gamache et al. (1990) parametrization which approximates the partition function as a third order polynomial on temperature:

$$Q(T) = a + bT + cT^2 + dT^3 \tag{A.11}$$

where the constants depend on the molecule/isotope under consideration. Typical values of the parameters for simple molecules are given in Table A.2.

The effects of pressure and temperature on the halfwidth are described in the form:

$$\gamma(p,T) p_{ref} = (\frac{T_{ref}}{T})^\eta (\gamma_{air}(p_{ref}, T_{ref})(p - ps) + \gamma_{self}(p_{ref}, T_{ref}) ps) \tag{A.12}$$

Table A.2: Partition function parameters for simple molecules (Gamache et al., 1990)

Molecule	Parameter			
	a	b	c	d
$^{14}N^{2}$	7.3548E-01	7.86628-01	-1.82828-06	6.8772E-09
$^{12}C^{16}$	-4.8544	3.4530E-01	5.4835E-05	-6.0682E-08
$^{16}O^{l2}$	-2.1995	9.67518-01	-8.0827E-04	2.80408-06
$H^{12}C^{14}N$	-9.7107E-01	2.9506	-1.6077E-03	6.11488-06
$^{14}N^{14}N^{l6}O$	-9.529l	1.5719E+0l	-1.20638-02	5.37818-05
$H^{12}C^{12}CH$	2.5863	l.l921	-7.928lE-04	4.62258-06

In the above p_s is the partial pressure of the absorbing molecule, γ_{self} is the self broadening halfwidth of the transition line and η is a constant. The last two parameters are also included in the HITRAN database. A typical value for η is 1/2 which is coming from collision theory. For most cases $\gamma_{air} \gg \gamma_{self}$ and if the molecule under consideration is a minor species then $p_s \ll p$. Then the above expression takes the more simple form:

$$\gamma(p,T) = \gamma_{air}(p_{ref},T_{ref})(\frac{T_{ref}}{T})^{\eta}\frac{p}{p_{ref}} \tag{A.13}$$

Finally the position of the line center for a specific transition can be affected from the pressure conditions. The database provides this information also, in the form of a pressure shift parameter, δ (cm^{-1}/atm):

$$\nu_{nn'}^{'} = \nu_{nn'} + \delta(p_{ref})p \tag{A.14}$$

A.1.2 Spectral line profiles

The shape of a spectral line depends upon the temperature and pressure conditions under which the molecule is excited. The natural broadening of the line profile, due to the Heisenberg uncertainty principle, is very small compared to the broadening induced by the thermal motion of the molecules (Doppler broadening) and the interactions between them (collision broadening). The last two processes have a dominant role in the atmospheric line profiles.

At low pressure conditions, the mean free path of the atmospheric molecules attains large values due to the small number of collisions allowed by the low density. In this case, and depending on the atmospheric temperature structure, the thermal velocities of the molecules can reach significant values in order to induce observable Doppler shifts to the line profiles. Under thermodynamic equilibrium conditions the distribution of molecules with velocity between v and v+dv is described by the Maxwellian distribution:

$$f(v)dv = \frac{1}{\sqrt{\pi}V}e^{-\frac{v^2}{V^2}}dv \tag{A.15}$$

with V being the most probable speed of the distribution, given by:

$$V = \sqrt{\frac{2RT}{\mu}} \tag{A.16}$$

with T the atmospheric temperature, R the universal gas constant and μ the mean molecular weight. Including the Doppler shift:

$$\mathrm{v} - \mathrm{v}_0 = \mathrm{v}_0 \frac{v}{c} \tag{A.17}$$

one can readily derive the functional form of the Doppler line profile:

$$f_D(u) = \frac{1}{\sqrt{\pi}} e^{-u^2} \tag{A.18}$$

with $u = (\nu - \nu_0)/\gamma_D$ and γ_D the Doppler line shift, (related to the Doppler width by $b_D = \gamma_D \sqrt{(ln2)}$) given by:

$$\gamma_D = \frac{\nu_0}{c} \sqrt{\frac{2RT}{\mu}} \tag{A.19}$$

From the above it becomes obvious that the Doppler profile is independent of the ambient pressure and that for each molecule, the resulting line profile will depend on the ambient temperature. Table A.3 presents the γ_D/ν_0 ratios at 180 K, for the important species involved in Titan's thermal radiation transfer.

As the pressure increases the number of collisions between molecules rises rapidly. The effect of this is to broaden the line profile giving rise to absorption wings which can extend over a large distance from the center of the line. The line shape under these conditions is described by the Lorentzian profile that results from the solution of the Scrödinger equation:

$$f_L(\nu - \nu_0) = \frac{b_L}{\pi} \frac{1}{(\nu - \nu_0)^2 + b_L^2} \tag{A.20}$$

where, b_L is the Lorentz width of the line. In terms of the unit-less line center distance, u, introduced above, the Lorentz profile can be given in the form:

$$f_L(u) = \frac{\alpha/\pi}{u^2 + \alpha^2} \tag{A.21}$$

Table A.3: Characteristic Doppler widths relative to the line center for important species in the thermal radiation transfer of Titan's atmosphere.

Species	$\gamma_D/(\nu_0 \sqrt{T}) \times 10^{-7}$	$\gamma_D/\nu_0 \times 10^{-6}$, T=180K
CH_4	1.075	1.442
HCN	0.8275	1.110
C_2H_6	0.7851	1.053
C_2H_4	0.8126	1.090
C_2H_2	0.8433	1.131

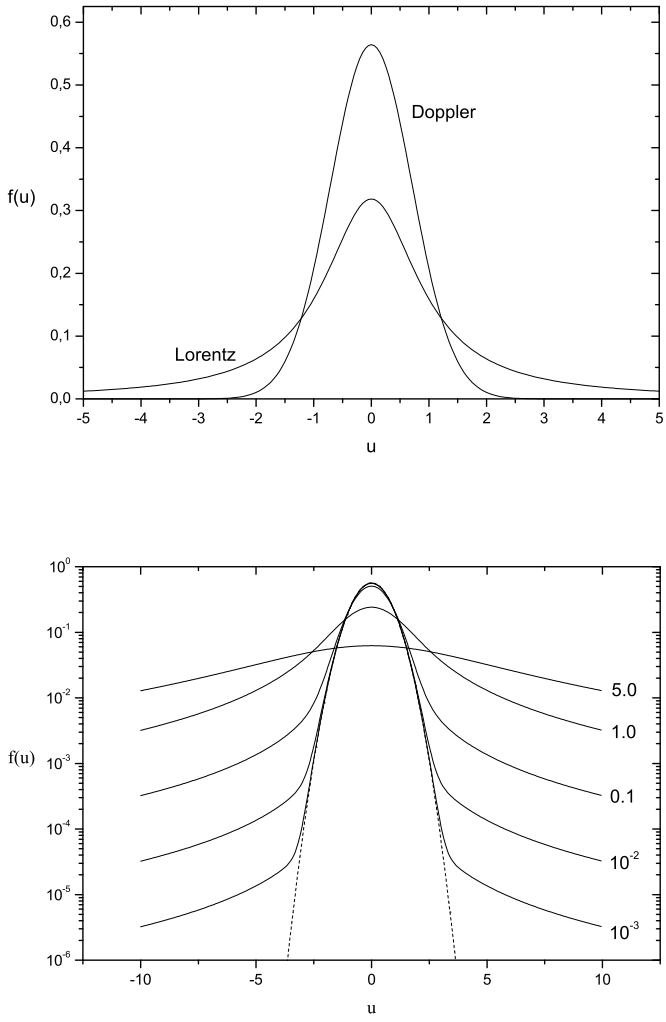

Figure A.2: Upper Panel: Normalized Doppler and Lorentzian profiles with a mixing parameter of 1. Lower Panel: Doppler profile (dashed line) along with different mixing parameter Voigt profiles.

Table A.4: References for the methane absorption coefficients at different regions of the spectrum.

Spectral Range (nm)	Data
5.6 - 51	Au et al. (1993)
52 - 125	Kameta et al. (2002)
126 - 152	Lee et al. (2001)
400 - 1000	Karkoscka (1994)
1000 - 1520	Irwin et al. (2006)
1520 - thermal IR	Boudon et al. (2004)

with α the Doppler to Lorentz line width ratio, know also as the mixing parameter:

$$\alpha = \frac{b_L}{\gamma_D} \tag{A.22}$$

The collision broadening depends both in pressure and temperature through the line width (see eq. A.13). At far distances from the center of the lines the real profiles start to diverge from the theoretical description provided by the Lorentzian profile and corrections that depend on the absorbing/emitting atom or molecule have to be included.

In order to have a general description of the line profiles, a common approach between modelers is to use the Voigt profile which depending on the input parameters (u and α) approaches the Doppler or Lorentz limit. It is the convolution of a Doppler shifted Lorentz profile with a Doppler profile, integrated over all the possible range of velocities:

$$f_V(u) = \frac{1}{\alpha_D \sqrt{\pi}} H(\alpha, u) \tag{A.23}$$

with $H(\alpha, u)$ the Voigt function:

$$H(\alpha, u) = \frac{\alpha}{\pi} \int_{-\infty}^{+\infty} \frac{e^{-\mathrm{v}^2}}{(u - \mathrm{v})^2 + \alpha^2} d\mathrm{v} \tag{A.24}$$

A.1.3 Methane coefficients

Methane has a broad absorption spectrum which extends from UV to thermal infrared. Table A.4 provides the references for the data used at different regions of the spectrum. Due to the large number of vibrational and rotational modes the thermal and near IR spectrum exhibit a strong spectral structure. The methane absorption coefficients in this part of the spectrum are derived from laboratory measurements (band models) and theoretical calculations.

In band models the measured transmission under certain conditions is averaged over bands of certain width $\Delta\nu$

$$\bar{t} = \frac{1}{\Delta\nu} \int t_\nu d\nu \tag{A.25}$$

with $t_\nu = exp(-k_\nu m)$. The conditions prevailing in Titan's atmosphere require the measurement of the absorption properties of methane at low temperatures and large pathlengths. In the current work the Irwin et al. (2006) transmissions have been used in the spectral region between 1 and 1.54 μm. These are based on the Sihra et al. (1998) low temperature and the Strong et al. (1993) large pathlengths transmission measurements which were fitted with a Goody-Voigt band model. In such a treatment the transmission, t, of a path is expressed as:

$$t = \exp\left(-2mk_{\bar{\nu}}^{'}(T)\int_0^\infty \frac{V(x,\alpha)}{1+m\delta k_{\bar{\nu}}^{'}(T)V(x,\alpha)/(\gamma_D^0\sqrt{T})}dx\right) \tag{A.26}$$

with m the absorber amount, δ the mean line spacing, $k_{\bar{\nu}}^{'}$(T) the mean absorption coefficient over the resolution of the band model (10 cm^{-1}), γ_D^0 the mean Doppler line-width at a reference temperature T_0 (296 K) defined as $\gamma_D^0 = \gamma_D/\sqrt{T}$ and V(x,y) the Voigt function but defined in such a way so it is $1/\sqrt{\pi}$ times the Voigt function presented in A.24. The parameter α is the mixing parameter, which, in terms of the reference conditions T_0 and P_0 (taken at 1 atm) can be given as

$$\alpha = \frac{b_L}{\gamma_D} = \frac{b_L^0}{\gamma_D^0}\frac{P}{P_0}\frac{\sqrt{T_0}}{T}\left(q + \frac{(1-q)}{SFB}\right) \tag{A.27}$$

In the above b_L^0 the mean Lorentz line-width at the reference temperature, q is the mole fraction and SFB the self-to-foreign broadening ratio. The mean absorption coefficient $k_{\bar{\nu}}$(T) was assumed to vary with temperature as

$$k_{\bar{\nu}}^{'} = \beta k_{\bar{\nu}}(T,E_1) + (1-\beta)k_{\bar{\nu}}(T,E_2) \tag{A.28}$$

where

$$k_{\bar{\nu}}(T,E_i) = k_{\bar{\nu}0}\left(\frac{T_0}{T}\right)^{1.5}\exp\left(\frac{hc}{k_B}E_i\left(\frac{1}{T_0}-\frac{1}{T}\right)\right) \tag{A.29}$$

with E_1 and E_2 the two lower state energies and hc/k_B=1.439. This parameterization that takes into account the two lower state energies instead of the E_1 only, improves the accuracy of the fits regarding the temperature dependence (Sromovsky et al., 2006). Parameter β ranges between 0 and 1 and in the current calculations it was set to 0.5 based on the results of (Irwin et al., 2006). The band parameterizations (http://www.atm.ox.ac.uk/user/irwin/) provide the values for $k_{\bar{\nu}0}$, δ/b_L^0, b_L^0/γ_D^0, E_1, E_2 and SFB with which the calculation of transmission for different amounts, pressures and temperatures can be readily performed.

At larger wavelengths ($\lambda > 1.54$ μm) the Boudon et al. (2004) line strengths that describe the methane absorption properties are used, assuming Voigt line profiles. At the far wings of the lines, the Hartmann et al. (2002) laboratory derived parameterizations have been used. These describe the divergence of the line profile from the theoretical expectations in terms of a multiplicative

correction factor, χ, that depends upon the distance $\nu - \nu_0$ from the line center, ν_0. The latter can be summarized as:

$$\chi(\nu) = \begin{cases} 1 & |\nu - \nu_0| < 26cm^{-1} \\ 8.72\exp(-\frac{\nu-\nu_0}{12}) & 26cm^{-1} < |\nu - \nu_0| < 60cm^{-1} \\ 0.0684\exp(-\frac{\nu-\nu_0}{393}) & |\nu - \nu_0| > 60cm^{-1} \end{cases} \quad \text{(A.30)}$$

Following the description presented in Section A.1.1 the calculation of the methane absorption coefficients was performed for different temperatures and pressures.

A.1.4 Correlated k-distribution coefficients

In the near-IR radiation transfer calculations, the band model formulation can not be used for inhomogeneous layers and layers with scattering properties, such as the ones addressed in Titan's atmosphere. The reason for that is that the transmission for a specific pathlength which is characterized by layers of different properties can not be estimated with the product of the individual transmissions and neither the use of scaling approximations, such as the Curtis-Godson one, can be applied since the source function is highly variable over each band interval. The latter approach is only applicable in the thermal radiation transfer where the Plank function is approximately constant over each band interval. A solution to the scattering problem was provided within the frame of the k-distribution method (for a more detailed description look in Goody and Yung (1989) an references therein).

Under this approach the average transmission within a band interval can be equivalently given by

$$\bar{t}(m) = \int_0^\infty f(k)\exp(-km)dk \quad \text{(A.31)}$$

with $f(k)$ the k-distribution. The physical meaning of this distribution is that f(k)dk describes the frequency domain of the band interval that is occupied by absorption lines having absorption coefficients between k and k+dk. From a different point of view the average band transmission is equal to the Laplace transformation of the k-distribution. If f(k) is known, then any function averaged over the band domain $\Delta\nu$

$$\bar{G}(m) = \frac{1}{\Delta\nu}\int G(k)dk \quad \text{(A.32)}$$

can be equivalently calculated with the use of the spectral function, as:

$$\bar{G}(m) = \int_0^\infty f(k)G(k)dk \quad \text{(A.33)}$$

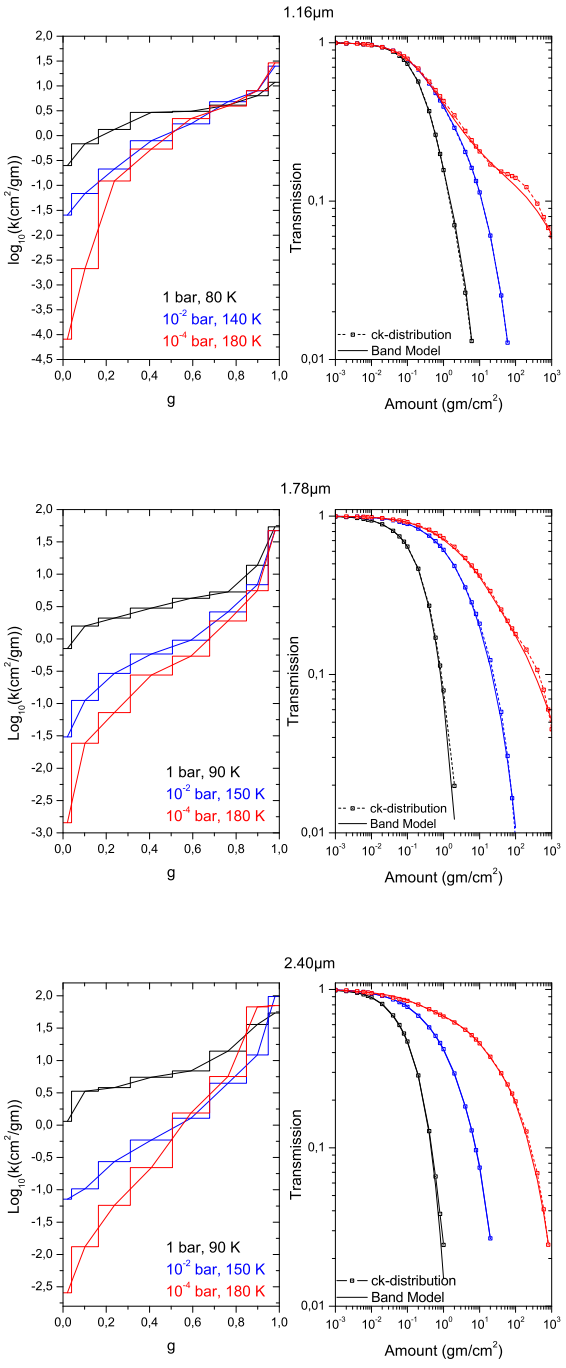

Figure A.3: Example of correlated k-distribution coefficients and corresponding transmissions for different pressure and temperature conditions for 3 wavelengths.

With the common formulation of band models (equation A.25) any information of the spectral variation of the absorption coefficient inside each band is lost due to the averaging. The advantage of the k-distribution method is that it conserves the information of the spectral variation within each band during the averaging. This allows the use of this method for scattering problems in which the source function is highly variable inside each band domain. In practical calculations the integral on the k-distribution can be approximated with a finite series of N terms:

$$\bar{t}(m) = \sum_{i=1}^{N} f(k_i)\delta k_i \exp(-k_i m) \tag{A.34}$$

The issue of non-homogeneous layer can be further addressed with the use of the correlated k-distribution. In this approach the cumulative distribution function of the initial k-distribution is used:

$$g(k) = \int_0^k f(k^{'})dk^{'} \tag{A.35}$$

Substituting $g(k)$, the average transmission at each band interval can be expressed as:

$$\bar{t}(m) = \int_0^1 \exp(-k(g)m)dg \tag{A.36}$$

or equivalently approximated with the sum:

$$\bar{t}(m) = \sum_{i=1}^{N} \exp(-k_i m)\Delta g_i \tag{A.37}$$

where the g domain is divided in N fractions with widths Δg_i and k_i is the average absorption coefficient in that fraction. The N number of points used in the integration and the fractions Δg_i can be define from numerical quadrature technics such as the Gaussian-Legendre integration. In the current calculation an 8-point quadrature approximation was used. The abscissae g_i and the gaussian weights Δg_i are given in Table A.5.

Comparison of the latter equation with A.25, shows that for a homogeneous layer the $\nu/\Delta\nu$ and g variables are interchangeable. For a non-homogeneous path that is divided into M homogeneous layer, the transmission is:

$$\bar{t}(m) = \int \exp\left(-\sum_{j=1}^{M} k_{\nu,j}\delta m_j\right) d(\nu/\Delta\nu) \tag{A.38}$$

The advantage of the correlated k-distribution approach is that there is a good correlation of transmissions calculated from A.38 and that assuming the

$$\bar{t}(m) = \int_0^1 \exp\left(-\sum_{j=1}^{M} k_j(g)\delta m_j\right) dg \tag{A.39}$$

Table A.5: Eight-point Gaussian quadrature abscissae & weights

	Abscissae	Weight
1	0.019855	0.050614
2	0.101667	0.111191
3	0.237234	0.156853
4	0.408283	0.181342
5	0.591717	0.181342
6	0.762766	0.156853
7	0.898333	0.111191
8	0.980145	0.050614

for the strong and weak absorption features of the various layers. This means that the $\nu/\Delta\nu$ - g interchangeability holds also for non-homogeneous paths. Hence, the same intervals Δg_i can be used for different atmospheric layers for which only the $g(k)$ functions have to be calculated. An example of the correlated k-distribution coefficients used in the model calculations is given in Fig. A.3. Note the monotonic variation of the k-coefficients with g, as implied by the cumulative distribution.

A.1.5 Collision induced absorption (CIA)

In the high pressure condition found in Titan's troposphere the rapid collision between the main molecules, N_2, CH_4 and H_2 induce temporal dipole moments and allow these molecules to absorb in the IR. In order to include this important source of opacity in the calculations, one needs to know the bimolecular absorption coefficients for each colliding pair. These have been theoretical calculated for different temperatures by A. Borysow and colleges for each of the possible pairs found in Titan's atmosphere (Table A.6). An example for the spectral contribution of each pair is given in Fig. A.4.

These were used for the calculation of the absorption coefficients at different temperatures which were tabulated in matrixes and used for the calculation of the CIA in the model. The opacity due to CIA within an atmospheric layer of width Δz can be calculated as:

$$\tau = k_{AB} \frac{n_A}{n_L} \frac{n_B}{n_L} \Delta z. \tag{A.40}$$

Table A.6: CIA pairs and references

Pair	Reference
N_2-N_2	Borysow & Frommhold (1986a)
N_2-H_2	Borysow & Frommhold (1986b)
N_2-CH_4	Borysow & Tang (1993)
H_2-CH_4	Borysow & Frommhold (1986c)
CH_4-CH_4	Borysow & Frommhold (1987)

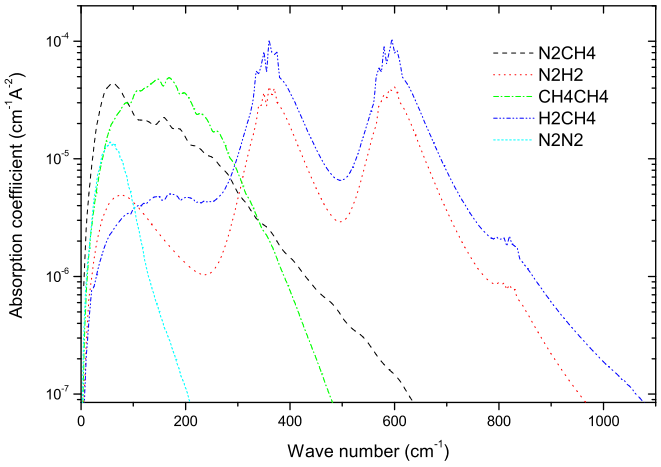

Figure A.4: Collision induced absorption coefficients at 90 K for each pair included in the model calculations

where k_{AB} is the collision induced absorption coefficient of each pair A-B in $\mathrm{cm}^{-1}\mathrm{A}^{-2}$, n_A and n_B are the number densities for each molecule of the pair and n_L is the Loschmidt number. This can be further simplified to give:

$$\tau = k_{AB}\left(\frac{T_0}{T}\right)^2\left(\frac{p}{p_0}\right)^2 f_A f_B \Delta z \tag{A.41}$$

where T_0 and p_0 are the standard temperature and pressure and x_A and f_B are the mole fraction of each species of the pair.

A.2 Scattering

Light as an ElectroMagnetic wave can be fully described by three vectors; the electric field, **E**, the magnetic field, **H** and the direction of propagation of the wave, **k**. The two first form an orthogonal set with the third in a way that:

$$\hat{k} \times \vec{E} = c\vec{B}$$

where $\hat{k}$ is the unit normal in the direction of propagation and c the velocity of light in the medium. Since from the equations of Maxwell there is a direct relationship between **E** and **H** for arbitrary direction of propagation, we can in our description of the scattering phenomena, to restrict ourselves only in the electric vector, **E**.

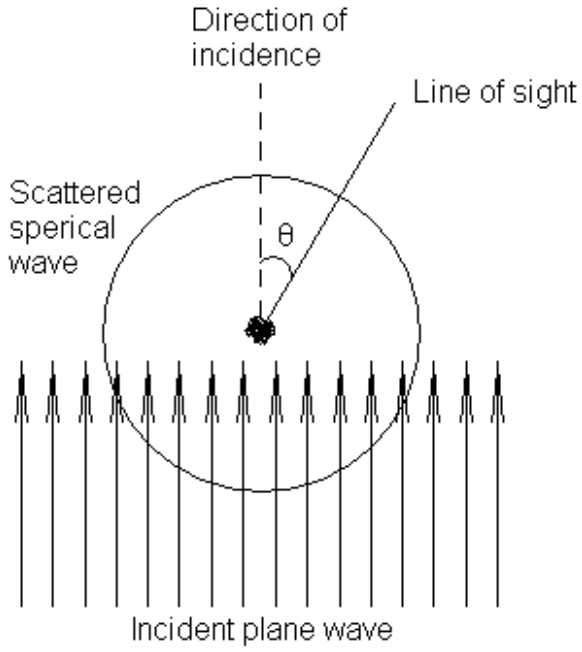

Figure A.5: Scattering geometry

In order to visualize the procedure, observe Fig. A.5. The incident light is thought as a plane wave approaching the scattering particle from below. The surrounding medium is taken homogenous; as the wave front reaches the surface of the particle, the change in the properties of the medium (in other words the change of the index of refraction) causes a decrease in the amplitude of the incident plane wave and the production of an outgoing spherical wave, the scattered wave, in distances large compared to the size of the particle and the wavelength. If we choose to observe the scattered spherical wave in a certain direction - the line of sight - the angle θ between the direction of incidence and the direction where we observe is called the scattering angle. The plane defined by the above two directions is the reference plane.

The equations of Maxwell provide a linear relationship between the incident and the scattered waves. The incident plane wave has a characteristic form described by:

$$u_0 = e^{-ikz+i\omega t} \tag{A.42}$$

with $k = 2\pi/\lambda$, the wave number. The outgoing spherical wave has a charac-

teristic form of the kind [1]:

$$u = S(\theta, \varphi)\frac{e^{ikr+i\omega t}}{ikr} \tag{A.43}$$

where S(θ,ϕ) is the amplitude function of the scattering particle, expressing the dependence of the spherical wave on the scattering and azimuthal angles and r the distance from the scattering center. The amplitude function depends only on the shape and the medium of the particle. From the above two, the connection between the incident and the scattered wave will have the form:

$$u = S(\theta, \varphi)\frac{e^{ikr+ikz}}{ikr}u_0 \tag{A.44}$$

In the general case of an elliptically polarized wave, the electric field of the incident plane wave can be described as:

$$\vec{E}_0 = E_0^l\hat{l} + E_0^r\hat{r} \tag{A.45}$$

where $\hat{l}$ and $\hat{r}$ are unit vectors parallel and perpendicular to the plane of reference in a way that:

$$\hat{r} \times \hat{l} = \hat{k}' \tag{A.46}$$

and $\hat{k}'$ the unit normal in the direction of the line of sight for the outgoing spherical wave (Fig A.6). Since the plane of reference depends on the line of sight the $\hat{r}$ and $\hat{l}$ vectors will change according to the direction of observation.

The generalization of the above relation between the incident and the scattered electric field components for an elliptically polarized electric vector will be:

[1] Here we assume that the scattered radiation has the same frequency with the incident (coherent scattering). Hence the wave numbers of the incident and scattered radiation are the same.

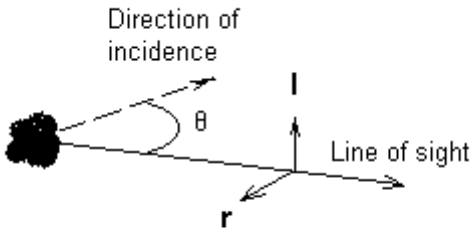

Figure A.6: Electric field vectors in scattering geometry

$$\begin{pmatrix} E_l \\ E_r \end{pmatrix} = \frac{e^{-ikr+ikz}}{ikr} \begin{pmatrix} S_2 & S_3 \\ S_4 & S_1 \end{pmatrix} \begin{pmatrix} E_0^l \\ E_0^r \end{pmatrix} \tag{A.47}$$

where the matrix on the right hand is the amplitude scattering matrix and, as the scattering function, depends only on the properties of the scattering particle and its orientation in space. It should be pointed out that the knowledge of the scattering matrix for a particular particle provides all the necessary information for the calculation of the properties of the scattered and propagating wave.

In certain cases the scattering matrix can take a simple form that leads to analytical solutions applicable to atmospheric scattering problems. Such one is that of a spherical and homogeneous scatterer (Mie Scattering). The limit of this case for very small particles is the Rayleigh scattering. Due to addressed symmetry, the S_3 and S_4 components of the matrix are zero and the S_1 and S_2 depend only on the scattering angle θ. Hence, the relation between the incident and scattered components of the electric field takes the form:

$$\begin{pmatrix} E^l \\ E^r \end{pmatrix} = \frac{e^{-ikr+ikz}}{ikr} \begin{pmatrix} S_2 & 0 \\ 0 & S_1 \end{pmatrix} \begin{pmatrix} E_0^l \\ E_0^r \end{pmatrix} \tag{A.48}$$

Under this simplified form it is possible to derive analytical solutions for the scattered electric field components. Further, in order to have a description of the way the scattered radiation is distributed in all angles around the particle, the phase function is used, which for spherical symmetry takes the simple form:

$$P(\theta) \sim \frac{1}{2}(i_1(\theta) + i_2(\theta)) \tag{A.49}$$

where $i_1(\theta) = |S_1(\theta)|^2$ and $i_2(\theta) = |S_2(\theta)|^2$. In the calculation of the phase function a normalizing multiplication factor must be considered in order to make sure that the integral in all angles (θ, ϕ) will give 4π (energy conservation in all directions).

A.2.1 Rayleigh scattering

For very small particles such as molecules and atoms, the induced electric field is approximately constant and equal to the external field, $\overrightarrow{E_0}$. In this case the scattered radiation is that of the induced dipole moment, $\overrightarrow{M}$, which relates to the polarizability tensor, α that depends on the properties of the scattering matter, through:

$$\overrightarrow{M} = \alpha \overrightarrow{E_0} \tag{A.50}$$

Under these conditions, the electric field at large distances compared to the size of the scattering center can be analytically calculated. In the special case of spherical symmetry, the polarizability becomes a scalar quantity and the scattering matrix takes the form:

$$\begin{pmatrix} S_2 & 0 \\ 0 & S_1 \end{pmatrix} = ik^3 a \begin{pmatrix} cos\theta & 0 \\ 0 & 1 \end{pmatrix} \tag{A.51}$$

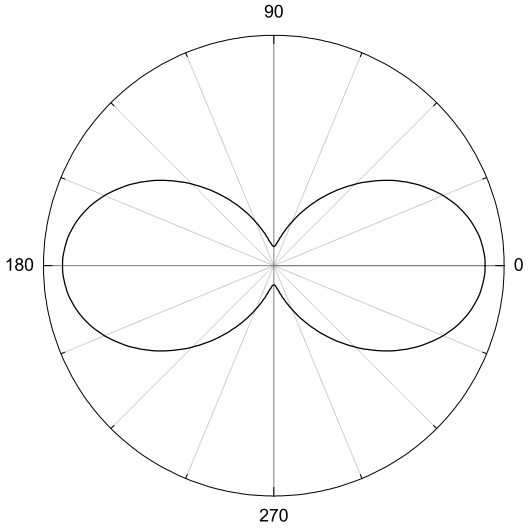

Figure A.7: Angle distribution of Rayleigh scattered radiation

This explains the symmetric variation of the scattered radiation with the scattering angle, θ (see Fig. A.7):

$$P(\theta) = (1 + cos^2(\theta)) \tag{A.52}$$

For molecules for which the spherical symmetry does not apply a correction factor must be included. This is the depolarization factor, Δ that can be readily measured for different species. In terms of a scattering cross section, the Rayleigh solution finally yields:

$$\sigma_R = \frac{32\pi^3}{3\lambda^4}\alpha^2\delta \tag{A.53}$$

with

$$\delta = \frac{6 + 3\Delta}{6 - 7\Delta} \tag{A.54}$$

The scalar polarizability can be calculated from:

$$a = \frac{(n-1)}{N} \tag{A.55}$$

with N the atoms or molecules per unit volume and n the refractive index of the scattering matter that in principle is wavelength dependent. The latter can be given in the form (Allen, 1976):

$$n - 1 = A(1 - B/\lambda^2)) \tag{A.56}$$

Table A.7: Rayleigh Scattering parameters for species found in Titan's atmosphere.

Species	A $\times 10^{-5}$	B $\times 10^{-3}$	Δ $\times 100$	δ
H_2	13.58	7.52	0.9	1.015
N_2	29.06	7.7	3.6	1.063
NH_3	37.00	12.0	1.0	1.017
CH_4	44.30	0	2.0×10^{-3}	1.000
C_2H_2			4.5	1.079
C_2H_4			2.9	1.050
C_2H_6			0.9	1.015
C_3H_6			2.9	1.050
C_3H_8			1.1	1.019
C_4H_{10}			1.2	1.020
C_6H_6			4.2	1.074
H_2O			2.0	1.034
CO	32.7	8.1	3.2	1.055
CO_2	43.9	6.4	7.2	1.131

with A and B constants that depend on the atom or molecule (see Table A.2.1). Replacing the above, the Rayleigh scattering cross section for an atom or molecule can be given from:

$$\sigma_R(cm^2) = 4.577 \times 10^{-21} \frac{\delta}{\lambda^4} A(1 + \frac{B}{\lambda^2}) \tag{A.57}$$

A.2.2 Mie scattering

G. Mie in 1908 and independently P. Debye in 1909 were the first to provide the solution for the problem of scattering in the case of a spherical and homogenous scatterer. The solution of the Maxwell's equations with the appropriate boundary conditions for the scattering problem of a sphere with radius α and refractive index m, will provide an analytic form for the $S_1(\theta)$ and $S_2(\theta)$.

For a periodic field with a circular frequency ω and without charges and currents, the Maxwell's equations can take the form:

$$\nabla \cdot \vec{E} = 0 \quad \nabla \times \vec{E} = ikm^2\vec{E}$$
$$\nabla \cdot \vec{H} = 0 \quad \nabla \times \vec{H} = -ik\vec{H}$$

where m is the complex index of refraction:

$$m = n + in' \tag{A.58}$$

The real part of the refractive index defines the propagating velocity of the wave through the medium and the imaginary part the medium's absorbing properties. The far field solution (meaning the scattered field solution for distances much

greater than the radius of the sphere) of the above equations, gives the following results for the form of the $S_1(\theta)$ and $S_2(\theta)$:

$$\begin{aligned} S_1(\theta) &= \sum_{n=1}^{\infty} \tfrac{2n+1}{n(n+1)}[a_n\pi_n(\cos\theta) + b_n\tau_n(\cos\theta)] \\ S_2(\theta) &= \sum_{n=1}^{\infty} \tfrac{2n+1}{n(n+1)}[b_n\pi_n(\cos\theta) + a_n\tau_n(\cos\theta)] \end{aligned} \tag{A.59}$$

where

$$a_n = \frac{\psi_n'(\mathrm{y})\psi_n(\mathrm{x}) - m\psi_n(\mathrm{y})\psi_n'(\mathrm{x})}{\psi_n'(\mathrm{y})\xi_n(\mathrm{x}) - m\psi_n(\mathrm{y})\xi_n'(\mathrm{x})} b_n = \frac{m\psi_n'(\mathrm{y})\psi_n(\mathrm{x}) - \psi_n(\mathrm{y})\psi_n'(\mathrm{x})}{m\psi_n'(\mathrm{y})\xi_n(\mathrm{x}) - \psi_n(\mathrm{y})\xi_n'(\mathrm{x})} \tag{A.60}$$

and

$$\begin{aligned} \pi_n(\cos\theta) &= \tfrac{1}{\sin\theta} P_n^1(\cos\theta) \\ \tau_n(\cos\theta) &= \tfrac{d}{d\theta} P_n^1(\cos\theta) \end{aligned} \tag{A.61}$$

In the above:

- $P_n^1(\cos\theta)$is the associated Legendre polynomial.
- $\psi_n, \xi_n$are the Ricatti-Bessel functions which relate with the Bessel functions as:
$$\begin{aligned} \psi_n(z) &= z \cdot j_n(z) = \sqrt{\tfrac{\pi z}{2}} J_{n+\frac{1}{2}}(z) \\ \xi_n(z) &= z \cdot h_n^{(2)}(z) = \sqrt{\tfrac{\pi z}{2}} H^{(2)}_{n+\frac{1}{2}}(z) \end{aligned}$$
with$j_n(z), h_n^{(2)}(z)$ the spherical Bessel functions, $J_{n+\frac{1}{2}}(z), H^{(2)}_{n+\frac{1}{2}}$ the half integer order Bessel functions and z complex. The prime denotes the first derivative with respect to the argument.
- x = kα and y=mx

In this solution the medium outside the sphere was taken to be vacuum (m=1). In the case that this is not true and the surrounding medium has an index of refraction m_1 (real) and the sphere m_2 (complex) the same solution still holds but with the corrections:

$$m \to \frac{m_1}{m_2} \quad , \quad k \to m_2 k \tag{A.62}$$

The efficiency factors have a straightforward relation with the elements of the scattering matrix. For the case of spherical, homogeneous particles the results of Mie's theory provide the following formula:

$$Q_{ext} = \frac{2}{x^2} \sum_{n=1}^{\infty} (2n+1) Re(a_n + b_n) \tag{A.63}$$

$$Q_{sca} = \frac{2}{x^2} \sum_{n=1}^{\infty} (2n+1)(|a_n|^2 + |b_n|^2) \tag{A.64}$$

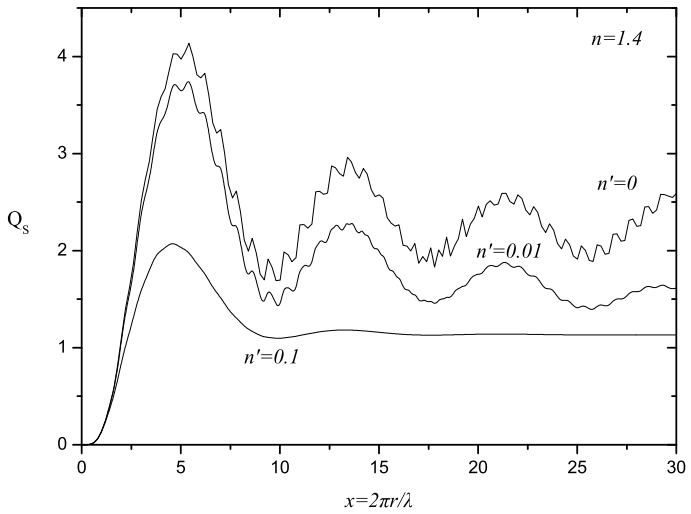

Figure A.8: Scattering efficiencies as a function of the size parameter for different absorption properties.

In radiation transfer calculations the relative proportions of the forward to the backward scattered radiation is needed and is described by the asymmetry factor, g. The last in the frame of Mie theory can be given by:

$$g = \frac{4}{\chi^2 Q_{sca}} \sum_{n=1}^{\infty} \frac{n(n+2)}{n+1} \Re(a_n a_{n+1}^* + b_n b_{n+1}^*) + \frac{2n+1}{n(n+1)} \Re(a_n b_n^*) \qquad \text{(A.65)}$$

Finally the polarization, P, of the scattered wave with respect to the scattering angle is given by:

$$P = \frac{i_1(\theta) - i_2(\theta)}{i_1(\theta) + i_2(\theta)} \qquad \text{(A.66)}$$

Using the above analytical solution for the case of a spherical scatterer and with the aid of the modern computers it is possible to compute the efficiency factors and the other parameters described above. The series in the infinite sums need to be extended up to terms of the order of [x] to have reliable results.

In Fig. A.8 the efficiency factors for scattering is plotted for the case of a complex refractive index with $n = 1.4$ and four possible values of n'. What can be readily observed for small values of the imaginary part of the refractive index is the rapid increase of Q_{sca} for values of the size parameter between 0 and 5 and the waveform for bigger x, which slowly disappears as n' increases. The waveform results from the interference of light travelling through the sphere

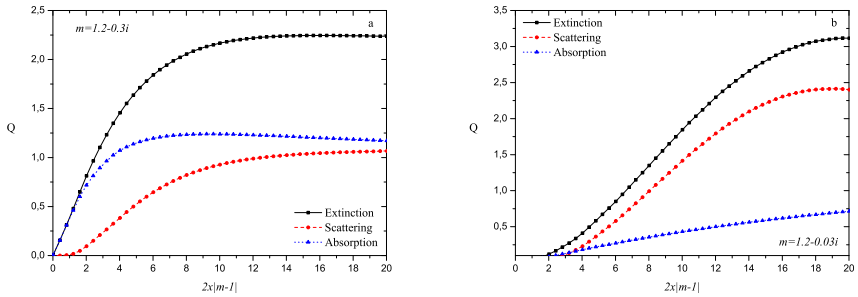

Figure A.9: The variation of the three efficiency factors with the size parameter for different imaginary refractive index.

(transmition) and light passing by the sphere (diffraction). The ripples which are observed for small n''s comes from edge phenomena around the sphere. As n' is increases, Q_{sca} decreases and the above two characteristics disappear gradually. In the case that $n' = 0$, Q_a is zero and hence Q_{sca}=Q_{ext}. For very big values of the size parameter we see that the extinction coefficient reaches asymptotically the value 2 which can be proved by taking in to account the properties of EM waves for large values of the size parameter.

Fig. A.9 presents, the three efficiency coefficients plotted for two cases of the refractive index as a function of the phase lag between the wave passing through the diameter of the sphere and the wave not intercepting the sphere:

$$\rho = \frac{2\pi m}{\lambda} 2a - \frac{2\pi}{\lambda} 2a = 2x\,|m-1| \tag{A.67}$$

As before, the increase of the imaginary part of the refractive index leads to the rise of Q_{abs} and the vanish of any maxima and minima.

Fig. A.10 presents the phase functions for refractive indexes corresponding to two different wavelengths of water vapor. At 3μm H_2O is highly absorbing as it can be seen from the value of the imaginary part of the refractive index, while at 5μm the absorptivity is significantly decreased. In the same time the real part of the refractive index exhibits a much smaller variation. It can be deduced from the figures that as the radius of the scattering particle increases the angle distribution becomes increasingly more complex for both wavelengths (see also Fig. A.11), while the increase of the particle's absorptivity, smooths out the strong angle variability for the same value of the size parameter. In all cases it is prominent the very strong forward scattering peak at θ=0 and the less intense backward peak, the relative ratio of which increases with increasing size. This last characteristic is also shown in Fig. A.12 which presents the variation of the asymmetry factor, g, with the size parameter for different values of the refractive index.

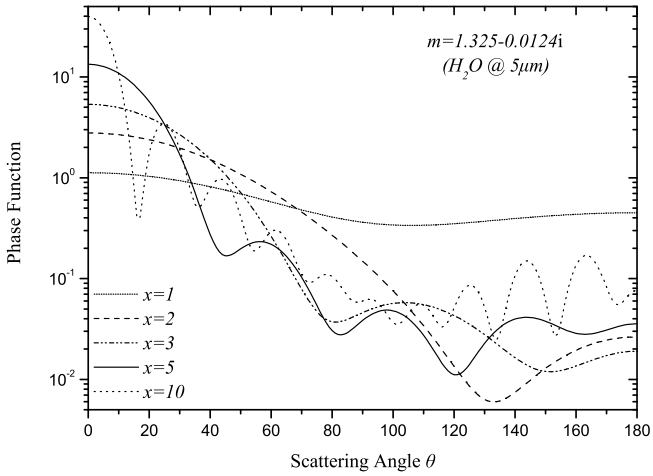

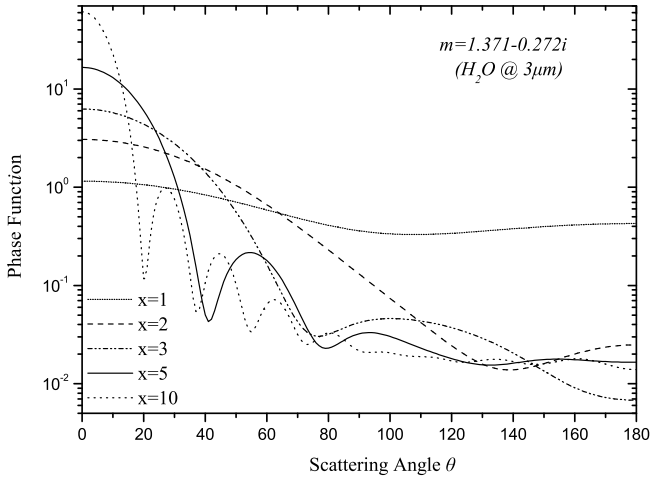

Figure A.10: Phase function of water vapor at two different wavelengths and for different size spheres.

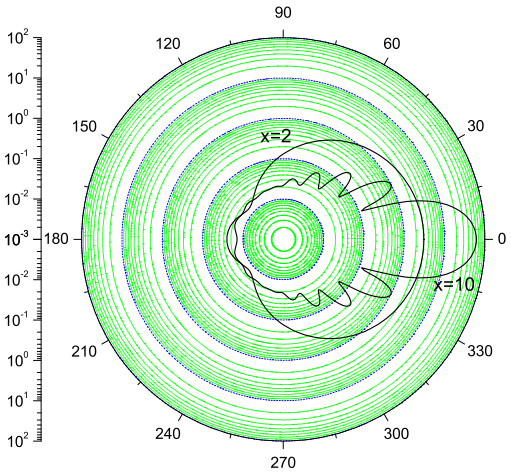

Figure A.11: Polar view of phase functions for H_2O at 3μm for two different size particles. Notice the radial log scale.

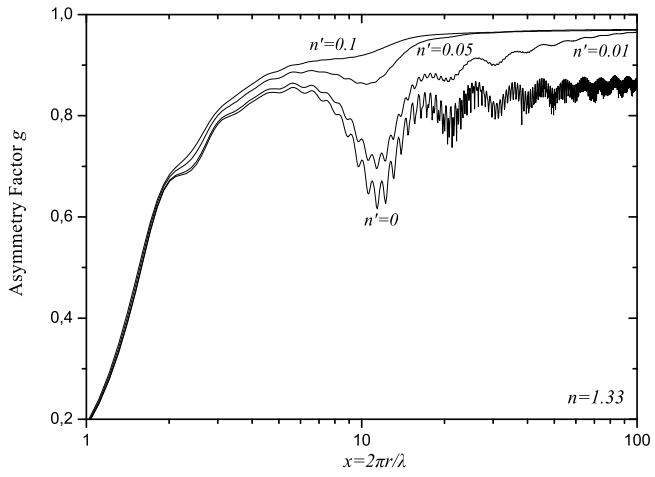

Figure A.12: Variation of asymmetry factor, g, with size parameter for different absorption properties.

Bibliography

Abramowitz M. & Stegun I.A., 1972. Handbook of Mathematical Functions, Dover publications.

Allen C.W., 1976. Astrophysical Quantities. The Athlone Press, University of London.

Au, J.W., Cooper, G., Burton, G.R., Olney, T.N., Brion, C.E., 1993. The valence shell photoabsorption of the linear alkanes, C_nH_{2n+2} (n=1,8): Absolute oscillator strengths (7-220 ev). Chem. Phys. 173, 209-239.

Borysow A., Frommhold, L., 1986a. Collision induced rototranslational absorption spectra of N_2-N_2 pairs for temperatures from 50 to 300 K. Astrophysical J. 311,1043-1057.

Borysow A., Frommhold, L., 1986b. Theoretical collision induced rototranslational absorption spectra for modeling Titan's atmosphere: H_2-N_2 pairs. Astrophysical J. 303,495-510.

Borysow A., Frommhold, L., 1986c. Theoretical collision induced rototranslational absorption spectra for the outer planets: H_2-CH_4 pairs. Astrophysical J. 304, 849-865.

Borysow A., Frommhold, L., 1987. Collision induced rototranslational absorption spectra of CH_4-CH_4 pairs at temperatures from 50 to 300 K. Astrophysical J. 318, 940-943.

Borysow A., Tang, C., 1993. Far infrared CIA spectra of N_2-CH_4 pairs for modeling of Titan's atmosphere. Icarus 105,175-183.

Boudon, V., Champion, J.-P., Gabard, T., Loëte, M., Michelot, F., Pierre, G., Rotger, M., Wenger, Ch., Rey, M., 2004. Symmetry-adapted tensorial formalism to model rovibrational and rovibronic spectra of molecules pertaining to various point groups. J. Mol. Spectrosc. 228, 620•-634.

Debye P., 1909. Der Lichtdruck auf Kugeln, Ann. Phys. 30, 755,Ph.D. thesis, Munich.

Gamache, R.R., Hawkins, R.L., Rothman, L.S., 1990. Total internal partition sums in the temperature range 70-3000 K: Atmospheric linear molecules. J. Molec. Spec. 142, 205-219.

Goody, R.M., Yung, Y.L., 1989. Atmospheric Radiation. Theoretical Basis, Second Edition. Oxford University Press.

Hartmann, J-M., Boulet, C., Brodbeck, C., van Thanh, N., Fouchet, T., Drossart, P., 2002. A far wing lineshape for H_2 broadened CH_4 infrared transitions. JQSRT 72, 117-122.

Irwin, P.G.J., Sromovsky, L.A., Strong, E.K., Sihra, K., Teanby, N.A., Bowles, Calcutt, S.B., Remedios, J.J., 2005. Improved near-infrared methane band models and k-distribution parameters from 2000 to 9500 cm^{-1} and implications for the interpretations of outer planet spectra. Icarus 181, 309-319.

Kameta, K., Kouchi, N., Ukai, M., Hatano, Y., 2002. Photoabsorption, photoionization and neutral-dissociation cross sections of simple hydrocarbons in the vacuum ultraviolet range. J. Quant. Spectrosc. Radiat. Transfer 123, 225-238.

Karkoschka, E., 1994. Spectrophotometry of the Jovian planets and Titan at 300 to 1000 nm wavelength: The methane spectrum. Icarus 111, 174•192.

Lee A.Y.T., Yung, Y.L., Cheng, B., Bahou, M., Chung, C., Lee, Y., 2001, Enhancement of deuterated ethane on Jupiter. Astrophys. J. 551, 93-96.

Mie G., 1908. Ann. Phys. 25, 377.

Sihra, K., 1998. Laboratory measurements of near-infrared methane bands for remote sensing of the jovian atmosphere. Ph.D. thesis. University of Oxford.

Sromovsky, L.A., Irwin, P.G.J., Fry, P.M., 2005. Near-IR methane absorption in outer planet atmospheres: Improved models of temperature dependence and applications for Uranus cloud structure. Icarus 182, 577-593.

Strong, K., Taylor, F.W., Calcutt, S.B., Remedios, J.J., Ballard, J., 1993. Spectral parameters for self- and hydrogen-broadened methane from 2000 to 9500 cm^{-1} for remote sounding of the atmosphere of Jupiter. J.Q.S.R.T. 50, 363-429.

Van de Hulst H.C. 1957, Light Scattering by small Particles; John Wiley & Sons (1957); Dover publications (1981)

Appendix B

Multiple Scattering Solution for Inhomogeneous Layers

Inside an inhomogeneous atmosphere, such as Titan's, multiple scattering has a very important role in the radiation transfer process. A solution of this problem has been initially provided with the aid of the Eddington approximation described in Shettle & Weinman (1970). The problem is addressed with the division of the inhomogeneous atmosphere into homogeneous layers within which its possible to obtain analytical solutions for the two-boundary problem. An improvement to the approach was the δ-Eddington method for highly anisotropic phase functions (Joseph et al., 1976).

Here, the δ-Eddington approximation is used for the simplification of the radiation transfer equation in terms of a numerical second-order ordinary differential equation method (Vardavas & Taylor, 2007) that provides a significantly faster solution for each monochromatic radiation transfer calculation compared to the analytic method suggested by Shettle & Weinman (1970). This efficient method allows the inclusion of the high resolution pressure grid in the radiation transfer calculations.

First, the simplified isotropic scattering form of the radiation transfer equation is discussed and based on this the δ-Eddington method and the way it is applied in the model are presented.

B.1 Isotropic scattering solution

The transfer equation for diffuse radiation is:

$$\mu \frac{\partial I_\lambda}{\partial \tau_\lambda} = -I_\lambda + S_\lambda \tag{B.1}$$

where $I_\lambda(\tau_\lambda, \mu, \phi)$ is the radiance, S_λ the source function, τ_λ the extinction optical depth, μ the zenith and ϕ the azimuth angle. Using the first three moments of the radiation field:

$$J_\lambda = \frac{1}{2}\int_{-1}^{+1} I_\lambda d\mu, H_\lambda = \frac{1}{2}\int_{-1}^{+1} \mu I_\lambda d\mu, K_\lambda = \frac{1}{2}\int_{-1}^{+1} \mu^2 I_\lambda d\mu \tag{B.2}$$

and the assumption of coherent and isotropic scattering, the transfer equation can take the following forms

$$\frac{\partial H_\lambda}{\partial \tau_\lambda} = -J_\lambda + S_\lambda \tag{B.3}$$

and

$$\frac{\partial K_\lambda}{\partial \tau_\lambda} = -H_\lambda \tag{B.4}$$

Using Eddington's approximation, were the zenith dependence of the radiance is approximated as:

$$I_\lambda = \alpha_\lambda + \mu b_\lambda \tag{B.5}$$

the three moments of the radiation field take the form:

$$J_\lambda = \alpha_\lambda$$

$$H_\lambda = \tfrac{1}{3} b_\lambda \tag{B.6}$$

$$K_\lambda = \tfrac{1}{3}\alpha = \tfrac{1}{3} J_\lambda$$

From Eq. B.6 and B.4:

$$H_\lambda = -\frac{1}{3}\frac{\partial J_\lambda}{\partial \tau_\lambda} \tag{B.7}$$

which on substitution in Eq. B.1 results in a second-order differential equation for the mean radiance J_λ in the form of a diffusion equation

$$\frac{1}{3}\frac{\partial^2 J_\lambda(\tau_\lambda)}{\partial \tau_\lambda^2} = J_\lambda(\tau_\lambda) - S_\lambda(\tau_\lambda) \tag{B.8}$$

with the angle-independent source function S_λ for coherent and isotropic scattering given by

$$S_\lambda = (1 - \omega_\lambda) B_\lambda + \omega_\lambda J_\lambda \tag{B.9}$$

where ω_λ is the single-scattering albedo. When the expression for the source function is inserted into the above diffusion equation we get

$$\frac{1}{3}\frac{\partial^2 J_\lambda(\tau_\lambda)}{\partial \tau_\lambda^2} = (1 - \omega_\lambda)(J_\lambda(\tau_\lambda) - B_\lambda(\tau_\lambda)). \tag{B.10}$$

Given appropriate boundary conditions, one can rapidly solve this boundary-valued problem using a numerical technique such as the Thomas algorithm (e.g. Vardavas & Taylor (2007)), if one replaces the second derivative by a three-term finite-differences expression.

B.2 Anisotropic scattering solution

The scattering phase function, $p(\vartheta)$, can be expressed as a series of associated Legendre polynomials as described in Chandrasekhar (1960). When the Eddington approximation is applied, the integral over μ and ϕ in the source function will vanish for all terms of the series except for the first two. Hence the phase function can be written as (Shettle & Weinman, 1970):

$$p(\vartheta) = 1 + 3g\cos\vartheta. \tag{B.11}$$

where ϑ is the scattering angle which can be written as:

$$cos\vartheta = \mu\mu^{'} + (1-\mu^2)^{1/2}(1-\mu^{'2})^{1/2}cos(\phi - \phi^{'}). \tag{B.12}$$

where $\mu^{'}$ is the cosine of the incoming zenith direction and μ that of the outgoing zenith direction. g is the asymmetry factor

$$g = \frac{1}{2}\int_{-1}^{+1} p(cos\vartheta)dcos\vartheta \tag{B.13}$$

which is a measure of the scattered radiations anisotropy:

$$g = \begin{cases} 1 & forward\ scattering \\ 0 & isotropic\ or\ symmetric\ scattering \\ -1 & backward\ scattering \end{cases} \tag{B.14}$$

For an azimuthally-averaged radiation field, we can average also the phase function over the incoming azimuthal direction by replacing $\cos\vartheta$ given by Eq. B.12 to obtain

$$p(\mu, \mu^{'}) = 1 + 3g\mu\mu^{'}. \tag{B.15}$$

The angle-dependent source function (Vardavas & Taylor, 2007) can now be expressed as

$$S_\lambda(\mu) = S_{e\lambda} + S_{s\lambda} + S_{i\lambda} \tag{B.16}$$

where the thermal emission source function is

$$S_{e\lambda} = (1-\omega_\lambda)B_\lambda \tag{B.17}$$

the scattering source function is

$$S_{s\lambda}(\mu) = \frac{\omega_\lambda}{2}\int_{-1}^{1} p(\mu, \mu^{'})I_\lambda(\mu^{'})d\mu^{'} \tag{B.18}$$

and the source function for the incoming direct solar radiation is

$$S_{i\lambda}(\mu) = \frac{\omega_\lambda}{4\pi}p(\mu, \mu_o)F^{\downarrow}_{d\lambda} \tag{B.19}$$

where

$$F^{\downarrow}_{d\lambda} = S_{\odot\lambda}e^{-\tau_\lambda/\mu_o} \tag{B.20}$$

is the direct solar flux, at optical depth τ_λ, normal to the direction of incidence defined by μ_o, the cosine of the solar zenith angle. $S_{\odot\lambda}$ is the incoming solar spectral flux (erg cm^{-2} s^{-1} μm^{-1}) at the Earth's orbit. Note that the phase function is divided by 4π sr so that $S_{i\lambda}(\mu)$ has units of radiance (erg cm^{-2} s^{-1} sr $^{-1}$ μm^{-1}.

If we take μ_o positive in the downwards direction (increasing optical depth), integrate over the incoming direction and use the Eddington approximation $I_\lambda = J_\lambda + 3\mu H_\lambda$, Eq. B.5, we get

$$S_\lambda(\mu) = (1-\omega_\lambda)B_\lambda + \omega_\lambda(J_\lambda + 3g\mu H_\lambda) + \frac{\omega_\lambda}{4\pi}(1+3g\mu\mu_o)F^\downarrow_{d\lambda} \tag{B.21}$$

where H_λ is the second moment of the radiance, I_λ, given in Eq. B.2, but now defined by

$$\frac{\partial H_\lambda}{\partial \tau_\lambda} = -J_\lambda + S_\lambda \tag{B.22}$$

where the angle-averaged source function (*first moment of the source function*) is given by

$$\begin{aligned} S_\lambda &= \frac{1}{2}\int_{-1}^{1} S_\lambda(\mu)d\mu & \text{(B.23)}\\ &= (1-\omega_\lambda)B_\lambda + \omega_\lambda J_\lambda + \frac{\omega_\lambda}{4\pi}F^\downarrow_{d\lambda}. & \text{(B.24)} \end{aligned}$$

The equation of the third moment of the radiance, can now be written

$$\frac{\partial K_\lambda}{\partial \tau_\lambda} = -H_\lambda + Q_\lambda \tag{B.25}$$

where Q_λ is here defined as the *second moment of the source function* defined by

$$\begin{aligned} Q_\lambda &= \frac{1}{2}\int_{-1}^{1} \mu S_\lambda(\mu)d\mu & \text{(B.26)}\\ &= \omega_\lambda g H_\lambda + \frac{\omega_\lambda}{4\pi} g\mu_o F^\downarrow_{d\lambda} & \text{(B.27)} \end{aligned}$$

Since $K = J/3$, Eq. B.6, we can replace K in terms of J in Eq. B.25 to obtain

$$\frac{1}{3}\frac{\partial J_\lambda(\tau_\lambda)}{\partial \tau_\lambda} = -\alpha H_\lambda(\tau_\lambda) + \beta \tag{B.28}$$

where

$$\begin{aligned} \alpha &= 1-\omega_\lambda g & \text{(B.29)}\\ \beta &= \frac{\omega_\lambda}{4\pi} g\mu_o F^\downarrow_{d\lambda}. & \text{(B.30)} \end{aligned}$$

We can divide the equation by α and differentiate a second time to obtain the radiation diffusion equation, , on replacing the derivative of H in terms of J from Eq. B.28

$$\frac{\partial}{\partial \tau_\lambda}\left(a(\tau_\lambda)\frac{\partial J_\lambda(\tau_\lambda)}{\partial \tau_\lambda}\right) = J(\tau_\lambda) - S(\tau_\lambda) + \frac{\partial b(\tau_\lambda)}{\partial \tau_\lambda} \tag{B.31}$$

where $a = 1/3\alpha$ and $b = \beta/\alpha$. For the case of isotropic scattering, $g = 0$, and for no incoming solar flux $a = 1/3$ and $b = 0$, and so we obtain the radiation diffusion equation given by Eq. B.10.

If we now substitute for the source function S_λ from Eq. B.16 we get a second-order differential equation

$$c_1 \frac{\partial^2 J_\lambda}{\partial \tau_\lambda^2} + c_2 \frac{\partial J_\lambda}{\partial \tau_\lambda} + c_3 J_\lambda + c_4 = 0 \tag{B.32}$$

where

$$c_1 = a(\tau_\lambda) \tag{B.33}$$

$$c_2 = \frac{\partial a_\lambda}{\partial \tau_\lambda} \tag{B.34}$$

$$c_3 = \omega_\lambda - 1 \tag{B.35}$$

$$c_4 = -c_3 B_\lambda - \frac{\partial b_\lambda}{\partial \tau_\lambda} + \frac{\omega_\lambda}{4\pi} F_{d\lambda}^{\downarrow} \tag{B.36}$$

that we can solve rapidly to obtain J_λ as a function of optical depth for each wavelength, given the boundary conditions at the top of the atmosphere and at the surface. The upwards and downwards diffuse spectral fluxes at each atmospheric level can then be calculated from

$$F_\lambda^{\uparrow} = \pi(J_\lambda - 2H_\lambda) \tag{B.37}$$

$$F_\lambda^{\downarrow} = \pi(J_\lambda + 2H_\lambda) \tag{B.38}$$

so that the net downwards diffusive flux is $4\pi H_\lambda$, while the total flux available for photolysis is $4\pi J_\lambda + \mu_o F_{d\lambda}^{\downarrow}$, so that the enhancement factor for photolysis is

$$f = \frac{4\pi J_\lambda + \mu_o F_{d\lambda}^{\downarrow}}{\mu_o S_{\odot\lambda}}. \tag{B.39}$$

H can be computed from

$$H_\lambda = -a \frac{\partial J_\lambda(\tau_\lambda)}{\partial \tau_\lambda} + b. \tag{B.40}$$

The total downwards flux, $F_{T\lambda}^{\downarrow}$, comprises the diffuse and direct components

$$F_{T\lambda}^{\downarrow} = F_\lambda^{\downarrow} + \mu_o F_{d\lambda}^{\downarrow} \tag{B.41}$$

and the net downwards flux is

$$F_{net\lambda}^{\downarrow} = F_{T\lambda}^{\downarrow} + F_{d\lambda}^{\uparrow}. \tag{B.42}$$

The surface boundary condition is then

$$F_\lambda^{\uparrow} = R_{s_\lambda} F_{T\lambda}^{\downarrow} \tag{B.43}$$

where R_{s_λ} is the surface spectral reflectance and both diffuse and direct solar radiation is diffusely reflected upwards at the surface. Thus the total upwards flux is equal to the diffuse component, $F^{\uparrow}_{T\lambda} = F^{\uparrow}_{\lambda}$. At the top of the atmosphere the boundary condition is that there is no incoming diffuse component so $F^{\downarrow}_{\lambda} = 0$. The boundary conditions in terms of J_λ then become

$$d_1 \frac{\partial J_\lambda(\tau_\lambda)}{\partial \tau_\lambda} + d_2 J_\lambda + d_3 = 0 \tag{B.44}$$

where for the surface boundary condition

$$\begin{aligned} d_1 &= 2\pi a(1 + R_{s\lambda}) && \text{(B.45)} \\ d_2 &= \pi(1 - R_{s\lambda}) && \text{(B.46)} \\ d_3 &= -\pi 2b(1 + R_{s\lambda}) - R_{s\lambda}\mu_o F^{\downarrow}_{d\lambda} && \text{(B.47)} \end{aligned}$$

while for the upper boundary condition

$$\begin{aligned} d_1 &= -2a && \text{(B.48)} \\ d_2 &= 1 && \text{(B.49)} \\ d_3 &= 2b. && \text{(B.50)} \end{aligned}$$

B.2.1 Enhancement factor for photolysis

The enhancement factor for photolysis is given by

$$f = \frac{4\pi J_\lambda + \mu_o S_{\odot\lambda}}{\mu_o S_{\odot\lambda}} \tag{B.51}$$

where $\mu_o S_{\odot\lambda}$ is equal to the incoming radiation at the top of the atmosphere (TOA). At TOA the boundary condition gives $J_\lambda = -2H_\lambda$ so that the upwards diffusive flux is then equal to $2\pi J_\lambda$. The maximum value for the enhancement factor for photolysis at TOA is then obtained for a purely scattering atmosphere which overlays a surface with reflectance $R_{s\lambda} = 1$. Under these conditions the upwards diffusive flux is equal to the incoming radiation so that $2\pi J_\lambda = \mu_o S_{\odot\lambda}$ and so the maximum value of f at TOA is 3.

Under the above scattering conditions, J_λ becomes constant deep in the atmosphere for large scattering optical depths, where the direct component vanishes, and given by

$$J_{deep\lambda} = \mu_o S_{\odot\lambda}\left(\frac{1}{2\pi} + \frac{3\mu_o}{4\pi}\right) \tag{B.52}$$

so that the maximum value for f is then attained for $\mu_o = 1$ and is equal to 5. We note that the ratio of $J_{TOA\lambda}$ to $J_{deep\lambda}$ is then

$$\frac{J_{TOA\lambda}}{J_{deep\lambda}} = \frac{2}{2 + 3\mu_o} \tag{B.53}$$

and hence, when $\mu_o = 1$ the above ratio is $\frac{2}{5}$.

B.2.2 Delta-Eddington approximation

An improvement to the Eddington method became possible with the δ-Eddington (Joseph et al., 1976). In this, the phase function included a Dirac delta function for the forward scattering along with the two term approximation:

$$p(\vartheta) = 2\mathrm{f}(1 - \cos\vartheta) + (1 - \mathrm{f})(1 + 3g\cos\vartheta). \tag{B.54}$$

This allowed for the improvement of the method's accuracy for highly asymmetric phase functions. In the above, f is the fraction of scattered photons in the forward direction. Assuming that the original phase function that they were approximating was the Henyey-Greenstein phase function, they obtained f$= g^2$. The advantage of this approach was that it provided a set of simple transformations for τ, ω and g which could be used in the Eddington method without the need for any other changes. These were

$$\begin{aligned} \tau^{'} &= (1 - \omega\mathrm{f})\,\tau \\ \omega' &= \frac{(1 - \mathrm{f})\,\omega}{1 - \omega\mathrm{f}} \\ g' &= \frac{g}{1 + g}. \end{aligned} \tag{B.55}$$

B.2.3 Inhomogeneous layers

For Titan's case, a large part of the atmosphere is filled with aerosols. This makes the composition of the atmosphere highly inhomogeneous since inside each atmospheric layer the opacity could have contributions from aerosols, gas molecules and cloud particles each with its one scattering and absorbing properties. The total extinction optical depth of each layer is:

$$\tau = \tau_{aers} + \tau_{aera} + \tau_{ma} + \tau_R \tag{B.56}$$

where τ_{aers} is the aerosol scattering optical depth, τ_{aera} is the aerosol absorption optical depth, τ_{ma} is that for molecular absorption, and τ_R is that for Rayleigh or molecular scattering. The single scattering albedo for each layer is

$$\begin{aligned} \omega &= \omega_c + \omega_{aer} + \omega_R \\ \omega_{aer} &= \tau_{aers}/\tau \\ \omega_R &= \tau_R/\tau \end{aligned} \tag{B.57}$$

where

$$g\omega = g_{aer}\omega_{aer} + g_R\omega_R \tag{B.58}$$

with g_{aer} being the aerosol asymmetry factors with the Rayleigh asymmetry factor $g_R = 0$.

Bibliography

Chandrasekhar, S., 1960. Radiative transfer, Dover Publications

Joseph, J. H., Wiscombe, W. J., Weinman, J. A., 1976. The Delta-Eddington approximation or radiative flux transfer. J. Atmos. Sci. 33, 2452-2459.

Shettle, E.P., Weinman, J.A., 1970. The transfer of solar irradiance through inhomogeneous turbid atmospheres evaluated by Eddington's approximation. J. Atmosp. Sci. 27, 1048-1055.

Vardavas, I.M., Taylor, F.W., 2007. Radiation and Climate, Oxford University Press.

Acronyms

ACP	Aerosol Collector Pyrolyser
CFHT	Canada-France-Hawaii Telescope
CIA	collision-induced absorption
CIRS	Composite Infrared Spectrometer
DISR	Descent Imager / Spectral Radiometer
ESA	European Space Agency
ESO	European Southern Observatory
FTS	Fourier Transform Spectrometer
GCM	General Circulation Model
GCMS	Gas Chromatograph-Mass Spectrometer
HASI	Huygens Atmospheric Structure Instrument
HST	Hubble Space Telescope
IRIS	Infrared Interferometer Spectrometer & Radiometer
ISO	Infrared Space Observatory
ISS	Imaging Science Subsystem
JPL	Jet Propulsion Laboratory
LTE	Local Thermodynamic Equilibrium
NASA	National Aeronautics & Space Administration
NSA	north-south asymmetry
RADAR	Radio Detection and Ranging Instrument
SC	Solar Cycle
SSP	Surface Science Package
TOA	Top OF the Atmosphere
UVS	Ultraviolet Spectrometer
VIMS	Visible and Infrared Mapping Spectrometer
VLT	Very Large Telescope

List of Figures

1.1 Christian Huygens 8
1.2 Titan as observed by the Cassini spacecraft 9
1.3 Natural Satellites of our Solar System 11
1.4 The Voyager 1 and Cassini/Huygens spacecrafts 12
1.5 Vertical temperature profiles retrieved by different instruments for the upper and lower atmosphere 14
1.6 Titan's geometric albedo 16
1.7 Vertical temperature profiles by CIRS, retrieved at different locations of Titan's disk 22
1.8 Cloud & Surface features observed by Cassini/Huygens 24

2.1 Model Flow Chart 32
2.2 Solar flux at the Earth's orbit 33
2.3 Solar Lyman-α profile 34
2.4 N_2 destruction rate due to GCR impact 36
2.5 Total opacities in IR 38
2.6 Tropospheric temperature profiles & lapse rate 42
2.7 N_2 cross section 45
2.8 CH_4 UV cross section 46
2.9 Model calculated photolysis rates for the most important species 48
2.10 CH_4 loss rates from photochemical processes 53
2.11 Condensation loss rate 70
2.12 Impact of geometry assumed in the vertical species profiles. Solid lines describe the mole fractions calculated under spherical geometry and dashed lines the ones under plane-parallel geometry. . . 71
2.13 Radial grid of microphysical model 77
2.14 Atmospheric parameters related with the microphysical description 80
2.15 Slip correction on settling speeds 81
2.16 Settling speed and diffusion coefficient from different size particles 82
2.17 Sticking efficiency & electrostatic repulsion between particles . . 84

3.1 Imaginary part of refractive index of laboratory produced-haze analogs. 108

4.1 Characteristic life time of C_2H_6 relative to characteristic time of transport due to eddy mixing. 122
4.2 The retrieval of the eddy diffusion coefficient used in the model calculations 123
4.3 Comparison of eddy diffusion profiles among different photochemical models. 125
4.4 Sensitivity of methane's thermospheric profile to the escape rate assumed. The measurement is the Yelle et al. (2006) derived abundance from INMS measurements. 127
4.5 Comparison of CH_3 absorption cross section at different temperatures. 128
4.6 Low pressure limit rates for methyl recombination 130
4.7 The effect of $^1CH_2$ on the chemical structure of methane and ethane 130
4.8 Model results for the mixing ratio of ethylene and acetylene . . . 132
4.9 Model calculated vertical profile of methylacetylene and its isomer allene. 134
4.10 Model calculated vertical profile of propane 135
4.11 Model calculated vertical profile of diacetylene 137
4.12 Heterogeneous loss rate for H 138
4.13 Impact of heterogeneous chemistry on atomic and molecular hydrogen 139
4.14 Model calculated vertical profile for C_6H_X species 141
4.15 Model calculated vertical profiles for methyleneimine and hydrogen cyanide 146
4.16 Calculated vertical profiles of NH_3 and C_2H_5N from the model. . 148
4.17 Model vertical profile for acetonitrile 149
4.18 Model vertical profile for acetonitrile 150
4.19 Model vertical profile for cyanoacetylene 151
4.20 Model vertical profiles for cyanogen and dicyanogen 153
4.21 Variation of photolysis rates for N_2 and CH_4 due to variability of the incoming solar flux during the solar cycle 155
4.22 Sensitivity of hydrocarbon species vertical profiles on the solar cycle 157
4.23 Sensitivity of nitrile species vertical profiles on the solar cycle . . 158

5.1 Haze vertical production profiles from aromatics. 166
5.2 Haze vertical production profiles from polyynes. 167
5.3 Haze vertical production profiles from copolymers. 168
5.4 Haze vertical production profiles from pure nitriles. 169
5.5 The vertical production profile of haze particles (monomers) from all pathway families 170
5.6 Impact of GCR on species and haze production 172
5.7 The impact of chemical loss to haze on the profiles of species involved in the haze pathways 175
5.8 The variation of haze production, haze opacity and HCN abundance with γ parameter 177

5.9 Haze production variability over solar cycle 178

6.1 Calculated geometric albedo for different values of the charging rate between aerosol particles. 182
6.2 Contour plot of the model size distribution for the haze particles 183
6.3 Impact of solar scaling factor for haze refractive index on the modelled geometric albedo. 185
6.4 The eddy mixing profile used for the aerosol particles 186
6.5 Haze total opacity 187
6.6 Haze extinction profiles from model and DISR observations . . . 188
6.7 Observed & modelled geometric albedo 190
6.8 Spectral variation of the surface albedo used in the model. 191
6.9 Model surface albedo inside the methane windows in the range 1.0 - 2.5 μm 192
6.10 Calculated and modelled vertical temperature profile 195
6.11 Sensitivity of vertical temperature profile on the scaling factors of the haze particles 196
6.12 Comparison of modelled and observed atmospheric mass density and pressure profiles 198
6.13 Impact of solar cycle variability on the calculated temperature structure 198
6.14 The impact of solar cycle variability on the modelled geometric albedo 200

A.1 UV cross sections for main species 213
A.2 Lorentz, Doppler & Voigt line profiles 218
A.3 ck-distribution examples 222
A.4 Collision induced absorption coefficients 225
A.5 Scattering geometry 226
A.6 Electric field vectors in scattering geometry 227
A.7 Angle distribution of Rayleigh scattered radiation 229
A.8 Scattering efficiencies as a function of the size parameter for different absorption properties. 232
A.9 The variation of the three efficiency factors with the size parameter for different imaginary refractive index. 233
A.10 Phase function of water vapor at two different wavelengths and for different size spheres. 234
A.11 Polar view of phase function for different size particles 235
A.12 Variation of asymmetry factor, g, with size parameter for different absorption properties. 235

List of Tables

1.1 Physical Properties of Titan's & Earth's atmospheres 13
1.2 Geometric albedo observations 17
1.3 Titan's Chemical Gas Composition 20

2.1 Suggested methane photochemical schemes at Ly-α 47
2.2 Photolysis Reactions 50
2.3 Chemical Reactions 58
2.4 Binary & thermal diffusion coefficients 67
2.5 Vapor pressure parameters & Heats of formation 69
2.6 The radial grid used in the microphysical model 78

3.1 Laboratory Haze Simulations 106
3.2 Reactions used for the gas-to-particle transformation 110

4.1 Mole fractions at 1200 km and escaping H & H_2 fluxes 140
4.2 Production and loss processes for methyleneimine used in the model calculations. 144
4.3 Column photochemical production and loss rates for the main hydrocarbon and nitrile species in Titan's atmosphere 155

5.1 Column production rates for the families studied at different regions of the atmosphere along with the total C, N and H lost in the chemical formation and growth of the haze monomers. 173
5.2 C/N and C/H ratios along with column production rate for different values of the γ ratio 176

A.1 Cross section units 214
A.2 Partition function parameters 216
A.3 Characteristic Doppler widths relative to the line center for important species in the thermal radiation transfer of Titan's atmosphere. 217
A.4 CH_4 cross section references 219
A.5 Eight-point Gaussian quadrature abscissae & weights 224
A.6 CIA pairs and references 224
A.7 Rayleigh Scattering parameters 230

Index

Atmospheric medium
    Dynamic Viscosity, 79
    Mean free path, 79
    Thermal velocity, 79

Boundary Conditions, 73

C/N & C/H ratios, 108, 174
Chemical Composition
    Acetonitrile, 148
    Acetylene, 133
    Acrylonitrile, 149
    Ammonia, 147
    Benzene, 141
    Benzyne & Triacetylene, 142
    Cyanoacetylene, 151
    Cyanogen & Dicyanogen, 152
    Diacetylene, 137
    Ethane, 127
    Ethylene, 131
    HCN, 143
    Hydrogen, 140
    Methyleacetylene & Allene, 133
    Methyleneimine, 143
    Observations, 17
    Propane, 135
Chemical loss to haze, 115, 174, 204
Chemistry
    Catalytic destruction, 52
    Hydrocarbons, 49
    Nitriles, 55
    Rates, 49
Clouds, 23, 185
Coagulation
    Brownian diffusion kernel, 81
    Brownian enhancement kernel, 82
    Charging rate, 83, 181
    Coalescence efficiency, 83
    Gravitational kernel, 83
Condensates, 23
Condensation, 67
Conduction coefficient, 42
Continuity equation, 68
Curtis-Godson approximation, 41

Delta-Eddington method, 39
Diffusion
    Eddy, 67, 121
    Molecular, 66
Diffusivity factor, 41

Effective radius, 182
Effective Temperature, 10
Emissivity, 40
Energy Sources, 32
    Electrons, 35
    Galactic cosmic rays (GCR), 35
    Solar photons, 32
Enhancement factor
    maximum values, 244

Flow Chart, 31

Geometric Albedo
    Modelled, 189
    Observations, 15

Haze
    Cut-off, 21
    Detached haze, 21
    Extinction profiles, 187
    Mixing profile, 184
    Observations, 19
    Particle shape, 21
Haze analogs, 105

Haze pathways, 109, 203
Haze production
    Aliphatic Copolymers, 167
    Aromatics, 165
    GCR impact, 171
    Nitrogen sink, 174
    Polyynes, 166
    Pure Nitriles, 168
    Vertical profile, 169
Henyey-Greenstein phase, 245
Heterogeneous chemistry, 138, 152, 204
Homopause, 122, 126

Lapse rate, 41
Lyman-α, 34

Mass density, 197
Methane Escape, 126
Methyl radicals, 127, 205
    Photolysis, 128
    Recombination rate, 129
Microphysics
    Knudsen, Reynolds & Schmidt Numbers, 79
    Continuity Equation, 75
    Diffusion Coefficient, 81
    Settling speed, 80
    Slip-correction, 81
    Volume fractions, 77
    Volume ratio grid, 76
Monomer size, 114

Net photochemical production, 153
Non-ideal factor, 37
North South Asymmetry (NSA), 22

Opacity Sources, 38
    Collision Induced Absorption, 224
    Haze, 186
    Methane, 219
    Mie Scattering, 230
    Rayleigh scattering, 228

Penetration altitude, 189
Photochemistry
    CH_4 photolysis, 45
    N_2 photolysis, 44, 204
    Photolysis rates, 49
Photolysis
    enhancement factor, 243, 244
Pressure Grid, 37

Radiance
    second moment, 242
    third moment, 242
Radiation diffusion equation, 242
Radiation Transfer, 37
    Conduction, 42
    Longwave , 40
    Shortwave, 39
Refractive index, 105
    Geometric albedo, 184
    Scaling factors, 184
    Temperature, 194

Scattering
    isotropic, 240
Seasonal Variability, 22
Solar Cycle, 32
Solar Flux, 34
Source function
    angle-dependent, 241
    angle-independent, 240
    first moment, 242
    incoming radiation, 241
    scattering, 241
    second moment, 242
    thermal emission, 241
Spatial Variability, 21
Spectral reflectance, 244
Spectrum Devision, 37
Spherical Geometry, 68
Surface
    Albedo, 25, 193
    Features, 25

Temperature
    Convective adjustment, 42
    Model Calculation, 41
    Modelled profile, 193
    Observations, 13
Thermal window, 39
Titan

Dominant species, 10
Mythology, 7
name, 8
physical properties, 10
Tracer Species, 121

Vapor pressure curves, 68

Waves, 15